

**Document Version**

Final published version

**Citation (APA)**

Ombrini, P. (2026). *Physically Consistent Modeling of Lithium Iron Phosphate Electrodes: From lattice properties to electrode microstructure*. [Dissertation (TU Delft), Delft University of Technology].  
<https://doi.org/10.4233/uuid:33ebc5e0-8956-46fa-9ce5-d25cefa99006>

**Important note**

To cite this publication, please use the final published version (if applicable).  
Please check the document version above.

**Copyright**

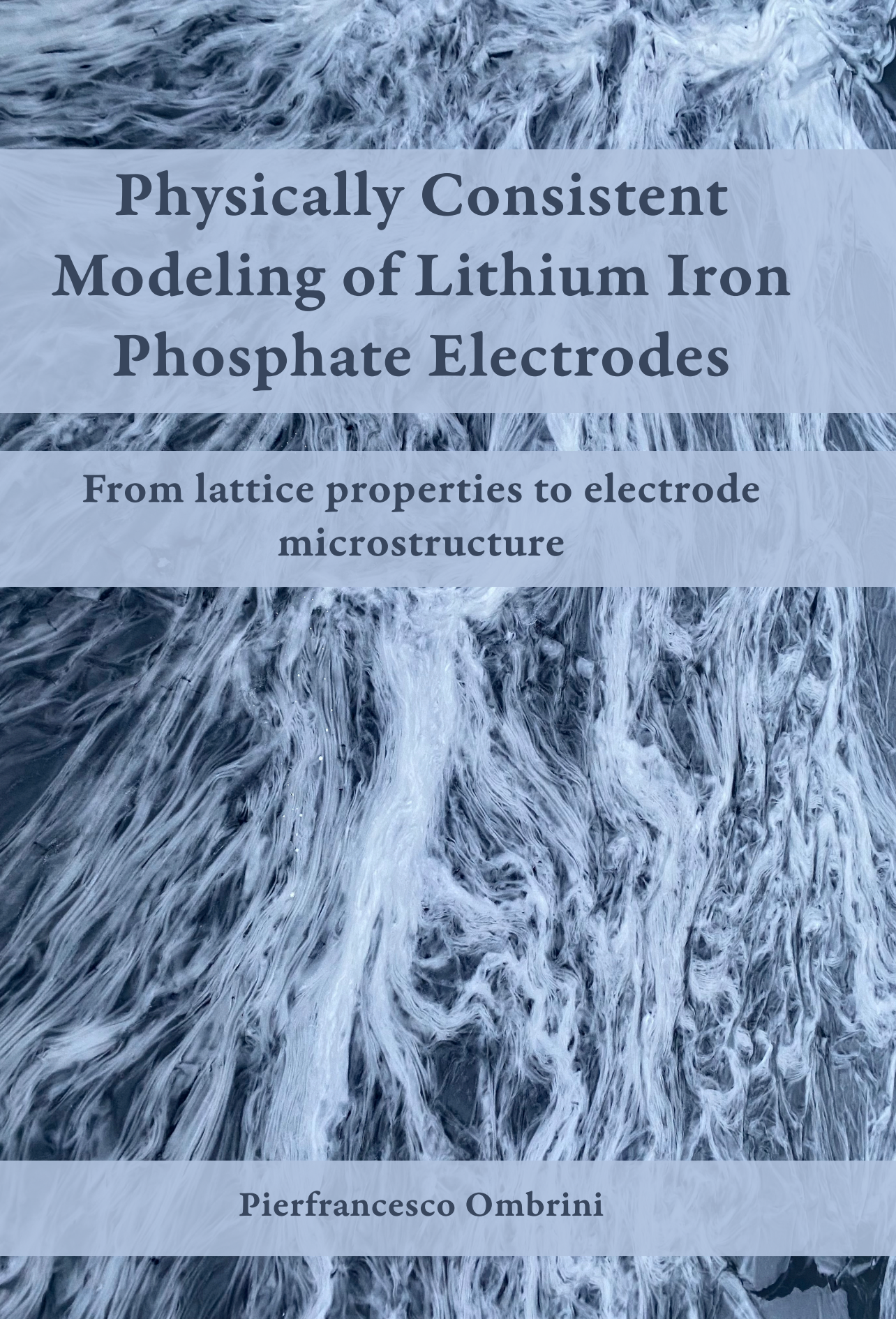
In case the licence states “Dutch Copyright Act (Article 25fa)”, this publication was made available Green Open Access via the TU Delft Institutional Repository pursuant to Dutch Copyright Act (Article 25fa, the Taverne amendment). This provision does not affect copyright ownership.  
Unless copyright is transferred by contract or statute, it remains with the copyright holder.

**Sharing and reuse**

Other than for strictly personal use, it is not permitted to download, forward or distribute the text or part of it, without the consent of the author(s) and/or copyright holder(s), unless the work is under an open content license such as Creative Commons.

**Takedown policy**

Please contact us and provide details if you believe this document breaches copyrights.  
We will remove access to the work immediately and investigate your claim.



# **Physically Consistent Modeling of Lithium Iron Phosphate Electrodes**

**From lattice properties to electrode  
microstructure**

**Pierfrancesco Ombrini**

# PHYSICALLY CONSISTENT MODELING OF LITHIUM IRON PHOSPHATE ELECTRODES

## FROM LATTICE PROPERTIES TO ELECTRODE MICROSTRUCTURE

### **DISSERTATION**

for the purpose of obtaining the degree of doctor  
at Delft University of Technology  
by the authority of the Rector Magnificus,  
Prof.dr.ir. H. Bijl,  
chair of the Board of Doctorates,  
to be defended publicly on  
Friday 17 April 2026 at 12:30

by

**Pierfrancesco Ombrini**



This dissertation has been approved by the (co)promotors.

Composition of the doctoral committee:

Rector Magnificus,	chairperson
Prof.dr.ir. M. Wagemaker,	Delft University of Technology, promotor
Dr.ir. A. Vasileiadis,	Delft University of Technology, copromotor

*Independent opponents:*

Prof.dr. F. M. Mulder,	Delft University of Technology
Prof.dr. M. Z. Bazant,	Massachusetts Institute of Technology, USA
Prof.dr. C. Grey,	University of Cambridge, UK
Dr. S. Cooper,	Imperial College London, UK
Prof.dr. F.C. Grozema	Delft University of Technology, <i>reserve member</i>



*Keywords:* Battery, Electrodes, Modeling, Thermodynamics, Simulations, Phase separation

*Cover:* Photo of the frozen Charles River taken by the author. No generative artificial intelligence was used to create the cover.

ISBN: 978-94-6534-321-1

Copyright © 2026 by P. Ombrini

All rights reserved

Printed by: Proefschriftmaken

An electronic copy of this this dissertation is available at

<https://respository.tudelft.nl>

*“Knowledge is like a baobab tree: no single person can embrace it all.”*

-Akan and Ewe proverb.

## SUMMARY

Decarbonizing energy usage is essential to sustain global development while avoiding the worst impacts of climate change. Energy storage plays a central role, enabling the integration of renewable sources and the decarbonization of transport. Among available technologies, Li-ion batteries are the fastest growing, offering high efficiency, reversibility, long cycle life, and rapidly decreasing costs. These features have made them ubiquitous, from grid stabilization to electric vehicles and residential storage.

Commercial Li-ion batteries, initially based on graphite (anode) and  $\text{LiCoO}_2$  (cathode), now mainly employ  $\text{LiNi}_x\text{Mn}_y\text{Co}_{1-x-y}\text{O}_2$  (NMC) or  $\text{LiFePO}_4$  (LFP) as cathode materials. Once considered a low-cost option for short-range vehicles, LFP has quickly become the dominant cathode material, powering high-end EVs and battery energy storage systems. This success is due to advances in material design and cell engineering, which improved active material use, minimized inactive components, and ensured safe operation. This transformation highlights the importance of system-level approaches, linking scales from atoms to full packs. Simulations play a key role in this process. For instance, atomistic methods can identify promising chemistries, fluid dynamics can optimize cooling, and electrode-level models connect physical properties to electro-thermal behavior. Such predictive tools accelerate development, improve safety, and help mitigate degradation.

Electrode-level modeling is typically carried out through the Doyle–Fuller–Newman (DFN) model, cornerstone of battery modeling for decades. However, it was originally developed for solid-solution electrodes as layered oxides (LCO, NMC) and rely heavily on empirical fitting. This makes it poorly suited for materials such as LFP which does not equilibrate at arbitrary lithium compositions, relaxing instead into Li-rich and Li-poor phases. The goal of this thesis is therefore to simulate the behavior of commercially relevant LFP electrodes (and related chemistries) using models grounded in thermodynamics, avoiding empirical relations. Starting from previous advanced and accurate models, described in **Chapter 2**, this work addressed the electrode scale by capturing the additional limitations occurring in commercial electrodes, while still adhering to validated single-particle dynamic models.

To highlight the necessity and the effects of using thermodynamically derived open-circuit potentials (OCPs), **Chapter 3** starts by introducing the simplest possible electrode model. Specifically, solid-solution materials are characterized by monotonic OCPs, while phase-separating materials are better captured by non-monotonic ones. This is shown to significantly affect electrode dynamics and rate capabilities. Moreover, comparing non-monotonic to

conventional flat OCPs demonstrates the shortcomings of semi-empirical methods, which force-fit battery behavior into DFN frameworks. Only thermodynamically consistent models reproduce phase separation, voltage hysteresis, and pulse cycling behavior.

**Chapter 4** extends this framework to  $\text{LiMn}_x\text{Fe}_{1-x}\text{PO}_4$  (LMFP), the latest evolution of LFP. The regular solution model, foundation of the previous chapter, is expanded to account for multiple redox species and sublattices within the crystal. By incorporating ion-vacancy interactions within and between sublattices, the model predicts OCPs for various LMFP compositions, including Co-substituted variants. This thermodynamic theory is integrated into a phase-field model, successfully reproducing phase transitions in both single and multi-particle systems, in agreement with operando x-ray diffraction experiments.

Having established the importance of using realistic potential profiles and a theory to obtain them, **Chapter 5** extends the model by incorporating intra-particle phase separation dynamics. This addition allows to capture the interplay between intra- and inter-particle phase separation, which strongly shapes electrode behavior under different current rates. Consistent with micro-beam x-ray diffraction, simulations show that higher rates increase the fraction of phase-separated particles. This improves particle utilization and reduces overpotentials in the later steps of the charging process. Once again, only physically rigorous phase-field models can capture both internal dynamics and voltage profiles, while DFN approaches prove inadequate.

Building on this foundation, **Chapter 6** applies the validated modeling framework to analyze the frequency response of these electrodes by computing their linearized impedance. The results reveal distinct characteristics: a marked asymmetry between charge and discharge at the same state of charge, and (as anticipated from Chapter 5) a strong dependence on the previously applied rate.

The approaches developed so far, however, break down when a different LFP electrode morphology is introduced. In Chapter 5, including diffusion-limited phase separation within a porous electrode theory was sufficient to capture the observed phenomena. **Chapter 7** shows that electrodes composed of platelet-like single-crystal particles cannot be modeled with the same method. The nanoscale nature of these particles prevents a complete contact with the conductive additives, and their limited electrical conductivity introduces an additional limiting factor: the inter-particle contact. The current is then forced to pass through several nanoparticles before reaching the reactive ones. This phenomenon has been known experimentally, yet it was always treated empirically in electrode modeling. In this work, the phenomenon is rigorously investigated through tomographic characterization of the microstructure and extraction of the electrical networks that govern the reactions. Including this effect proved essential to

reproducing the electrochemical response with minimal fitting, while relying only on physically validated models.

Having established two different methods for single-crystal LFP electrodes, **Chapter 8** shift the attention to nanoporous secondary particles. Instead of a discrete system of connected single-crystals, these secondary particles can be modeled as homogenized porous reactive systems. In these systems, the limiting factor remains the electrical potential drop within the secondary particles. This effect is so included in three-dimensional single-particle simulations, and their results are used to build a reduced-order model. Including the model in a porous electrode framework, the performance of both thin and thick electrodes can be reproduced. The resulting model is thus including inter-particle phase separation, hierarchical ionic and electronic transport processes, and validated reaction kinetics. With these tools, the model can connect the electrode microstructure to the performance, suggesting optimal composition and thicknesses for specific applications.

Finally, **Chapter 9** broadens the investigation by reconsidering ion transport in LFP from a fundamental perspective. It is shown that lithium diffusion in the one-dimensional channels of LFP follows a single-file diffusion regime, where ions cannot pass each other. Using tracer-exchange experiments supported by Kinetic Monte Carlo simulations, we identify the crossover from single-file to ordinary diffusion and extract reaction rate constants. This combined approach also allows us to separate ionic and electronic limitations in the reaction process, revealing that electron transport is the dominant rate-limiting factor in LFP.

This work demonstrates that simulating LFP electrodes requires advanced, thermodynamically consistent models. Only by explicitly accounting for phase separation the electrochemical response can be captured with accuracy. At the same time, electronic transport plays a critical role, both at the electrode scale, through the connectivity of the conductive network, and at the particle scale, where electron transfer limits the reaction itself.

Future work should validate the role of electronic pathways across different morphologies, coatings, and conductive additives, and extend the analysis of the reaction kinetics of LMFP. Particular attention should be given to separating ionic and electronic contributions in electrode dynamics, since electron transport can be a dominant limiting factor. On the modeling side, the challenge is to reduce the computational cost of phase-field models. If this is achieved, they can be integrated into two- and three-dimensional cell models and, eventually, into control strategies. Beyond LFP, the framework developed here can serve as a guide for studying other phase-separating materials with low electronic conductivity, such as sodium-ion chemistries. By combining rigorous thermodynamic models with explicit treatment of electronic transport, it will be possible to achieve a more complete and predictive understanding of these systems, ultimately supporting their optimization for next-generation energy storage technologies.



# SAMENVATTING

Het decarboniseren van het energiegebruik is essentieel om de wereldwijde ontwikkeling in stand te houden en tegelijkertijd de zwaarste gevolgen van klimaatverandering te vermijden. Energieopslag speelt hierbij een centrale rol: het maakt de integratie van hernieuwbare bronnen en de verduurzaming van transport mogelijk. Onder de beschikbare technologieën groeien Li-ionbatterijen het snelst, dankzij hun hoge efficiëntie, omkeerbaarheid, lange levensduur en snel dalende kosten. Deze eigenschappen hebben ze alomtegenwoordig gemaakt, van netstabilisatie tot elektrische voertuigen en residentiële opslag.

Commerciële Li-ionbatterijen, aanvankelijk gebaseerd op grafiet (anode) en  $\text{LiCoO}_2$  (kathode), maken tegenwoordig voornamelijk gebruik van  $\text{LiNi}_x\text{Mn}_y\text{Co}_{1-x-y}\text{O}_2$  (NMC) of  $\text{LiFePO}_4$  (LFP) als kathodematerialen. LFP werd ooit beschouwd als een goedkope optie voor voertuigen met een korte actieradius, maar is inmiddels snel uitgegroeid tot het dominante kathodemateriaal. Het voedt nu hoogwaardige EV's en batterij-energiesystemen. Dit succes is te danken aan vooruitgang in materiaalontwerp en celengineering, waardoor het gebruik van actief materiaal is verbeterd, inactieve componenten zijn geminimaliseerd en een veilige werking is verzekerd. Deze transformatie benadrukt het belang van systeemgerichte benaderingen, die schalen verbinden van atomen tot volledige batterijpacks. Simulaties spelen hierin een sleutelrol. Zo kunnen atomistische methoden veelbelovende chemieën identificeren, kan stromingsleer de koeling optimaliseren en koppelen elektrode-modellen fysische eigenschappen aan elektrothermisch gedrag. Dergelijke voorspellende hulpmiddelen versnellen de ontwikkeling, verbeteren de veiligheid en helpen degradatie te beperken.

Modellering op elektrode-niveau wordt doorgaans uitgevoerd met behulp van het Doyle–Fuller–Newman (DFN)-model, dat al decennia de hoeksteen van batterijmodellering vormt. Het werd echter oorspronkelijk ontwikkeld voor vaste-oplossingselektroden zoals gelaagde oxiden (LCO, NMC) en steunt sterk op empirische fitmethoden. Dit maakt het slecht geschikt voor materialen zoals LFP, die niet bij willekeurige lithiumsamenstellingen in evenwicht zijn, maar in plaats daarvan relaxeren naar Li-rijke en Li-arme fasen. Het doel van dit proefschrift is daarom het gedrag van commercieel relevante LFP-elektroden (en verwante chemieën) te simuleren met modellen die in de thermodynamica zijn verankerd, waarbij empirische relaties worden vermeden. Uitgaande van eerdere geavanceerde en nauwkeurige modellen, beschreven in **Hoofdstuk 2**, richt dit werk zich op de elektrode-schaal door de bijkomende beperkingen vast te leggen die optreden in commerciële elektroden, terwijl het trouw blijft aan gevalideerde single-particle dynamische modellen.

Om de noodzaak en de effecten van het gebruik van thermodynamisch afgeleide open-circuit potentialen (OCP's) te benadrukken, introduceert **Hoofdstuk 3** het eenvoudigst mogelijke elektrode-model. Concreet worden vaste-oplossingsmaterialen gekarakteriseerd door monotoon verlopende OCP's, terwijl fase-separerende materialen beter worden beschreven met niet-monotone OCP's. Dit blijkt de elektrodedynamica en de laadsnelheden aanzienlijk te beïnvloeden. Bovendien laat de vergelijking van niet-monotone met conventionele vlakke OCP's de tekortkomingen zien van semi-empirische methoden, die het batterijgedrag geforceerd inpassen in DFN-kaders. Alleen thermodynamisch consistente modellen kunnen fase-separatie, spanningshysterese en puls-cyclisch gedrag correct reproduceren.

**Hoofdstuk 4** breidt dit kader uit naar  $\text{LiMn}_x\text{Fe}_{1-x}\text{PO}_4$  (LMFP), de nieuwste evolutie van LFP. Het regular solution model, dat de basis vormde van het vorige hoofdstuk, wordt uitgebreid om meerdere redoxsoorten en subroosters binnen het kristal in aanmerking te nemen. Door ion-vacature-interacties binnen en tussen subroosters op te nemen, voorspelt het model OCP's voor verschillende LMFP-samenstellingen, inclusief Co-gesubstitueerde varianten. Deze thermodynamische theorie wordt geïntegreerd in een faseveldmodel, dat met succes faseovergangen in zowel single- als multi-particle systemen reproduceert, in overeenstemming met operando röntgendiffractie-experimenten.

Na het belang van realistische potentiaalprofielen en een theorie om ze te verkrijgen te hebben vastgesteld, breidt **Hoofdstuk 5** het model uit door intra-deeltjes fase-separatiedynamica op te nemen. Deze toevoeging maakt het mogelijk de wisselwerking tussen intra- en inter-deeltjes fase-separatie vast te leggen, die het elektrodegedrag onder verschillende stroomsnelheden sterk beïnvloedt. In overeenstemming met microbeam-röntgendiffractie laten simulaties zien dat hogere stroomsnelheden de fractie fase-gescheiden deeltjes vergroten. Dit verbetert het gebruik van deeltjes en vermindert de overspanningen in de latere fasen van het laadproces. Opnieuw kunnen alleen fysisch rigoureuze faseveldmodellen zowel interne dynamica als spanningsprofielen vastleggen, terwijl DFN-benaderingen tekortschieten.

Op deze basis past **Hoofdstuk 6** het gevalideerde modelleringskader toe om de frequentierespons van deze elektroden te analyseren door hun gelineariseerde impedantie te berekenen. De resultaten onthullen duidelijke kenmerken: een uitgesproken asymmetrie tussen laden en ontladen bij dezelfde ladingstoestand, en (zoals voorspeld in Hoofdstuk 5) een sterke afhankelijkheid van de eerder toegepaste laadsnelheid.

De tot nu toe ontwikkelde benaderingen lopen echter stuk wanneer een andere LFP-elektrodemorfologie wordt geïntroduceerd. In Hoofdstuk 5 volstond het opnemen van diffusiebeperkte fase-separatie binnen een poreuze-elektrode-theorie om de waargenomen fenomenen vast te leggen. **Hoofdstuk 7** toont aan dat elektroden die bestaan uit plaatvormige

enkelkristal-deeltjes niet met dezelfde methode kunnen worden gemodelleerd. De nanoschaal van deze deeltjes voorkomt een volledig contact met de geleidende additieven, en hun beperkte elektrische geleidbaarheid introduceert een bijkomende beperkende factor: het inter-deeltjes contact. De stroom wordt daardoor gedwongen door verschillende nanodeeltjes te gaan voordat deze de reactieve deeltjes bereikt. Dit fenomeen was experimenteel al bekend, maar werd altijd empirisch behandeld in elektrode-modellering. In dit werk wordt het fenomeen rigoureus onderzocht via tomografische karakterisering van de microstructuur en extractie van de elektrische netwerken die de reacties beheersen. Het opnemen van dit effect bleek essentieel om de elektrochemische respons met minimale fitting te reproduceren, terwijl uitsluitend werd vertrouwd op fysisch gevalideerde modellen.

Na de vaststelling van twee verschillende methoden voor enkelkristal LFP-elektroden, verlegt **Hoofdstuk 8** de aandacht naar nanoporeuze secundaire deeltjes. In plaats van een discreet systeem van verbonden enkelkristallen kunnen deze secundaire deeltjes worden gemodelleerd als gehomogeniseerde poreuze reactieve systemen. In deze systemen blijft de beperkende factor de elektrische potentiaalval binnen de secundaire deeltjes. Dit effect wordt opgenomen in driedimensionale single-particle simulaties, waarvan de resultaten worden gebruikt om een gereduceerd-orde model op te stellen. Door dit model op te nemen in een poreus elektrode-kader kan de prestatie van zowel dunne als dikke elektroden worden gereproduceerd. Het resulterende model omvat dus inter-deeltjes fase-separatie, hiërarchische ionische en elektronische transportprocessen en gevalideerde reactiekinetiek. Met deze hulpmiddelen kan het model de elektrode-microstructuur koppelen aan de prestaties en optimale samenstellingen en diktes voor specifieke toepassingen suggereren.

Ten slotte verruimt **Hoofdstuk 9** het onderzoek door het ionentransport in LFP vanuit een fundamenteel perspectief opnieuw te bekijken. Er wordt aangetoond dat lithiumpdiffusie in de eendimensionale kanalen van LFP een single-file diffusie-regime volgt, waarbij ionen elkaar niet kunnen passeren. Met behulp van tracer-uitwisselingsexperimenten, ondersteund door Kinetic Monte Carlo simulaties, identificeren we de overgang van single-file naar gewone diffusie en extraheren we reactiesnelheidsconstanten. Deze gecombineerde aanpak maakt het ook mogelijk om ionische en elektronische beperkingen in het reactieproces te scheiden, waarbij wordt onthuld dat elektronentransport de dominante snelheidsbepalende factor in LFP is.

Dit werk toont aan dat het simuleren van LFP-elektroden geavanceerde, thermodynamisch consistente modellen vereist. Alleen door fase-separatie expliciet mee te nemen kan de elektrochemische respons met nauwkeurigheid worden vastgelegd. Tegelijkertijd speelt elektronentransport een cruciale rol, zowel op elektrode-schaal, via de connectiviteit van het geleidende netwerk, als op deeltjes-schaal, waar elektronoverdracht de reactie zelf beperkt.

Toekomstig werk zou de rol van elektronische paden in verschillende morfologieën, coatings en geleidende additieven moeten valideren, en de analyse van de reactiekinetiek van LMFP moeten uitbreiden. Bijzondere aandacht moet worden besteed aan het scheiden van ionische en elektronische bijdragen in elektrodynamica, aangezien elektronentransport een dominante beperkende factor kan zijn. Aan de modelleringskant ligt de uitdaging in het verlagen van de rekenkosten van faseveldmodellen. Als dit wordt bereikt, kunnen ze worden geïntegreerd in twee- en driedimensionale celmodellen en uiteindelijk in regelstrategieën. Buiten LFP kan het hier ontwikkelde kader dienen als leidraad voor het bestuderen van andere fase-separerende materialen met lage elektronische geleidbaarheid, zoals natrium-ionchemieën. Door rigoureuze thermodynamische modellen te combineren met een expliciete behandeling van elektronentransport kan een vollediger en voorspellender begrip van deze systemen worden bereikt, wat uiteindelijk hun optimalisatie voor energieopslagtechnologieën van de volgende generatie ondersteunt.



# TABLE OF CONTENTS

<b>1 The need for battery modeling</b>	<b>1</b>
1.1 CO <sub>2</sub> Emission by Sector.....	2
1.1.1 Transportation.....	3
1.1.2 Energy generation and management .....	3
1.1.3 Industrial Sector and Building Sector.....	4
1.2 The history.....	4
1.3 The working principle.....	5
1.4 The challenges.....	6
1.5 Lithium Iron Phosphate .....	8
1.6 Battery Modeling.....	9
1.6.1 Ab Initio Methods .....	10
1.6.2 Kinetic Monte Carlo.....	11
1.6.3 Mesoscale modeling .....	12
1.7 Outline of the thesis .....	13
References .....	15
<b>2 Multiphase porous electrode theory</b>	<b>21</b>
2.1 Electrode-scale model.....	22
2.2 Coupling electrode and particle scales.....	25
2.3 Reaction kinetics .....	26
2.4 Phase-field modeling .....	28
2.5 Particle-scale models .....	30
2.5.1 Diffusion-Limited Model .....	31
2.5.2 Reaction-Limited Model.....	33
2.6 Advanced modeling.....	34
References .....	36

<b>3</b>	<b>The Influence of Open Circuit Potential on Electrode Dynamics</b>	<b>41</b>
3.1	Introduction .....	43
3.2	From the free energy to the open circuit potentials.....	45
3.3	Model's equations.....	48
3.4	Results .....	52
3.5	Constant current protocol.....	53
3.6	GITT protocol.....	56
3.7	The effect of kinetic parameters .....	58
3.8	Comparison between physically derived and fitted OCPs.....	59
3.9	Discussion and Conclusion.....	61
	References.....	63
<b>4</b>	<b>Thermodynamics of multi-sublattice active materials</b>	<b>69</b>
4.1	Introduction .....	71
4.2	Theory .....	72
4.3	Multi-sublattice model .....	74
4.4	Application to phospho-olivine cathodes.....	78
4.5	Phase-field modeling.....	82
4.6	Single particle simulations .....	83
4.7	Porous electrode simulations.....	84
4.8	Conclusions .....	87
	References.....	89
	Supplementary Information.....	95
<b>5</b>	<b>Kinetically Induced Memory Effect in Li-ion Batteries</b>	<b>111</b>
5.1	Introduction .....	113
5.2	Memory effect in commercial battery electrode materials .....	114
5.3	Monitoring the phase transition in individual grains .....	116
5.4	Electrochemical modeling of the memory effect.....	119
5.5	Analytical approximation .....	122

5.6	Conclusions.....	124
	Materials and Methods.....	128
	References.....	131
	Supplementary Information.....	134
<b>6</b>	<b>The impedance response of phase separating electrodes</b>	<b>165</b>
6.1	Introduction.....	167
6.2	Cahn-Hilliard Reaction Model.....	169
6.3	Charge transfer resistance in phase-separating materials.....	172
6.4	The impedance of the SPM-CHR model.....	174
6.5	The impedance of the DFN-CHR model.....	176
6.6	The impedance of the multi-particle DFN-CHR model.....	178
6.7	Brute force method.....	181
6.8	Conclusions.....	183
	References.....	185
	Supplementary Information.....	188
<b>7</b>	<b>Modeling Single-Crystal Electrodes as a Network of Primary Particles</b>	<b>193</b>
7.1	Introduction.....	195
7.2	The electrode as a network of connected reactive particles.....	197
7.3	Intercalation dynamics in single-crystal electrodes.....	200
7.4	The effect of temperature.....	202
7.5	Conclusions.....	203
	Methods.....	205
	References.....	206
	Supplementary Information.....	210
<b>8</b>	<b>Multiscale modeling of Lithium Iron Phosphate electrodes composed by nanoporous secondary particles</b>	<b>245</b>
8.1	Introduction.....	247

8.2	Model overview .....	249
8.3	The effect of CBD distribution on the single particle dynamics .....	253
8.4	Reduce order modeling of the effect of CBD distribution.....	255
8.5	Predicting the voltage profile with the multi-particle DFN model ....	257
8.6	Electrode dynamics .....	259
8.7	Optimizing electrode loading .....	262
8.8	Conclusions .....	263
	Methods.....	265
	References.....	266
	Supplementary Information.....	269
<b>9</b>	<b>Non-Fickian Ionic Diffusion in Lithium Iron Phosphate</b>	<b>279</b>
9.1	Introduction .....	281
9.2	Subdiffusion in ${}^6\text{Li}$ - ${}^7\text{Li}$ exchange.....	286
9.3	Kinetic Monte Carlo simulations .....	287
9.4	The role of carbon coating on the reaction kinetics .....	290
9.5	Conclusions .....	292
	Materials and Methods.....	294
	References.....	296
	Supplementary Information.....	298
	<b>List of Publications</b>	<b>307</b>
	<b>Curriculum Vitae</b>	<b>309</b>
	<b>Acknowledgements</b>	<b>310</b>



# 1 THE NEED FOR BATTERY MODELING

## 1.1 CO<sub>2</sub> EMISSION BY SECTOR

The accumulation of carbon dioxide (CO<sub>2</sub>) in the atmosphere is a primary driver of global warming and climate change. As underscored by the Intergovernmental Panel on Climate Change (IPCC), achieving the targets set by the Paris Agreement (limiting global temperature rise to below 2 °C) requires a rapid reduction in CO<sub>2</sub> emissions across all sectors<sup>1</sup>. Analyzing emissions by sector (Fig. 1.1), we can see the largest share of CO<sub>2</sub> emissions originating from electricity and heat generation, which remains heavily reliant on fossil fuels. Transportation and industrial activities are also major contributors, driven by their dependence on internal combustion engines and high-temperature fossil-fueled processes, respectively. Emissions in these sectors can be substantially reduced by transitioning to cleaner energy sources and increasing electrification.

Global Greenhouse Gas Emissions by Sector (2021)

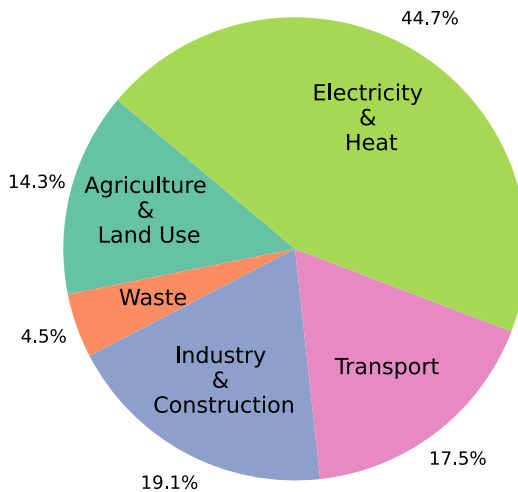


Figure 1.1 CO<sub>2</sub> emission by sector as of 2021. The data are obtained from Ref.<sup>2</sup>.

In this context, nuclear and hydroelectric power can play an important role, as they offer programmable carbon-free power generation. However, both require high capital investment and face slow rates of global expansion due to political constraints. Wind and solar are faster in deployment and cost-competitive. Despite these advantages, their aleatory nature requires advanced grid management and energy storage solutions<sup>3</sup>. As a result, there is an increasing need for flexible, dispatchable energy storage technologies. For sectors such as industry and transport, there is also a need for portable energy carriers. Hydrogen is often proposed as a solution due

to its high energy density; however, its development remains slow, and costs are currently prohibitive for widespread use<sup>4</sup>.

Lithium-ion batteries (LIBs) represent the most commercially mature and scalable energy storage technology currently available<sup>5</sup>. Developed for applications in consumer electronics, they are now deployed in electric vehicles (EVs) and battery energy storage systems (BESS) in power grids. Emerging battery technologies, such as sodium-ion batteries and redox flow batteries, are under active development<sup>5</sup>. However, given the current technological maturity and dominant market share of LIBs<sup>6,7</sup>, this thesis focuses specifically on the role of Li-ion batteries in reducing CO<sub>2</sub> emissions in key sectors.

### 1.1.1 Transportation

LIBs are becoming the primary energy source for passenger vehicles<sup>7</sup>. By powering electric motors with stored electricity, EVs can operate with zero tailpipe emissions. Even when accounting for emissions from electricity generation, EVs emit significantly less CO<sub>2</sub> over their lifecycle than internal combustion engine vehicles<sup>7</sup>. As electric grids become increasingly decarbonized, the climate benefits of EVs will grow further. Beyond cars, LIBs are being adopted in buses and heavy-duty trucks. Electrification of transport also brings indirect emissions benefits, reducing emissions associated with petroleum extraction and refining. Additionally, electric vehicles offer opportunities to support grid decarbonization through vehicle-to-grid technology. Parked EVs can feed stored energy back into the grid during peak demand periods, helping balance intermittent renewable generation and reducing the need for fossil fuel-based peaker plants<sup>8</sup>.

### 1.1.2 Energy generation and management

Although LIBs were originally designed for high energy density, for consumer electronics and EVs, their widespread production has led to substantial cost reductions<sup>5,9</sup>. This economy of scale made LIBs increasingly viable for BESS, even though lower-density and potentially cheaper technologies might be more suitable for such uses. By storing excess energy during periods of low demand and releasing it during peak demand, BESS stabilizes the grid and reduces reliance on fossil-fueled peaking plants. In effect, BESS enables a higher percentage of renewables on the grid. According to the International Energy Agency (IEA), achieving approximately 70% penetration of solar and wind power by 2050, a key milestone for net-zero goals, will require a massive expansion in grid flexibility and energy storage<sup>6</sup>. In addition to large-scale systems, decentralized solar plus LIBs solutions are revolutionizing energy access in remote and underserved regions<sup>10</sup>, avoiding the need for diesel generators.

### 1.1.3 Industrial Sector and Building Sector

The industrial sector presents substantial opportunities for decarbonization through LIBs use. Particularly, in applications that rely on mobile, diesel-powered machinery, LIBs are enabling a growing number of electric alternatives that reduce on-site emissions. For example, electric forklifts can replace internal combustion models, or mining haul trucks and excavators can be used in various mining operations<sup>11</sup>. BESS are also being deployed within industrial facilities, reducing the facility's draw from the grid at high-demand times, easing grid stress, and reducing the need for carbon-intensive peaking power generation<sup>12</sup>. In the building sector, LIBs are increasingly paired with rooftop solar panels<sup>13</sup>. By storing midday solar energy and making it available during the evening, LIBs enable buildings to maximize solar self-consumption. This reduces reliance on grid electricity, contributing to indirect reductions in CO<sub>2</sub> emissions and to grid stability.

Concluding, if deployed at scale and combined with complementary decarbonization strategies, battery technologies could contribute to 30–40% of the global emissions reductions required to limit warming to 1.5 °C. This aligns with broader analyses showing that consumer electrification (e.g., EVs, heat pumps) and renewable energy adoption, both enabled by energy storage, could account for nearly half of the required emissions cuts under Paris Agreement targets<sup>6</sup>.

## 1.2 THE HISTORY

The achievements, potential, and challenges of modern batteries can be appreciated by tracing their historical development. The origin of electrical energy storage dates back to the 18th century with the invention of the *Leyden jar*. Although technically a capacitor, it was the first device capable of storing electrical energy and delivering it in a controlled manner. The first true battery is attributed to *Alessandro Volta*, who in the 1800s invented the Voltaic pile, a stack of alternating zinc and copper discs separated by salt-soaked cloth. This device demonstrated that chemical reactions could produce a continuous flow of electrical current. The Voltaic pile is considered the first *primary* battery, meaning it can deliver electrical energy but cannot be recharged once depleted. Over the years, primary batteries have evolved in many forms, such as zinc-carbon, alkaline, and lithium-based chemistries; each offering improvements in energy density, cost, and shelf life<sup>14</sup>.

The first significant breakthrough in rechargeable (*secondary*) batteries came with the invention of the lead-acid battery in the mid-19th century. This battery type uses a reversible electrochemical reaction, allowing the battery to be charged and discharged repeatedly, since the

chemical products formed during discharge could be converted back into their original reactants during charging. Lead-acid batteries offered high reliability and sufficient power output, making them the standard energy storage device for automobiles and backup power systems.

It was not until the late 20th century that a combination of advances in materials science, electrochemistry, and manufacturing enabled the commercial development of *lithium-ion* batteries. These batteries offered significantly higher energy density, lower weight, and longer cycle life than previous technologies, making them ideal for portable electronics and, more recently, electric vehicles and grid storage. The culmination of decades of research was recognized in 2019, when the Nobel Prize in Chemistry was awarded to John B. Goodenough, M. Stanley Whittingham and Akira Yoshino for their foundational contributions to lithium-ion technology. Whittingham laid the groundwork in the 1970s by developing the first lithium-based battery, using titanium disulfide as the cathode and lithium metal as the anode<sup>15</sup>. Building on this, Goodenough introduced lithium cobalt oxide as a cathode material, dramatically increasing the battery's voltage and energy density<sup>16</sup>. Yoshino then created the first safe and commercially viable lithium-ion battery by replacing the reactive lithium metal anode with graphite, thus making the technology robust enough for widespread adoption<sup>17</sup>.

### 1.3 THE WORKING PRINCIPLE

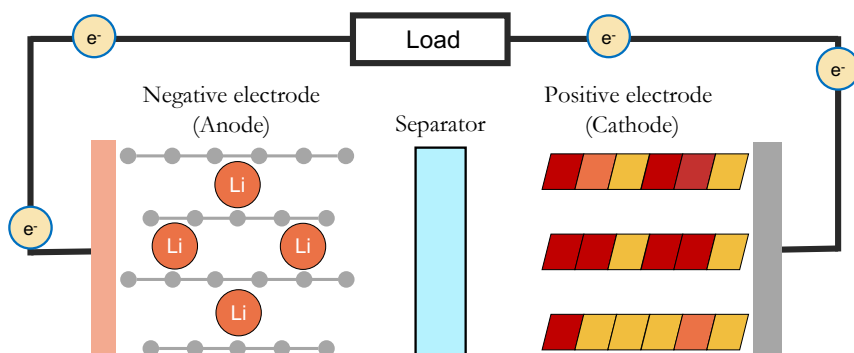


Figure 1.2. Working principle of a Li-ion battery.

The working principle of batteries, including lithium-ion and sodium-ion systems, is based on electrochemical reactions, specifically redox processes that convert *chemical energy* into *electrical energy* and vice versa. A battery consists of a negative electrode (*anode*) and a positive electrode (*cathode*), immersed in an electrolyte that allows ionic movement. During discharge, the anode undergoes oxidation, releasing electrons into the external circuit and ions into the electrolyte, while the cathode undergoes reduction by accepting those electrons and ions. This occurs

1 because the cathodic electrochemical potential is lower than the anodic one, so that a spontaneous ionic flux is favorable<sup>18</sup>. This electron flow through the external circuit powers electrical devices. In rechargeable batteries this process can be reversed by applying an external voltage during charging, driving the ions and electrons back to the anode and restoring the battery's capacity. Specifically, in most lithium-ion batteries, the ions shuttle between a graphite anode and a transition metal oxide cathode through a liquid or solid electrolyte.

## 1.4 THE CHALLENGES

Despite the rapid advancement of LIB technologies, several critical challenges must be addressed to ensure their scalability and long-term sustainability. As of now, global LIB manufacturing capacity is in the range of a few hundred gigawatt-hours per year. However, projected demand is expected to surpass several terawatt-hours annually by 2030, necessitating the construction of numerous gigafactories worldwide<sup>6,9</sup>. Scaling production at this rate poses considerable logistical, economic, and environmental hurdles, particularly when accounting for the dependence on multiple critical raw materials within the LIB supply chain.

Among the three main components of a LIB, the positive electrode is typically composed of lithium, cobalt, and nickel<sup>19,20</sup>. These elements are classified as critical materials due to concerns surrounding their limited availability, geopolitical concentration, and environmental impact<sup>20–22</sup>. Although the exact definition of “critical” varies by region, minimizing the use of such materials, especially in large-scale and long-term deployments, is essential for a sustainable battery future. Addressing this issue requires a multifaceted approach that targets both materials innovation and supply chain reform.

Lithium remains indispensable for high-performance batteries due to its unmatched energy density, a property rooted in its atomic mass and electrochemical potential. This characteristic is determined by the element's fundamental atomic structure and cannot be compensated for by technological improvements. As an alternative, sodium-ion batteries, based on similar principles, replace lithium with the more abundant and geographically accessible sodium. While sodium-ion technologies show promise for applications such as BESS and short-range EVs, their inherently lower energy density, due to sodium's higher atomic mass (~23 u vs. ~7 u for lithium), makes them unsuitable for long-range EVs or weight-sensitive applications like electric aviation<sup>5</sup>. Nevertheless, ongoing improvements in electrode materials and cell engineering are helping close this performance gap, positioning sodium-ion batteries as a complementary technology. Their development will be crucial to ensuring that lithium is reserved for applications where energy and power density are paramount.

The widespread use of cobalt and nickel stems from the dominance of layered oxide materials in commercial cathodes. First introduced in the form of lithium cobalt oxide ( $\text{LiCoO}_2$  or LCO), these materials remain prevalent today, often modified with additional elements to form compositions like  $\text{LiNi}_x\text{Co}_y\text{Mn}_{1-x-y}\text{O}_2$  (NMC) and  $\text{LiNi}_x\text{Co}_y\text{Al}_{1-x-y}\text{O}_2$  (NCA). From a materials standpoint, their appeal lies in their combination of high specific capacity (typically in the range of 270–280 mAh/g) and high operating voltages (3.6–4.2 V vs.  $\text{Li}/\text{Li}^+$ )<sup>23</sup>, both of which contribute to high energy density. Furthermore, the two-dimensional lithium-ion diffusion pathways in their crystal structures enable fast charge and discharge capabilities<sup>24</sup>. Their well-established manufacturing processes and proven cycling stability contribute to long-term reliability. However, these benefits are counterbalanced by safety concerns. At high states of charge, layered oxide cathodes can undergo exothermic decomposition, potentially leading to thermal runaway. This necessitates advanced battery management systems (BMS), which increase system complexity and costs.

Beyond technical performance, cobalt use presents significant ethical, environmental, and geopolitical challenges. Approximately 70% of the world's cobalt supply originates from the Democratic Republic of Congo, where mining practices have been widely criticized for human rights violations, including child labor and unsafe working conditions. Many miners are exposed to toxic substances without adequate protective measures, leading to severe health risks and unsafe environments<sup>21,22</sup>. Additionally, the global cobalt supply chain is geographically concentrated, with China dominating refining and consumption. This creates vulnerabilities for other regions, such as the United States and the European Union, which rely heavily on imports, raising concerns over long-term supply security<sup>20,25</sup>.

In response, intense research and policy efforts are focused on reducing the reliance on critical materials and mitigating their associated impacts. Battery recycling is a key area of development, aimed at recovering valuable metals and reducing raw material demand. Simultaneously, “second life” applications (repurposing EV batteries for use in BESS) are emerging as effective strategies to extend battery utility and lower lifecycle emissions. Advances in BMS are also playing a crucial role. Modern BMS can optimize charge and discharge cycles, minimize degradation, and improve overall performance, particularly in grid-scale and commercial fleet applications where longevity and safety are essential<sup>26–29</sup>.

Addressing these challenges through material innovation, ethical sourcing, recycling infrastructure, and system-level efficiency is essential to building a battery industry that is not only high-performing but also socially and environmentally responsible.

## 1.5 LITHIUM IRON PHOSPHATE

A more sustainable and ethically responsible battery industry can be achieved by transitioning away from cobalt- and nickel-dependent cathode chemistries. One of the most successful examples of this shift is the adoption of lithium iron phosphate ( $\text{LiFePO}_4$ , or LFP), which belongs to the family of olivine phosphate materials. First introduced by Padhi et al<sup>30</sup> in the 90s, LFP offered a compelling alternative to layered oxide cathodes such as LCO and NMC. Its appeal lies in the use of abundant, non-toxic, and low-cost elements: lithium, iron, and phosphorus. This drastically reduces both material costs and environmental impact. For instance, LFP batteries are associated with approximately 15% lower  $\text{CO}_2$  emissions compared to NMC batteries<sup>31</sup>.

LFP has found widespread application in both EVs and BESS. While its lower specific capacity ( $\sim 160$  mAh/g) and moderate operating voltage (around 3.42 V vs.  $\text{Li}/\text{Li}^+$ ) suggest a trade-off in energy density, its other advantages have driven rapid global adoption. As of 2024, LFP accounts for approximately 54% of the global market<sup>32</sup>, surpassing other chemistries in market share in several regions.

The core advantage of LFP lies in its olivine crystal structure, which differs fundamentally from the layered oxides structures. The olivine framework consists of a robust three-dimensional arrangement of corner-shared  $\text{FeO}_6$  octahedra and  $\text{PO}_4$  tetrahedra, forming a stable and rigid lattice. Lithium ions occupy well-defined one-dimensional channels along the [010] direction, through which they can diffuse. This structure offers two critical benefits: thermal stability and structural robustness during cycling. The strong covalent bonding in the  $\text{PO}_4$  groups makes LFP significantly less susceptible to oxygen release and thermal runaway, compared to layered oxides<sup>33</sup>. As a result, LFP batteries can be operated at higher temperatures and with reduced reliance on complex BMS. This inherent safety margin allows for tighter cell packing with minimal inactive material (e.g., casing, cooling systems), helping to partially offset the lower theoretical energy density<sup>29</sup>. These developments illustrate how a holistic design approach, which considers both material and system-level properties, can enhance performance while reducing the reliance on critical raw materials.

Furthermore, LFP batteries are known for their exceptional cycle life, often exceeding several thousand cycles with minimal capacity fade<sup>34</sup>. This makes them particularly attractive for high-utilization applications, such as commercial EV fleets and grid storage, where total cost of ownership and long-term reliability are key considerations. A notable example is the recent work of Chen et al.<sup>35</sup> where an external  $\text{LiSO}_2\text{CF}_3$  source could extend the cycle life of a commercial graphite | LFP battery to tens of thousands of cycles.

Recent progress in material design has further extended the capabilities of olivine phosphate cathodes. One promising example is lithium manganese iron phosphate ( $\text{LiMn}_x\text{Fe}_{1-x}\text{PO}_4$ , or LMFP), in which Mn is partially substituted for Fe in the crystal structure. The key motivation behind this substitution is to increase the energy density by exploiting the higher redox potential of the  $\text{Mn}^{3+}/\text{Mn}^{2+}$  couple, which occurs at approximately 4.0 V vs.  $\text{Li}/\text{Li}^+$ . This allows LMFP to achieve higher voltages than standard LFP, moving closer to the energy density of layered oxides.

However, increasing the Mn content introduces trade-offs. Manganese-rich olivine phases tend to exhibit poorer electronic conductivity and slower lithium diffusion kinetics, both of which can negatively affect rate capability and cycle life<sup>36,37</sup>. Research continues into mitigating these limitations through particle morphology control, carbon coating, and doping strategies, aiming to combine the safety and sustainability of the olivine structure with the higher energy demands of next-generation applications<sup>38,39</sup>.

## 1.6 BATTERY MODELING

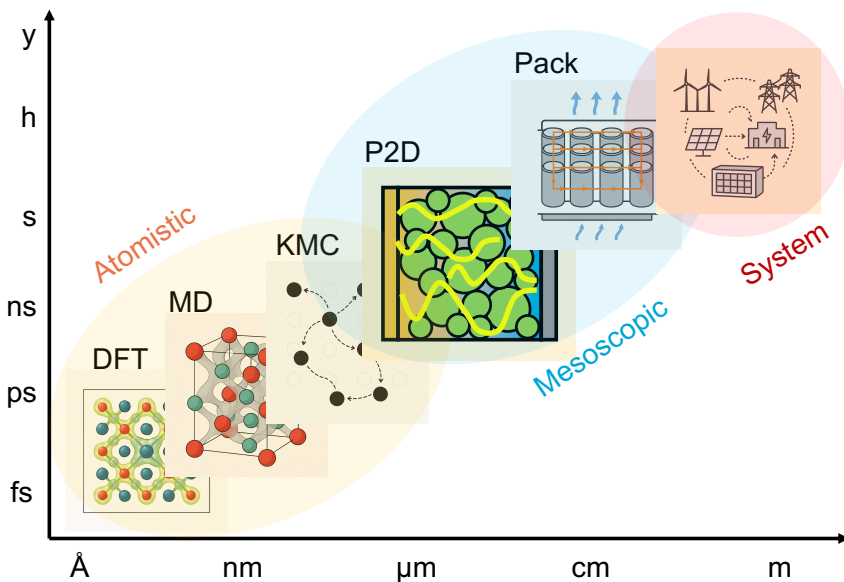


Figure 1.3. Multiscale modeling ranging time and length scales.

In response to the challenges outlined in the previous section, this thesis aims to understand, model, and predict the behavior of olivine phosphate positive electrode materials. In fact, reliable

models can significantly enhance the performance and broaden the applicability of olivine-based LIBs.

Various scales require different models with different tradeoffs between accuracy and computational costs. For instance, atomic-scale modeling can guide improvements in material properties by predicting the effects of transition metal substitution and doping on kinetic properties<sup>40</sup>. Particle-scale and electrode-scale models can assist in optimizing electrode architecture, including particle size distributions<sup>41,42</sup>, porosity<sup>43–45</sup>, electrode thickness<sup>46</sup>, and the volume fraction of conductive additives<sup>46,47</sup>; tailoring the design to specific applications. Cell- and pack-level models<sup>48–50</sup> are crucial for system-level engineering and product integration<sup>29</sup>.

The basic principles of these models will be presented in the introduction of this thesis, while the method section will outline the basics of electrode-level modeling, cornerstone of this work.

### 1.6.1 Ab Initio Methods

At the atomic level, density functional theory (DFT) is a foundational tool for describing and predicting the properties of materials<sup>51</sup>. It works by determining the electron density that minimizes the total energy of a system through self-consistent iterations. This makes DFT a powerful approach for evaluating thermodynamic properties of battery materials<sup>52–56</sup>. For example, DFT can be used to assess the stability of solid and liquid electrolytes<sup>57,58</sup>, or to calculate the redox potential and phase diagrams of active materials<sup>59,60</sup>.

While DFT is, in principle, a parameter-free method, requiring only the atomic identities of the system, it relies on approximations that introduce tunable parameters. A key challenge in modeling olivine phosphates, and many other transition metal compounds, is accurately accounting for localized electrons in partially filled *d*-orbitals<sup>60–63</sup>. This localization is often treated using the Hubbard *U* correction, which adds an on-site Coulomb interaction term to conventional DFT functionals<sup>64–66</sup>. The parameter *U*, expressed in eV, quantifies the strength of this interaction, but its value is not known a priori. Although self-consistent determination of *U* is possible<sup>66,67</sup>, it does not always yield satisfactory accuracy. To address this, more advanced techniques such as DFT+*U*+*V* have been developed<sup>68,69</sup>, where an additional inter-site interaction term (*V*) is introduced. Wannier function-based approaches can also be employed to capture the spatial distribution of electronic states more accurately<sup>70,71</sup>.

Although DFT is well-suited for predicting equilibrium thermodynamic properties at 0 K, it can be extended to explore kinetics. The Nudged Elastic Band (NEB) method enables calculation of the minimum energy path and associated barriers for ion migration within a crystal lattice<sup>72–74</sup>. Molecular dynamics (MD) simulations, on the other hand, incorporate finite temperature

effects by simulating atomic trajectories based on interatomic forces computed from DFT<sup>75</sup>. MD allows the study of collective ionic motion and thermally activated processes, providing insight into kinetic behavior.

Despite their high accuracy, DFT-based techniques are computationally intensive, typically limiting simulations to systems with only a few hundred atoms over nanometer scales and picosecond timescales. Additionally, debates persist regarding the best method to represent transition metal oxidation states<sup>67,68,71</sup>. Although future advancements in machine learning and theoretical methods may overcome these limitations<sup>76,77</sup>, current *ab initio* approaches do not yet offer the reliability needed to directly simulate full charge/discharge processes in olivine phosphates. Therefore, this thesis emphasizes the use of higher-level, lower-fidelity techniques that are partially informed by *ab initio* results but primarily validated against experimental data.

### 1.6.2 Kinetic Monte Carlo

One such atomic-scale technique utilized in this thesis is Kinetic Monte Carlo (KMC)<sup>78–80</sup>. Originally developed for simulating reaction kinetics in various systems, KMC offers a flexible framework for modeling long-timescale dynamics in materials science. Compared to molecular dynamics, KMC is computationally more efficient and can simulate larger systems. Moreover, KMC does not require periodic boundary conditions, making it suitable for studying systems with more realistic geometries, such as those described in Chapter 9.

The core concept of KMC is to model the evolution of a system by probabilistically selecting and executing discrete events over time. In the context of ion transport in battery materials, these events correspond to ion hopping between lattice sites. Each hop is associated with a transition rate, typically determined by the energy barrier between the initial and final positions. These barriers can be obtained from NEB calculations, while the site energetics can be derived from cluster expansion methods: a statistical modeling approach that uses DFT data to estimate the energy landscape based on local atomic configurations<sup>81–83</sup>. KMC models can incorporate site-specific energy barriers and occupancy-dependent transition rates, enabling simulations of large-scale systems (thousands of atoms, tens of nanometers) over extended timescales<sup>84</sup>.

Such models are particularly useful for exploring the impact of crystal structure and chemical composition on ionic mobility, critical factors in determining the rate capability of olivine-based electrodes.

### 1.6.3 Mesoscale modeling

To understand and predict the behavior of battery materials and electrodes at the mesoscale, the atomistic perspective becomes impractical, since these systems span length scales from hundreds of nanometers to centimeters and time scales from minutes to years. Instead, a continuum modeling approach must be adopted. In this framework, discrete spatiotemporal events are described by partial differential equations (PDEs), which capture the averaged behavior of physical quantities such as concentration, potential, and temperature<sup>85</sup>. These equations are grounded in thermodynamic principles and respect the conservation of mass, charge, and energy, allowing for physically consistent simulations across a wide range of conditions<sup>86,87</sup>.

Continuum models are highly flexible and can be tailored to different levels of complexity and resolution. They can simulate the behavior of a single active material particle under electrochemical stimuli<sup>88,89</sup>, or describe the coupled behavior of multiple components within a composite porous electrode, including active material particle<sup>90,91</sup>, conductive binder domains (CBD)<sup>92</sup>, and electrolyte-filled pores<sup>93</sup>. Beyond the electrode scale, similar modeling principles extend to full-cell models incorporating thermal effects<sup>48</sup>, mechanical stresses<sup>94</sup>, and even system-level interactions in EVs<sup>95</sup> or BESS<sup>96</sup>.

This thesis focuses specifically on the electrode level, which lies at the heart of any battery architecture. Accurate modeling at this scale is critical for performance prediction, design optimization, and potential integration into BMS<sup>27,95,97</sup>. A core principle of this work is the exclusive use of physically consistent modeling techniques, intentionally avoiding empirical or curve-fitted relations<sup>98–100</sup>. While such empirical models may be effective for reproducing specific datasets, they often lack generality and offer limited insight into the underlying physics. Instead, the models developed in this thesis are built upon experimentally validated frameworks<sup>89</sup>, enabling both predictive capability and interpretability.

A crucial aspect of continuum modeling is the selection of fidelity level, which must balance physical accuracy with computational efficiency. The computational domain is discretized using methods such as finite differences, finite volumes, or finite elements, depending on the system geometry and complexity. Finite volume methods are typically used for lower-dimensional systems (1D or 2D), while finite element methods are better suited for three-dimensional domains<sup>101</sup>. The size of discretized volumes or elements directly affects the resolution and stability of the solution and must be carefully chosen based on the specific application. Once the spatial discretization is performed, the governing PDEs are converted into a system of differential-algebraic equations (DAEs), which are then integrated in time using appropriate numerical solvers.

At the high-fidelity end of the spectrum lies three-dimensional microstructural modeling, where a 3D representation of the electrode is constructed using either tomographic imaging data<sup>92</sup> or stochastic microstructure generation techniques<sup>46,102</sup>. The resulting simulation domain is divided into active material, CBD, and electrolyte. Ions migrate through the electrolyte and react at the surface of the active material particles, where electrochemical reactions occur based on local chemical potentials. The inserted ions then diffuse within the active material under chemical potential gradients. While this approach provides highly detailed insight into ion transport and reaction heterogeneity, its computational cost limits its applicability to small electrode volumes containing only a few particles<sup>92</sup>.

To overcome these limitations, pseudo-two-dimensional (P2D) models, also known as Doyle–Fuller–Newman (DFN) models, have been developed<sup>103–106</sup>, and also extended including phase-field methods<sup>86,87</sup>. These models reduce computational demand by introducing simplifying assumptions that preserve physical fidelity. Due to these properties, they have become the standard in electrode-level battery modeling. Since they serve as the foundation for much of the work presented in this thesis, a detailed explanation is given in the Chapter 2.

## 1.7 OUTLINE OF THE THESIS

After describing the main modeling framework in Chapter 2, the thesis proceeds as follows:

**Chapter 3** explores the effects of including in a P2D model an open circuit potential (OCP) derived from thermodynamics, specifically from the regular solution model. Unlike profiles obtained by fitting experimental data, these OCPs can be non-monotonic in case of phase separating materials. In this case, using a physically accurate non-monotonic OCP not only ensures a correct treatment of inter-particle phase separation dynamics but also alters the electrode behavior, predicting a reduction in rate performance. This approach also improves the simulation of pulsed protocols, enabling the prediction of more realistic dynamic scenarios.

**Chapter 4** extends the regular solution model to materials with multiple redox species and sublattices. This novel theory is applied to  $\text{LiMn}_x\text{Fe}_{1-x}\text{PO}_4$ , a common evolution of LFP, to predict its chemical potentials (and thus voltage profile). Coupled with a P2D phase-field framework, the model unveils the internal dynamics of these electrodes and suggests optimal compositions for high-power or high-energy applications.

**Chapter 5** applies a similar methodology to spheroidal particles morphologies (spheroidal) and materials to investigate a strong kinetically induced memory effect. The simulations explain and quantify the reduced electrode resistivity observed experimentally after high-rate operations. In

agreement with operando microbeam X-ray diffraction, they reveal how larger currents increase particle utilization and enable more efficient internal current distribution.

**Chapter 6** uses the model to study the frequency response of these electrodes. The resulting impedance spectra show unexpected features, including a secondary arc associated with diffusion of phase-separated particles. Furthermore, the impedance of different model extensions is shown to depend strongly on the reaction direction and on the previously applied rate. This work lays the foundation for physics-based impedance analysis of phase-separating materials, whose features can differ significantly from those of solid solutions.

**Chapter 7** further extends the framework by including the effect of conductive additive distribution. In the investigated LFP electrode, composed of thin particles not limited by solid diffusion, the rate performance is instead limited by inter-particle electrical connections. These single-crystal particles form an electrical network where current flows from the conductive additive into different regions of the microstructure. Tomographic techniques are used to analyze these features, which are then abstracted into a graph and embedded in the P2D model. This extension allows simulations to reproduce constant-current and pulsed protocols with minimal fitting parameters. Thanks to its physical consistency, the model can now predict the results of varying currents, temperatures, and electrode loadings.

**Chapter 8** completes the modeling of particle morphologies by considering nanoporous secondary LFP particles. These particles also suffer from severe electronic transport bottlenecks. First, a three-dimensional model is used to study the impact of conductive additive distribution on their surface. Then, a reduced-order one-dimensional model is built to capture their behavior in a fast and scalable simulation. Incorporated into a P2D framework, this model reproduces the experimental behavior of thin and thick electrodes, identifies the limiting factors, and suggests optimal electrode loadings.

**Chapter 9** concludes the thesis by investigating the olivine phosphate structure at the atomistic scale. Using Kinetic Monte Carlo methods, the isotopic exchange in  $\text{LiFePO}_4$  is simulated and explained. The results, consistent with experiments, show that the crystal structure enforces single-file diffusion during the early stages of non-faradaic exchange, transitioning to conventional diffusion at later stages. The extracted transition rates are then used to compare faradaic (involving both electrons and ions) and non-faradaic (only ion hopping) processes, underscoring the importance of including electronic limitations in reaction kinetics theories.

## REFERENCES

1. Ippc. Global Warming of 1.5°C: IPCC Special Report on Impacts of Global Warming of 1.5°C above Pre-Industrial Levels in Context of Strengthening Response to Climate Change, Sustainable Development, and Efforts to Eradicate Poverty. (Cambridge University Press, 2022). doi:10.1017/9781009157940.
2. Hannah Ritchie, Pablo Rosado, & Max Roser. Breakdown of carbon dioxide, methane and nitrous oxide emissions by sector. Our World in Data (2020) doi:https://ourworldindata.org/emissions-by-sector.
3. IRENA. Global Energy Transformation: A Roadmap to 2050. (2018).
4. Moritz, M., Schönfisch, M. & Schulte, S. Estimating global production and supply costs for green hydrogen and hydrogen-based green energy commodities. *Int. J. Hydrog. Energy* **48**, 9139–9154 (2023).
5. Emerging Battery Technologies to Boost the Clean Energy Transition: Cost, Sustainability, and Performance Analysis. (Springer International Publishing, Cham, 2024). doi:10.1007/978-3-031-48359-2.
6. Birol, D. F. Batteries and Secure Energy Transitions. IEA (2024).
7. IEA. Global EV Outlook 2025. (2025).
8. Aguilar Lopez, F., Lauinger, D., Vuille, F. & Müller, D. B. On the potential of vehicle-to-grid and second-life batteries to provide energy and material security. *Nat. Commun.* **15**, 4179 (2024).
9. Mauler, L., Duffner, F., Zeier, W. G. & Leker, J. Battery cost forecasting: a review of methods and results with an outlook to 2050. *Energy Environ. Sci.* **14**, 4712–4739 (2021).
10. Falk, J., Nedjalkov, A., Angelmahr, M. & Schade, W. Applying Lithium-Ion Second Life Batteries for Off-Grid Solar Powered System—A Socio-Economic Case Study for Rural Development. *Z. Für Energiewirtschaft* **44**, 47–60 (2020).
11. Wei, M., McMillan, C. A. & De La Rue Du Can, S. Electrification of Industry: Potential, Challenges and Outlook. *Curr. Sustain. Energy Rep.* **6**, 140–148 (2019).
12. Bereczki, B., Hartmann, B. & Kertesz, S. Industrial Application of Battery Energy Storage Systems: Peak shaving, in 2019 7th International Youth Conference on Energy (IYCE) 1–5 (IEEE, Bled, Slovenia, 2019). doi:10.1109/IYCE45807.2019.8991594.
13. Figgenger, J. et al. Multi-year field measurements of home storage systems and their use in capacity estimation. *Nat. Energy* **9**, 1438–1447 (2024).
14. Scrosati, B. History of lithium batteries. *J. Solid State Electrochem.* **15**, 1623–1630 (2011).
15. Whittingham, M. S. Electrical Energy Storage and Intercalation Chemistry. *Science* **192**, 1126–1127 (1976).
16. Mizushima, K., Jones, P. C., Wiseman, P. J. & Goodenough, J. B.  $\text{LiCoO}_2$  ( $0 < x < 1$ ): A new cathode material for batteries of high energy density. **15**.
17. Yoshino, A. & Nakajima, T. Secondary Battery. (1987).
18. Finkelstein, S. H., Ricci, M., Böttcher, T. & Schmidt-Rohr, K. How lithium-ion batteries work conceptually: thermodynamics of Li bonding in idealized electrodes. *Phys. Chem. Chem. Phys.* **26**, 24157–24171 (2024).
19. Schmich, R., Wagner, R., Hörpel, G., Placke, T. & Winter, M. Performance and cost of materials for lithium-based rechargeable automotive batteries. *Nat. Energy* **3**, 267–278 (2018).
20. Olivetti, E. A., Ceder, G., Gaustad, G. G. & Fu, X. Lithium-Ion Battery Supply Chain Considerations: Analysis of Potential Bottlenecks in Critical Metals. *Joule* **1**, 229–243 (2017).
21. Lee, S. & Manthiram, A. Can Cobalt Be Eliminated from Lithium-Ion Batteries? *ACS Energy Lett.* **7**, 3058–3063 (2022).

22. Sovacool, B. K. The precarious political economy of cobalt: Balancing prosperity, poverty, and brutality in artisanal and industrial mining in the Democratic Republic of the Congo. *Extr. Ind. Soc.* **6**, 915–939 (2019).
23. Rozier, P. & Tarascon, J. M. Review—Li-Rich Layered Oxide Cathodes for Next-Generation Li-Ion Batteries: Chances and Challenges. *J. Electrochem. Soc.* **162**, A2490–A2499 (2015).
24. Van der Ven, A. & Ceder, G. Lithium diffusion mechanisms in layered intercalation compounds. *J. Power Sources* **97–98**, 529–531 (2001).
25. Cheng, A. L., Fuchs, E. R. H., Karplus, V. J. & Michalek, J. J. Electric vehicle battery chemistry affects supply chain disruption vulnerabilities. *Nat. Commun.* **15**, 2143 (2024).
26. Borah, M., Wang, Q., Moura, S., Sauer, D. U. & Li, W. Synergizing physics and machine learning for advanced battery management. *Commun. Eng.* **3**, 134 (2024).
27. Lee, S. B., Thiagarajan, R. S., Subramanian, V. R. & Onori, S. Advanced Battery Management Systems: Modeling and Numerical Simulation for Control. in *2022 American Control Conference (ACC) 4403–4414* (IEEE, Atlanta, GA, USA, 2022). doi:10.23919/ACC53348.2022.9867639.
28. Olabi, A. G. et al. Battery thermal management systems: Recent progress and challenges. *Int. J. Thermofluids* **15**, 100171 (2022).
29. Weng, J. et al. Fast-charging lithium-ion batteries require a systems engineering approach. *Nat. Energy* (2025) doi:10.1038/s41560-025-01813-w.
30. Padhi, A. K., Nanjundaswamy, K. S. & Goodenough, J. B. Phospho-olivines as Positive-Electrode Materials for Rechargeable Lithium Batteries. *J. Electrochem. Soc.* **144**, 1188–1194 (1997).
31. Degen, F., Mitterfellner, M. & Kampker, A. Comparative life cycle assessment of lithium-ion, sodium-ion, and solid-state battery cells for electric vehicles. *J. Ind. Ecol.* **29**, 113–128 (2025).
32. Rostami, H., Valio, J., Tynjälä, P., Lassi, U. & Suominen, P. Life Cycle of LiFePO<sub>4</sub> Batteries: Production, Recycling, and Market Trends. *ChemPhysChem* **25**, e202400459 (2024).
33. Malik, R., Abdellahi, A. & Ceder, G. A Critical Review of the Li Insertion Mechanisms in LiFePO<sub>4</sub> Electrodes. *J. Electrochem. Soc.* **160**, A3179–A3197 (2013).
34. Severson, K. A. et al. Data-driven prediction of battery cycle life before capacity degradation. *Nat. Energy* **4**, 383–391 (2019).
35. Chen, S. et al. External Li supply reshapes Li deficiency and lifetime limit of batteries. *Nature* **638**, 676–683 (2025).
36. Huang, W. et al. Revealing the Degradation Mechanism of LiMn<sub>x</sub>Fe<sub>1-x</sub>PO<sub>4</sub> by the Single-Particle Electrochemistry Method. *ACS Appl. Mater. Interfaces* **11**, 957–962 (2019).
37. Hu, Q. et al. Revealing the voltage decay of LiMn<sub>0.7</sub>Fe<sub>0.3</sub>PO<sub>4</sub> cathodes over cycling. *Nano Energy* **123**, 109422 (2024).
38. Deng, Y. et al. Recent Advances of Mn-Rich LiFe<sub>1-y</sub>Mn<sub>y</sub>PO<sub>4</sub> (0.5 ≤ y < 1.0) Cathode Materials for High Energy Density Lithium Ion Batteries. *Adv. Energy Mater.* **7**, 1601958 (2017).
39. Tolganbek, N., Yerkinbekova, Y., Kalybekkyzy, S., Bakenov, Z. & Mentbayeva, A. Current state of high voltage olivine structured LiMPO<sub>4</sub> cathode materials for energy storage applications: A review. *J. Alloys Compd.* **882**, 160774 (2021).
40. Molenda, J., Kulka, A., Milewska, A., Zając, W. & Świerczek, K. Structural, Transport and Electrochemical Properties of LiFePO<sub>4</sub> Substituted in Lithium and Iron Sublattices (Al, Zr, W, Mn, Co and Ni). *Materials* **6**, 1656–1687 (2013).
41. Kirk, T. L., Evans, J., Please, C. P. & Chapman, S. J. Modelling electrode heterogeneity in lithium-ion batteries: unimodal and bimodal particle-size distributions. (2020).
42. Van der Ven, A. & Wagemaker, M. Effect of surface energies and nano-particle size distribution on open circuit voltage of Li-electrodes. *Electrochem. Commun.* **11**, 881–884 (2009).
43. Karanth, P. et al. A phase inversion strategy for low-tortuosity and ultrahigh-mass-loading nickel-rich layered oxide electrodes. *Cell Rep. Phys. Sci.* 101972 (2024) doi:10.1016/j.xcrp.2024.101972.

44. Newman, J. Optimization of Porosity and Thickness of a Battery Electrode by Means of a Reaction-Zone Model. *J. Electrochem. Soc.* **142**, 97–101 (1995).
45. Cernak, S., Schuerholz, F., Kesppe, M. & Nirschl, H. Three-Dimensional Numerical Simulations on the Effect of Particle Porosity of Lithium-Nickel–Manganese–Cobalt–Oxide on the Performance of Positive Lithium-Ion Battery Electrodes. *Energy Technol.* **9**, 2000676 (2021).
46. Kench, S. et al. Li-ion battery design through microstructural optimization using generative AI. *Matter* S2590238524004466 (2024) doi:10.1016/j.matt.2024.08.014.
47. Lu, X. et al. Multi-length scale microstructural design of lithium-ion battery electrodes for improved discharge rate performance. *Energy Environ. Sci.* **14**, 5929–5946 (2021).
48. O'Regan, K., Brosa Planella, F., Widanage, W. D. & Kendrick, E. Thermal-electrochemical parameters of a high energy lithium-ion cylindrical battery. *Electrochimica Acta* **425**, 140700 (2022).
49. Ai, W., Kraft, L., Sturm, J., Jossen, A. & Wu, B. Electrochemical Thermal-Mechanical Modelling of Stress Inhomogeneity in Lithium-Ion Pouch Cells. *J. Electrochem. Soc.* **167**, 013512 (2019).
50. Ramirez-Meyers, K., Rawn, B. & Whitacre, J. F. A statistical assessment of the state-of-health of LiFePO<sub>4</sub> cells harvested from a hybrid-electric vehicle battery pack. *J. Energy Storage* **59**, 106472 (2023).
51. He, Q., Yu, B., Li, Z. & Zhao, Y. Density Functional Theory for Battery Materials. *ENERGY Environ. Mater.* **2**, 264–279 (2019).
52. Vasileiadis, A., Carlsen, B., De Klerk, N. J. J. & Wagemaker, M. Ab Initio Study of Sodium Insertion in the  $\lambda$ -Mn<sub>2</sub>O<sub>4</sub> and Dis/Ordered  $\lambda$ -Mn<sub>1.5</sub>Ni<sub>0.5</sub>O<sub>4</sub> Spinels. *Chem. Mater.* **30**, 6646–6659 (2018).
53. Ganapathy, S., Vasileiadis, A., Heringa, J. R. & Wagemaker, M. The Fine Line between a Two-Phase and Solid-Solution Phase Transformation and Highly Mobile Phase Interfaces in Spinel Li<sub>4+x</sub>Ti<sub>5</sub>O<sub>12</sub>. *Adv. Energy Mater.* **7**, 1601781 (2017).
54. Li, Y. et al. Origin of fast charging in hard carbon anodes. *Nat. Energy* (2024) doi:10.1038/s41560-023-01414-5.
55. Vasileiadis, A., Li, Y., Lu, Y., Hu, Y.-S. & Wagemaker, M. Role of Defects, Pores, and Interfaces in Deciphering the Alkali Metal Storage Mechanism in Hard Carbon. *ACS Appl. Energy Mater.* **6**, 127–140 (2023).
56. Urban, A., Seo, D.-H. & Ceder, G. Computational understanding of Li-ion batteries. *Npj Comput. Mater.* **2**, 16002 (2016).
57. Arroyo y de Dompablo, M. E., Van der Ven, A. & Ceder, G. First-principles calculations of lithium ordering and phase stability on Li<sub>x</sub>NiO<sub>2</sub>. *Phys. Rev. B* **66**, 064112 (2002).
58. Schwietert, T. K. et al. Clarifying the relationship between redox activity and electrochemical stability in solid electrolytes. *Nat. Mater.* **19**, 428–435 (2020).
59. Perez, I. Ab initio methods for the computation of physical properties and performance parameters of electrochemical energy storage devices. *Phys. Chem. Chem. Phys.* **25**, 1476–1503 (2023).
60. Hörmann, N. G. & Groß, A. Phase field parameters for battery compounds from first-principles calculations. *Phys. Rev. Mater.* **3**, 055401 (2019).
61. Wang, L., Maxisch, T. & Ceder, G. Oxidation energies of transition metal oxides within the GGA + U framework. *Phys. Rev. B* **73**, 195107 (2006).
62. Zhou, F., Cococcioni, M., Marianetti, C. A., Morgan, D. & Ceder, G. First-principles prediction of redox potentials in transition-metal compounds with LDA + U. *Phys. Rev. B* **70**, 235121 (2004).
63. Zhou, F., Cococcioni, M., Kang, K. & Ceder, G. The Li intercalation potential of LiMPO<sub>4</sub> and LiMSiO<sub>4</sub> olivines with M=Fe, Mn, Co, Ni. *Electrochem. Commun.* **6**, 1144–1148 (2004).

64. Timrov, I., Kotiuga, M. & Marzari, N. Unraveling the effects of inter-site Hubbard interactions in spinel Li-ion cathode materials. *Phys. Chem. Chem. Phys.* **25**, 9061–9072 (2023).
65. Meredig, B., Thompson, A., Hansen, H. A., Wolverton, C. & Van De Walle, A. Method for locating low-energy solutions within DFT + U. *Phys. Rev. B* **82**, 195128 (2010).
66. Cococcioni, M. & De Gironcoli, S. Linear response approach to the calculation of the effective interaction parameters in the LDA + U method. *Phys. Rev. B* **71**, 035105 (2005).
67. Binci, L. & Marzari, N. Noncollinear DFT + U and Hubbard parameters with fully relativistic ultrasoft pseudopotentials. *Phys. Rev. B* **108**, 115157 (2023).
68. Timrov, I., Aquilante, F., Cococcioni, M. & Marzari, N. Accurate Electronic Properties and Intercalation Voltages of Olivine-Type Li-Ion Cathode Materials from Extended Hubbard Functionals. *PRX Energy* **1**, 033003 (2022).
69. Timrov, I., Marzari, N. & Cococcioni, M. HP – A code for the calculation of Hubbard parameters using density-functional perturbation theory. *Comput. Phys. Commun.* **279**, 108455 (2022).
70. Ting, Y.-Y. & Kowalski, P. M. Refined DFT + U method for computation of layered oxide cathode materials. *Electrochimica Acta* **443**, 141912 (2023).
71. Tesch, R. & Kowalski, P. M. Hubbard U parameters for transition metals from first principles. *Phys. Rev. B* **105**, 195153 (2022).
72. Schreiner, M., Bhowmik, A., Vegge, T., Jorgensen, P. B. & Winther, O. NeuralNEB—neural networks can find reaction paths fast. *Mach. Learn. Sci. Technol.* **3**, 045022 (2022).
73. Luong, H. D., Dinh, V. A., Momida, H. & Oguchi, T. Insight into the diffusion mechanism of sodium ion–polaron complexes in orthorhombic P2 layered cathode oxide  $\text{Na}_x\text{MnO}_2$ . *Phys. Chem. Chem. Phys.* **22**, 18219–18228 (2020).
74. Luong, H. D., Xu, C., Jalem, R. & Tateyama, Y. Evaluation of battery positive-electrode performance with simultaneous ab-initio calculations of both electronic and ionic conductivities. *J. Power Sources* **569**, 232969 (2023).
75. *Modern Methods and Algorithms of Quantum Chemistry.* (NIC, Jülich, 2000).
76. Lama, B., Smirnova, A. L. & Paudel, T. R. Enhanced Li-Ion Diffusivity of  $\text{LiFePO}_4$  by Ru Doping: Ab Initio and Machine Learning Force Field Results. *ACS Appl. Energy Mater.* [acsaem.3c01429](https://doi.org/10.1021/acsaem.3c01429) (2023) doi:10.1021/acsaem.3c01429.
77. Vandermause, J. Training machine learned potentials on the fly. *Protein Fold.* (2018).
78. Hoffmann, M. J., Matera, S. & Reuter, K. kmos: A lattice kinetic Monte Carlo framework. *Comput. Phys. Commun.* **185**, 2138–2150 (2014).
79. Rego, A. S. C. & Brandão, A. L. T. General Method for Speeding Up Kinetic Monte Carlo Simulations. *Ind. Eng. Chem. Res.* **59**, 9034–9042 (2020).
80. Xiao, P. & Henkelman, G. Kinetic Monte Carlo Study of Li Intercalation in  $\text{LiFePO}_4$ . *ACS Nano* **12**, 844–851 (2018).
81. Malik, R., Zhou, F. & Ceder, G. Kinetics of non-equilibrium lithium incorporation in  $\text{LiFePO}_4$ . *Nat. Mater.* **10**, 587–590 (2011).
82. Barroso-Luque, L. et al. Cluster expansions of multicomponent ionic materials: Formalism and methodology. *Phys. Rev. B* **106**, 144202 (2022).
83. Wang, Z. et al. Phase stability and sodium-vacancy orderings in a NaSICON electrode. *J. Mater. Chem. A* **10**, 209–217 (2022).
84. Wang, Z. et al. Kinetic Monte Carlo Simulations of Sodium Ion Transport in NaSICON Electrodes. *ACS Mater. Lett.* **5**, 2499–2507 (2023).
85. Landstorfer, M. & Jacob, T. Mathematical modeling of intercalation batteries at the cell level and beyond. *Chem. Soc. Rev.* **42**, 3234 (2013).
86. Ferguson, T. R. & Bazant, M. Z. Nonequilibrium Thermodynamics of Porous Electrodes. *J. Electrochem. Soc.* **159**, A1967–A1985 (2012).

87. Smith, R. B. & Bazant, M. Z. Multiphase Porous Electrode Theory. *J. Electrochem. Soc.* **164**, E3291–E3310 (2017).
88. Cogswell, D. A. & Bazant, M. Z. Size-dependent phase morphologies in LiFePO<sub>4</sub> battery particles. *Electrochem. Commun.* **95**, 33–37 (2018).
89. Zhao, H. et al. Learning heterogeneous reaction kinetics from X-ray videos pixel by pixel. *Nature* **621**, 289–294 (2023).
90. Li, Y. et al. Current-induced transition from particle-by-particle to concurrent intercalation in phase-separating battery electrodes. *Nat. Mater.* **13**, 1149–1156 (2014).
91. Li, Y. & others. Fluid-enhanced surface diffusion controls intraparticle phase transformations. *Nat. Mater.* **17**, 915–922 (2018).
92. Tredenick, E. C. et al. Bridging the Gap between Microstructurally Resolved Computed Tomography-Based and Homogenised Doyle-Fuller-Newman Models for Lithium-Ion Batteries. *J. Electrochem. Soc.* **172**, 030503 (2025).
93. Xu, H. et al. Guiding the Design of Heterogeneous Electrode Microstructures for Li-Ion Batteries: Microscopic Imaging, Predictive Modeling, and Machine Learning. *Adv. Energy Mater.* **11**, 2003908 (2021).
94. Ipers, G. et al. Rapid Simulation of Electro-Chemo-Mechanical Deformation of Li-ion Batteries Based On Porous Electrode Theory. *J. Electrochem. Soc.* **171**, 050557 (2024).
95. Habib, A. K. M. A. et al. Lithium-Ion Battery Management System for Electric Vehicles: Constraints, Challenges, and Recommendations. *Batteries* **9**, 152 (2023).
96. Reniers, J. M., Mulder, G. & Howey, D. A. Unlocking extra value from grid batteries using advanced models. *J. Power Sources* **487**, 229355 (2021).
97. Liu, K. et al. Electrochemical modeling and parameterization towards control-oriented management of lithium-ion batteries. *Control Eng. Pract.* **124**, 105176 (2022).
98. Thomas-Alyea, K. E. Modeling Resistive-Reactant and Phase-Change Materials in Battery Electrodes. *ECS Trans.* **16**, 155–165 (2008).
99. Wycisk, D., Oldenburger, M., Stoye, M. G., Mrkonjic, T. & Latz, A. Modified Plett-model for modeling voltage hysteresis in lithium-ion cells. *J. Energy Storage* **52**, 105016 (2022).
100. Prada, E. et al. A simplified electrochemical and thermal aging model of LiFePO<sub>4</sub>-graphite Li-ion batteries: power and capacity fade simulations. *J. Electrochem. Soc.* **160**, A616 (2013).
101. Nikishkov, G. P. Introduction to the Finite Element Method. (UCLA, 2001).
102. Usseglio-Viretta, F. L. E. et al. MATBOX: An Open-source Microstructure Analysis Toolbox for microstructure generation, segmentation, characterization, visualization, correlation, and meshing. *SoftwareX* **17**, 100915 (2022).
103. Doyle, M., Fuller, T. F. & Newman, J. Modeling of Galvanostatic Charge and Discharge of the Lithium/Polymer/Insertion Cell. *J. Electrochem. Soc.* **140**, 1526–1533 (1993).
104. Fuller, T. F., Doyle, M. & Newman, J. Simulation and Optimization of the Dual Lithium Ion Insertion Cell. *J. Electrochem. Soc.* **141**, 1–10 (1994).
105. Srinivasan, V. & Newman, J. Discharge Model for the Lithium Iron-Phosphate Electrode. *J. Electrochem. Soc.* **151**, A1517 (2004).
106. Brosa Planella, F. et al. A continuum of physics-based lithium-ion battery models reviewed. *Prog. Energy* **4**, 042003 (2022).



# 2 MULTIPHASE POROUS ELECTRODE THEORY

To apply the developed physiochemical knowledge in the optimization of lithium-ion batteries, a comprehensive yet computationally efficient model is essential. Such a model must accurately simulate the electrochemical and physical responses of electrodes (or even entire cells), enabling the development of physics-informed control protocols and the design of task-specific electrodes and modules.

Among the most effective models for this purpose are the pseudo-two-dimensional (P2D) models, which are presented here in their conventional formulations. The term "pseudo-two-dimensional" reflects a key conceptual feature: the separation of spatial scales within the system. The *macroscopic dimension (electrode-scale)*, spanning the electrode thickness (typically 10–100  $\mu\text{m}$ ), governs electrolyte transport, while the *microscopic dimension (particle-scale)*, spanning the size of individual particles (10–1000 nm), captures diffusion and reaction of ions within the active material. By decoupling these two scales, P2D models can simulate the performance of full electrodes or even entire cells while remaining computationally tractable.

## 2.1 ELECTRODE-SCALE MODEL

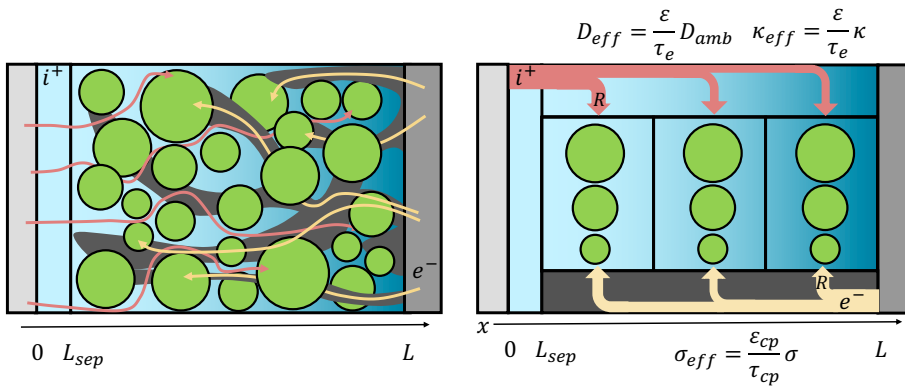


**Figure 2.1. P2D treatment of transport phenomena in a battery electrode.** Schematic of a porous electrode composed of particles of various sizes (green), pores containing the electrolyte (blue) and conductive binder (grey), where ions (red) and electrons (yellow) travel in tortuous paths. Schematic of a P2D model where ion and electron are assumed to follow the simulated direction ( $x$ ) and react at specified discrete points along the electrode thickness. Their transport properties are scaled by the volume fractions and the tortuosities of the corresponding phases.

At the electrode scale, relevant transport phenomena such as *electrolyte diffusion* and *electron conduction* occur over micron-scale dimensions. The microscale complexity of the porous electrode, i.e. its tortuosity, porosity, and phase distribution, is incorporated into continuum

models by defining *effective transport properties*. These effective properties average over the heterogeneous microstructure and allow for tractable macroscopic simulations<sup>1</sup>.

In a porous electrode composed of electronically conductive solid phase (active material and conductive binder) and an ionically conductive electrolyte-filled pores, the *effective electrical conductivity* ( $\sigma_{eff}$ ) and *effective ionic conductivity* ( $\kappa_{eff}$ ) can be expressed as:

$$\sigma_{eff} = \frac{\varepsilon_{cp}}{\tau_{cp}} \sigma(T) \quad (2.1)$$

$$\kappa_{eff} = \frac{\varepsilon}{\tau_e} \kappa(c_e, T) \quad (2.2)$$

Here,  $\varepsilon_{cp}$  and  $\varepsilon$  are the volume fractions of the conductive phase and the electrolyte phase, respectively;  $\tau_{cp}$  and  $\tau_e$  are their respective tortuosities;  $\sigma(T)$  and  $\kappa(c_e, T)$  are the intrinsic conductivities of the solid phase and electrolyte, possibly temperature- and concentration-dependent.

Similarly, the *effective diffusivity* in the electrolyte-filled porous structure is given by:

$$D_{eff} = \frac{\varepsilon}{\tau_e} D_{amb}(c_e, T) \quad (2.3)$$

Where  $D_{amb}$  is the ambipolar diffusivity, which reflects the coupled transport of ionic species in the electrolyte and may depend on the local concentration  $c_e$  and temperature  $T$ <sup>1,2</sup>.

The electrolyte concentration  $c_e$  evolves over the electrode domain ( $x \in [0, L]$ ), governed by a mass conservation equation derived from porous electrode theory. Dividing the spatial domain into finite volumes, each with a local reaction rate a  $R(x)$ , the conservation of mass for an electrolyte with a concentration-dependent transference number  $t^+$  is written as:

$$\varepsilon \frac{dc_e}{dt} = \nabla \cdot (D_{eff} \nabla c_e) + (1 - t^+)R \quad (2.4)$$

where the second term combines the effect of the electrolyte flux ( $N_e = -D_{eff} \nabla c_e$ ) and the local reaction rate at position  $x$ . This equation, at the core of *porous electrode theory* (PET), originates from the assumption of electroneutrality, i.e. the absence of space charge layers where positive and negative ion concentrations are unbalanced.

## 2 | MULTIPHASE POROUS ELECTRODE THEORY

The ionic flux and reaction terms are coupled to charge conservation equations in both the electrolyte and solid phases:

$$\nabla \cdot i_e = e R \quad (2.5)$$

$$\nabla \cdot i_s = -e R \quad (2.6)$$

where  $e$  is the electron charge and the solid phase current  $i_s$  can be computed from the gradient of the solid phase potential  $\phi_s$ , using Ohm's law

$$i_s = -\sigma_{eff} \nabla \phi_s \quad (2.7)$$

In the electrolyte, the current  $i_e$  depends on both the gradient of the potential  $\phi_e$  and the gradient of the electrolyte concentration  $c_e$ , modified by the thermodynamic factor:

$$i_e = \kappa_{eff} \left[ \frac{k_B T}{e} 2(1 - t^+) \left( 1 + \frac{\partial \ln f}{\partial \ln c_e} \right) \frac{\nabla c_e}{c_e} - \nabla \phi_e \right] \quad (2.8)$$

This expression stems from concentrated solution theory, where the electrolyte deviates from ideal behavior<sup>1,3</sup>. The thermodynamic factor  $(1 + \partial \ln f / \partial \ln c_e)$  originates from the Stefan–Maxwell formulation and is typically measured experimentally along with  $\kappa$ ,  $t^+$  and  $D_{amb}$ <sup>3–7</sup>.

The boundary conditions for these equations depend on the battery under investigation. In this thesis we focused on half-cells, so batteries composed by a working porous electrode and a thick Li-metal counter electrode, the capacity of which far exceed the one of the working electrode. This is done to assure a simplified treatment of the Li-metal electrode, that can be considered as an infinite Li source at fixed potential. Therefore, the reaction term  $R(x)$  is zero within the separator ( $x \in [0, L_{sep}]$ ) and different from zero in the electrode ( $x \in [L_{sep}, L]$ ). The Li-metal electrode will still present a solid electrolyte interface (SEI) and the formation of dendrites. However, we neglect the latter and assume the former to be included in the series resistance  $R_{ser}$ . The boundary conditions are therefore assumed to have the following form:

$$\frac{dc_e}{dx} \Big|_{x=L} = 0 \quad (2.9)$$

$$\frac{dc_e}{dx} \Big|_{x=0} = -i_{cell} \frac{1 - t^+}{e D_{eff}} \quad (2.10)$$

where the electrolyte flux is assumed to be imposed by the cell current ( $i_{cell}$ ) on the Li-metal side ( $x = 0$ ) and to be zero against the positive current collector, since no ions can infiltrate it. Consequently, the electrolyte potential includes the zero-flux condition for the ionic current at the positive current collector and the reference redox potential of the Li-metal reaction:

$$\phi_e|_{x=L} = E_{Li/Li^+} = 0 \text{ V} \quad (2.11)$$

$$\frac{d\phi_e}{dx}|_{x=L} = 0 \quad (2.12)$$

Moreover, the boundary conditions for the electric potential consider the imposed electron current ( $i_{cell}$ ) and the separator to be electrically insulating:

$$\frac{d\phi_s}{dx}|_{x=L} = -\frac{i_{cell}}{\sigma_{eff}} \quad (2.13)$$

$$\frac{d\phi_s}{dx}|_{x=L_{sep}} = 0 \quad (2.14)$$

Finally, the battery voltage can be defined based on the solid-phase potentials of both electrodes and the series resistance ( $R_{ser}$ ) so that:

$$V = \phi_s - E_{Li/Li^+} - R_{ser} i_{cell} \quad (2.15)$$

## 2.2 COUPLING ELECTRODE AND PARTICLE SCALES

Having established the macroscopic, depth-wise framework for modeling porous electrodes, we now turn our attention to the particle scale, where ion insertion and extraction occur. The behavior of individual active material particles is governed by surface reaction kinetics, solid-state diffusion, and thermodynamic phase transitions. It ultimately determines the local reaction rate, which serves as a source term in the electrode-scale model ( $R(x)$ ).

Given a set of particles with varying volumes  $V_i$  and surface areas  $S_i$ , the reaction rate can be computed from the individual particle contributions:

$$R = -\frac{\varepsilon_s \sum_i I_i}{e \sum_i V_i} \quad (2.16)$$

Here,  $\varepsilon_s$  is the volume fraction of active material, and  $I_i$  is the total current associated with particle  $i$ , obtained by integrating the local surface current density  $j_i$  over its surface:

$$I_i = \int_{S_i} j_i dS \quad (2.17)$$

The surface current density in each region of the particle surface, now referred to as  $j$  by dropping the subscript for clarity, depends on the local reaction overpotential  $\eta$  and solid surface concentration  $c_s$ .

$$j = k_0 f(\eta, c_e, c_s, T) \quad (2.18)$$

where  $k_0$  is the exchange current density prefactor and  $f$  can have various functional forms depending on the approximation<sup>8</sup>. The  $f$  function also considers the effect of temperature ( $T$ ), electrolyte concentration ( $c_e$ ) at the specific electrode position  $x$ .

In general,  $c_s$  depends on the particle's properties at the specified electrode depth, and  $\eta$  is defined based on  $\phi_s$ ,  $\phi_e$ , and the surface chemical potential  $\mu(c_s)$ :

$$\eta = \phi_s - \phi_e + \frac{\mu(c_s)}{e} \quad (2.19)$$

Equations 16-19 clarify the coupling between macroscopic porous electrode dimension, responsible for computing the  $\phi_s(x)$ ,  $\phi_e(x)$ ,  $c_e(x)$  and the particle-scale dynamics, that specifies  $\mu(c_s)$  and  $c_s$ .

## 2.3 REACTION KINETICS

Conventionally, the reaction rate is calculated by using the *Butler-Volmer* equation (BV) which predicts an exponential dependence of reaction rate on overpotential<sup>9</sup>:

$$f_{BV} = \tilde{c}_e^{1-\alpha} c^\alpha (1-c)^{1-\alpha} \left( e^{-\alpha \frac{e\eta}{k_B T}} - e^{(1-\alpha) \frac{e\eta}{k_B T}} \right) \quad (2.20)$$

where  $\alpha$  is the charge transfer coefficient,  $c = c_s/c_{max}$  is the *normalized* concentration and  $\tilde{c}_e = c_e/c_{e,ref}$  is the normalized electrolyte concentration, usually divided by a reference concentration  $c_{e,ref}$  of one molar.

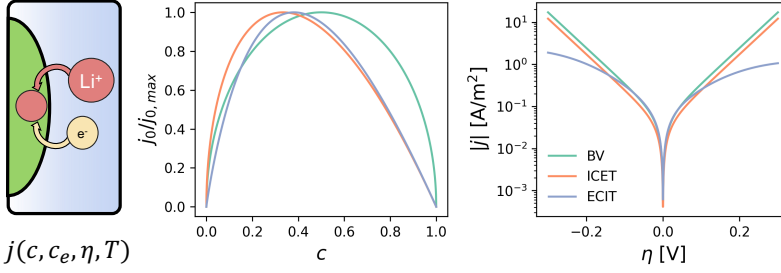


Figure 2.2. Normalized exchange current density dependence on concentration for the various reaction kinetics. Tafel plot of the current density evolution at various overpotentials for the case of  $c = 0.5$  and  $k_0 = 0.1 \text{ A m}^{-2}$ .

Recent progresses have expanded charge transfer theories by properly accounting for both electrons and ionic processes involved in the reaction rates<sup>9,10</sup>. This novel theory, known as *Coupled Ion-Electron Transfer* (CIET) theory, can be applied by using one of the two main approximations: *electron-coupled ion transfer* (ECIT) and *ion-coupled electron transfer* (ICET). ECIT refers to the case where the electron transfer is the limiting factor, and ICET to the ionic-limited case. The resulting relations are:

$$f_{ICET} = \tilde{c}_e^{1-\alpha} c^\alpha (1-c) \left( e^{-\alpha \frac{e\eta}{k_B T}} - e^{(1-\alpha) \frac{e\eta}{k_B T}} \right) \quad (2.21)$$

$$f_{ECIT} = \left( \frac{1-c}{2} \right) \left( \frac{\tilde{c}_e}{1+e^{\tilde{\eta}_f}} - \frac{c}{1+e^{-\tilde{\eta}_f}} \right) \text{erfc} \left( \frac{\tilde{\lambda} - \sqrt{\tilde{\eta}_f^2 + 1 + \sqrt{\tilde{\lambda}}}}{2\sqrt{\tilde{\lambda}}} \right) \quad (2.22)$$

As shown in Fig. 2.2, these approximations substantially differ in their functional form. In ICET, similarly to BV, the reaction rate grows exponentially with the overpotential applied, but the exchange current density evolves differently with the concentration. In particular, the BV case with a  $\alpha = 0.5$ , we obtain a symmetric relation with a peak at  $c = 0.5$ . On the contrary, the ICET predicts the maximum exchange current to occur at  $c \sim 0.4$  with a linear decrease at higher concentrations. The ECIT approximation includes the reorganization energy for the electron jump  $\lambda$ , here reported in normalized form ( $\tilde{\lambda} = \lambda/k_B T$ ), and a formal overpotential  $\tilde{\eta}_f = \frac{e\eta}{k_B T} + \ln\left(\frac{\tilde{c}_e}{c}\right)$ . Aside also showing a maximum exchange current density at  $c \sim 0.4$ , it does not follow an exponential relation with  $\eta$ . It instead presents saturation at high overpotentials, resembling Marcus–Hush–Chidsey theory<sup>11–13</sup>, so that if  $\eta \gtrsim 0.5 \text{ V}$  no further increase in current is observed.

## 2.4 PHASE-FIELD MODELING

A key variable in defining the reaction rate and ion transport within a particle is the chemical potential  $\mu$ . In simple models<sup>2,14</sup>,  $\mu$  is often obtained by measuring the open circuit voltage ( $U$ ) of the electrode and assuming:

$$\mu(c) = -eU(c) \quad (2.23)$$

This relation may hold for homogeneous solid-solution particles that are stable across the full concentration range. However, it breaks down in the case of *phase-separating materials*, where miscibility gaps exist and only specific lithium concentrations are thermodynamically stable<sup>1,15</sup>. Since this thesis focuses on olivine phosphates, which undergo phase separation into Li-rich and Li-poor phases, a more advanced thermodynamic treatment is required.

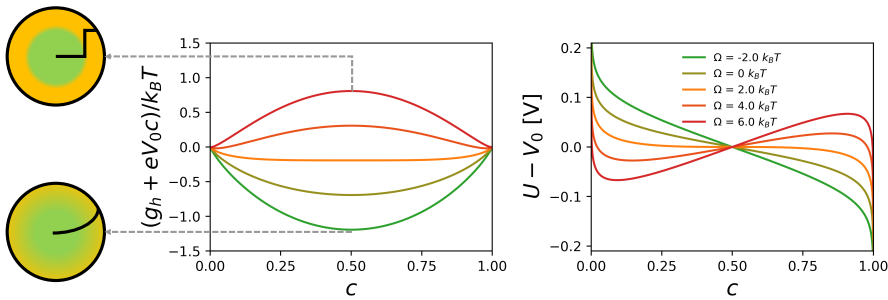


Figure 2.3. Relation between the regular solution parameter  $\Omega$ , the free energy  $g$ , and the open circuit potential  $U$ .

From classical thermodynamics, the chemical potential is defined as the derivative of the free energy with respect to concentration<sup>16–18</sup>. For a homogeneous particle, the chemical potential  $\mu_h$  can be derived from the homogeneous free energy density  $g_h$  as:

$$\mu_h = \frac{dg_h}{dc} \quad (2.24)$$

The free energy function  $g_h(c)$  can be obtained via DFT calculations at different lithium concentrations<sup>19,20</sup>. However, because DFT is performed at 0 K, entropic contributions must be included separately. One approach involves cluster expansions and sampling at finite temperatures, but this is computationally demanding, particularly for transition metal compounds<sup>21,22</sup>.

A more tractable alternative is to use *regular solution theory*<sup>1,23,24</sup>, a mean-field thermodynamic model that approximates the ion–vacancy interactions using a single parameter,  $\Omega$ , the *regular solution parameter*. In this framework, the homogeneous free energy is given by:

$$g_h = -eV_0c + k_B T [c \ln(c) + (1 - c)\ln(1 - c)] + \Omega c(1 - c) \quad (2.25)$$

where  $\Omega$  represents the energetic penalty for mixing ions and vacancies,  $V_0$  is the standard redox potential, which is defined based on the system's energy  $E$  as:

$$eV_0 = E(c = 1) - E(c = 0) - E_{Li} \quad (2.26)$$

and can be derived from DFT<sup>25–27</sup> or thermodynamics data<sup>28</sup>,

This model aligns well with results from more advanced methods, particularly for olivine phosphates<sup>29</sup>. The corresponding homogenous chemical potential becomes:

$$\mu_h = -eV_0 + k_B T \ln\left(\frac{c}{1 - c}\right) + \Omega(1 - 2c) \quad (2.27)$$

As shown in Fig. 2.3, increasing  $\Omega$  alters the concavity of the free energy and the monotonicity of  $\mu$ . In particular, if  $\Omega > 2 k_B T$ , the free energy exhibits two minima, indicating a *miscibility gap*. Experimentally, this manifests as flat regions in the open circuit voltage (*plateau*), where ionic insertion/extraction occurs at constant voltage with a persistent *thermodynamic hysteresis* between charge and discharge even at close-to-zero currents<sup>30</sup>.

To model non-equilibrium effects and spatial heterogeneities, the homogeneous free energy is extended into a *free energy functional*  $G$ , defined over the particle's particle domain  $D$ :

$$G = \int_D c_{max} \left[ g_h + \frac{1}{2} \kappa (\nabla c)^2 \right] dV + \int_{\partial D} \gamma dS \quad (2.28)$$

This functional includes a *phase boundary energy* term,  $\kappa(\nabla c)^2/2$ , where  $\kappa$  is a gradient energy coefficient and *surface wetting energy*  $\gamma(c)$  which depends on the surface concentration. The functional can also include a mechanical energy term<sup>31</sup>, neglected here for the sake of clarity.

The local chemical potential  $\mu$  for an inhomogeneous system is then given by the *functional derivative* of  $G$ :

$$\mu = \frac{1}{c_{max}} \frac{\delta G}{\delta c} = \mu_h - \kappa \nabla^2 c \quad (2.29)$$

Combining this equation with the natural boundary conditions for the wetting energy, ( $\mathbf{n} \cdot \kappa \nabla c = d\gamma/dc$ ), we form the basis of *phase-field* methodology, originally developed in metallurgy, now widely applied to simulate phase separation within and between battery materials particles.

## 2.5 PARTICLE-SCALE MODELS

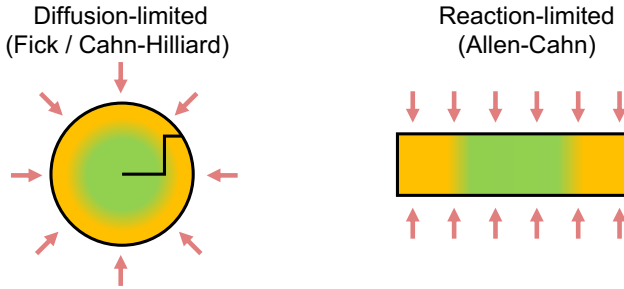


Figure 2.4. One-dimensional particle models.

Depending on the morphology and characteristic timescales of active material particles, different models can be considered. Accurately simulating particle-scale dynamics requires solving three-dimensional models, which requires computational costs<sup>32,33</sup>. Therefore, reduced-order approximations are often employed, such as one-dimensional models, which balance fidelity and efficiency. The selection of the appropriate model depends on the particle morphology<sup>34</sup>, which we explore in the next section.

In this thesis, one-dimensional models are classified into two main categories: *reaction-limited* and *diffusion-limited*. In reaction-limited models, it is assumed that the ion concentration is uniform along the particle depth, i.e.  $c_s(\mathbf{x}) = c(\mathbf{x})$ . These models emphasize heterogeneous reactions across the particle width and are appropriate when diffusion within the particle is much faster than interfacial kinetics. This regime is typically valid for thin platelet-like particles, where the diffusion timescale is short relative to the reaction timescale<sup>35</sup>. In contrast, diffusion-limited models assume a uniform surface concentration across the particle interface, i.e.  $c_s(r_i) = c_s(r_j)$ , but resolve the non-uniform concentration profile within the particle volume. This is more suitable for spheroidal or cylindrical particles with longer diffusion paths<sup>25,36,37</sup>.

It is also important to distinguish between *primary particles*<sup>38</sup>, which can often be treated as independent units, and *agglomerated secondary particles*<sup>36,39,40</sup>, where multiple grains are fused into a larger structure. In the latter case, it is sometimes acceptable to approximate the entire agglomerate as a single particle with coherent behavior, ignoring intergranular effects<sup>2,41</sup>. However, for higher fidelity, *hierarchical models*<sup>39</sup> can be used to explicitly account for intra-agglomerate transport and local reaction dynamics within nanopores. Such multi-scale models will be discussed in detail in Chapter 8.

Throughout this thesis, different approximations are adopted based on the particle morphology and the level of detail required. For example, in Chapters 3 and 7, a zero-dimensional approximation is used for nanoparticles, while in Chapter 5 and 6, phase-field models are applied to simulate phase separation in larger spheroidal particles.

### 2.5.1 Diffusion-Limited Model

In diffusion-limited models, the concentration of lithium evolves primarily due to solid-state diffusion within the particle. The conservation of mass inside the particle can be expressed in terms of the internal lithium flux  $F_s$ :

$$\frac{dc}{dt} = -\nabla \cdot F_s \quad (2.30)$$

Traditional DFN models, initially developed for layered oxide materials, assume spherical secondary particles in which lithium diffuses according to Fick's law<sup>1,2</sup>:

$$F_s = -D_s \nabla c \quad (2.31)$$

Here,  $D_s$  is the solid-phase diffusivity, which can vary with both concentration and temperature. The boundary conditions for a spherical particle of radius  $R_p$  are then applied at the particle surface:

$$\frac{dc}{dr}\Big|_{r=R_p} = \frac{j}{e D_s(c_{surf})} \quad (2.32)$$

and at the center (by symmetry):

$$\frac{dc}{dr}\Big|_{r=0} = 0 \quad (2.34)$$

## 2 | MULTIPHASE POROUS ELECTRODE THEORY

While Fickian diffusion can be effective for *solid-solution* materials, for *phase separating* materials, it is more thermodynamically consistent to express flux in terms of chemical potential, using the formulation derived in the previous section:

$$F_s = -c_{max} D_s(c) c \nabla \left( \frac{\mu}{k_B T} \right) \quad (2.35)$$

In this case, the diffusivity is often modeled using an *excluded-site approximation*<sup>8</sup>:

$$D_s(c) = D_0(1 - c) \quad (2.36)$$

This form reflects the fact that ions require both an occupied site to jump from and a vacant site to jump into. Moreover, in the case of solid solution materials without boundary energy penalty, Eq. 2.34 recovers Eq. 2.30.

The boundary conditions for the chemical potential are:

$$\frac{d\mu}{dr}|_{r=R_p} = \frac{k_B T}{e} \frac{j}{c_{surf} D_s(c_{surf}) c_{max}} \quad (2.37)$$

$$\frac{d\mu}{dr}|_{r=0} = 0 \quad (2.38)$$

Because this results in a fourth-order PDE, additional natural boundary conditions must be applied to the concentration field. These involve the wetting energy  $\gamma$  as a function of surface concentration<sup>42</sup>:

$$\frac{dc}{dr}|_{r=R_p} = \frac{d\gamma}{dc} \quad (2.39)$$

$$\frac{dc}{dr}|_{r=0} = 0 \quad (2.40)$$

This diffusion-limited phase-field model, often referred to as the *Cahn–Hilliard Reaction* (CHR) model<sup>23,43</sup>, has successfully reproduced the phase behavior of LFP<sup>44</sup>, LTO<sup>25</sup>, and graphite<sup>36,37</sup> electrodes.

## 2.5.2 Reaction-Limited Model

In the reaction-limited regime, solid-state diffusion is assumed to be fast compared to interfacial kinetics, so the lithium concentration is uniform along the particle depth and evolves due solely to surface reactions<sup>35</sup>. For a slab-shaped particle of thickness  $h$ , assuming heterogenous reactions solely along  $x_p \in [0, l_p]$ , the concentration evolves as:

$$\frac{dc}{dt} \Big|_{x_p} = \frac{j(x_p)}{eh} \quad (2.41)$$

and symmetric wetting boundary conditions are applied at both surfaces:

$$\frac{dc}{dx} \Big|_{x=l_p} = \frac{d\gamma}{dc} \quad (2.42)$$

$$\frac{dc}{dx} \Big|_{x=0} = -\frac{d\gamma}{dc} \quad (2.43)$$

In such systems, the non-monotonic chemical potential and the presence of surface energy effects lead to spatially heterogeneous reactions<sup>45</sup>, concentrating the current at thermodynamically favorable positions along the surface.

When particles are within the nanoscale, surface energy, elastic effects, and wetting can suppress phase separation entirely, resulting in uniform lithiation and delithiation. For such particles, a zero-dimensional reaction-limited approximation can be used<sup>35,45–48</sup>. In this case, the chemical potential is defined using a size-dependent regular solution parameter  $\Omega(s)$ , where particle characteristic size  $s$  affects thermodynamic behavior:

$$\mu = -eV_0 + k_B T \ln\left(\frac{c}{1-c}\right) + \Omega(s)(1-2c) \quad (2.44)$$

For instance, in the case of LFP nanoparticle,  $\Omega(s)$  decreases as particle size decreases, with values reaching  $\sim 50$  meV for particles approaching 30 nm, as surface and mechanical effects reduce the energetic penalty for mixing. This ensures nanoparticles to evolve homogenously, as predicted by more advanced models<sup>35,45–47</sup>.

The lithium concentration then evolves according to:

$$\frac{dc}{dt} = \frac{S j(\eta, c, c_e)}{V e} \quad (2.45)$$

This zero-dimensional particle model, still able to capture most of the behavior of nanostructured olivine phosphates particles, is highly computationally efficient, making it useful for modeling composite electrodes with nano-sized active materials.

## 2.6 ADVANCED MODELING

In this section, we have outlined the foundations of P2D modeling for battery electrodes. Several studies have demonstrated the capabilities of this approach. Vasileiadis, for instance, integrated porous electrode theory with DFT and MD simulations to develop a predictive model for LTO electrodes, capable of accurately capturing rate performance without any adjustable parameters<sup>25</sup>. Schwietert included the effects of solid electrolytes, highlighting how the absence of electrolyte polarization and the presence of solid-solid contact losses can significantly alter battery behavior<sup>49</sup>. The intricate relationship between particle size, rate capability, surface wetting, and mechanical effects in LFP electrodes has also been explored<sup>31–33,35,45,46</sup>, improving the understanding of their performance. Extensions of regular solution theory to multi-layered materials have enabled detailed mesoscopic modeling of graphite electrodes<sup>37</sup>, capturing their behavior beyond the classical assumptions. When these models are combined with operando measurements, they reveal the often-overlooked role of charge transfer kinetics in layered oxide cathodes<sup>50</sup>.

Beyond performance modeling, porous electrode models can be enriched to account for irreversible degradation mechanisms, allowing us to predict and mitigate long-term battery aging. For example, Li plating on graphite, the formation of metallic Li during fast charging, has been modeled by coupling phase-field and hierarchical particle models with nucleation theories, yielding predictive tools to optimize charging protocols<sup>36,51,52</sup>. Similarly, chemical degradation has been modeled through descriptions of solid electrolyte interface (SEI) growth on anode surfaces<sup>53</sup>, with extensions to include temperature effects<sup>54</sup>, making it possible to distinguish between calendar aging, time-dependent, and cycle-induced degradation<sup>55</sup>; an essential consideration for batteries in EVs and BESS<sup>56</sup>.

Mechanical and thermal expansions have also been incorporated into porous electrode frameworks<sup>57</sup>, correlating internal degradation with externally measurable quantities such as cell

swelling<sup>58</sup> and temperature rise<sup>54,59</sup>. This enables more effective use of the extensive data collected from commercial batteries under real-world conditions<sup>60,61</sup>.

Ultimately, these model advancements enable the co-optimization of design<sup>62</sup> and control<sup>63</sup>. For example, microstructural insights<sup>64</sup> can guide the engineering of tailored electrode architectures, while performance simulations can inform both particle morphology and electrode layout<sup>65</sup>. Scaling up, electrode-level models can be extended to cell and pack-level simulations to support system integration<sup>66</sup>. Furthermore, once validated, computationally efficient battery models can be embedded into model-predictive control frameworks<sup>67,68</sup>, enabling safe fast charging, real-time health estimation<sup>69</sup>, or economic optimization<sup>56</sup> in grid-scale BESS applications.

## REFERENCES

1. Ferguson, T. R. & Bazant, M. Z. Nonequilibrium Thermodynamics of Porous Electrodes. *J. Electrochem. Soc.* **159**, A1967–A1985 (2012).
2. Brosa Planella, F. *et al.* A continuum of physics-based lithium-ion battery models reviewed. *Prog. Energy* **4**, 042003 (2022).
3. Lagnoni, M., Nicoletta, C. & Bertei, A. Comparison of Electrolyte Transport Modelling in Lithium-ion Batteries: Concentrated Solution Theory Vs Generalized Nernst-Planck Model. *J. Electrochem. Soc.* **169**, 020570 (2022).
4. Bizeray, A. M., Howey, D. A. & Monroe, C. W. Resolving a Discrepancy in Diffusion Potentials, with a Case Study for Li-Ion Batteries. *J. Electrochem. Soc.* **163**, E223–E229 (2016).
5. Valøen, L. O. & Reimers, J. N. Transport Properties of LiPF<sub>6</sub>-Based Li-Ion Battery Electrolytes. *J. Electrochem. Soc.*
6. Nyman, A., Behm, M. & Lindbergh, G. Electrochemical characterisation and modelling of the mass transport phenomena in LiPF<sub>6</sub>-EC-EMC electrolyte. *Electrochimica Acta* **53**, 6356–6365 (2008).
7. Landesfeind, J. & Gasteiger, H. A. Temperature and Concentration Dependence of the Ionic Transport Properties of Lithium-Ion Battery Electrolytes. *J. Electrochem. Soc.* **166**, A3079–A3097 (2019).
8. Bazant, M. Z. Theory of Chemical Kinetics and Charge Transfer based on Nonequilibrium Thermodynamics. *Acc. Chem. Res.* **46**, 1144–1160 (2013).
9. Bazant, M. Z. Unified quantum theory of electrochemical kinetics by coupled ion-electron transfer. *Faraday Discuss.* 10.1039.D3FD00108C (2023) doi:10.1039/D3FD00108C.
10. Fraggedakis, D. *et al.* Theory of coupled ion-electron transfer kinetics. *Electrochimica Acta* **367**, 137432 (2021).
11. Marcus, R. A. On the Theory of Electron-Transfer Reactions. VI. Unified Treatment for Homogeneous and Electrode Reactions. *J. Chem. Phys.* **43**, 679–701 (1965).
12. Zeng, Y., Smith, R. B., Bai, P. & Bazant, M. Z. Simple formula for Marcus–Hush–Chidsey kinetics. *J. Electroanal. Chem.* **735**, 77–83 (2014).
13. Bai, P. & Bazant, M. Z. Charge transfer kinetics at the solid–solid interface in porous electrodes. *Nat. Commun.* **5**, 3585 (2014).
14. Boettcher, S. W. *et al.* Potentially Confusing: Potentials in Electrochemistry. *ACS Energy Lett.* **6**, 261–266 (2021).
15. Smith, R. B. & Bazant, M. Z. Multiphase Porous Electrode Theory. *J. Electrochem. Soc.* **164**, E3291–E3310 (2017).
16. Cahn, J. W. & Hilliard, J. E. Free Energy of a Nonuniform System. I. Interfacial Free Energy.
17. Cahn, J. W. & Hilliard, J. E. Free Energy of a Nonuniform System. III. Nucleation in a Two-Component Incompressible Fluid.
18. Piazza, R. *Statistical Physics: A Prelude and Fugue for Engineers.* (Springer International Publishing, Cham, 2017). doi:10.1007/978-3-319-44537-3.
19. Perez, I. *Ab initio* methods for the computation of physical properties and performance parameters of electrochemical energy storage devices. *Phys. Chem. Chem. Phys.* **25**, 1476–1503 (2023).
20. Hörmann, N. G. & Groß, A. Phase field parameters for battery compounds from first-principles calculations. *Phys. Rev. Mater.* **3**, 055401 (2019).
21. Barroso-Luque, L. *et al.* Cluster expansions of multicomponent ionic materials: Formalism and methodology. *Phys. Rev. B* **106**, 144202 (2022).

22. Malik, R., Zhou, F. & Ceder, G. Kinetics of non-equilibrium lithium incorporation in LiFePO<sub>4</sub>. *Nat. Mater.* **10**, 587–590 (2011).
23. Lee, D. *et al.* Physical, mathematical, and numerical derivations of the Cahn–Hilliard equation. *Comput. Mater. Sci.* **81**, 216–225 (2014).
24. Zelič, K. & Kตราšnik, T. Thermodynamically consistent derivation of chemical potential of a battery solid particle from the regular solution theory applied to LiFePO<sub>4</sub>. *Sci. Rep.* **9**, 2123 (2019).
25. Vasileiadis, A. *et al.* Toward Optimal Performance and In-Depth Understanding of Spinel Li<sub>4</sub>Ti<sub>5</sub>O<sub>12</sub> Electrodes through Phase Field Modeling. *Adv. Funct. Mater.* **28**, 1705992 (2018).
26. Ganapathy, S., Vasileiadis, A., Heringa, J. R. & Wagemaker, M. The Fine Line between a Two-Phase and Solid-Solution Phase Transformation and Highly Mobile Phase Interfaces in Spinel Li<sub>4+x</sub>Ti<sub>5</sub>O<sub>12</sub>. *Adv. Energy Mater.* **7**, 1601781 (2017).
27. Urban, A., Seo, D.-H. & Ceder, G. Computational understanding of Li-ion batteries. *Npj Comput. Mater.* **2**, 16002 (2016).
28. CALPHAD: *Calculation of Phase Diagrams - A Comprehensive Guide*. vol. 1 (Elsevier, 1998).
29. Zhao, H. *et al.* Learning heterogeneous reaction kinetics from X-ray videos pixel by pixel. *Nature* **621**, 289–294 (2023).
30. Dreyer, W. *et al.* The thermodynamic origin of hysteresis in insertion batteries. *Nat. Mater.* **9**, 448–453 (2010).
31. Cogswell, D. A. & Bazant, M. Z. Coherency Strain and the Kinetics of Phase Separation in LiFePO<sub>4</sub> Nanoparticles. *ACS Nano* **6**, 2215–2225 (2012).
32. Daubner, S., Weichel, M., Schneider, D. & Nestler, B. Modeling intercalation in cathode materials with phase-field methods: Assumptions and implications using the example of Li FePO<sub>4</sub>. *Electrochimica Acta* **421**, 140516 (2022).
33. Daubner, S. *et al.* Multiphase-field modeling of spinodal decomposition during intercalation in an Allen-Cahn framework. *Phys. Rev. Mater.* **5**, 035406 (2021).
34. Fraggedakis, D. *et al.* A scaling law to determine phase morphologies during ion intercalation. *Energy Environ. Sci.* **13**, 2142–2152 (2020).
35. Bai, P., Cogswell, D. A. & Bazant, M. Z. Suppression of Phase Separation in LiFePO<sub>4</sub> Nanoparticles During Battery Discharge. *Nano Lett.* **11**, 4890–4896 (2011).
36. Lian, H. & Bazant, M. Z. Modeling Lithium Plating Onset on Porous Graphite Electrodes Under Fast Charging with Hierarchical Multiphase Porous Electrode Theory. *J. Electrochem. Soc.* **171**, 010526 (2024).
37. Smith, R. B., Khoo, E. & Bazant, M. Z. Intercalation Kinetics in Multiphase-Layered Materials. *J. Phys. Chem. C* **121**, 12505–12523 (2017).
38. Li, Y. *et al.* Effects of Particle Size, Electronic Connectivity, and Incoherent Nanoscale Domains on the Sequence of Lithiation in LiFePO<sub>4</sub> Porous Electrodes. *Adv. Mater.* **27**, 6591–6597 (2015).
39. Birkholz, O. & Kamlah, M. Electrochemical Modeling of Hierarchically Structured Lithium-Ion Battery Electrodes. *Energy Technol.* **9**, 2000910 (2021).
40. Chen, H., Xu, S., Zhou, M., Zhang, X. & Zhou, H. Hierarchical porous Na<sub>3</sub>V<sub>2</sub>(PO<sub>4</sub>)<sub>3</sub>/graphene microspheres with enhanced sodium-ion storage properties. *J. Mater. Sci. Mater. Electron.* **34**, 2196 (2023).
41. Brosa Planella, F., Sheikh, M. & Widanage, W. D. Systematic derivation and validation of a reduced thermal-electrochemical model for lithium-ion batteries using asymptotic methods. *Electrochimica Acta* **388**, 138524 (2021).
42. Nadkarni, N. *et al.* Interplay of phase boundary anisotropy and electro-auto-catalytic surface reactions on the lithium intercalation dynamics in Li X FePO<sub>4</sub> plateletlike nanoparticles. *Phys. Rev. Mater.* **2**, 085406 (2018).
43. Zeng, Y. & Bazant, M. Z. Cahn-Hilliard Reaction Model for Isotropic Li-ion Battery Particles. *MRS Proc.* **1542**, mrrs13-1542-g02-01 (2013).

44. Ombrini, P. *et al.* Kinetically induced memory effect in Li-ion batteries. *EES Batter.* 10.1039/D5EB00014A (2025) doi:10.1039/D5EB00014A.
45. Cogswell, D. A. & Bazant, M. Z. Theory of Coherent Nucleation in Phase-Separating Nanoparticles. *Nano Lett.* **13**, 3036–3041 (2013).
46. Cogswell, D. A. & Bazant, M. Z. Size-dependent phase morphologies in LiFePO<sub>4</sub> battery particles. *Electrochem. Commun.* **95**, 33–37 (2018).
47. Van der Ven, A. & Wagemaker, M. Effect of surface energies and nano-particle size distribution on open circuit voltage of Li-electrodes. *Electrochem. Commun.* **11**, 881–884 (2009).
48. Ferguson, T. R. & Bazant, M. Z. Phase Transformation Dynamics in Porous Battery Electrodes. *Electrochimica Acta* **146**, 89–97 (2014).
49. Schwietert, T. K. *et al.* Phase-Field Computational Framework for Addressing Challenges in Solid-State Batteries. *PRX Energy* **2**, 033014 (2023).
50. Park, J. *et al.* Fictitious phase separation in Li layered oxides driven by electro-autocatalysis. *Nat. Mater.* **20**, 991–999 (2021).
51. Lu, X. *et al.* Multiscale dynamics of charging and plating in graphite electrodes coupling operando microscopy and phase-field modelling. *Nat. Commun.* **14**, 5127 (2023).
52. Gao, T. *et al.* Interplay of Lithium Intercalation and Plating on a Single Graphite Particle. *Joule* **5**, 393–414 (2021).
53. Pinson, M. B. & Bazant, M. Z. Theory of SEI Formation in Rechargeable Batteries: Capacity Fade, Accelerated Aging and Lifetime Prediction. *J. Electrochem. Soc.* **160**, A243–A250 (2013).
54. Prada, E. *et al.* A simplified electrochemical and thermal aging model of LiFePO<sub>4</sub>-graphite Li-ion batteries: power and capacity fade simulations. *J. Electrochem. Soc.* **160**, A616 (2013).
55. Karger, A. *et al.* Modeling Particle Versus SEI Cracking in Lithium-Ion Battery Degradation: Why Calendar and Cycle Aging Cannot Simply be Added. *J. Electrochem. Soc.* **171**, 090512 (2024).
56. Reniers, J. M., Mulder, G. & Howey, D. A. Unlocking extra value from grid batteries using advanced models. *J. Power Sources* **487**, 229355 (2021).
57. Ipers, G. *et al.* Rapid Simulation of Electro-Chemo-Mechanical Deformation of Li-ion Batteries Based On Porous Electrode Theory. *J. Electrochem. Soc.* **171**, 050557 (2024).
58. Ai, W., Kraft, L., Sturm, J., Jossen, A. & Wu, B. Electrochemical Thermal-Mechanical Modelling of Stress Inhomogeneity in Lithium-Ion Pouch Cells. *J. Electrochem. Soc.* **167**, 013512 (2019).
59. O'Regan, K., Brosa Planella, F., Widanage, W. D. & Kendrick, E. Thermal-electrochemical parameters of a high energy lithium-ion cylindrical battery. *Electrochimica Acta* **425**, 140700 (2022).
60. Geslin, A. *et al.* Dynamic cycling enhances battery lifetime. *Nat. Energy* (2024) doi:10.1038/s41560-024-01675-8.
61. Lam, V. N. *et al.* A decade of insights: Delving into calendar aging trends and implications. *Joule* 101796 (2024) doi:10.1016/j.joule.2024.11.013.
62. Lain, M. J., Brandon, J. & Kendrick, E. Design Strategies for High Power vs. High Energy Lithium Ion Cells. *Batteries* **5**, 64 (2019).
63. Lee, S. B., Thiagarajan, R. S., Subramanian, V. R. & Onori, S. Advanced Battery Management Systems: Modeling and Numerical Simulation for Control. in *2022 American Control Conference (ACC)* 4403–4414 (IEEE, Atlanta, GA, USA, 2022). doi:10.23919/ACC53348.2022.9867639.
64. Cooper, S. J., Bertei, A., Shearing, P. R., Kilner, J. A. & Brandon, N. P. TauFactor: An open-source application for calculating tortuosity factors from tomographic data. *SoftwareX* **5**, 203–210 (2016).
65. Kench, S. *et al.* Li-ion battery design through microstructural optimization using generative AI. *Matter* S2590238524004466 (2024) doi:10.1016/j.matt.2024.08.014.
66. Ramirez-Meyers, K., Rawn, B. & Whitacre, J. F. A statistical assessment of the state-of-health of LiFePO<sub>4</sub> cells harvested from a hybrid-electric vehicle battery pack. *J. Energy Storage* **59**, 106472 (2023).

67. Duan, X. *et al.* Electrochemical Modeling of Fast Charging in Batteries. *Adv. Energy Mater.* 2400710 (2024) doi:10.1002/aenm.202400710.
68. Azimi, V., Allam, A. & Onori, S. Extending Life of Lithium-Ion Battery Systems by Embracing Heterogeneities via an Optimal Control-Based Active Balancing Strategy. *IEEE Trans. Control Syst. Technol.* 1–15 (2022) doi:10.1109/TCST.2022.3215610.
69. Lim, J.-H. *et al.* Efficient Electrochemical State of Health Model for Lithium Ion Batteries under Storage Conditions. *J. Phys. Chem. C* **127**, 2183–2193 (2023).



# 3 THE INFLUENCE OF OPEN CIRCUIT POTENTIAL ON ELECTRODE DYNAMICS

This chapter has been published as: Ombrini P, Vasileiadis A, Wagemaker M. The Influence of Open Circuit Potential on Electrode Dynamics. Journal of The Electrochemical Society. 2025.

## ABSTRACT

3 Phase separation, inducing a miscibility gap and non-monotonic open-circuit potential (OCP), is typical for widespread Li-ion battery electrodes such as  $\text{LiFePO}_4$ ,  $\text{Li}_4\text{T}_5\text{O}_{12}$  and Graphite. Although particle-scale effects of phase separation are well documented, its influence on transport-limited, porous electrodes remains largely overlooked. Here we embed physically consistent non-monotonic OCP profiles in a simplified Doyle–Fuller–Newman (DFN) framework to compare their behavior against that of solid-solution materials with monotonic OCPs. Our findings provide deeper and general understanding of the different electrode ensemble behavior of solid solution (monotonic OCP) and phase separating (non-monotonic OCP) electrode materials, demonstrating why larger miscibility gaps are associated with decreasing rate capabilities and electrode utilization, amplifying local current heterogeneity and electrolyte depletion. By contrast, simulations employing conventional flat, fitted OCPs mask these effects and overpredict performance—particularly under dynamic cycling protocols such as galvanostatic intermittent titration (GITT). Our results reveal why accounting for realistic OCPs is essential for reliable modelling of high-loading electrodes, providing fundamental understanding and guidance for model-driven design and control of next-generation batteries.

### 3.1 INTRODUCTION

Modeling electrodes for design and protocol optimization is necessary to advance both experimental research and commercial battery applications<sup>1,2</sup>. These models must be meticulously adapted to the properties of the active materials, and reflect their intrinsic thermodynamics, with phase separation being a critical yet often overlooked aspect. Conventional layered oxides, such as  $\text{LiCoO}_2$  (LCO) and  $\text{LiNi}_x\text{Mn}_y\text{Co}_{1-x-y}\text{O}_2$  (NMC), undergo lithiation and delithiation as single-phase solid solutions, where ions and vacancies uniformly mix at all ionic concentrations<sup>3</sup>. In contrast, numerous prominent materials for Li-ion and Na-ion batteries—including  $\text{LiFePO}_4$  (LFP)<sup>4-7</sup>,  $\text{LiMn}_x\text{Fe}_{1-x}\text{PO}_4$  (LMFP)<sup>8,9</sup>,  $\text{Li}_4\text{Ti}_5\text{O}_{12}$  (LTO)<sup>10</sup>, graphite<sup>11-13</sup>,  $\text{Na}_3\text{V}_2(\text{PO}_4)_3$  (NVP)<sup>14</sup>, and Prussian blue analogues (PB)<sup>15</sup>, exhibit a thermodynamic propensity to phase separate into ion-rich and ion-poor regions. This phase separation leads to a miscibility gap, preventing the material from achieving equilibrium across certain compositional ranges. For example, an LFP particle under equilibrium conditions can only be composed of two phases, having a filling fraction below  $\sim 0.15$  or above  $\sim 0.85$ <sup>16-18</sup>. This phase separation behavior manifests as flat voltage plateaus and thermodynamic hysteresis, characterized by a persistent (small) voltage gap between charging and discharging even under equilibrium conditions<sup>19-21</sup>. Such phenomena directly influence key aspects of electrochemical performance, including energy efficiency, rate capability, and cycle life. Consequently, accurately modeling and optimizing battery performance necessitates addressing the effects of phase separation.

Significant advancements have been made in simulating the phase separation kinetics of both individual particles and particle ensembles. Depending on particle size and material diffusivity, particles may be categorized as either reaction-limited (charge transfer) or diffusion-limited (ion diffusion through the electrode particle)<sup>22</sup>. For instance, LFP is generally synthesized with nanoscale particles to minimize diffusion length and enhance the surface-to-volume ratio, rendering it reaction-limited<sup>4</sup>. Phase-field models, such as Allen-Cahn reaction (ACR) model, have been developed to describe and predict the appearance or suppression of phase separation in single primary particles under varying current conditions<sup>16,17,23,24</sup>. In these cases, the model neglects the diffusion limitations and focus its attention on the heterogenous surface reaction kinetics<sup>23</sup>. Conversely, graphite, which is often utilized in larger particle sizes, typically exhibits diffusion-limited behavior<sup>12,13,25</sup>. In this case, Cahn-Hilliard reaction (CHR) models<sup>7,10,26</sup> effectively characterize the phase separation kinetics and predict concentration gradients along the particle's radius. Modeling the energy penalties associated with these gradients is necessary for estimating surface concentrations and thus improving the prediction of lithium plating risks and reaction kinetics<sup>11,27</sup>. Moreover, the electrochemical response of such systems can deeply vary when compared to similar electrodes that do not phase separate, misleading the interpretation of experimental and simulated results if the CHR dynamics is not considered<sup>7,10,28</sup>.

### 3 | THE INFLUENCE OF OPEN CIRCUIT POTENTIAL ON ELECTRODE DYNAMICS

3 While modeling and understanding single-particle kinetics is integral to material engineering, the collective dynamics of multi-particle systems within an electrode play a decisive role in determining its overall performance<sup>20,29</sup>. Phase-separating electrodes exhibit distinct population kinetics due to the presence of an energy barrier for the nucleation of the secondary phase. Even under uniform electrochemical conditions, particle reactions occur heterogeneously. Certain particles, either due to smaller size or stochastic thermal fluctuations, nucleate first and dominate the reaction<sup>29</sup>. Consequently, the system evolves via particle-by-particle sequential reaction. At higher currents, more particles are utilized to sustain the reaction, increasing number of active particles<sup>20</sup>. These studies underscore the necessity of precise particle-scale models to properly assess the collective behavior. Nevertheless, they primarily focused on ultra-thin electrodes where the particles experience homogenous ionic and electronic potentials and dominant effects arise from interparticle dynamics rather than electrolyte polarization.

In practical applications, high-loading electrode behavior ( $> 4 \text{ mAh cm}^{-2}$ ) is predominantly governed by electrolyte and electronic transport<sup>30,31</sup>. Therefore, electrode design efforts prioritize minimizing tortuosity and optimizing active material volume fractions<sup>2</sup>. Semiconductor-based materials, like LFP, exhibit lower electronic conductivity and solid-state diffusivity than transition metal oxides like LCO or NMC<sup>32</sup>. As a result, these electrodes require additional engineering measures, including carbon coatings, nanoscale particle design, and conductive additives<sup>33</sup>. These morphological and compositional strategies aim to overcome intrinsic charge and ion mobility limitations. This added complexity in structure and transport behavior, in turn, affects how phase separation manifests and evolves within the electrode<sup>30,31</sup>. Consequently, the role of phase separation in determining the performance of thick electrodes remains difficult to isolate, resulting in transport kinetics studies that focus microstructural properties<sup>2,34</sup> without considering thermodynamic effects<sup>30</sup>.

To gain insight in the role of phase separation, inducing a non-monotonic OCP, we simulate an idealized, one-dimensional porous electrode composed of reaction-limited particles of identical size. Each particle is assumed to remain homogeneous, hence solid-state diffusion cannot obscure electrode-scale phenomena. Throughout all simulations, kinetic parameters are held constant, while equilibrium thermodynamic properties are varied. Specifically, we use the regular solution model<sup>8,35–37</sup> to calculate each particle's free energy landscape under different ion–vacancy interaction energies. As the repulsion between ions and vacancies increases, the material's OCP—computed from its homogeneous chemical potential—transitions from a monotonic to a strongly non-monotonic profile. This framework enables us to uncover the role of depth-wise inter-particle phase separation in governing reaction localization, electrode utilization, and electrolyte transport under both constant-current (CC) and galvanostatic intermittent titration (GITT) protocols.

Notably, this thermodynamic framework naturally reproduces the voltage plateaus and hysteresis characteristic of materials with a miscibility gap. In contrast, conventional models often fit experimental OCPs of materials like LFP and LTO using voltage curves obtained from slow (C/100) lithiation and delithiation. This approach yields two artificially flat OCPs<sup>38</sup>, one for charge and one for discharge, and requires empirical approximations to interpolate between them during dynamic cycling<sup>39</sup>. In this context, we compare the physically consistent model to the flat-plateau approximation, quantifying the errors that arise when phase-separating materials are represented using monotonic OCP profiles.

The remainder of the paper is organized as follows. In Section 1, we introduce the theoretical framework, describing the OCP model and its derivation from free energy and the parameter  $\Omega$ , which controls phase-separation tendency and miscibility gaps. In Section 2, we analyze the system under constant-current (CC) conditions, evaluating its behavior across different OCP profiles. Section 3 explores dynamic response under a galvanostatic intermittent titration technique (GITT) protocol. In Section 4, we investigate the influence of kinetic parameters, particularly the characteristic diffusion and reaction times, and their effects on reaction localization and electrode utilization. In Section 5, we compare the physically consistent OCP model to a conventional flat OCP approximation, highlighting differences in both behavior and implementation under CC and GITT conditions. We conclude by summarizing the key findings and discussing broader implications for phase-separating electrode materials and model-based electrode design.

### 3.2 FROM THE FREE ENERGY TO THE OPEN CIRCUIT POTENTIALS

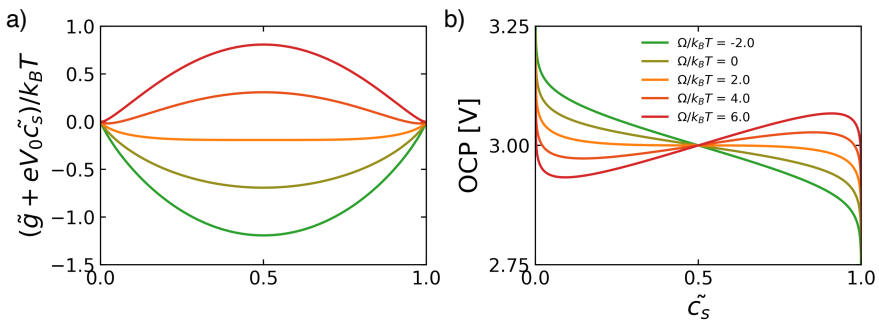


**Figure 3.1. From the free energy to the OCP.** a) Free energy of the regular solution model at various  $\Omega$ s. b) Open circuit potential at various  $\Omega$ s in case of  $V_0 = 3$  V.

### 3 | THE INFLUENCE OF OPEN CIRCUIT POTENTIAL ON ELECTRODE DYNAMICS

To generalize this study and capture a continuous range of materials differing only in their OCP and phase transition characteristics, we adopt a general formulation derived from thermodynamic principles. In this framework, the OCP is directly related to the free energy of the system. Specifically, the homogeneous free energy landscape  $g(\tilde{c}_s)$  can be modeled using regular solution theory<sup>8,35–37</sup>:

$$g(\tilde{c}_s) = -eV_0\tilde{c}_s + k_B T [\tilde{c}_s \ln \tilde{c}_s + (1 - \tilde{c}_s)\ln(1 - \tilde{c}_s)] + \Omega \tilde{c}_s(1 - \tilde{c}_s) \quad (3.1)$$

where  $V_0$  is the reference potential,  $\tilde{c}_s$  is the normalized solid particle concentration ( $\tilde{c}_s = c_s/c_{max}$ ),  $k_B$  is the Boltzmann constant,  $e$  is the electron charge, and  $T$  is the temperature. The main factor regulating the free energy is  $\Omega$ , called the regular solution parameter. It controls the interaction between inserted species and vacancies, so that when  $\Omega < 0$  an attractive interaction between ions and vacancy is considered, while  $\Omega > 0$  indicates a repulsive interaction. If  $\Omega = 0$  the system is an ideal solution where the mixing free energy is solely regulated by the entropic contribution and the minimum of  $g(\tilde{c}_s)$  coincides with the maximum mixing at  $\tilde{c}_s = 0.5$ . This case is thus considered a solid solution. At  $\Omega = 2 k_B T$  the entropic and enthalpic energies compensate each other, leading to a flat free energy landscape (Fig. 3.1a). If  $\Omega$  exceeds this threshold, the free energy presents two minima, signifying that the system's energy is minimized by a combination of two phases, each of them having concentration corresponding with the minima (Fig. 3.1a). This condition leads to a thermodynamic drive for phase separation. Increasing  $\Omega$  leads to diverging minima, increasing the miscibility gap.

The open circuit potential can be derived from the regular solution free energy:

$$U(\tilde{c}_s) = -\frac{1}{e} \frac{dg}{d\tilde{c}_s} = V_0 - \frac{k_B T}{e} \ln \frac{\tilde{c}_s}{1 - \tilde{c}_s} - \frac{\Omega}{e} (1 - 2\tilde{c}_s) \quad (3.2)$$

The effect of  $\Omega$  on the OCP is shown in Fig. 3.1b. When  $\Omega > 2 k_B T$  the OCP results non-monotonic. This corresponds to phase-separating materials, whereas for  $\Omega < 2 k_B T$  the OCP decreases monotonically with increasing filling fraction, similarly to the behavior of transition metal oxides such as LCO and NMC<sup>40,41</sup>. Although this simplified representation does not capture all the nuances of real materials, it effectively models key characteristics observed in materials such as LFP<sup>7,16</sup>, LMFP<sup>8</sup>, LTO<sup>10</sup>, etc. Moreover, advanced models that reconstruct the full free energy landscape have validated this approach<sup>16</sup>. It is important to note that the total free energy of a non-homogeneous particle, and consequently its OCP, also depends on additional factors such as boundary energy penalties and chemo-mechanical effects<sup>5,6,23</sup>.

However, for the sake of clarity and the focus on the impact of the OCP, in this work these factors are neglected, thus assuming the particles remain homogeneous.

Within this theoretical framework, the existence of multiple minima in the free energy landscape, leading to phase separation, is consistently linked to miscibility gaps, voltage plateaus, and thermodynamic hysteresis. In fact, while the OCP of a single particle can be non-monotonic, the collective behavior of multiple particles leads to the experimentally observed voltage plateaus and hysteresis. During (de)insertion, the particles rapidly equilibrate their chemical potential to the global maximum (or minimum), effectively smoothing out the non-monotonic features<sup>19</sup>.

Aside from the local inter-particle phase separation behavior, the insertion dynamics of a transport-limited electrode are inherently influenced by the monotonicity of the OCP, as illustrated in Fig. 3.2. Under near-equilibrium conditions, a thin, reaction-limited electrode composed of phase-separating particles would react heterogeneously due to thermal fluctuations and particle size differences<sup>20,29</sup>. In contrast, in transport-limited electrodes operating under dynamic conditions, a non-monotonic OCP induces depth-wise heterogeneous reactions.

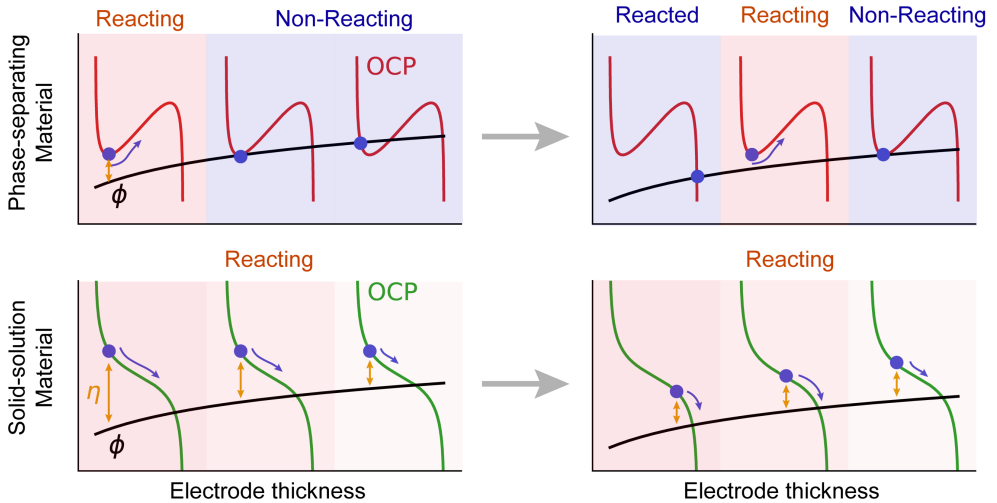


**Figure 3.2.** Schematic representation comparing the electrode dynamic of a solid solution material and a phase-separating material during an insertion process. The separator is assumed to be on the left of the electrode, while the current collector is on the right. The OCP of the phase-separating material is shown in red, while the OCP of the solid solution material is in green. The potential difference between electron-conducting and ion-conducting phases ( $\phi$ ), sloping due to transport limitations, is represented in black. The reaction overpotential ( $\eta$ ), leading to an insertion process, is depicted in yellow.

For the case of non-monotonic OCP (phase-separating material in Fig. 3.2), initially, transport-induced potential drops allow only the region near the separator–electrode interface to exceed the insertion threshold, while deeper sections remain inactive. As insertion progresses in the reactive region, the increasing solid-phase concentration raises the particle surface potential, which in turn enhances the local overpotential and accelerates the reaction. This autocatalytic mechanism concentrates the reaction within a narrow zone of the electrode. Once the reacting particles in this zone complete insertion, the reaction front advances further into the electrode (second step of Fig. 3.2). Owing to the symmetric shape of the OCP, this phenomenon occurs during both insertion and de-insertion in phase-separating materials, driving the system toward a phase-separated state.

In contrast, monotonically decreasing OCPs (solid-solution material in Fig. 3.2) are less susceptible to this localization. As the local solid-phase concentration increases, the particle potential decreases, reducing the overpotential and thus the reaction rate. This autoinhibitory effect, combined with the absence of a potential threshold, enables the entire electrode to react more uniformly. Although the reaction still initiates near the separator, the continuous variation in overpotential leads to a more homogeneous current distribution.

In this illustrative example, we neglected electrolyte concentration variations, so the localized reaction arises solely from changes in particle potential. However, as shown in the results section, non-monotonic OCPs also significantly affect electrolyte dynamics, further enhancing reaction localization.

### 3.3 MODEL'S EQUATIONS

To investigate these effects, we employ a simplified one-dimensional porous electrode model of a homogenous electrode, hereby described. In this model, a porous electrode, of length  $L$ , is considered filled with a binary monovalent dilute electrolyte of concentration  $c_e$ , having equal diffusivities of positive and negative ions ( $D_- = D_+$ ), so that the ambipolar diffusivity ( $D_{amb}$ ) coincides with  $D_+$  and the transference number is  $1/2$ . Given a porosity  $\varepsilon$  and a tortuosity  $\tau_e$  the governing equation for the electrolyte concentration results<sup>35,36,42–44</sup>

$$\varepsilon \frac{dc_e}{dt} = \frac{d}{dx} \left( \frac{\varepsilon}{\tau_e} D_+ \frac{dc_e}{dx} \right) + \frac{a j(x)}{2F} \quad (3.3)$$

where  $a$  is the specific reactive surface area ( $\text{m}^2/\text{m}^3$ ), and the local current density  $j(x)$  changes along the domain axis  $x$ , depending on the local reaction rate. In this work we neglect the

concentration dependence of the electrolyte diffusivity and assume a tortuosity equal to one. Neglecting also the electric losses along the electrode's thickness, we can define an electrode potential difference  $\phi$  which will be regulated by the charge conservation in the electrolyte:

$$\frac{d}{dx} \left( \kappa \frac{d\phi}{dx} \right) = a j(x) \quad (3.4)$$

with the electrolyte conductivity  $\kappa$  being the one of a dilute electrolyte

$$\kappa = 2 \frac{F^2}{RT} \frac{\varepsilon}{\tau_e} D_+ c_e \quad (3.5)$$

where,  $F$  is the Faraday constant and  $R$  the gas constant, and the concentration term disappear since  $D_+ = D_-$ . The electrode potential difference  $\phi$  is conventionally defined as the difference between the solid phase potential  $\phi_s$  and the electrolyte potential  $\phi_e$ <sup>42</sup>. In this work, since the ohmic losses in the solid phase are assumed negligible, we can use a single variable  $\phi = \phi_s - \phi_e$ . Moreover, neglecting the presence of separator or resistance between the current collector and the active material, the output voltage is  $V = \phi(x = 0)$  and its initial condition, depends on the initial solid concentration is  $V(t = 0) = U(\tilde{c}_s(t = 0))$ . The local reaction rate is expressed in using the symmetric Butler-Volmer kinetics ( $\alpha = 1/2$ ):

$$j = k_0 \sqrt{\tilde{c}_e} \sqrt{\tilde{c}_s(1 - \tilde{c}_s)} \left[ e^{\frac{F\eta}{RT}} - e^{-\frac{F\eta}{RT}} \right] \quad (3.6)$$

so that it depends on the exchange current density  $k_0$  ( $\text{A m}^{-2}$ ), the normalized electrolyte concentration  $\tilde{c}_e = c_e/c_e(t = 0)$ , the normalized particle concentration  $\tilde{c}_s$ , and the reaction overpotential

$$\eta = \phi - U(\tilde{c}_s) \quad (3.7)$$

Finally, the particles are simulated as homogenous and using a zero-dimensional approximation, so their concentration evolves as

$$\varepsilon_s \frac{d\tilde{c}_s}{dt} = - \frac{a j}{c_{max} F} \quad (3.8)$$

### 3 | THE INFLUENCE OF OPEN CIRCUIT POTENTIAL ON ELECTRODE DYNAMICS

where  $\varepsilon_s$  is the active material volume fraction, here coinciding with  $1 - \varepsilon$ , since no conductive domains or binders are considered. We scale the imposed current density and the boundaries ( $I$ ) by the C-rate (where C-rate = 1 indicates the full (dis)charge of the electrode in 1 h):

$$I = c_{max} F \varepsilon_s L C_{rate} \quad (3.9)$$

So that the boundary conditions result from assuming no ionic flux at the outer boundary (current collector):

$$\frac{dc_e}{dx} \Big|_{x=L} = 0 \quad (3.10)$$

$$\frac{d\phi}{dx} \Big|_{x=L} = 0 \quad (3.11)$$

and imposed current at the inner boundary, i.e. considered as an infinite ionic source:

$$\varepsilon \frac{dc_e}{dx} \Big|_{x=0} = - \frac{I \tau_e}{2 F D_+} \quad (3.12)$$

$$\frac{d\phi}{dx} \Big|_{x=0} = \frac{I}{\kappa(x=0)} \quad (3.13)$$

While more advanced electrochemical descriptions are available<sup>36,42,44</sup>, the presented model is built to only focus on two limiting factors: electrolyte transport and the reaction kinetics at the active material-electrolyte interface. These two processes define the overall behavior of the idealized electrode and can be characterized by two fundamental timescales:

Reaction time: 
$$\tau_R = \frac{\varepsilon_s c_{max} F}{a k_0} \quad (3.14)$$

Diffusion time: 
$$\tau_D = \frac{\tau_e L^2}{\varepsilon D_+} \quad (3.15)$$

These characteristic timescales are then compared to the charging timescale,  $\tau_C$ , defined based on the C-rate:

$$\tau_C = \frac{L c_{max} F \varepsilon_s}{I} = \frac{1}{C_{rate}} \quad (3.16)$$

The ratio of these timescales determines the dominant transport mechanism. For instance, when  $\tau_C < \tau_D$ , the diffusion process is slower than the insertion, leading to the development of concentration gradients. Conversely, when  $\tau_C < \tau_R$ , the reaction kinetics become the limiting factor, significantly increasing the overpotential. To further quantify the distribution of the reaction within the electrode, we define a normalized current density  $\tilde{j}$ :

$$\tilde{j} = \frac{a L j}{I} \quad (3.17)$$

So that, in a perfectly uniform electrode, the average volumetric current density ( $I/L$ ) coincides with the local volumetric current density ( $a j$ ), resulting in  $\tilde{j} = 1$ . However, non-uniform insertion rates increase  $\tilde{j}$ , indicating the formation of localized reaction and the presence of current hotspots.

The model was implemented using the open-source software PyBaMM<sup>45</sup>. Specifically, the BaseModel class was extended to include the specified set of equations and boundary conditions and using the software we implemented 300 spatial discretization points. The time integration was performed using CasADi solver<sup>46</sup>.

### 3 | THE INFLUENCE OF OPEN CIRCUIT POTENTIAL ON ELECTRODE DYNAMICS

Variable	Governing equations	Boundary conditions	Assumptions
Electrolyte concentration $c_e$	$\varepsilon \frac{dc_e}{dt} = \frac{d}{dx} \left( \frac{\varepsilon}{\tau_e} D_+ \frac{dc_e}{dx} \right) + \frac{aj(x)}{2F}$	$\varepsilon \frac{dc_e}{dx} \Big _{x=0} = -\frac{I\tau_e}{2FD_+}$ $\frac{dc_e}{dx} \Big _{x=L} = 0$	No separator Monovalent dilute electrolyte $D_+ = D_-$ $D_+$ independent on concentration
Electrode potential difference $\phi$	$\frac{d}{dx} \left( \kappa \frac{d\phi}{dx} \right) = aj(x)$	$\frac{d\phi}{dx} \Big _{x=0} = \frac{I}{\kappa(x=0)}$ $\frac{d\phi}{dx} \Big _{x=L} = 0$	Negligible ohmic losses in the solid phase Dilute electrolyte conductivity: $\kappa = 2 \frac{F^2}{RT} \frac{\varepsilon}{\tau_e} D_+ c_e$
Normalized solid concentration $\tilde{c}_s$	$j = k_0 \sqrt{\tilde{c}_e} \sqrt{\tilde{c}_s(1-\tilde{c}_s)} \left[ e^{\frac{F\eta}{RT}} - e^{-\frac{F\eta}{RT}} \right]$ $\eta = \phi - U(\tilde{c}_s)$ $U(\tilde{c}_s) = V_0 - \frac{k_B T}{e} \ln \frac{\tilde{c}_s}{1-\tilde{c}_s} - \frac{\Omega}{e} (1-2\tilde{c}_s)$ $\varepsilon_s \frac{d\tilde{c}_s}{dt} = -\frac{aj}{c_{max} F}$		Negligible solid diffusion limitations Uniform reaction on the particles surface Identical size OCP described by regular solution theory

Table 1. Summary of the governing equations, boundary conditions and assumptions.

## 3.4 RESULTS

To evaluate the impact of varying  $\Omega$  on electrode kinetics, we simulated an electrode where the characteristic timescales were set to be equal, i.e.,  $\tau_c = \tau_D = \tau_R$ . The simulations were performed for an insertion process with an initial normalized concentration of  $\tilde{c}_i = 0.01$ . It is important to clarify the terminology used in conventional battery protocols. Typically, the discharge process refers to ion insertion into the positive electrode. Since this study presents a general analysis of an insertion process, and we set the average potential at  $V_0 = 3$  V, we define our applied protocols as discharge. However, due to the symmetry of the open circuit potential (OCP) and reaction kinetics, the same results can be extended to the de-insertion process—corresponding to the charge of a positive electrode or the discharge of a negative electrode.

To account for differences in OCPs across simulations, we imposed a cutoff voltage based on the total overpotential, setting  $V - U = -0.5 \text{ V}$ . The electrode porosity was fixed at 0.5. A realistic example of such a system would be a half-cell discharging at a rate of 5C (completing a full (dis)charge in 720 seconds) with an electrolyte diffusivity of  $D_+ = 10^{-10} \text{ m}^2 \text{ s}^{-1}$ , and an electrode of thickness of  $190 \text{ }\mu\text{m}$ . Moreover, to assure a negligible solid diffusion the electrode could be composed by particles of  $50 \text{ nm}$  of radius ( $a = 3 \cdot 10^7 \text{ m}^{-1}$ ), having  $k_0 = 4 \cdot 10^{-2} \text{ A m}^{-2}$ . Using these parameters, we simulated two distinct cases: a constant current scenario and a galvanostatic intermittent titration protocol (GITT). We then proceeded to analyze the effects of varying  $\tau_D$  and  $\tau_R$  on electrode performance and kinetics, providing insight into how phase separation influences transport limitations and reaction localization.

### 3.5 CONSTANT CURRENT PROTOCOL

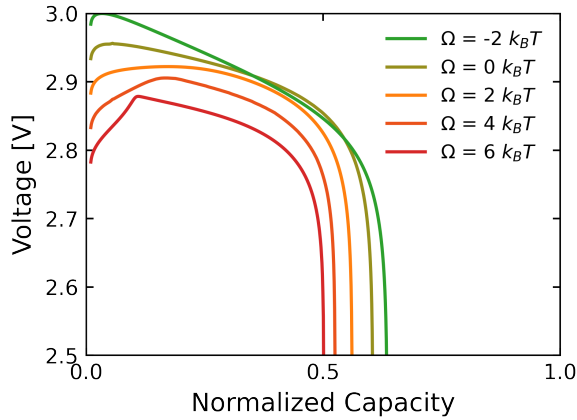


**Figure 3.3.** Comparison between the constant current responses of the model at varying  $\Omega$ s. The various colors indicate different values of  $\Omega$ .

Fig. 3.3 presents a comparison of the constant current responses of the model across different values of  $\Omega$ . An unexpected result emerges: the properties of the open circuit potential (OCP) influence the capacity retention of the system. Despite identical discharge rates and electrode kinetic properties, higher values of  $\Omega$ , corresponding to a stronger tendency for phase separation, lead to greater capacity losses. Notably, this effect is not limited to the transition from solid solution behavior ( $\Omega < 2 k_B T$ ) to phase-separating behavior ( $\Omega > 2 k_B T$ ) but rather persists as  $\Omega$  increases continuously. Specifically, the initial potential drops are related to the reaction kinetics, where the lower exchange current density at lower solid concentrations increase the overpotential, and the utilized electrode surface scales with  $\Omega$ .

### 3 | THE INFLUENCE OF OPEN CIRCUIT POTENTIAL ON ELECTRODE DYNAMICS

The subsequent sloping voltage profile is instead related to the electrolyte transport, where the influence of OCP on kinetic performance can be understood by analyzing the evolution of key variables during the insertion process, as shown in Fig. 3.4. When comparing the limiting cases of  $\Omega = -2 k_B T$  and  $\Omega = 6 k_B T$ , significant differences emerge. In the former case, the solid concentration  $\tilde{c}_s$  remains uniform throughout the electrode, whereas in the latter case, it exhibits an abrupt transition, forming a strong concentration gradient (Fig. 3.4a,d). This depth-resolved phase separation is driven purely by the non-monotonic OCP. As in thin electrode phase separation occurs either between or within particles, in this transport-limited system it manifests along the electrode thickness.

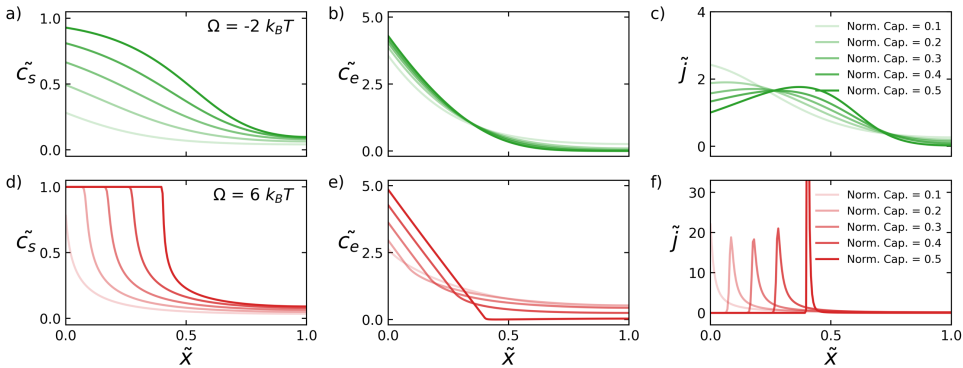


**Figure 3.4. Evolution during the constant current protocol.** Evolution of normalized solid concentration  $\tilde{c}_s$  (a,d), normalized electrolyte concentration  $\tilde{c}_e$  (b,e), and normalized volumetric current density  $\tilde{j}$  (c,f), during the constant current protocol along the normalized electrode thickness  $\tilde{x} = x/L$ . The green lines correspond to the case with  $\Omega = -2 k_B T$  while the red lines represent the case with  $\Omega = 6 k_B T$ . Transparency indicates the corresponding normalized capacity.

This phenomenon is closely coupled with the evolution of electrolyte concentration  $\tilde{c}_e$  (Fig. 3.4b,e). In the solid solution case,  $\tilde{c}_e$  quickly stabilizes, reaching a quasi-steady-state early in the process and undergoing minimal changes throughout the reaction. Conversely, in the phase-separating case  $\tilde{c}_e$  continues evolving during the entire insertion process. This difference arises due to variations in the local reaction rate, as illustrated in Fig. 3.4 c and f. When the material undergoes phase separation, the local current density can be up to 20 times higher than the average value, leading to a highly localized reaction at the interface between reacted and unreacted regions.

This localized reaction leads to electrolyte depletion, which increases electrolyte polarization and ultimately reduces capacity retention. Additionally, higher local current densities correlate with

increased overpotential and the onset of degradation mechanisms. These findings, in line with experimental results<sup>30</sup>, highlight the importance of accounting for phase-separation effects when designing electrodes and optimizing charging protocols for phase-separating materials.

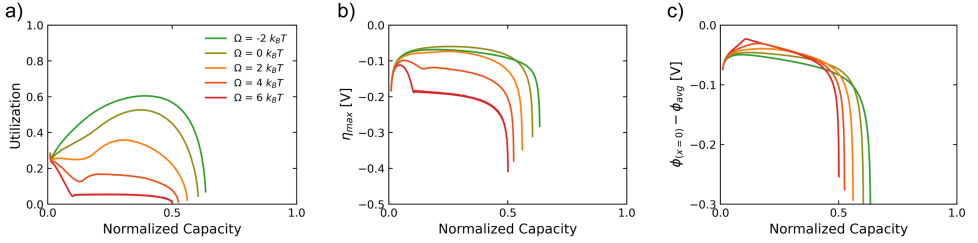


**Figure 3.5. Evolution of relevant internal variables.** Evolution of utilization (a), maximum reaction overpotential (b) and transport overpotential (c) during the constant current protocol. The various colors indicate different values of  $\Omega$ .

Finally, we examine the evolution of key indicators during the reaction process<sup>47</sup>. The heterogeneous nature of the reaction at the electrode scale manifests as an increasing disparity between the imposed current density and the local current density. This effect can be quantified using the utilization, defined as:

$$Utilization = \frac{1}{\max \tilde{j}} \quad (3.18)$$

In the case of a perfectly homogeneous current distribution, where  $\tilde{j} = 1$  (i.e.  $aj = J/L$ ), the utilization is equal to 1, indicating that the entire electrode volume participates in the reaction. However, when the current is localized, only a fraction of the electrode is actively utilized during the insertion process. Fig. 3.5a presents the evolution of utilization over the discharge process, highlighting a striking contrast in the effective use of active material between phase-separating and solid solution materials. As the miscibility gap increases (i.e., with increasing  $\Omega$ ), utilization decreases significantly.

The consequences of this reduced utilization are evident in Fig. 3.5 b and c, which show the evolution of the maximum reaction overpotential  $\eta_{max}$  and the transport overpotential ( $\phi_{x=0} - \phi_{avg}$ ) as functions of  $\Omega$ . The behavior of  $\eta_{max}$  reveals an initial decrease due to the increased exchange current density in the Butler-Volmer kinetics. However, in phase-separating cases, once the system surpasses the miscibility gap,  $\eta_{max}$  abruptly increases to overcome the nucleation barrier. As the reaction progresses, the need to activate particles located further from the ion source (separator) maintains this high overpotential until a reduction in  $c_e$  forces the system to reach the cutoff voltage.

The transport overpotential follows a different trend. In phase-separating systems, the presence of a reaction front near the separator initially results in a lower transport overpotential compared to solid solution cases. However, as the reaction extends deeper into the electrode and electrolyte depletion becomes more pronounced, the transport overpotential in phase-separating cases eventually surpasses that of solid solution materials.

### 3.6 GITT PROTOCOL

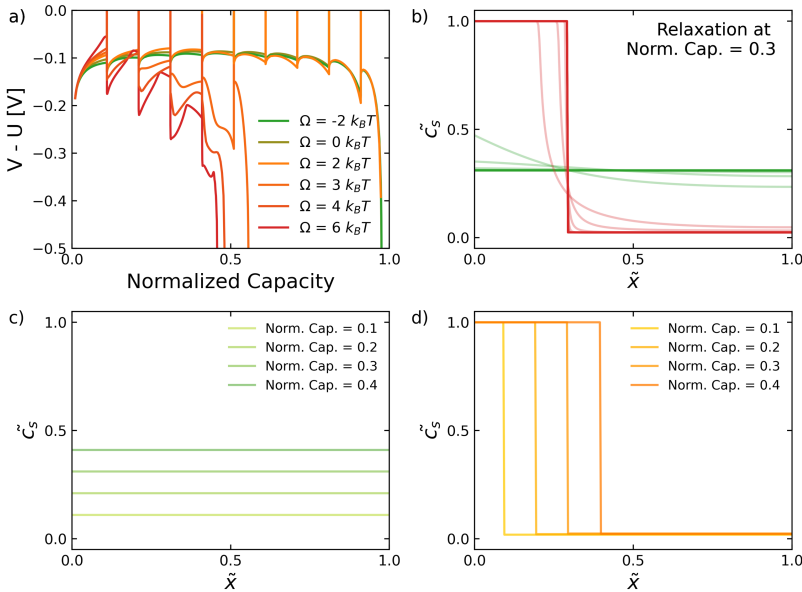


**Figure 3.6. Evolution during the GITT protocol.** a) Evolution of the total overpotential ( $V - U$ ) during the various pulses, plotted against the normalized capacity. b) Relaxation of the normalized solid concentration after the third pulse along the normalized electrode thickness  $\tilde{x}$ . The green lines refer to the  $\Omega = -2 k_B T$  case, the red lines to the  $\Omega = 6 k_B T$  case. The transparent lines correspond to the result after the pulse and subsequent relaxation. The opaque line corresponds to the profile reached at the end of the relaxation process. c,d) Normalized depth-resolved solid concentration at various normalized capacities during the GITT protocol at the end of the relaxation, for the  $\Omega = -2 k_B T$  case (c) and the  $\Omega = 6 k_B T$  case (d).

The presence of non-monotonic chemical potentials is also affecting the electrode dynamics during resting periods and subsequent current pulses. To establish its impact, we simulated a galvanostatic intermitted titration (GITT) protocol where the electrode was pulsed multiple times for a duration of  $\tau_C/10$  and rested for  $5\tau_D$ , until the cutoff voltage was reached. As shown

in Fig. 3.6a, while the constant current case exhibits only minor differences among OCPs (Fig. 3.3), the extracted capacity and overpotential in the GITT protocol are significantly affected by the OCP, and consequently, by phase separation dynamics. In the case of  $\Omega \leq 2 k_B T$ , the total overpotential remains stable across multiple pulses. During the resting period, the solid concentration returns to a homogeneous and stable value (Fig. 3.6b-c), ensuring that each pulse follows similar dynamics, governed primarily by the concentration dependence of reaction kinetics (Eq. 7). For  $\Omega > 2 k_B T$ , however, the system reaches an equilibrium concentration profile composed of two distinct regions with strongly differing concentrations (Fig. 3.6b,d). The portion of the electrode near the separator equilibrates in a fully inserted state, while the remaining electrode volume becomes depleted. This pattern repeats with each pulse, resulting in a continuous reaction across the entire electrode for  $\Omega \leq 2 k_B T$  case (Fig. 3.6c), while for  $\Omega > 2 k_B T$  a narrow insertion front develops and propagates from the separator (Fig. 3.6d). This behavior arises as the system seeks to minimize its total free energy.

The consequences of this heterogeneous concentration profile become apparent in subsequent pulses. In phase-separating materials ( $\Omega > 2 k_B T$ ), since the system reaches thermodynamic equilibrium as separated into two distinct phases, the electrolyte must transport ions over a greater distance to reach the non-reacted region, and the total amount of active material available for the reaction decreases during subsequent pulses. As the protocol progresses, these effects lead to an overpotential buildup that persists despite the resting periods. In other words, the electrode retains a memory, meaning that the concentration inhomogeneities formed during prior pulses do not dissipate during open circuit rest, further influencing the response of subsequent cycles. We also show how this effect is proportional to  $\Omega$ , i.e. proportional to the miscibility gap: the wider the concentration difference between the two phases, the greater the remaining heterogeneity after relaxation. These findings complement previously reported results, where various protocols applied to phase-separating materials show path-dependencies<sup>7,18,48,49</sup> and unusual features<sup>28</sup>, strengthening the need for physically consistent modeling of phase separating materials.

### 3.7 THE EFFECT OF KINETIC PARAMETERS

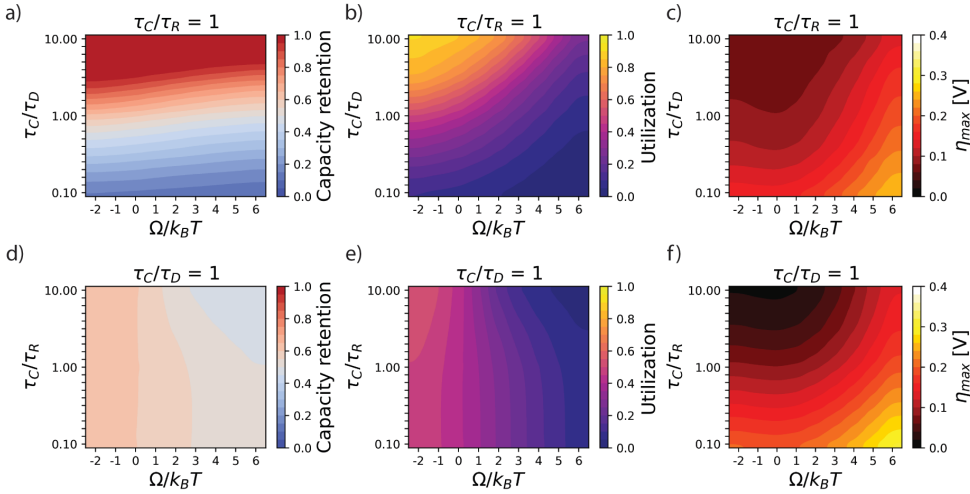


**Figure 3.7. The effect of kinetic parameters on the constant current protocol.** Capacity retention at varying kinetic ratios:  $\tau_C/\tau_D$  (a) and  $\tau_C/\tau_R$  (d). Mean utilization during the discharge at varying  $\tau_C/\tau_D$  (b) and  $\tau_C/\tau_R$  (e). Maximum absolute value of the reaction overpotential during the discharge at varying  $\tau_C/\tau_D$  (c) and  $\tau_C/\tau_R$  (f). Where  $\tau_C = 1/C\_rate$ ,  $\tau_D$  is the characteristic diffusion time along the electrode thickness and  $\tau_R$  is the characteristic reaction time.

Having established the significant impact of the miscibility gap on electrode kinetics and performance, we now examine the effect of varying the ratio between characteristic timescales. As expected, capacity retention improves when the diffusion time is reduced, such as in the case of a thinner electrodes, slower discharging or improved ionic diffusivity. This trend is observed consistently across all values of  $\Omega$  (Fig. 3.7a). A similar effect is seen in average utilization, which exhibits a strong dependence on both diffusion time and  $\Omega$  (Fig. 3.7b). Additionally, as  $\tau_D$  increases, the local reaction rate becomes more homogeneous, while its overall magnitude increases with larger  $\Omega$  (Fig. 3.7c).

More unexpectedly, in the case of phase separating materials ( $\Omega > 2 k_B T$ ), a reduction in reaction time  $\tau_R$  (decrease in charge transfer resistance) leads to a decrease in capacity retention (Fig. 3.7d), indicating that improving charge transfer kinetics can actually reduce the extracted capacity at the same rates. This counterintuitive behavior can be explained by the sharp decline in utilization observed for lower  $\tau_R$  (Fig. 3.7e). When deviations from the equilibrium potential occur, local reaction kinetics increase significantly, promoting stronger inhomogeneous

reactivity. This results in a more localized reaction front (Fig. 3.7f), which rapidly depletes the electrolyte near the reaction sites, ultimately causing a sudden voltage drop.

### 3.8 COMPARISON BETWEEN PHYSICALLY DERIVED AND FITTED OCPs

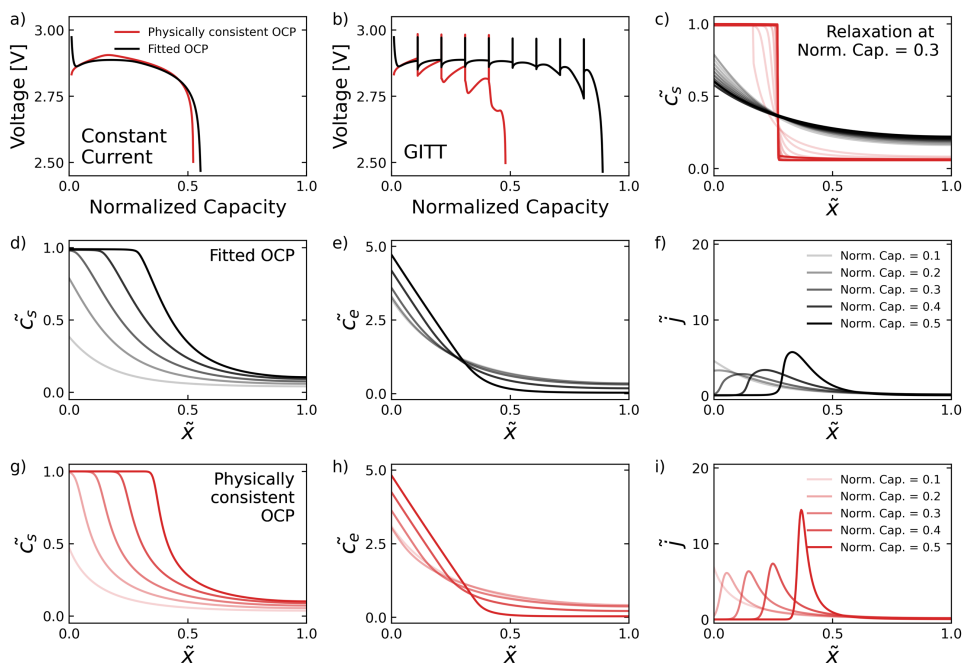


**Figure 3.8.** Comparison between physically-consistent non-monotonic OCP and fitted flat OCP. Voltage responses of the constant current protocol at  $\tau_C = \tau_D = \tau_R$  (a). Voltage responses to the GITT protocol (b). Relaxation of the normalized solid concentration after the third pulse along the normalized electrode thickness  $\tilde{x}$ . The transparent lines correspond to the result after the pulse and subsequent relaxation. The opaque line corresponds to the profile reached at the end of the relaxation process ( $5\tau_D$ ) (c). Kinetic evolution of normalized solid concentration  $\tilde{c}_s$  (d,g), normalized electrolyte concentration  $\tilde{c}_e$  (e,h), and normalized volumetric current density  $\tilde{j}$  (f,i), during the constant current protocol along the normalized electrode thickness  $\tilde{x}$ . The black lines correspond to the case flat OCP case, while the red lines represent the physics-based case with  $\Omega = 4 k_B T$ . Transparency indicates the corresponding normalized capacity.

Finally, we compare the results obtained using the physics-based OCP with those from the conventional fitted flat voltage plateau<sup>38</sup>. For  $\Omega = 4 k_B T$ , the resulting energy barrier is consistent with values typically observed for LFP<sup>17</sup>. Under constant current conditions, the

### 3 | THE INFLUENCE OF OPEN CIRCUIT POTENTIAL ON ELECTRODE DYNAMICS

voltage profiles obtained from both approaches appear comparable (Fig. 3.8a). This apparent similarity is likely the reason why the fitted approach remains widely used.

However, while the constant current response may seem indistinguishable, the underlying electrode kinetics differ significantly. When applying the GITT protocol, a clear discrepancy emerges between the physics-based and fitted models (Fig. 3.8b). The physically consistent model naturally incorporates the thermodynamic drive for phase separation, preventing the electrode from fully relaxing during the  $5 \tau_D$  resting period. As a result, the system enters each subsequent pulse in a heterogeneous state, where the region near the separator becomes fully intercalated, while the area further away remains depleted (Fig. 3.8c). Consequently, during the next pulse, the reaction is sustained primarily by material located further from the current collector, reducing the amount of available active material for continued intercalation. These effects lead to increased overpotential between pulses and limited capacity retention, even after the electrode has undergone a rest period.

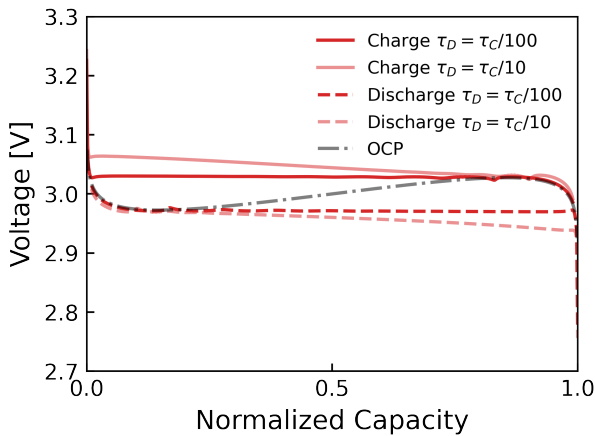


**Figure 3.9. Hysteresis.** Charge and discharge curves at negligible reaction limitation ( $\tau_R = \tau_C/100$ ) at varying  $\tau_D$ . The gray line shows the open circuit potential as function of normalized capacity, in this example the entire cyclable capacity is used. The red curves show the results of slow insertion (bottom dotted lines) and de-insertion (top continuous lines) during a slow (dis)charge ( $\tau_D, \tau_R \ll \tau_C$ ).

In contrast, the flat voltage model predicts complete relaxation of the concentration profile, similar to what is observed in solid solution materials (Fig. 3.8c). Following the resting period, the homogeneous electrode can efficiently sustain the next pulse by utilizing the entire electrode volume, ultimately artificially increasing the delivered capacity. These properties suggest the physically consistent non-monotonic OCP should be regarded as the best solution for simulating

phase-separating materials. The ability to reproduce the features of a GITT protocol makes this method suitable for intermittent scenarios, such as dynamic driving cycles, where current frequently alternates between charge and discharge, and rest periods are prolonged.

Moreover, it can naturally reproduce the voltage hysteresis without needing empirical algorithms (Fig. 3.9) and explain its features. Specifically, the apparent flat OCPs result from the multi-particle ensemble quickly reacting and equilibrating with the total system voltage, in line with theoretical predictions<sup>19</sup>. However, the obtained low-rate voltage profile is not exactly a flat plateau, but it possesses a slight slope. In the case considered by this study, this is originating from the reaction front moving further away from the separator and thus, like in the GITT case, requiring higher overpotentials to react. Similar effects can be seen in case of thin electrodes with a wide particle size distributions, where the system sequentially react with particles of increasing sizes<sup>21</sup>. In both cases the experimental OCPs, even if obtained applying close-to-zero currents, would show an overpotential buildup resulting in monotonically sloping OCPs and would not be suitable for a physically consistent simulation of phase-separating materials.

### 3.9 DISCUSSION AND CONCLUSION

This work demonstrates the critical influence of open-circuit potential (OCP) characteristics on electrode dynamics, particularly in case of thick electrode composed by phase-separating nanoparticles. Compared to an electrode composed of solid solution nanoparticles, characterized by a monotonically decreasing OCP, a phase-separating material, with a non-monotonic OCP, exhibits drastically different electrolyte and solid concentration dynamics. By solely focusing on a transport limited electrode, we have shown how, aside from the differences in intra-particle dynamics<sup>7,10,26,28</sup>, these systems are also more susceptible to transport-induced limitations due to highly localized reactions, which accelerate electrolyte depletion. During insertion, the phase-separating electrode develops distinct inserted and depleted zones, a division that persists even when the current is stopped and the electrode is allowed to rest under open-circuit conditions. This effect manifests as an overpotential buildup during successive pulses in a GITT protocol, leading to a reduction in capacity retention that scales with the miscibility gap. Further studies should focus on the effect this phenomenon on more complex dynamic protocols. Additionally, while improvements in electrolyte diffusion enhance capacity retention and utilization across all materials, improvements in reaction kinetics negatively impact phase-separating materials by further increasing localized reactions.

We also evaluated the non-monotonic OCP approximation to the conventional flat OCP commonly used to simulate phase-separating materials such as LFP. While the two approaches yield similar voltage responses under constant current conditions, the GITT protocol reveals key differences. The flat OCP fails to capture internal phase separation dynamics, allowing for

### 3 | THE INFLUENCE OF OPEN CIRCUIT POTENTIAL ON ELECTRODE DYNAMICS

an unphysical relaxation of the solid concentration. This discrepancy carries significant implications for modeling dynamic cycling behavior: only non-monotonic OCPs accurately preserve path dependencies, charge-discharge hysteresis, and localized reaction evolution.

The results presented in this work are based on an idealized electrode composed of perfectly connected nanoparticles with negligible diffusion limitations. However, real battery electrodes exhibit additional complexities, such as diffusion-limited particles<sup>7,10,12,13,28</sup>, broad particle size distributions<sup>20</sup>, electron transport limitations<sup>32,33,50</sup>, and heterogeneous porosity<sup>41</sup>, hierarchical structures<sup>11,40,51</sup>, contact losses<sup>52</sup>, mechanical effects<sup>53,54</sup>, etc.; all of which can mitigate the degree of reaction localization observed in this study. Moreover, the electrolyte dynamics can be better expressed using concentrated solution theory<sup>35,36,42,43,55</sup> and the reaction rate can be calculated by means of coupled ion-electron transfer theory<sup>56</sup>. The consequences of OCP monotonicity can also be investigated in realistic cell formats, observing how heat generation is affected<sup>57</sup>. Nonetheless, our findings emphasize the importance of implementing physically consistent, non-monotonic OCPs for phase-separating materials. The incorporation of this approach does not require substantial modifications to existing models<sup>36,42,45</sup> and retains computational efficiency comparable to the flat OCP method. Conversely, neglecting this feature may result in inaccurate predictions of dynamic cycling performance, lithium plating, and heterogeneous reaction distributions in large-format cells. Future efforts in electrode modeling and engineering for phase-separating materials should compare the results of physically consistent and simplified approaches before employing reduced-order models. For example, if the material consists of nanoparticles with negligible diffusion limitations and a fast simulation is required, a homogeneous one-dimensional porous electrode model may be more suitable than a single-particle model<sup>42,55</sup>. This framework is, therefore, essential for advancing the understanding of both existing and novel materials, providing critical insights necessary for the design, optimization, and modeling of phase-separating materials in next-generation energy storage systems.

## REFERENCES

1. Reniers, J. M.; Mulder, G.; Howey, D. A. Unlocking Extra Value from Grid Batteries Using Advanced Models. *J. Power Sources* 2021, 487, 229355. <https://doi.org/10.1016/j.jpowsour.2020.229355>.
2. Kench, S.; Squires, I.; Dahari, A.; Brosa Planella, F.; Roberts, S. A.; Cooper, S. J. Li-Ion Battery Design through Microstructural Optimization Using Generative AI. *Matter* 2024, S2590238524004466. <https://doi.org/10.1016/j.matt.2024.08.014>.
3. Park, J.; Zhao, H.; Kang, S. D.; Lim, K.; Chen, C.-C.; Yu, Y.-S.; Braatz, R. D.; Shapiro, D. A.; Hong, J.; Toney, M. F.; Bazant, M. Z.; Chueh, W. C. Fictitious Phase Separation in Li Layered Oxides Driven by Electro-Autocatalysis. *Nat. Mater.* 2021, 20 (7), 991–999. <https://doi.org/10.1038/s41563-021-00936-1>.
4. Malik, R.; Abdellahi, A.; Ceder, G. A Critical Review of the Li Insertion Mechanisms in LiFePO<sub>4</sub> Electrodes. *J. Electrochem. Soc.* 2013, 160 (5), A3179–A3197. <https://doi.org/10.1149/2.029305jes>.
5. Cogswell, D. A.; Bazant, M. Z. Coherency Strain and the Kinetics of Phase Separation in LiFePO<sub>4</sub> Nanoparticles. *ACS Nano* 2012, 6 (3), 2215–2225. <https://doi.org/10.1021/nn204177u>.
6. Cogswell, D. A.; Bazant, M. Z. Size-Dependent Phase Morphologies in LiFePO<sub>4</sub> Battery Particles. *Electrochem. Commun.* 2018, 95, 33–37. <https://doi.org/10.1016/j.elecom.2018.08.015>.
7. Ombrini, P.; Wang, Q.; Vasileiadis, A.; Wu, F.; Gao, Z.; Hu, X.; Van Hulzen, M.; Li, B.; Zhao, C.; Wagemaker, M. Kinetically Induced Memory Effect in Li-Ion Batteries. *EES Batter.* 2025, 10.1039/D5EB00014A. <https://doi.org/10.1039/D5EB00014A>.
8. Ombrini, P.; Bazant, M. Z.; Wagemaker, M.; Vasileiadis, A. Thermodynamics of Multi-Sublattice Battery Active Materials: From an Extended Regular Solution Theory to a Phase-Field Model of LiMnyFe<sub>1-y</sub>PO<sub>4</sub>. *Npj Comput. Mater.* 2023, 9 (1), 148. <https://doi.org/10.1038/s41524-023-01109-1>.
9. Timrov, I.; Aquilante, F.; Cococcioni, M.; Marzari, N. Accurate Electronic Properties and Intercalation Voltages of Olivine-Type Li-Ion Cathode Materials from Extended Hubbard Functionals. *PRX Energy* 2022, 1 (3), 033003. <https://doi.org/10.1103/PRXEnergy.1.033003>.
10. Vasileiadis, A.; de Klerk, N. J. J.; Smith, R. B.; Ganapathy, S.; Harks, P. P. R. M. L.; Bazant, M. Z.; Wagemaker, M. Toward Optimal Performance and In-Depth Understanding of Spinel Li<sub>4</sub>Ti<sub>5</sub>O<sub>12</sub> Electrodes through Phase Field Modeling. *Adv. Funct. Mater.* 2018, 28 (16), 1705992. <https://doi.org/10.1002/adfm.201705992>.
11. Lian, H.; Bazant, M. Z. Modeling Lithium Plating Onset on Porous Graphite Electrodes Under Fast Charging with Hierarchical Multiphase Porous Electrode Theory. *J. Electrochem. Soc.* 2024, 171 (1), 010526. <https://doi.org/10.1149/1945-7111/ad1e3d>.
12. Smith, R. B.; Khoo, E.; Bazant, M. Z. Intercalation Kinetics in Multiphase-Layered Materials. *J. Phys. Chem. C* 2017, 121 (23), 12505–12523. <https://doi.org/10.1021/acs.jpcc.7b00185>.
13. Lu, X.; Lagnoni, M.; Bertei, A.; Das, S.; Owen, R. E.; Li, Q.; O'Regan, K.; Wade, A.; Finegan, D. P.; Kendrick, E.; Bazant, M. Z.; Brett, D. J. L.; Shearing, P. R. Multiscale Dynamics of Charging and Plating in Graphite Electrodes Coupling Operando Microscopy and Phase-Field Modelling. *Nat. Commun.* 2023, 14 (1), 5127. <https://doi.org/10.1038/s41467-023-40574-6>.
14. Park, S.; Wang, Z.; Deng, Z.; Moog, I.; Canepa, P.; Fauth, F.; Carlier, D.; Croguennec, L.; Masquelier, C.; Chotard, J.-N. Crystal Structure of Na<sub>2</sub>V<sub>2</sub>(PO<sub>4</sub>)<sub>3</sub>, an Intriguing Phase Spotted in the Na<sub>3</sub>V<sub>2</sub>(PO<sub>4</sub>)<sub>3</sub>–Na<sub>1</sub>V<sub>2</sub>(PO<sub>4</sub>)<sub>3</sub> System. *Chem. Mater.* 2022, 34 (1), 451–462. <https://doi.org/10.1021/acs.chemmater.1c04033>.
15. Xiao, Y.; Xiao, J.; Zhao, H.; Li, J.; Zhang, G.; Zhang, D.; Guo, X.; Gao, H.; Wang, Y.; Chen, J.; Wang, G.; Liu, H. Prussian Blue Analogues for Sodium-Ion Battery Cathodes: A Review of

- Mechanistic Insights, Current Challenges, and Future Pathways. *Small* 2024, 2401957. <https://doi.org/10.1002/smll.202401957>.
16. Zhao, H.; Deng, H. D.; Cohen, A. E.; Lim, J.; Li, Y.; Fraggedakis, D.; Jiang, B.; Storey, B. D.; Chueh, W. C.; Braatz, R. D.; Bazant, M. Z. Learning Heterogeneous Reaction Kinetics from X-Ray Videos Pixel by Pixel. *Nature* 2023, 621 (7978), 289–294. <https://doi.org/10.1038/s41586-023-06393-x>.
  17. Bai, P.; Cogswell, D. A.; Bazant, M. Z. Suppression of Phase Separation in LiFePO<sub>4</sub> Nanoparticles During Battery Discharge. *Nano Lett.* 2011, 11 (11), 4890–4896. <https://doi.org/10.1021/nl202764f>.
  18. Katrašnik, T.; Moškon, J.; Zelič, K.; Mele, I.; Ruiz-Zepeda, F.; Gabersčček, M. Entering Voltage Hysteresis in Phase-Separating Materials: Revealing the Electrochemical Signature of the Intraparticle Phase-Separated State. *Adv. Mater.* 2023, 35 (31), 2210937. <https://doi.org/10.1002/adma.202210937>.
  19. Dreyer, W.; Jamnik, J.; Guhlke, C.; Huth, R.; Moškon, J.; Gabersčček, M. The Thermodynamic Origin of Hysteresis in Insertion Batteries. *Nat. Mater.* 2010, 9 (5), 448–453. <https://doi.org/10.1038/nmat2730>.
  20. Li, Y.; El Gabaly, F.; Ferguson, T. R.; Smith, R. B.; Bartelt, N. C.; Sugar, J. D.; Fenton, K. R.; Cogswell, D. A.; Kilcoyne, A. L. D.; Tylliszczak, T.; Bazant, M. Z.; Chueh, W. C. Current-Induced Transition from Particle-by-Particle to Concurrent Intercalation in Phase-Separating Battery Electrodes. *Nat. Mater.* 2014, 13 (12), 1149–1156. <https://doi.org/10.1038/nmat4084>.
  21. Ferguson, T. R.; Bazant, M. Z. Phase Transformation Dynamics in Porous Battery Electrodes. *Electrochimica Acta* 2014, 146, 89–97. <https://doi.org/10.1016/j.electacta.2014.08.083>.
  22. Fraggedakis, D.; Nadkarni, N.; Gao, T.; Zhou, T.; Zhang, Y.; Han, Y.; Stephens, R. M.; Shao-Horn, Y.; Bazant, M. Z. A Scaling Law to Determine Phase Morphologies during Ion Intercalation. *Energy Environ. Sci.* 2020, 13 (7), 2142–2152. <https://doi.org/10.1039/D0EE00653J>.
  23. Deng, H. D.; Zhao, H.; Jin, N.; Hughes, L.; Savitzky, B. H.; Ophus, C.; Fraggedakis, D.; Borbély, A.; Yu, Y.-S.; Lomeli, E. G.; Yan, R.; Liu, J.; Shapiro, D. A.; Cai, W.; Bazant, M. Z.; Minor, A. M.; Chueh, W. C. Correlative Image Learning of Chemo-Mechanics in Phase-Transforming Solids. *Nat. Mater.* 2022, 21 (5), 547–554. <https://doi.org/10.1038/s41563-021-01191-0>.
  24. Daubner, S.; Kubendran Amos, P. G.; Schoof, E.; Santoki, J.; Schneider, D.; Nestler, B. Multiphase-Field Modeling of Spinodal Decomposition during Intercalation in an Allen-Cahn Framework. *Phys. Rev. Mater.* 2021, 5 (3), 035406. <https://doi.org/10.1103/PhysRevMaterials.5.035406>.
  25. Rykner, M.; Chandesaris, M. Free Energy Model for Lithium Intercalation in Graphite: Focusing on the Coupling with Graphene Stacking Sequence. *J. Phys. Chem. C* 2022, 126 (12), 5457–5472. <https://doi.org/10.1021/acs.jpcc.1c10800>.
  26. Zeng, Y.; Bazant, M. Z. Cahn-Hilliard Reaction Model for Isotropic Li-Ion Battery Particles. *MRS Proc.* 2013, 1542, mrss13-1542-g02-01. <https://doi.org/10.1557/opl.2013.740>.
  27. Gao, T.; Han, Y.; Fraggedakis, D.; Das, S.; Zhou, T.; Yeh, C.-N.; Xu, S.; Chueh, W. C.; Li, J.; Bazant, M. Z. Interplay of Lithium Intercalation and Plating on a Single Graphite Particle. *Joule* 2021, 5 (2), 393–414. <https://doi.org/10.1016/j.joule.2020.12.020>.
  28. Lagnoni, M.; Bertei, A. Electrochemical Diffusion Signatures of Solid-Solution and Phase-Separating Active Materials in Li-Ion Batteries. *J. Phys. Energy* 2025, 7 (3), 035024. <https://doi.org/10.1088/2515-7655/ade5ca>.
  29. Zhuang, D.; Bazant, M. Z. Scaling Analysis of Mosaic Phase Separation in Li-Ion Batteries. *Phys. Rev. E* 2024, 110 (6), 064142. <https://doi.org/10.1103/PhysRevE.110.064142>.

30. Li, Z.; Wang, F.; Gao, Y.; Wang, H.; Wang, Z.; Yang, Y.; Ai, Q.; Ge, M.; Liu, Y.; Meyer, M.; Terlier, T.; Xiao, X.; Lee, W.; Wang, Y.; Lou, J.; Kiss, A.; Agarwal, H.; Stephens, R.; Tang, M. Probing the Effect of Electrode Thermodynamics on Reaction Heterogeneity in Thick Battery Electrodes. *Adv. Mater.* 2025, 2502299. <https://doi.org/10.1002/adma.202502299>.
31. Zhang, Y.; Yang, Z.; Tian, C. Probing and Quantifying Cathode Charge Heterogeneity in Li Ion Batteries. *J. Mater. Chem. A* 2019, 7 (41), 23628–23661. <https://doi.org/10.1039/C9TA06977A>.
32. Li, Y.; Meyer, S.; Lim, J.; Lee, S. C.; Gent, W. E.; Marchesini, S.; Krishnan, H.; Tyliczszak, T.; Shapiro, D.; Kilcoyne, A. L. D.; Chueh, W. C. Effects of Particle Size, Electronic Connectivity, and Incoherent Nanoscale Domains on the Sequence of Lithiation in LiFePO<sub>4</sub> Porous Electrodes. *Adv. Mater.* 2015, 27 (42), 6591–6597. <https://doi.org/10.1002/adma.201502276>.
33. Iarchuk, A. R.; Nikitina, V. A.; Karpushkin, E. A.; Sergeyev, V. G.; Antipov, E. V.; Stevenson, K. J.; Abakumov, A. M. Influence of Carbon Coating on Intercalation Kinetics and Transport Properties of LiFePO<sub>4</sub>. *ChemElectroChem* 2019, 6 (19), 5090–5100. <https://doi.org/10.1002/celec.201901219>.
34. Tredenick, E. C.; Boyce, A. M.; Wheeler, S.; Li, J.; Sun, Y.; Drummond, R.; Duncan, S. R.; Grant, P. S.; Shearing, P. R. Bridging the Gap between Microstructurally Resolved Computed Tomography-Based and Homogenised Doyle-Fuller-Newman Models for Lithium-Ion Batteries. *J. Electrochem. Soc.* 2025, 172 (3), 030503. <https://doi.org/10.1149/1945-7111/adb684>.
35. Smith, R. B.; Bazant, M. Z. Multiphase Porous Electrode Theory. *J. Electrochem. Soc.* 2017, 164 (11), E3291–E3310. <https://doi.org/10.1149/2.0171711jes>.
36. Ferguson, T. R.; Bazant, M. Z. Nonequilibrium Thermodynamics of Porous Electrodes. *J. Electrochem. Soc.* 2012, 159 (12), A1967–A1985. <https://doi.org/10.1149/2.048212jes>.
37. Zelič, K.; Katrašnik, T. Thermodynamically Consistent Derivation of Chemical Potential of a Battery Solid Particle from the Regular Solution Theory Applied to LiFePO<sub>4</sub>. *Sci. Rep.* 2019, 9 (1), 2123. <https://doi.org/10.1038/s41598-019-38635-2>.
38. Prada, E.; Di Domenico, D.; Creff, Y.; Bernard, J.; Sauvant-Moynot, V.; Huet, F. A Simplified Electrochemical and Thermal Aging Model of LiFePO<sub>4</sub>-Graphite Li-Ion Batteries: Power and Capacity Fade Simulations. *J. Electrochem. Soc.* 2013, 160 (4), A616. <https://doi.org/10.1149/2.053304jes>.
39. Wycisk, D.; Oldenburger, M.; Stoye, M. G.; Mrkonjic, T.; Latz, A. Modified Plett-Model for Modeling Voltage Hysteresis in Lithium-Ion Cells. *J. Energy Storage* 2022, 52, 105016. <https://doi.org/10.1016/j.est.2022.105016>.
40. Birkholz, O.; Kamlah, M. Electrochemical Modeling of Hierarchically Structured Lithium-Ion Battery Electrodes. *Energy Technol.* 2021, 9 (6), 2000910. <https://doi.org/10.1002/ente.202000910>.
41. Karanth, P.; Weijers, M.; Ombrini, P.; Ripepi, D.; Ooms, F.; Mulder, F. M. A Phase Inversion Strategy for Low-Tortuosity and Ultrahigh-Mass-Loading Nickel-Rich Layered Oxide Electrodes. *Cell Rep. Phys. Sci.* 2024, 101972. <https://doi.org/10.1016/j.xcrp.2024.101972>.
42. Brosa Planella, F.; Ai, W.; Boyce, A. M.; Ghosh, A.; Korotkin, I.; Sahu, S.; Sulzer, V.; Timms, R.; Tranter, T. G.; Zyskin, M.; Cooper, S. J.; Edge, J. S.; Foster, J. M.; Marinescu, M.; Wu, B.; Richardson, G. A Continuum of Physics-Based Lithium-Ion Battery Models Reviewed. *Prog. Energy* 2022, 4 (4), 042003. <https://doi.org/10.1088/2516-1083/ac7d31>.
43. Lagnoni, M.; Nicoletta, C.; Bertei, A. Comparison of Electrolyte Transport Modelling in Lithium-Ion Batteries: Concentrated Solution Theory Vs Generalized Nernst-Planck Model. *J. Electrochem. Soc.* 2022, 169 (2), 020570. <https://doi.org/10.1149/1945-7111/ac51f4>.
44. Bizeray, A. M.; Howey, D. A.; Monroe, C. W. Resolving a Discrepancy in Diffusion Potentials, with a Case Study for Li-Ion Batteries. *J. Electrochem. Soc.* 2016, 163 (8), E223–E229. <https://doi.org/10.1149/2.0451608jes>.

### 3 | THE INFLUENCE OF OPEN CIRCUIT POTENTIAL ON ELECTRODE DYNAMICS

45. Sulzer, V.; Marquis, S. G.; Timms, R.; Robinson, M.; Chapman, S. J. Python Battery Mathematical Modelling (PyBaMM). *J. Open Res. Softw.* 2021, 9 (1), 14. <https://doi.org/10.5334/jors.309>.
46. Andersson, J. A. E.; Gillis, J.; Horn, G.; Rawlings, J. B.; Diehl, M. CasADi: A Software Framework for Nonlinear Optimization and Optimal Control. *Math. Program. Comput.* 2019, 11 (1), 1–36. <https://doi.org/10.1007/s12532-018-0139-4>.
47. Delft University of Technology; Haverkort, W. Electrolysers, Fuel Cells and Batteries; TU Delft OPEN Publishing, 2024. <https://doi.org/10.59490/tb.93>.
48. Srinivasan, V.; Newman, J. Existence of Path-Dependence in the LiFePO<sub>4</sub> Electrode.
49. Deng, H. D.; Jin, N.; Attia, P. M.; Lim, K.; Kang, S. D.; Kapate, N.; Zhao, H.; Li, Y.; Bazant, M. Z.; Chueh, W. C. Beyond Constant Current: Origin of Pulse-Induced Activation in Phase-Transforming Battery Electrodes. *ACS Nano* 2024, 18 (3), 2210–2218. <https://doi.org/10.1021/acsnano.3c09742>.
50. Ombrini, P.; Pathak, S.; Ntagkras, D.; Pal, S. K.; Karanth, P.; Mulder, F. M.; Wagemaker, M.; Bazant, M. Z.; Vasileiadis, A. Modeling Single-Crystal Electrodes as a Network of Primary Particles.
51. Daubner, S.; Weichel, M.; Reder, M.; Schneider, D.; Huang, Q.; Cohen, A. E.; Bazant, M. Z.; Nestler, B. Simulation of Intercalation and Phase Transitions in Nano-Porous, Polycrystalline Agglomerates. *Npj Comput. Mater.* 2025, 11 (1), 211. <https://doi.org/10.1038/s41524-025-01707-1>.
52. Schwietert, T. K.; Ombrini, P.; Ootes, L. S.; Oostrum, L.; Azizi, V.; Cogswell, D.; Zhu, J.; Bazant, M. Z.; Wagemaker, M.; Vasileiadis, A. Phase-Field Computational Framework for Addressing Challenges in Solid-State Batteries. *PRX Energy* 2023, 2 (3), 033014. <https://doi.org/10.1103/PRXEnergy.2.033014>.
53. Ipers, G.; Jiao, J.; Pathak, S.; Fang, R.; Berliner, M. D.; Li, W.; Li, W.; Braatz, R. D.; Bazant, M. Z.; Zhu, J. Rapid Simulation of Electro-Chemo-Mechanical Deformation of Li-Ion Batteries Based On Porous Electrode Theory. *J. Electrochem. Soc.* 2024, 171 (5), 050557. <https://doi.org/10.1149/1945-7111/ad4f1e>.
54. Ai, W.; Kraft, L.; Sturm, J.; Jossen, A.; Wu, B. Electrochemical Thermal-Mechanical Modelling of Stress Inhomogeneity in Lithium-Ion Pouch Cells. *J. Electrochem. Soc.* 2019, 167 (1), 013512. <https://doi.org/10.1149/2.0122001JES>.
55. Marquis, S. G.; Sulzer, V.; Timms, R.; Please, C. P.; Chapman, S. J. An Asymptotic Derivation of a Single Particle Model with Electrolyte. *J. Electrochem. Soc.* 2019, 166 (15), A3693–A3706. <https://doi.org/10.1149/2.0341915jes>.
56. Bazant, M. Z. Unified Quantum Theory of Electrochemical Kinetics by Coupled Ion-Electron Transfer. *Faraday Discuss.* 2023, 10.1039.D3FD00108C. <https://doi.org/10.1039/D3FD00108C>.
57. O'Regan, K.; Brosa Planella, F.; Widanage, W. D.; Kendrick, E. Thermal-Electrochemical Parameters of a High Energy Lithium-Ion Cylindrical Battery. *Electrochimica Acta* 2022, 425, 140700. <https://doi.org/10.1016/j.electacta.2022.140700>.





# 4 THERMODYNAMICS OF MULTI-SUBLATTICE ACTIVE MATERIALS

This chapter has been published as: Ombrini, P., Bazant, M. Z., Wagemaker, M. & Vasileiadis, A. Thermodynamics of multi-sublattice battery active materials: from an extended regular solution theory to a phase-field model of  $\text{LiMn}_y\text{Fe}_{1-y}\text{PO}_4$ . *npj Comput Mater* **9**, 148 (2023).

## ABSTRACT

Phase separation during the lithiation of redox-active materials is a critical factor affecting battery performance, including energy density, charging rates, and cycle life. Accurate physical descriptions of these materials are necessary for understanding underlying lithiation mechanisms, performance limitations, and optimizing energy storage devices. This work presents an extended regular solution model that captures mutual interactions between sublattices of multi-sublattice battery materials, typically synthesized by metal substitution. We apply the model to phospho-olivine materials and demonstrate its quantitative accuracy in predicting the composition-dependent redox shift of the plateaus of  $\text{LiMn}_y\text{Fe}_{1-y}\text{PO}_4$  (LFMP),  $\text{LiCo}_y\text{Fe}_{1-y}\text{PO}_4$  (LFCP),  $\text{LiCo}_x\text{Mn}_y\text{Fe}_{1-x-y}\text{PO}_4$  (LFMCP), as well as their phase separation behavior. Furthermore, we develop a phase-field model of LFMP that consistently matches experimental data and identifies  $\text{LiMn}_{0.4}\text{Fe}_{0.6}\text{PO}_4$  as a superior composition that favors a solid solution phase transition, making it ideal for high-power applications.

## 4.1 INTRODUCTION

Li-ion batteries are fundamental to the upcoming transition towards sustainable energy production, electric mobility, and energy storage<sup>1</sup>. Although the early storage requirements were satisfied by active materials such as graphite and  $\text{LiCoO}_2$ <sup>2,3</sup>, higher energy densities, sustainability, cheaper elements, and improved safety require developing more sophisticated battery active materials. Li-ion battery electrode materials also have other emerging applications<sup>4</sup>, such as electrochromic displays<sup>5</sup>, ion-tunable electrocatalysis, resistive switching memory<sup>6-9</sup>, water desalination and purification<sup>10</sup>, and lithium extraction from brines<sup>11,12</sup>. In all of these applications, the design space for electrode materials with various desired properties has hardly been explored.

Blending or modifying existing electrode materials is a promising method to improve properties, which is gaining attention, albeit with limited theoretical guidance. While the anode materials are moving towards silicon<sup>13</sup>, silicon/graphite composites, or Li-metal<sup>14</sup>, cathode development is running behind, with most advancements focusing on substituting cobalt in layered oxide materials with Ni, Mn, or Al developing  $\text{LiNi}_x\text{Mn}_y\text{Co}_{1-x-y}\text{O}_2$  (NMC) and  $\text{LiNi}_x\text{Al}_y\text{Co}_{1-x-y}\text{O}_2$  (NCA) cathodes<sup>15,16</sup>. These approaches show the advantages of modifying the composition of an existing cathode with well-established lithiation mechanisms to reduce its cost and environmental impact and to improve energy density and cycle life. Applying the same approach to  $\text{LiFePO}_4$  (LFP), a phospho-olivine material introduced by Goodenough and co-workers in 1997<sup>17</sup>, which has advantages over the layered oxides in lower cost and toxicity with greater stability and recyclability<sup>18</sup>, various partial or complete substitutions of Fe with Mn, Co, and Ni have been attempted. Higher redox potential and similar specific capacities can be obtained, improving the overall energy density<sup>19-21</sup> while sustaining decent diffusivity and cycle life. Currently,  $\text{LiMn}_y\text{Fe}_{1-y}\text{PO}_4$  (LFMP)<sup>21-23</sup> exhibits the most promising characteristics and is rapidly being incorporated into commercial batteries. Therefore, it is crucial to gain a deep understanding of the basic physics of LFMP through modeling. Other materials in the same family, such as  $\text{LiCo}_y\text{Fe}_{1-y}\text{PO}_4$  (LFCP)<sup>24-29</sup> and  $\text{LiCo}_x\text{Mn}_y\text{Fe}_{1-x-y}\text{PO}_4$  (LFMCP)<sup>19,20,30</sup>, also display intriguing properties and merit further investigation as well.

First-principles calculations struggle to provide a complete picture of the underlying mechanisms, in part due to the heavy impact of the practical choice of the pseudopotentials on the predicted redox potential<sup>31,32</sup> and partly because the use of Monte Carlo simulations aided by cluster expansion<sup>33</sup> prevent the understanding of the behavior of the material in a realistic battery system at finite temperature.

Mesoscale modeling, based on mean-field theories of electrochemical nonequilibrium thermodynamics<sup>34</sup>, is instead a suitable tool to investigate the effects of different chemistries,

morphologies, and cycling strategies in Li-ion batteries due to its low computational costs and flexibility. Different models have been developed depending on the goal and the required precision<sup>35–39</sup>. Progress has been made in modeling phase-separating active materials regarding single particle behavior<sup>40–46</sup> and collective dynamics in a battery environment<sup>35,47–54</sup>.

In order to develop an accurate thermodynamic description, it was essential to model the behavior of individual particles using phase-field methods, which generalize the Cahn-Hilliard formalism<sup>55–61</sup> for driven electrochemical systems<sup>34,48,52</sup>. This approach has led to realistic models of diffusion and reaction models for materials such as graphite<sup>62,63</sup>, anatase TiO<sub>2</sub><sup>45</sup>, LTO<sup>46</sup>, LCO<sup>8</sup> and LFP<sup>64–68</sup>, showing excellent agreement with experiments, guiding researchers to properly understand the reasons for various peculiar behaviors occurring in phase-separating materials and helping companies in the optimization of these kinds of batteries. Recently, phase-field modeling of LFP has succeeded in reproducing a vast dataset of *operando* x-ray images of nanoparticles cycling at different rates pixel by pixel<sup>69</sup>, while learning the two-phase free-energy landscape, the reaction kinetics of coupled ion-electron transfer<sup>70</sup>, and the heterogeneity of surface reactivity, correlated with variations in carbon coating thickness. An open-source code, MPET (Multiphase Porous Electrode Theory)<sup>48</sup> has been developed to facilitate the implementation of these models for specific cells and control algorithms<sup>71</sup>. With its modular design, users can quickly incorporate phase-field models of the studied material within a porous electrode theory framework, providing insights into both the individual particle and the collective system responses.

In this study, we applied a thermodynamic-based approach to investigate the impact of composition on the performance of phospho-olivine materials. We extended the regular-solution theory<sup>61,72</sup>, originally applied to single-lattice LFP<sup>34,73</sup>, to consider the presence of multiple sublattices for the intercalated species, which have distinct properties and redox potentials. Our theory reveals how interactions between sublattices explain the composition dependence on redox potential and phase transition behavior. By applying the theory to a phase-field simulation of an LFMP half-cell, we gain fundamental insights into the optimal transition metal ratio, which demonstrate the possibility of using mean-field phase-field models to design active materials.

## 4.2 THEORY

The mathematical modeling of a closed thermodynamic system starts by defining the Helmholtz free energy  $F$ , given by  $F = E - TS$ <sup>61,72</sup>. To determine the properties of a solid solution, we need the temperature  $T$ , a function for the entropy  $S$ , linked to all possible configurations the system can have, and the internal energy  $E$ , representing interactions between the particles of

the system. The regular solution model, which is equivalent to a mean-field lattice-gas model with pair interactions, offers an elegant and straightforward way to describe solid solutions, and it was implemented successfully in various battery active materials<sup>34,40,44–46,48,73,74</sup>. However, its application is mainly limited to materials where the intercalated species encounter one lattice type, such as LFP or LTO<sup>46</sup>, or two non-interacting sublattices, such as TiO<sub>2</sub><sup>45</sup>. Phase-field models of staging phase transitions in graphite have been developed with multiple, periodic interacting crystal layers<sup>40</sup>, but the parameters must be fitted to experimental data to describe the complex phase diagram of the material<sup>62,63,75</sup>.

To summarize this mean-field theory, we can start considering an active material containing  $N$  lattice sites that can host intercalating species (e.g., lithium) whose relative concentration is defined as  $\tilde{c} = N_{occupied}/N$ . The entropy  $S = -k_B N [\tilde{c} \ln(\tilde{c}) + (1 - \tilde{c}) \ln(1 - \tilde{c})]$ , where  $k_B$  is the Boltzmann constant, is derived from the possible configurations of the intercalated system, and the internal energy  $E = Nz \left[ \frac{1}{2} \epsilon_{oo} \tilde{c} + \frac{1}{2} \epsilon_{vv} (1 - \tilde{c}) + \frac{\Omega}{z} \tilde{c} (1 - \tilde{c}) \right]$  is obtained considering only pair interaction energies,  $\epsilon_{oo}$ ,  $\epsilon_{vv}$ ,  $\epsilon_{vo}$  between two occupied sites, two vacancies, or a vacancy and an occupied site, respectively<sup>61</sup>. These are then multiplied by the number of atoms and the number of closest neighbors  $z$ . To apply the model is therefore not necessary to know all the interaction energies, but it is sufficient to know  $\Omega = z \left( \epsilon_{vo} - \frac{1}{2} \epsilon_{oo} - \frac{1}{2} \epsilon_{vv} \right)$ , which represents the mixing enthalpy, determining whether the material will favor phase separation during (de)intercalation. In the context of rechargeable battery materials, the absolute value of the energy carries no physical meaning, while the difference between the completely intercalated state and the empty state provides the standard chemical potential  $\mu^\ominus = \frac{E(\tilde{c}=1) - E(\tilde{c}=0)}{N}$ . The standard chemical potential can so be associated with the interaction energies,  $\mu^\ominus = z \left( \frac{\epsilon_{oo}}{2} - \frac{\epsilon_{vv}}{2} \right)$ , and the total energy can be rewritten as  $E = N[\Omega \tilde{c} (1 - \tilde{c}) + \mu^\ominus \tilde{c}]$ . A connection is so established between the approximation governing the regular solution theory and the redox potential as intrinsic physical property of the material. The regular solution theory finally provides the occupation-dependent chemical potential of the intercalated materials as  $\mu(\tilde{c}) = \frac{1}{N} \frac{\partial F}{\partial \tilde{c}} = k_B T \ln \frac{\tilde{c}}{1 - \tilde{c}} + \Omega(1 - 2\tilde{c}) + \mu^\ominus$ .

One way to obtain the parameters introduced above is by performing first-principles calculations, attaining the energies of the structure at different fractions of intercalation, and subsequently determining the mixing energy and the redox potential<sup>76</sup>. Moreover, it is possible to measure the chemical potential experimentally during close-to-equilibrium (de)intercalation; fitting the voltage hysteresis gap will then capture the difference between the local minima and maxima of the  $\Omega$  dependent chemical potential<sup>44,77</sup>.

A practical example of the application of this model is  $\text{LiFePO}_4$ , in which for every intercalated Li-ion, an adjacent Fe is reduced from  $\text{Fe}^{3+}$  to  $\text{Fe}^{2+}$  so that an occupied site consists of an ensemble of  $\text{Li}^+$ ,  $\text{Fe}^{2+}$ , and  $\text{PO}_4$ , forming what is approximated as a neutral specie, while a vacancy consists of  $\text{Fe}^{3+}$ ,  $\text{PO}_4$  and an empty lattice position. The standard chemical potential is then usually redefined with respect to the redox potential of the redox reaction Li metal -  $\text{Li}^+$ .

### 4.3 MULTI-SUBLATTICE MODEL

Aiming to describe a general multi-sublattice material in which the lattice sites are mixed uniformly, the usual regular solution model must be modified to account for the various interactions that the intercalated species can have in the material.

We consider a lattice composed of  $N$  intercalating sites, divided into  $n$  sublattices, of which  $N_i = y_i N$  belong to the sublattice  $i$ . Assuming that the lattice sites of different types are fixed in space after the synthesis of the entropy for the sublattice  $i$ , having an occupation  $\tilde{c}_i = N_{\text{occupied}_i}/N_i$ , is calculated using the solid solution approach, resulting in

$$S = - \sum_{i=1}^n k_B N_i [\tilde{c}_i \ln(\tilde{c}_i) + (1 - \tilde{c}_i) \ln(1 - \tilde{c}_i)] \quad (4.1)$$

The internal energy of the general system with  $n$  different sublattices  $E$  is computed using a mean-field pair interaction approach so that the effect of the sublattices interactions arises naturally.

Using the same logic behind the regular solution model, we can start considering a scheme represented in Fig. 4.1, in which, for clarity, only two types of sites are considered. It shows how an intercalated particle in the occupied lattice site  $i$  will interact with other occupied sites of type  $i$ , the vacancies of the sites  $i$ , but also with the vacancies and the occupied sites of type  $j$ , leading to 9 different interaction energies for a 2-sublattice material.

The evaluation of the interaction energies between different sites  $\epsilon_{ij}$ , in such complex systems, is challenging and would involve atomistic quantum mechanical computations. As a first approximation, we calculate them as an average between the same-site interactions  $\epsilon_{ij} = (\epsilon_{ii} + \epsilon_{jj})/2$ .

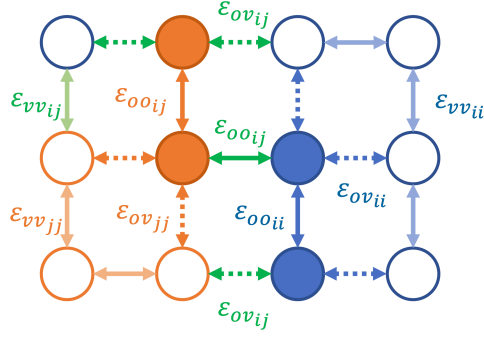


**Figure 4.1.** Schematic representation of the interaction of a 2-sublattice material according to the extended regular solution model. The empty and full circles indicate vacancies and occupied sites, respectively. The species in the sublattice "i" (blue) interact with themselves through interaction energies  $\varepsilon_{ooii}$ ,  $\varepsilon_{ovij}$ ,  $\varepsilon_{vvii}$  (full dark blue arrow, dotted blue arrow, full light blue arrow). Same for the species in the sublattice "j" (orange)  $\varepsilon_{oojj}$ ,  $\varepsilon_{ovjj}$ ,  $\varepsilon_{vvjj}$  (full dark orange arrow, dotted orange arrow, full light orange arrow). The intra-sublattice interactions are represented in green:  $\varepsilon_{ooij}$ ,  $\varepsilon_{ovij}$ ,  $\varepsilon_{vvij}$  (full dark green arrow, dotted green arrow, full light green arrow). The squared crystal structure and number of interactions of each type are for visual intent, not representative of the physics of the system.

Assuming that the site-site interactions  $\varepsilon_{ij}$  are not influenced by the ratio between the compounds  $y_i$ , the total internal energy will so be obtained considering that an atom or a vacancy in the sublattice  $i$ , having  $z$  close neighbors, will interact with  $Z_i = y_i z$  neighbors with an energy  $\varepsilon_{ooii}$ ,  $\varepsilon_{vvii}$  or  $\varepsilon_{voui}$  depending on their occupation state, but also with  $Z_j = y_j z$  neighbors with an energy  $\varepsilon_{ooij}$ ,  $\varepsilon_{vvij}$  or  $\varepsilon_{vovj}$ . Applying this concept and considering all the possible combinations, the internal energy is

$$E = \sum_{i=1}^n \sum_{j=1}^n \frac{N_i Z_j}{2} \left[ \varepsilon_{ooij} \left( \frac{\tilde{c}_i + \tilde{c}_j}{2} \right) + \varepsilon_{vvij} \left( 1 - \frac{\tilde{c}_i + \tilde{c}_j}{2} \right) + \frac{\Omega_{ij}}{z} (\tilde{c}_i + \tilde{c}_j - 2\tilde{c}_i \tilde{c}_j) \right] \quad (4.2)$$

Where  $\Omega_{ij}$  can be calculated as

$$\Omega_{ij} = \frac{(\Omega_{ii} + \Omega_{jj})}{2} \quad (4.3)$$

and it will coincide with  $\Omega_{ii} = z \left( \varepsilon_{voui} - \frac{1}{2} \varepsilon_{ooii} - \frac{1}{2} \varepsilon_{vvii} \right)$ , the value for the single lattice structure where only one kind of interaction is present. A complete derivation of Eq. 4.2 is presented in the supplementary information.

Eq. 4.2 links the properties of the original materials, which are summarized in  $\Omega_{ii}, \Omega_{jj}, \dots, \Omega_{nn}$ , to the properties of the mixed compound. We can thus conclude that this one equation describes the system in all its possible compositions, becoming a powerful tool for alloy engineering.

Distinguishing now between the absolute energy dependence on concentration (first two terms in Eq. 4.2) and the enthalpy of mixing (last term in Eq. 4.2), the free energy of the system can be rewritten as

$$F = N \left\{ \sum_{i=1}^n \sum_{j=1}^n y_i y_j \Omega_{ij} \left( \frac{\tilde{c}_i + \tilde{c}_j}{2} - \tilde{c}_i \tilde{c}_j \right) + \sum_{i=1}^n y_i k_B T [\tilde{c}_i \ln(\tilde{c}_i) + (1 - \tilde{c}_i) \ln(1 - \tilde{c}_i)] + \sum_{i=1}^n y_i \tilde{c}_i \mu_i^\ominus \right\} \quad (4.4)$$

Where  $\mu_i^\ominus$  is the standard chemical potential for the sublattice  $i$ , which is related, as described above, to the standard half-cell potential of the reacting sublattice  $V_i^\ominus$ , and conserve the intrinsic physical property of the redox potential for the specific sublattice.

Once the regular solution theory has been reformulated for a multi-sublattice active material, it is crucial to analyze the analytical solution to gain insight into the impact of various alloying elements on the material's behavior before obtaining the free energy functional needed to construct a comprehensive phase-field model.

To predict the behavior of the system is necessary to build an  $n$  dimensional energy space and follow the concentration path that minimizes the energy extracted to transform the system from a completely deintercalated state, where  $\tilde{c}_1, \tilde{c}_2, \dots, \tilde{c}_n = 0$ , to a fully occupied system where  $\tilde{c}_1, \tilde{c}_2, \dots, \tilde{c}_n = 1$ . In this way, it is possible to numerically obtain a solution for  $F(\tilde{c})$ , and from it, a voltage curve for a homogenous single particle system can be obtained  $V(\tilde{c})$ .

If the difference in standard chemical potential between the lattice sites is significant compared to  $\Omega_{ij}$  we will observe a series of redox plateaus in the voltage curve. Conversely, a more complicated energy path will be followed (see supplementary information). Limiting ourselves to the first case, we can analytically calculate the chemical potential, and so the voltage curve of the various plateaus as

$$\mu_i = \frac{1}{y_i N} \frac{\partial F}{\partial \tilde{c}_i} \quad (4.5)$$

$$\mu_i = k_B T \ln \left( \frac{\tilde{c}_i}{1 - \tilde{c}_i} \right) + \sum_{j=1}^n y_j \Omega_{ij} (1 - 2\tilde{c}_j) + \mu_i^\ominus \quad (4.6)$$

This simple formulation allows us to analytically capture how the system behaves depending on the compositions  $y_i, y_j, \dots, y_n$  and the known factors  $\Omega_{ii}, \Omega_{jj}, \dots, \Omega_{nn}$ .

In fact, considering an intercalation process, we can deduce that in case  $\mu_1^\ominus < \mu_{2,3,\dots}^\ominus$  the intercalated species will initially sit in the lattice sites here defined as "1" keeping  $\tilde{c}_{2,3,\dots} = 0$ , and then, once  $\tilde{c}_1 \sim 1$  the second lattice sites will react, and so on. Therefore, the effective standard chemical potentials measured will be

$$\mu_{1eff}^\ominus = \mu_1^\ominus + \sum_{j=2}^n y_j \Omega_{1j} \quad (4.7)$$

From Eq. 4.7, we can conclude that, due to the enthalpic contributions of the surrounding sublattices, the effective chemical potential, and so the measured redox potential  $V_i^\ominus$ , will be decreased by a value corresponding to the sum of the pair mixing energy coefficients, weighted by their corresponding stoichiometry. For the second plateau, we instead expect that since  $\tilde{c}_1 \sim 1$  the redox potential will increase by a factor  $y_1 \Omega_{12}$  and be reduced by a factor  $\sum_{i=3}^n y_i \Omega_{2i}$ .

Moreover, it is worth noticing how the effective enthalpic interaction  $\Omega_{ieff} = y_i \Omega_{ii}$  is now a function of the stoichiometry of the compound. In the case of phase-separating materials, this will impact the voltage hysteresis gap and the overall phase separation behavior with respect to the pure original lattice. Knowing that if  $\Omega_{ieff} < 2k_B T$  no phase separation will occur during the plateau of the specie "i", we can directly calculate the compositions that assure a solid-solution transition  $y_{iss} < 2k_B T / \Omega_{ii}$  depending directly on temperature and the mixing energy of the original compound.

The theory can so be straightforwardly applied to intercalating electrode materials. Following the example of the phospho-olivine materials, a single sublattice position will be composed by the ensemble of an intercalated specie, a transition metal and the  $\text{PO}_4$  tetrahedron. The stoichiometry of the transition metal "i" will thus correspond to  $y_i$ , while  $\tilde{c}_i$  indicates the fraction of transition metal which lattice spot is occupied.

Moreover, the presented theoretical structure can also be compared with the compound energy formalism (CEF)<sup>78</sup> of the CALPHAD approach to solution modeling<sup>79</sup>. Specifically, to develop

the theory, we followed the point of view of intercalated atoms so that we defined a sublattice as a set of lattice positions composed of the inserted specie and the corresponding reduced transition metal. From another perspective, the system can be seen as a single lattice having  $2n$  species: a vacancy and an occupied spot for each insertion site. In this context, Eq. 4.4 can be considered as an expression of the free energy, including the excess free energy, in terms of the site interactions within the same sublattice, and Eq. 4.3 as a generalized approximated form of the bond energy model for multiple species<sup>80</sup>. Finally, it must be stated that we do not expect the obtained model to be able to predict the complete phase diagram since, differently from the CALPHAD approach, the parameters are directly taken from the regular solution model interpretation of electrochemical data rather than fitted to experimental phase diagrams. While for general solid compounds, the CALPHAD approach is feasible and necessary, its application to battery materials requires a wide set of experiments and strongly depends on the choice of the end-members model<sup>81</sup>. Our approach is instead applicable to electrochemical data making it more suitable for active material battery modeling.

#### 4.4 APPLICATION TO PHOSPHO-OLIVINE CATHODES

The available literature and the need for a reliable electrochemical model make phospho-olivine cathodes an excellent candidate for a critical verification of the developed theory by testing its implications on the redox potential shift and the order of the phase transition. We focus on the most promising iron substitutions in  $\text{LiFePO}_4$  (LFP) by Mn and Co. Cyclic voltammetry and voltage curve data from the literature can provide the necessary information to implement in the model. For obtaining the enthalpies of mixing of the single sublattice of  $\text{LiFePO}_4$  ( $\Omega_{FeFe}$  in our multi-sublattice notation) and  $\mu_{Fe}^\ominus$ , we can rely on previous regular solution models for LFP were  $\Omega_{FeFe} = 4.63 k_B T$  and  $\mu_{Fe}^\ominus = -3.422 eV/\text{Li atom}$ . However, for  $\text{LiMnPO}_4$  (LMP) and  $\text{LiCoPO}_4$  (LCP), no previously developed models are available, so we must obtain  $\Omega_{MnMn} = 7.44 k_B T$  and  $\mu_{Mn}^\ominus = -4.09 eV/\text{Li atom}$  from fitting the voltage curve from Tasaduk et al.<sup>20</sup> and the cyclic voltammetry of Kobayashi et al.<sup>82</sup>, respectively. Obtaining values for  $\text{LiCoPO}_4$  presents particular challenges due to its instability with the current electrolyte<sup>24</sup>, limiting the available data. Nevertheless, we note that the peak separation of the cyclic voltammetry in the work of Jalkanen et al.<sup>83</sup> is close to that of LFP. Since the peak separation is proportional to the voltage gap due to phase separation, we can assume that  $\Omega_{CoCo} \approx \Omega_{FeFe}$  and that  $\mu_{Co}^\ominus = -4.78 eV/\text{Li atom}$  can be determined from the peak midpoint.

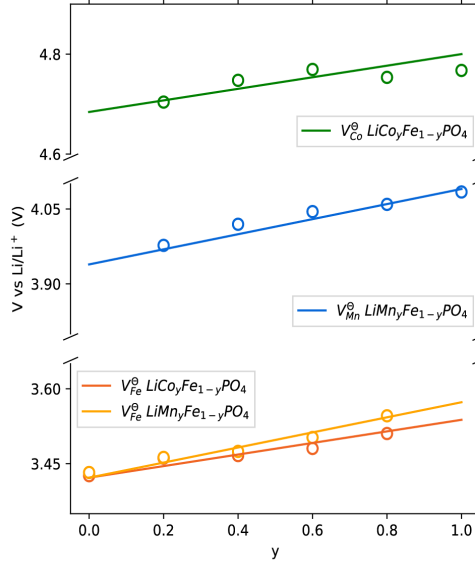


**Figure 4.2.** Comparison between the calculated (lines) and the measured (empty dots) redox potentials at various Mn and Co substitutions ( $y$ ). The green line is the redox potential shift of the Co plateau in  $\text{LiCo}_y\text{Fe}_{1-y}\text{PO}_4$ , while the dark orange is its counterpart in the Fe plateau. The blue line is the redox potential shift in  $\text{LiMn}_y\text{Fe}_{1-y}\text{PO}_4$ , and the light orange one is the redox shift in the corresponding Fe plateau.

Starting by analyzing the shift in redox potential, we can compare the midpoints of the cyclic voltammetry results at different Fe substitutions from references [57] and [59] with the redox shift obtained from the theory. The expected dependence of the redox potential on the Mn content  $y$  for the plateaus in  $\text{LiMn}_y\text{Fe}_{1-y}\text{PO}_4$  will so be

$$V_{Mn_{eff}}^{\theta} = V_{Mn}^{\theta} + y\Omega_{FeMn} \quad (4.8)$$

$$V_{Fe_{eff}}^{\theta} = V_{Fe}^{\theta} - (1 - y)\Omega_{FeMn} \quad (4.9)$$

Making the same calculations for the LFCP, we can see in Fig. 4.2 how the theory predicts the experimental values without any fitting parameters. A strong indication of the validity of the theory is in the quantitative prediction of the shift in the Fe plateau  $\Delta V_{Fe}^{\theta} = (y - 1)\Omega_{FeX}$  which clearly does not depend on the original redox potential but only on the value of the average enthalpic interaction  $\Omega_{FeX}$ , which is different for the case of Co and Mn substitution. For the  $\text{LiCoPO}_4$  case, we could have been more precise by considering the double redox plateau

present, seemingly linked to a staging behavior<sup>28,29</sup>. At present, we chose to neglect this effect, assuming it would pose minimal effect on the pair interaction energies, therefore, the chemical potential of LCP can be approximately modeled in the same fashion as that of LFP and LMP.

These results establish a strong foundation for the mean-field theory and offer a clear explanation for how the redox shift can be attributed to the interaction between surrounding lattice sites, in agreement with the Monte Carlo calculations of Malik et al.<sup>33</sup> in which the shift in redox potential was attributed to the effect of the pair interaction energies. It is remarkable that the straightforward assumption of averaging the two interaction energies, as demonstrated in Eq. 4.3, continues to hold true, even when the phenomenon is rooted in atomistic behavior.

4

Exploiting now the predictive capabilities of the model, in particular, the possibility of calculating the solid-solution compositions  $y_{i_{ss}} < 2k_B T / \Omega_{ii}$ , we can analyze the previously mentioned olivine phosphates, creating a ternary phase diagram (Fig. 4.3) revealing the order of phase transition (solid-solution or phase separation) for the corresponding plateau based on the compositions of  $\text{LiCo}_x\text{Mn}_y\text{Fe}_{1-x-y}\text{PO}_4$ . Explicitly considering the mixing energies described above, we calculate the solid-solution composition at ambient temperature of the Mn sublattice to be  $y_{Mn_{ss}} = 0.26$ , where for every other composition of Fe or Co, the particle transforms as a solid solution during the Mn plateau. Applying the same concept to Fe and Co, we obtain  $y_{Co_{ss}} = y_{Fe_{ss}} = 0.43$ .

The predicted equilibrium phase transition behavior aligns with the available data in the literature. The experiments of Jalkanen<sup>83</sup> and Kobayashi<sup>82</sup> show the CV peak separation of the corresponding plateau to be linearly dependent on the composition of the olivine material. Further, the works of Ravnsbæk<sup>84–86</sup> and Strobridge<sup>29</sup> analyze the operando XRD profiles of different compositions of LFMP and LFCP, exposing the absence of phase separation for the corresponding sublattice if the composition is below the one calculated from the model.

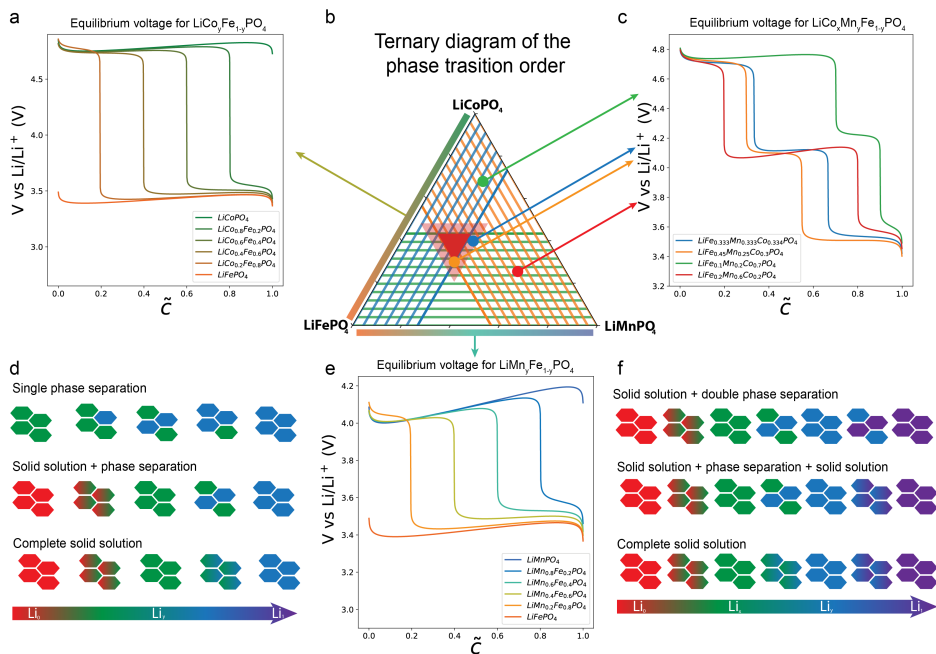


Figure 4.3. Voltage curves of  $\text{LiMn}_x\text{Fe}_{1-y}\text{PO}_4$ ,  $\text{LiCo}_x\text{Fe}_{1-y}\text{PO}_4$ ,  $\text{LiCo}_x\text{Mn}_y\text{Fe}_{1-x-y}\text{PO}_4$  (bottom center, top left, top right) originated from analytical calculations of the ternary phase transition diagram (center). The dark red zone indicates the compositions in which a thermodynamically consistent solid solution behavior is expected during the entire (de)lithiation. The light red zone is a qualitative extension indicating that the solid solution zone may be wider due to other stabilizing effects, such as coherency strain and lattice mismatch. Demonstration of the possible phase transition combinations (bottom left, right) depending on the stoichiometry of the various metals.

Therefore, the mathematical theory and the associated phase diagram can become tools for the practical engineering of these alloys. For example, they enable the selection of a composition range in which the material behaves as a complete solid solution (red triangle), at least from an equilibrium thermodynamics perspective. We expect a wider zone (light red) in which the real system could behave as a solid solution due to the stabilizing effects of coherency strain<sup>41</sup>, auto-inhibitory intercalation reactions<sup>52</sup>, and the relation between the particle dimensions and the phase separation front<sup>29,87</sup>. To specifically characterize this wider zone a full phase-field model of each composition should be created. Within the solid solution region, it is also possible to select the composition that minimizes the Co content (orange curve for LFCMP in Fig. 4.3). The complete solid-solution behavior is confirmed by experiments on both  $\text{LiMn}_{1/3}\text{Co}_{1/3}\text{Fe}_{1/3}\text{PO}_4$ <sup>30</sup>, and  $\text{LiMn}_{0.3}\text{Co}_{0.2}\text{Fe}_{0.5}\text{PO}_4$ <sup>88</sup> in which the systems show a monotonically decreasing voltage curve.

These conclusions come directly from the analytic application of the extended regular solution theory and the consistent calculations of  $\Omega_{Fe}$ ,  $\Omega_{Mn}$  and  $\Omega_{Co}$  without the need for ab-initio simulations. The mean-field model also helps in the phenomenological description of the system. The dilution of a sublattice, and its consequent reduction in first neighbors, weakens the attractive interaction between the intercalated atoms allowing the entropic contribution to take over, leading to a solid solution. Since this effect is subtle, a temperature change will also lead to different behavior (see supplementary information). This conclusion differs from the one reported by Malik et al.<sup>33</sup> in which the disappearance of the phase separation for certain compositions was attributed to the reduction in the Li composition difference between the initial and the final state.

4

Finally, the combination of the predictions for the redox potential shift and the phase transition naturally leads to the possibility of calculating the voltage curves for every composition, including LFMP, LFCP, and LFMCP, in good accordance with the previously cited experimental results.

## 4.5 PHASE-FIELD MODELING

Having demonstrated a correspondence between experimental data and the analytical solution of the model, it is now interesting to investigate other factors that may come into play when the system is out of equilibrium. This can be accomplished by employing a complete phase-field simulation, which takes into account factors such as coherency strain and gradient penalties. Beginning with a simulation of a single particle, the behavior will be observed during both charging and discharging, with the aim of gaining insight into the collective dynamics that arise at various compositions.

Given the wealth of available experimental data in the literature and the potential for commercial applications<sup>89</sup>, we have narrowed our focus to LFMP simulations. We implement our model in the open-source code MPET<sup>48</sup>, freely available in its GitHub repository. The complete set of equations and the parameters of the phase-field simulations can be found in the supplementary information, alongside a comparison of the simulated and measured voltage curves at equilibrium.

## 4.6 SINGLE PARTICLE SIMULATIONS

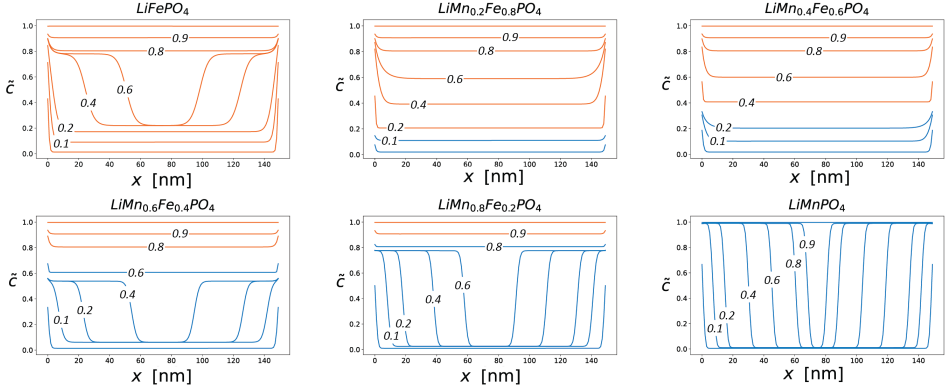


**Figure 4.4.** Evolution of the normalized Li concentration inside a 150 nm particle upon lithiation. The blue lines correspond to the Mn plateau, the orange lines to the Fe plateau. The labels show the average composition of the particle.

The single particle simulations in equilibrium ( $C/1000$ ) (Fig. 4.4) show how modifying the enthalpic contribution at different compositions affects the system. Given  $y$  the fraction of Mn in  $\text{LiMn}_y\text{Fe}_{1-y}\text{PO}_4$ , for the cases of  $y = 0.6$  and  $y = 0.8$ , we obtain  $\Omega_{\text{Fe}eff} < 2k_B T$  at ambient temperature so that the particle, as expected from the analytical calculations, behaves as a solid solution during the (de)intercalation of the Fe plateau and phase separate when in the Mn plateau. In contrast, for intermediate values of  $y$  within the range of 0.2 to 0.4, although the effective interaction energies  $\Omega_{\text{Fe}eff}$  and  $\Omega_{\text{Mn}eff}$  exceed the critical threshold of  $2k_B T$  for phase separation, the coherency strain provides a stabilizing effect that leads to the transformation of the particle into a solid solution. The insertion direction in our one-dimensional model is the one in which the coherency strain is minimum, which coincides with the preferential direction for phase separation<sup>41</sup>. This implies that the observed solid-solution behavior will remain consistent when considering a three-dimensional particle.

This claim requires further experimental verification, keeping in mind that the composition where we experience suppression of the phase separation may slightly differ from the one observed in simulations due to the documented sensitivity of the calculated coherency strain values on ab-initio simulation parameters<sup>90,91</sup>. However, the single-particle simulations rationalize how the composition  $\text{LiMn}_{0.4}\text{Fe}_{0.6}\text{PO}_4$  with its probable solid-solution behavior can limit the problems due to the measured low Li diffusivity<sup>92</sup>.

## 4.7 POROUS ELECTRODE SIMULATIONS

We used our single-particle model in a multiparticle simulation in which the simulated particles are considered part of a porous electrode regulated by the porous electrode theory<sup>43,48,93</sup>. We can so include the electrolyte transport limitations, described by the Stefan-Maxwell concentrated electrolyte theory<sup>48</sup>, obtaining a realistic representation of the distribution of the Li concentration along the depth of a cathode.

In particular, it is interesting to simulate the effect of the composition on the possible suppression of phase separation, already known for LFP, and on the lithium distribution along the depth. We distinguish the phenomena by performing simulations at two different Mn content: the first consists of simulating the charge and discharge process of a thin electrode at  $C/10$  to assess the collective dynamic, and the second involves a 1C discharge of a thicker electrode to focus on the transport limitations. All the simulations are done on an ensemble of 400 particles with lognormal size distribution. The computed evolution of the concentration during the  $C/10$  cycle was collected in a probability distribution and converted to normalized volume expansion (see supplementary information) to better compare the result with the work of Ravnsbæk<sup>85</sup> et al.

The results, shown in Fig. 4.5, not only strongly agree with the work of Ravnsbæk et al.<sup>85</sup>, but they also offer a thermodynamically consistent explanation of them. Both in experiments and simulations, a bimodal volume distribution is present in the plateaus where the theory predicts phase separation. Moreover, it is essential to state that, considering the cases of  $\text{LiMn}_{0.2}\text{Fe}_{0.8}\text{PO}_4$  and  $\text{LiMn}_{0.4}\text{Fe}_{0.6}\text{PO}_4$  where, as discussed in the previous paragraph, we predict a solid solution transition for the single particle, the collective dynamics are dominated by the non-monotonic shape of the chemical potential and its subsequent concentration-dependent exchange current density<sup>52</sup>. Since we are close to equilibrium conditions ( $C/10$ ), we can conclude that the origin of this bimodal distribution is established by the inter-particle separation (mosaic lithiation) in which the smaller particles are more lithiated than, the bigger ones, as also observed for LFP<sup>102</sup>.

Focusing on the asymmetry between charge and discharge, for  $\text{LiMn}_{0.4}\text{Fe}_{0.6}\text{PO}_4$ , both in simulations and experiments, the phase separation of the Fe plateau is present only during charging. From this observation, Ravnsbæk et al.<sup>84</sup> suggested that the intrinsic order of the phase transition in  $\text{LiMn}_{0.4}\text{Fe}_{0.6}\text{PO}_4$  depends on the direction of the transition and attributed the reason to coherency strain effects. Our consistent thermodynamic model enables us to reinterpret these conclusions offering a physical explanation for the observed experimental behavior.

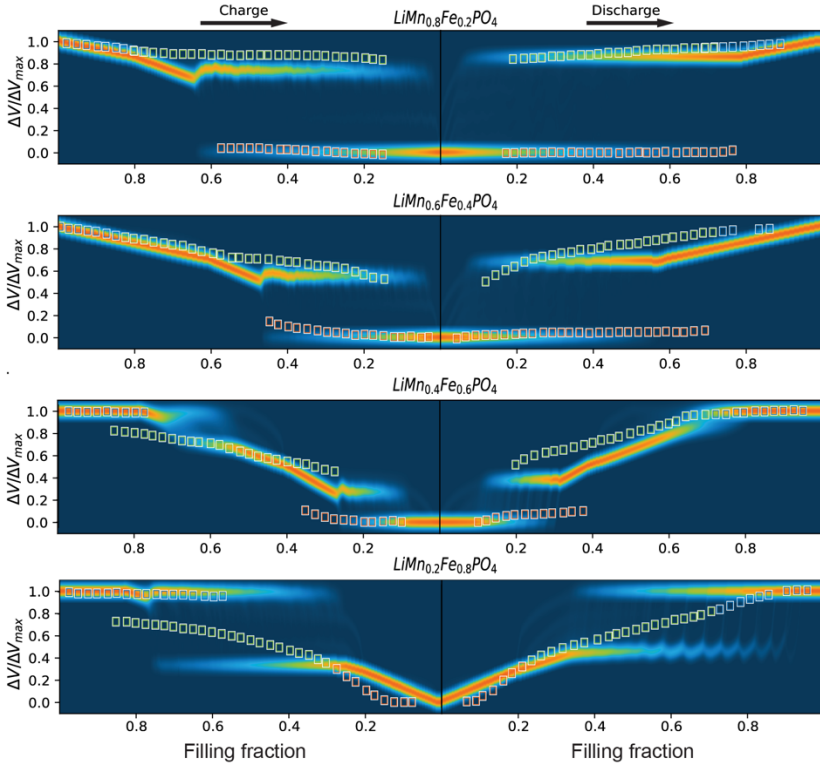
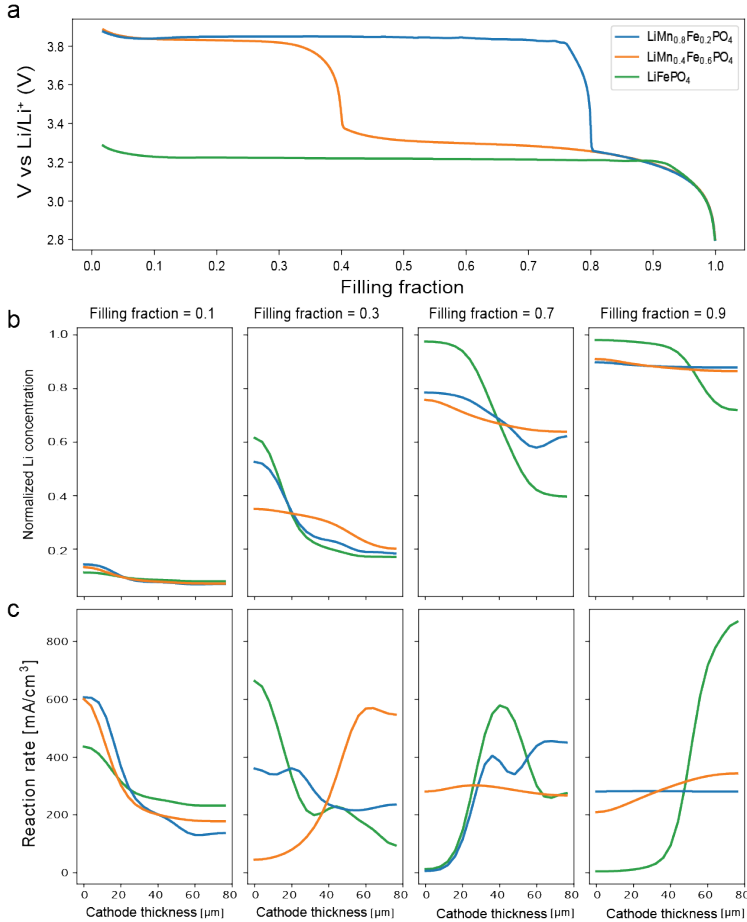


Figure 4.5. Volume evolution for  $\text{LiMn}_y\text{Fe}_{1-y}\text{PO}_4$  during charge and discharge compared to experiments. The heatmaps represent the simulated probability of the normalized calculated volume evolving during a charge-discharge cycle at  $C/10$  from fully lithiated ( $\Delta V/\Delta V_{max} = 1$ ) to fully delithiated ( $\Delta V/\Delta V_{max} = 0$ ). The simulated data are broadened, applying a Gaussian convolution for visual intent<sup>54</sup>. The empty squares are the experimental data points of the Rietveld refinement from the work of Ravnsbæk<sup>85</sup> et al.

Our simulations indicate the significance of the collective auto-inhibitory and auto-catalytic behavior upon lithiation and delithiation, respectively<sup>52</sup>. Due to the asymmetric concentration dependence of the exchange current density upon delithiation, an enhanced particle-by-particle reaction is observed, while during lithiation, the inter-particle separation is suppressed, as previously observed in LFP<sup>102</sup> and NMC<sup>54</sup> porous electrodes. While this phenomenon is only observed when cycling LFP at high rates, it is instead already present at  $C/10$  in the Fe plateau of LFMP due to the low  $\Omega_{\text{Fe}eff}$ . The only observed mismatch in Fig. 4.5 occurs in discharge case of  $\text{LiMn}_{0.2}\text{Fe}_{0.8}\text{PO}_4$  and can be attributed to various phenomena not included in the model such as a possible metastable phase for the Fe plateau<sup>103,104</sup>, effect of particle size<sup>87,105</sup> or non-linear dependence of the volume on the Li concentration.

Finally, it is expected that already at 1C, in the case of a thin cathode, in the range  $0.2 < y < 0.4$ , the inter-particle separation is completely suppressed during lithiation (see supplementary information), even if low intra-particle diffusivity may lead to different experimental results.



**Figure 4.6. Effect of composition on transport limitations.** Voltage curves of a 1C discharge of  $\text{LiFePO}_4$ ,  $\text{LiMn}_{0.4}\text{Fe}_{0.6}\text{PO}_4$ ,  $\text{LiMn}_{0.8}\text{Fe}_{0.2}\text{PO}_4$  (top). Normalized Lithium concentration along the depth of the simulated cathodes at various states of the discharge (center), the separator is posed on the left side ( $x = 0 \mu\text{m}$ ), while the current collector is on the right ( $x = 80 \mu\text{m}$ ). Reaction rate along the depth of the simulated cathodes at various states of the discharge (bottom).

To complete the picture, we studied the effect of the composition on the lithium depth profile during a 1C discharge of a commercial-like cathode. The simulated half-cell has a cathode thickness of  $80 \mu\text{m}$  a porosity of 30%, the transport limitations of Li in the electrolyte are

therefore not negligible anymore. Due to the absence of the nucleation barrier, solid solution materials tend to lithiate relatively uniformly along the depth, even in the case of strong transport limitation. On the other hand, phase-separating materials show steeper gradients in the Li concentration<sup>106,107</sup>. The mixed phase separation – solid solution behavior of LFMP makes it an exciting candidate to evaluate this effect since the different compositions affect the phase transition. As shown in Fig. 4.7, if  $\text{LiMn}_{0.8}\text{Fe}_{0.2}\text{PO}_4$  is used, the Mn plateau will show an inhomogeneous redox activity, typical of phase-separating materials, while the last 20% of the discharge, corresponding to the Fe plateau, will have a uniform reaction along the depth. Similar considerations can be made on  $\text{LiMn}_{0.4}\text{Fe}_{0.6}\text{PO}_4$  in which a small but visible peak in redox activity can be seen in both plateaus due to the non-monotonicity of the chemical potential, which is still present even if the single particle is not phase separating.

We can so conclude that the Li distribution along the depth of the electrode at different states of charge is severely affected by the concentration of Mn. Taking LFP as a reference, it is clear that the change in the degree of phase separation helps guarantee uniform lithiation along the depth, and the case of  $\text{LiMn}_{0.4}\text{Fe}_{0.6}\text{PO}_4$  is the one that most favors homogeneity. This result significantly impacts the cycle life, thanks to the possibility of reducing current hot spots, and offers a new route for a composition-based optimization of a commercial electrode.

## 4.8 CONCLUSIONS

In this study, we expanded the regular solution theory to explain and predict the behavior of phospho-olivine cathodes. The inclusion of multiple sublattices and their interactions provided an elegant explanation for the shift in redox potential and phase separation behavior. The mean-field theory formalization offers an intuitive understanding of these phenomena, which can enable research on new active materials. This approach can serve as a valuable alternative to computationally extensive ab-initio calculations, delivering clear insights starting from simple concepts instead. Our phenomenological description of the mathematical derivation demonstrates that the redox shift is due to the interactions of the non-reacting sublattice. Furthermore, we found that a redox plateau that previously showed phase separation can transform into a solid solution. This transformation occurs due to the reduced number of closest neighbors within the same sublattice, which lowers the effective interactions of the intercalated species.

The application of our model to well-studied materials such as LFMP, LFCP, and LFMCP and their possible compositions shows how quantitative and accurate this theory is, even if the examined system is considered complex. The subsequent application in a phase-field framework was able to reproduce and explain various experimental results whose interpretations were incomplete and lacked mathematical support. The firm conclusion about the absence of phase

separation in low Mn content LFMP is still to be confirmed experimentally. However, the proposed mechanism to explain the operando XRD peak shift sheds light on the importance of considering multi particles behavior when experimenting with a collective system such as a half-cell.

4 Finally, this model strongly indicates the optimal composition for a high-power cathode, showing how  $\text{LiMn}_{0.4}\text{Fe}_{0.6}\text{PO}_4$  may be an excellent candidate thanks to its solid solution behavior and low transport-induced inhomogeneity. To verify this claim, further experiments are necessary, and a 2-dimensional model, able to capture the known transport limitation in the particle, is also advised. The interplay between the concentrations of the two sublattices may play an essential role in explaining the out-of-equilibrium behavior opening the route for optimization of the (dis)charging procedure to exploit these effects<sup>108</sup>. We expect that the new theory may be applied to other popular active materials such as  $\text{LiMn}_{1.5}\text{Ni}_{0.5}\text{O}_4$  (LMNO) or the various compositions of NMC, explaining the effect of metal ratios on the performances. To do so, it will be necessary to consider the structural modifications occurring in the spinel or the layered structure that, at the moment, are not taken into account in the theory. It is finally hoped that overcoming these limitations may expand the domain of this theory in such a way that, as particle dimension, porosity, and thickness, also the composition of the materials can be included in the parameters to optimize when a battery is designed, improving cycle life and energy efficiency.

## REFERENCES

1. Goodenough, J. B. & Park, K.-S. The Li-Ion Rechargeable Battery: A Perspective. *J. Am. Chem. Soc.* **135**, 1167–1176 (2013).
2. Zhang, H., Yang, Y., Ren, D., Wang, L. & He, X. Graphite as anode materials: Fundamental mechanism, recent progress and advances. *Energy Storage Mater.* **36**, 147–170 (2021).
3. Lyu, Y. *et al.* An Overview on the Advances of LiCoO<sub>2</sub> Cathodes for Lithium-Ion Batteries. *Adv. Energy Mater.* **11**, 2000982 (2021).
4. Sood, A. *et al.* Electrochemical ion insertion from the atomic to the device scale. *Nat. Rev. Mater.* **6**, 847–867 (2021).
5. Rauh, R. D. Electrochromic windows: an overview. *Electrochimica Acta* **44**, 3165–3176 (1999).
6. Gonzalez-Rosillo, J. C. *et al.* Lithium-Battery Anode Gains Additional Functionality for Neuromorphic Computing through Metal–Insulator Phase Separation. *Adv. Mater.* **32**, 1907465 (2020).
7. Tian, H. & Bazant, M. Z. Interfacial Resistive Switching by Multiphase Polarization in Ion-Intercalation Nanofilms. *Nano Lett.* **22**, 5866–5873 (2022).
8. Nadkarni, N., Zhou, T., Fraggedakis, D., Gao, T. & Bazant, M. Z. Modeling the Metal–Insulator Phase Transition in Li<sub>x</sub>CoO<sub>2</sub> for Energy and Information Storage. *Adv. Funct. Mater.* **29**, 1902821 (2019).
9. Wang, H. *et al.* Direct and continuous strain control of catalysts with tunable battery electrode materials. *Science* **354**, 1031–1036 (2016).
10. Alkhadra, M. A. *et al.* Electrochemical Methods for Water Purification, Ion Separations, and Energy Conversion. *Chem. Rev.* **122**, 13547–13635 (2022).
11. Wu, L. *et al.* Lithium recovery using electrochemical technologies: Advances and challenges. *Water Res.* **221**, 118822 (2022).
12. Zhao, X. *et al.* Recent progress on key materials and technical approaches for electrochemical lithium extraction processes. *Desalination* **546**, 116189 (2023).
13. Sun, L. *et al.* Recent progress and future perspective on practical silicon anode-based lithium ion batteries. *Energy Storage Mater.* **46**, 482–502 (2022).
14. Zhang, Y. *et al.* Towards better Li metal anodes: Challenges and strategies. *Mater. Today* **33**, 56–74 (2020).
15. Zhao, H. *et al.* Cobalt-Free Cathode Materials: Families and their Prospects. *Adv. Energy Mater.* **12**, 2103894 (2022).
16. Hebert, A. & McCalla, E. The role of metal substitutions in the development of Li batteries, part I: cathodes. *Mater. Adv.* **2**, 3474–3518 (2021).
17. Padhi, A. K., Nanjundaswamy, K. S. & Goodenough, J. B. Phospho-olivines as Positive-Electrode Materials for Rechargeable Lithium Batteries. *J. Electrochem. Soc.* **144**, 1188–1194 (1997).
18. Wang, M. *et al.* Recycling of lithium iron phosphate batteries: Status, technologies, challenges, and prospects. *Renew. Sustain. Energy Rev.* **163**, 112515 (2022).
19. Tolganbek, N., Yerkinbekova, Y., Kalybekkyzy, S., Bakenov, Z. & Mentbayeva, A. Current state of high voltage olivine structured LiMPO<sub>4</sub> cathode materials for energy storage applications: A review. *J. Alloys Compd.* **882**, 160774 (2021).
20. Wani, T. A. & Suresh, G. A comprehensive review of LiMnPO<sub>4</sub> based cathode materials for lithium-ion batteries: current strategies to improve its performance. *J. Energy Storage* **44**, 103307 (2021).
21. Mauger, A. & Julien, C. Olivine Positive Electrodes for Li-Ion Batteries: Status and Perspectives. *Batteries* **4**, 39 (2018).

22. Deng, Y. *et al.* Recent Advances of Mn-Rich  $\text{LiFe}_{1-y}\text{Mn}_y\text{PO}_4$  ( $0.5 \leq y < 1.0$ ) Cathode Materials for High Energy Density Lithium Ion Batteries. *Adv. Energy Mater.* **7**, 1601958 (2017).
23. Yang, L. *et al.* Olivine  $\text{LiMn}_x\text{Fe}_{1-x}\text{PO}_4$  cathode materials for lithium ion batteries: restricted factors of rate performances. *J. Mater. Chem. A* **9**, 14214–14232 (2021).
24. Zhang, M., Garcia-Araez, N. & Hector, A. L. Understanding and development of olivine  $\text{LiCoPO}_4$  cathode materials for lithium-ion batteries. *J. Mater. Chem. A* **6**, 14483–14517 (2018).
25. Li, Y. & Taniguchi, I. Synthesis of  $\text{LiNi}_{1-x}\text{Co}_x\text{PO}_4/\text{C}$  nanocomposite cathode for lithium ion batteries by a combination of aerosol and powder technologies. *Adv. Powder Technol.* **30**, 180–189 (2019).
26. Bramnik, N. N., Trots, D. M., Hofmann, H. J. & Ehrenberg, H. Mixed  $\text{LiCo}_{0.6}\text{M}_{0.4}\text{PO}_4$  ( $\text{M} = \text{Mn, Fe, Ni}$ ) phosphates: cycling mechanism and thermal stability. *Phys. Chem. Chem. Phys.* **11**, 3271 (2009).
27. Mauger, A., Julien, C. M., Armand, M., Goodenough, J. B. & Zaghbi, K.  $\text{Li}(\text{Ni,Co})\text{PO}_4$  as cathode materials for lithium batteries: Will the dream come true? *Curr. Opin. Electrochem.* **6**, 63–69 (2017).
28. Palmer, M. G. *et al.* In situ phase behaviour of a high capacity  $\text{LiCoPO}_4$  electrode during constant or pulsed charge of a lithium cell. *Chem. Commun.* **52**, 14169–14172 (2016).
29. Strobridge, F. C. *et al.* Unraveling the Complex Delithiation Mechanisms of Olivine-Type Cathode Materials,  $\text{LiFe}_x\text{Co}_{1-x}\text{PO}_4$ . *Chem. Mater.* **28**, 3676–3690 (2016).
30. Muñoz-García, A. B. *et al.* Structural evolution of disordered  $\text{LiCo}_{1/3}\text{Fe}_{1/3}\text{Mn}_{1/3}\text{PO}_4$  in lithium batteries uncovered. *J. Mater. Chem. A* **8**, 19641–19653 (2020).
31. Timrov, I., Aquilante, F., Cococcioni, M. & Marzari, N. Accurate electronic properties and intercalation voltages of olivine-type Li-ion cathode materials from extended Hubbard functionals. *PRX Energy* **1**, 033003 (2022).
32. Snyder, D. H. & Wolverton, C. Transition-Metal Mixing and Redox Potentials in  $\text{Li}_x(\text{M}_{1-y}\text{M}'_y)\text{PO}_4$  ( $\text{M, M}' = \text{Mn, Fe, Ni}$ ) Olivine Materials from First-Principles Calculations. *J. Phys. Chem. C* **120**, 5932–5939 (2016).
33. Malik, R., Zhou, F. & Ceder, G. Phase diagram and electrochemical properties of mixed olivines from first-principles calculations. *Phys. Rev. B* **79**, 214201 (2009).
34. Bazzant, M. Z. Theory of Chemical Kinetics and Charge Transfer based on Nonequilibrium Thermodynamics. *Acc. Chem. Res.* **46**, 1144–1160 (2013).
35. Wang, Q. *et al.* Application of phase-field method in rechargeable batteries. *Npj Comput. Mater.* **6**, 176 (2020).
36. Birkholz, O. & Kamlah, M. Electrochemical Modeling of Hierarchically Structured Lithium-Ion Battery Electrodes. *Energy Technol.* **9**, 2000910 (2021).
37. Liu, K. *et al.* Electrochemical modeling and parameterization towards control-oriented management of lithium-ion batteries. *Control Eng. Pract.* **124**, 105176 (2022).
38. Zhao, H. Data-driven Modeling of Lithium Intercalation Materials.
39. Nguyen, T.-T. *et al.* Mathematical Modeling of Energy-Dense NMC Electrodes: I. Determination of Input Parameters. *J. Electrochem. Soc.* **169**, 040546 (2022).
40. Smith, R. B., Khoo, E. & Bazant, M. Z. Intercalation Kinetics in Multiphase-Layered Materials. *J. Phys. Chem. C* **121**, 12505–12523 (2017).
41. Cogswell, D. A. & Bazant, M. Z. Coherency Strain and the Kinetics of Phase Separation in  $\text{LiFePO}_4$  Nanoparticles. *ACS Nano* **6**, 2215–2225 (2012).
42. Li, Y. *et al.* Fluid-enhanced surface diffusion controls intraparticle phase transformations. *Nat. Mater.* **17**, 915–922 (2018).
43. Ferguson, T. R. & Bazant, M. Z. Nonequilibrium Thermodynamics of Porous Electrodes. *J. Electrochem. Soc.* **159**, A1967–A1985 (2012).

44. Bai, P., Cogswell, D. A. & Bazant, M. Z. Suppression of Phase Separation in LiFePO<sub>4</sub> Nanoparticles During Battery Discharge. *Nano Lett.* **11**, 4890–4896 (2011).
45. de Klerk, N. J. J., Vasileiadis, A., Smith, R. B., Bazant, M. Z. & Wagemaker, M. Explaining key properties of lithiation in TiO<sub>2</sub>-anatase Li-ion battery electrodes using phase-field modeling. *Phys. Rev. Mater.* **1**, 025404 (2017).
46. Vasileiadis, A. *et al.* Toward Optimal Performance and In-Depth Understanding of Spinel Li<sub>4</sub>Ti<sub>5</sub>O<sub>12</sub> Electrodes through Phase Field Modeling. *Adv. Funct. Mater.* **28**, 1705992 (2018).
47. Agrawal, S. & Bai, P. Dynamic interplay between phase transformation instabilities and reaction heterogeneities in particulate intercalation electrodes. *Cell Rep. Phys. Sci.* **3**, 100854 (2022).
48. Smith, R. B. & Bazant, M. Z. Multiphase Porous Electrode Theory. *J. Electrochem. Soc.* **164**, E3291–E3310 (2017).
49. Ferguson, T. R. & Bazant, M. Z. Phase Transformation Dynamics in Porous Battery Electrodes. *Electrochimica Acta* **146**, 89–97 (2014).
50. Zhao, H. & Bazant, M. Z. Population dynamics of driven autocatalytic reactive mixtures. *Phys. Rev. E* **100**, 012144 (2019).
51. Dreyer, W., Guhlke, C. & Huth, R. The behavior of a many-particle electrode in a lithium-ion battery. *Phys. Nonlinear Phenom.* **240**, 1008–1019 (2011).
52. Bazant, M. Z. Thermodynamic stability of driven open systems and control of phase separation by electro-autocatalysis. *Faraday Discuss.* **199**, 423–463 (2017).
53. Bai, P. & Tian, G. Statistical kinetics of phase-transforming nanoparticles in LiFePO<sub>4</sub> porous electrodes. *Electrochimica Acta* **89**, 644–651 (2013).
54. Park, J. *et al.* Fictitious phase separation in Li layered oxides driven by electro-autocatalysis. *Nat. Mater.* **20**, 991–999 (2021).
55. Cahn, J. W. & Hilliard, J. E. Free Energy of a Nonuniform System. I. Interfacial Free Energy.
56. Cahn, J. W. & Hilliard, J. E. Free Energy of a Nonuniform System. III. Nucleation in a Two-Component Incompressible Fluid.
57. Cahn, J. W. & Hilliard, J. E. Spinodal decomposition: A reprise. *Acta Metall.* **19**, 151–161 (1971).
58. Binder, K. Theory of first-order phase transitions. *Rep. Prog. Phys.* **50**, 783–859 (1987).
59. Daubner, S. *et al.* Multiphase-field modeling of spinodal decomposition during intercalation in an Allen-Cahn framework. *Phys. Rev. Mater.* **5**, 035406 (2021).
60. Zeng, Y. & Bazant, M. Z. Cahn-Hilliard Reaction Model for Isotropic Li-ion Battery Particles. *MRS Proc.* **1542**, mrrs13-1542-g02-01 (2013).
61. Lee, D. *et al.* Physical, mathematical, and numerical derivations of the Cahn–Hilliard equation. *Comput. Mater. Sci.* **81**, 216–225 (2014).
62. Chandresris, M., Caliste, D., Jamet, D. & Pochet, P. Thermodynamics and Related Kinetics of Staging in Intercalation Compounds. *J. Phys. Chem. C* **123**, 23711–23720 (2019).
63. Rykner, M. & Chandresris, M. Free Energy Model for Lithium Intercalation in Graphite: Focusing on the Coupling with Graphene Stacking Sequence. *J. Phys. Chem. C* **126**, 5457–5472 (2022).
64. Di Leo, C. V., Rejovitzky, E. & Anand, L. A Cahn–Hilliard-type phase-field theory for species diffusion coupled with large elastic deformations: Application to phase-separating Li-ion electrode materials. *J. Mech. Phys. Solids* **70**, 1–29 (2014).
65. Afshar, A. & Di Leo, C. V. A thermodynamically consistent gradient theory for diffusion–reaction–deformation in solids: Application to conversion-type electrodes. *J. Mech. Phys. Solids* **151**, 104368 (2021).
66. Zhang, X., Shyy, W. & Marie Sastry, A. Numerical Simulation of Intercalation-Induced Stress in Li-Ion Battery Electrode Particles. *J. Electrochem. Soc.* **154**, A910 (2007).
67. Castelli, G. F., von Kolzenberg, L., Horstmann, B., Latz, A. & Dörfler, W. Efficient Simulation of Chemical–Mechanical Coupling in Battery Active Particles. *Energy Technol.* **9**, 2000835 (2021).

68. Daubner, S., Weichel, M., Schneider, D. & Nestler, B. Modeling intercalation in cathode materials with phase-field methods: Assumptions and implications using the example of LiFePO<sub>4</sub>. *Electrochimica Acta* **421**, 140516 (2022).
69. Bazant, M. *et al.* *Learning Heterogeneous Reaction Kinetics from X-Ray Movies Pixel-by-Pixel*. <https://www.researchsquare.com/article/rs-2320040/v1> (2022) doi:10.21203/rs.3.rs-2320040/v1.
70. Fraggedakis, D. *et al.* Theory of coupled ion-electron transfer kinetics. *Electrochimica Acta* **367**, 137432 (2021).
71. G. Galuppini, M. D. Berliner, H. Lian, D. Zhuang, M. Z. Bazant and R. D. Braatz. Efficient computation of safe, fast charging protocols for multiphase lithium-ion batteries: A lithium iron phosphate case study. *Appear J Power Sources* (2023).
72. Piazza, R. *Statistical Physics: A Prelude and Fugue for Engineers*. (Springer International Publishing, Cham, 2017). doi:10.1007/978-3-319-44537-3.
73. Han, B. C., Van der Ven, A., Morgan, D. & Ceder, G. Electrochemical modeling of intercalation processes with phase field models. *Electrochimica Acta* **49**, 4691–4699 (2004).
74. Rykner, M. & Chandesaris, M. Free Energy Model for Lithium Intercalation in Graphite: Focusing on the Coupling with Graphene Stacking Sequence. *J. Phys. Chem. C* **126**, 5457–5472 (2022).
75. Tardif, S. *et al.* Combining *operando* X-ray experiments and modelling to understand the heterogeneous lithiation of graphite electrodes. *J. Mater. Chem. A* **9**, 4281–4290 (2021).
76. Hörmann, N. G. & Groß, A. Phase field parameters for battery compounds from first-principles calculations. *Phys. Rev. Mater.* **3**, 055401 (2019).
77. Dreyer, W. *et al.* The thermodynamic origin of hysteresis in insertion batteries. *Nat. Mater.* **9**, 448–453 (2010).
78. Hillert, M. The compound energy formalism. *J. Alloys Compd.* **320**, 161–176 (2001).
79. CALPHAD: Calculation of Phase Diagrams - A Comprehensive Guide. vol. 1 (Elsevier, 1998).
80. Hillert, M. Some properties of the compound energy model. *Calphad* **20**, 333–341 (1996).
81. Phan, A. T., Gheribi, A. E. & Chartrand, P. Modelling of phase equilibria of LiFePO<sub>4</sub>-FePO<sub>4</sub> olivine join for cathode material. *Can. J. Chem. Eng.* **97**, 2224–2233 (2019).
82. Kobayashi, G. *et al.* Shift of redox potential and kinetics in Li<sub>x</sub>(M<sub>ny</sub>Fe<sub>1-y</sub>)PO<sub>4</sub>. *J. Power Sources* **189**, 397–401 (2009).
83. Jalkanen, K. & Karpinen, M. Electrochemical Performance and Delithiation/Lithiation Characteristics of Mixed LiFe<sub>1-y</sub>M<sub>y</sub>PO<sub>4</sub> (M = Co, Ni) Electrode Materials. *J. Electrochem. Soc.* **162**, A2780–A2788 (2015).
84. Ravnsbæk, D. B. *et al.* Extended Solid Solutions and Coherent Transformations in Nanoscale Olivine Cathodes. *Nano Lett.* **14**, 1484–1491 (2014).
85. Ravnsbæk, D. B. *et al.* Engineering the Transformation Strain in LiMn<sub>y</sub>Fe<sub>1-y</sub>PO<sub>4</sub> Olivines for Ultrahigh Rate Battery Cathodes. *Nano Lett.* **16**, 2375–2380 (2016).
86. Ravnsbæk, D. B. *et al.* In-Situ Study of Electrochemically-Driven Phase Transitions in LiMn<sub>y</sub>Fe<sub>1-y</sub>PO<sub>4</sub>. *ECS Meet. Abstr.* **MA2013-02**, 255–255 (2013).
87. Cogswell, D. A. & Bazant, M. Z. Size-dependent phase morphologies in LiFePO<sub>4</sub> battery particles. *Electrochem. Commun.* **95**, 33–37 (2018).
88. Zhong, Y. *et al.* Microwave-assisted rheological phase synthesis of LiFe<sub>0.5</sub>Mn<sub>0.3</sub>Co<sub>0.2</sub>PO<sub>4</sub>/C cathode materials for lithium ion batteries. *Mater. Res. Express* **6**, 035003 (2018).
89. Nwachukwu, I. M., Nwanya, A. C., Ekwealor, A. B. C. & Ezema, F. I. Recent progress in Mn and Fe-rich cathode materials used in Li-ion batteries. *J. Energy Storage* **54**, 105248 (2022).
90. Xie, Y., Yu, H.-T., Yi, T.-F. & Zhu, Y.-R. Understanding the Thermal and Mechanical Stabilities of Olivine-Type LiMPO<sub>4</sub> (M = Fe, Mn) as Cathode Materials for Rechargeable Lithium Batteries from First Principles. *ACS Appl. Mater. Interfaces* **6**, 4033–4042 (2014).

91. Lethole, N. L., Ngoepe, P. E. & Chauke, H. R. First-principles study: Effect of lithium and sodium intercalation in transition metal phosphates,  $MPO_4$  (M: Mn, Fe, Co). *Comput. Condens. Matter* **22**, e00437 (2020).
92. Hashambhoy, A. M. & Whitacre, J. F. Li Diffusivity and Phase Change in  $LiFe_{0.5}Mn_{0.5}PO_4$ : A Comparative Study using Galvanostatic Intermittent Titration and Cyclic Voltammetry. *J. Electrochem. Soc.* **158**, A390 (2011).
93. Fuller, T. F., Doyle, M. & Newman, J. Simulation and Optimization of the Dual Lithium Ion Insertion Cell. *J. Electrochem. Soc.* **141**, 1–10 (1994).
94. Liu, H. *et al.* Capturing metastable structures during high-rate cycling of  $LiFePO_4$  nanoparticle electrodes. *Science* **344**, 1252817 (2014).
95. Levi, M. D. *et al.* Collective Phase Transition Dynamics in Microarray Composite  $Li_xFePO_4$  Electrodes Tracked by In Situ Electrochemical Quartz Crystal Admittance. *J. Phys. Chem. C* **117**, 15505–15514 (2013).
96. Katrašnik, T. *et al.* Entering Voltage Hysteresis in Phase Separating Materials: Revealing the Thermodynamic Origin of a Newly Discovered Phenomenon and Its Impact on the Electric Response of a Battery. *SSRN Electron. J.* (2022) doi:10.2139/ssrn.4030045.
97. Yamanaka, T. *et al.* Evolution and Migration of Lithium-Deficient Phases during Electrochemical Delithiation of Large Single Crystals of  $LiFePO_4$ . *ACS Appl. Energy Mater.* **1**, 1140–1145 (2018).
98. Koyama, Y. *et al.* Hidden Two-Step Phase Transition and Competing Reaction Pathways in  $LiFePO_4$ . *Chem. Mater.* **29**, 2855–2863 (2017).
99. Sharma, N., Yu, D. H., Zhu, Y., Wu, Y. & Peterson, V. K. In operando neutron diffraction study of the temperature and current rate-dependent phase evolution of  $LiFePO_4$  in a commercial battery. *J. Power Sources* **342**, 562–569 (2017).
100. Delmas, C., Maccario, M., Croguennec, L., Le Cras, F. & Weill, F. Lithium deintercalation in  $LiFePO_4$  nanoparticles via a domino-cascade model. *Nat. Mater.* **7**, 665–671 (2008).
101. Zhang, X. *et al.* Rate-Induced Solubility and Suppression of the First-Order Phase Transition in Olivine  $LiFePO_4$ . *Nano Lett.* **14**, 2279–2285 (2014).
102. Li, Y. *et al.* Current-induced transition from particle-by-particle to concurrent intercalation in phase-separating battery electrodes. *Nat. Mater.* **13**, 1149–1156 (2014).
103. Zhou, F., Maxisch, T. & Ceder, G. Configurational Electronic Entropy and the Phase Diagram of Mixed-Valence Oxides: The Case of  $Li_xFePO_4$ . *Phys. Rev. Lett.* **97**, 155704 (2006).
104. Delacourt, C., Poizot, P., Tarascon, J.-M. & Masquelier, C. The existence of a temperature-driven solid solution in  $Li_xFePO_4$  for  $0 \leq x \leq 1$ . *Nat. Mater.* **4**, 254–260 (2005).
105. Cogswell, D. A. & Bazant, M. Z. Theory of Coherent Nucleation in Phase-Separating Nanoparticles. *Nano Lett.* **13**, 3036–3041 (2013).
106. Verhallen, T. W., Lv, S. & Wagemaker, M. Operando Neutron Depth Profiling to Determine the Spatial Distribution of Li in Li-ion Batteries. *Front. Energy Res.* **6**, 62 (2018).
107. Zhang, X. In operando phase transition and lithium ion transportation in  $LiFePO_4$ .
108. Azimi, V., Allam, A. & Onori, S. Extending Life of Lithium-Ion Battery Systems by Embracing Heterogeneities via an Optimal Control-Based Active Balancing Strategy. *IEEE Trans. Control Syst. Technol.* 1–15 (2022) doi:10.1109/TCST.2022.3215610.
109. Zelič, K. & Katrašnik, T. Thermodynamically consistent derivation of chemical potential of a battery solid particle from the regular solution theory applied to  $LiFePO_4$ . *Sci. Rep.* **9**, 2123 (2019).
110. Cahn, J. W. On spinodal decomposition in cubic crystals. *Acta Metall.* **10**, 179–183 (1962).
111. Bai, P. & Bazant, M. Z. Charge transfer kinetics at the solid–solid interface in porous electrodes. *Nat. Commun.* **5**, 3585 (2014).
112. Bernardi, D. M. & Go, J.-Y. Analysis of pulse and relaxation behavior in lithium-ion batteries. *J. Power Sources* **196**, 412–427 (2011).



## SUPPLEMENTARY INFORMATION

### Derivation of the extended regular solution internal energy

Considering a sublattice  $i$  with  $N_i = y_i N$  lattice spots and, on average  $z_i = y_i z$  closest neighbors, for every occupied lattice spot and every closest neighbor, the internal energy will be increased by  $\varepsilon_{ooii}\tilde{c}_i^2$ ; applying the same concept to vacancies  $(1 - \tilde{c}_i)$  interacting with energy  $\varepsilon_{vvii}$  and to the interaction between occupied lattice spots and vacancies  $\varepsilon_{voii}$ , normalizing everything by 2 to avoid counting twice, the single sublattice internal energy  $E_{ss_i}$  is calculated as

$$E_{ss_i} = N_i z_i \left[ \frac{1}{2} \varepsilon_{ooii} \tilde{c}_i^2 + \frac{1}{2} \varepsilon_{vvii} (1 - \tilde{c}_i)^2 + \varepsilon_{voii} \tilde{c}_i (1 - \tilde{c}_i) \right] \quad (E1)$$

Considering now, in general  $N_i$  lattice spots interacting with  $z_j = y_j z$  closest neighbors of type  $j$  through average interactions  $\varepsilon_{ooij}$ ,  $\varepsilon_{vvij}$ ,  $\varepsilon_{voij}$  and applying the same considerations showed above, the energy coming from the interaction between the sublattice  $E_{ss_{ij}}$  becomes

$$E_{ss_{ij}} = N_i z_j \left[ \frac{1}{2} \varepsilon_{ooij} \tilde{c}_i \tilde{c}_j + \frac{1}{2} \varepsilon_{vvij} (1 - \tilde{c}_i)(1 - \tilde{c}_j) + \frac{1}{2} \varepsilon_{voij} \tilde{c}_i (1 - \tilde{c}_j) + \frac{1}{2} \varepsilon_{voji} \tilde{c}_j (1 - \tilde{c}_i) \right] \quad (E2)$$

Which is reduced to Eq. E1 for  $i = j$ . To obtain the total internal energy, we need to sum over all the  $n$  sublattices considering both the self-interactions and the pair interactions.

Noticing that  $N_i z_j = N_j z_i = N z y_j y_i$ ; considering symmetric interactions:  $\varepsilon_{ooij} = \varepsilon_{ooji}$ ,  $\varepsilon_{vvij} = \varepsilon_{vvji}$ ,  $\varepsilon_{voij} = \varepsilon_{voji}$ ; assuming that  $\varepsilon_{ooij} = \frac{1}{2}(\varepsilon_{ooii} + \varepsilon_{oojj})$ ,  $\varepsilon_{vvij} = \frac{1}{2}(\varepsilon_{vvii} + \varepsilon_{vvjj})$ ,  $\varepsilon_{voij} = \frac{1}{2}(\varepsilon_{voii} + \varepsilon_{vojj})$ ; summing and subtracting  $\frac{\varepsilon_{ooij}}{2} \tilde{c}_i$ ,  $\frac{\varepsilon_{ooij}}{2} \tilde{c}_j$ , and collecting the terms, we arrive at the following general equation for the internal energy

$$E = \sum_{i=1}^n \sum_{j=1}^n \frac{N_i z_j}{2} \left[ \frac{\varepsilon_{ooij}}{2} (\tilde{c}_i + \tilde{c}_j) + \frac{\varepsilon_{vvij}}{2} (2 - \tilde{c}_i + \tilde{c}_j) + \left( \varepsilon_{voij} - \frac{\varepsilon_{ooij}}{2} - \frac{\varepsilon_{vvij}}{2} \right) (\tilde{c}_i + \tilde{c}_j - 2\tilde{c}_i \tilde{c}_j) \right] \quad (E3)$$

Defining  $\Omega_{ij} = z \left( \varepsilon_{voij} - \frac{1}{2} \varepsilon_{ooij} - \frac{1}{2} \varepsilon_{vvij} \right)$  we reach Eq. 4.2 of the main text.

It is vital to notice how the standard chemical potential of the whole material can be consistently calculated as  $\mu^\ominus = \frac{1}{N} [E(c_i = 1, c_j = 1, \dots) - E(c_i = 0, c_j = 0, \dots)]$  which, applying Eq. E3 and using the previous approximation (Eq. 4.3 of the main text) for combined interaction energies  $\varepsilon_{ij}$ , becomes

$$\mu^\ominus = \sum_{i=1}^n y_i z \left( \frac{\varepsilon_{ooii}}{2} - \frac{\varepsilon_{vvii}}{2} \right) = \sum_{i=1}^n y_i \mu_i^\ominus \quad (E4)$$

consistent with physical intuition, the total energy difference between the fully intercalated and de-intercalated states must be conserved.

## Single particle phase field model

To accurately apply the extended regular solution model, a complete phase field model is needed. It is necessary to return to the Cahn-Hilliard formalism and derive the free energy functional, including the effects of nonuniform compositions. In this approach, the free energy of a nonuniform system depends not only on the concentration but also on the higher-order gradient terms  $\nabla \tilde{c}_i, \nabla^2 \tilde{c}_i$ . It was chosen to neglect the effects of the mutual interaction of  $\tilde{c}_i$  and  $\tilde{c}_j$  on the gradient terms and, therefore, to directly add to the homogenous free energy the term  $\frac{1}{2} \kappa_i |\nabla \tilde{c}_i|^2$  to account for gradient penalties. The concentrations are defined such that  $\bar{c} = \sum_{i=1}^n y_i \tilde{c}_i$ ,  $\bar{c}$  is the overall mean concentration of the particle and  $c_{max} = \sum_{i=1}^n y_i \tilde{c}_{i_{max}}$ .

To calculate how  $\kappa_i$  depends on the composition is necessary to recall the formulation found by Zelič and al.<sup>109</sup>

$$\kappa_i = \frac{Nzd^2}{m} \Omega_{ii} \quad (E5)$$

In which  $d$  represent the distance between crystal planes and  $m$  is a geometrically deduced parameter. Following that theory, in a case in which the structure is not heavily modified by the metal substitution, the effective boundary energy can be calculated by multiplying the original  $\kappa_i$  by  $y_i^2$ .

Another effect that must be considered in the case of a nonuniform system is the coherency strain energy within the elastic deformation regime, which was proven to be fundamental to explaining the anisotropy of the phase separation in LFP<sup>41</sup>.

Given the limited energy scale of the coherency strain energy, it was not considered necessary to reformulate the original theory developed for two-phase materials in the presence of multiple stable phases. Thus, the formulation<sup>41,76</sup>:

$$B(\mathbf{n}) = C_{ijkl}\epsilon_{ij}^0\epsilon_{kj}^0 - n_i\sigma_{ij}^0\omega_{ij}(\mathbf{n})\sigma_{lm}^0n_m, \quad (E6)$$

where  $[\omega^{-1}]_{ij} = C_{ijkl}n_kn_l$ , and  $\sigma_{ij}^0 = C_{ijkl}\epsilon_{kl}^0$ .  $B(\mathbf{n})$  is the coherency strain pressure along the direction  $\mathbf{n}$ ,  $C_{ijkl}$  is the stiffness tensor and  $\epsilon_{ij}^0$  is the strain matrix, and  $\omega_{ij}$  is related to the elastic Green tensor.

Finally, for dimensionality reduction, the Cahn approach was implemented<sup>41,76,110</sup>:  $B_0$  is selected as the minima amongst the different directions and a term  $\frac{1}{2}\frac{B_0}{c_{max}}(\tilde{c} - \bar{c})^2$  is added to the free energy functional.

The total  $B_0$  is instead computed as  $B_0 = \sum_{i=1}^n y_i B_i(n_0)$ , since the correct value for a compound material would require a consistent number of first-principles calculations without a valuable gain in accuracy.

The complete specific Gibbs free energy will be given by

$$g = c_{max} \left\{ \frac{F}{N} + \sum_{i=1}^n \frac{1}{2} y_i^2 \kappa_i |\nabla \tilde{c}_i|^2 + \frac{1}{2} \frac{B_0}{c_{max}} (\tilde{c} - \bar{c})^2 \right\} \quad (E7)$$

With  $F$  being the Helmholtz free energy described in Eq. 4.4 of the main text.

For the phase-field approach<sup>34,43</sup>, it is now sufficient to calculate the chemical potentials  $\mu_i$  in the sublattice  $i \neq j$  as a functional derivative of  $G = \int_V g dV$  so that

$$\mu_i = k_B T \ln \left( \frac{\tilde{c}_i}{1 - \tilde{c}_i} \right) + \sum_{j=1}^n y_j \Omega_{ij} (1 - 2\tilde{c}_j) + \frac{B_0}{c_{max}} (\tilde{c} - \bar{c}) - y_i \kappa_i \nabla^2 \tilde{c}_i + \mu_i^\ominus \quad (E8)$$

Since the crystal structure of LFMP is equivalent to the one of LFP ( $Pnma$ ) it is possible to use the same approach used by Cogswell and al.<sup>44</sup> to simulate an LFP particle so that the platelet-shaped particles can be simulated along the [101] dimension. The concentration along the depth of the platelet is considered uniform, all the points of the array are in contact with the electrolyte, and they react with it depending on their chemical potential. Therefore, the system is considered open and can be included in the Allen-Chan formalism.

Due to the known transport limitation of LFMP<sup>23</sup>, the depth-averaged approximation prevents the model from reliably accounting for fast (de)lithiation making it suitable only to explore close to equilibrium conditions, approximately up to 1C for thin platelet particles. It was therefore not implemented a diffusion model for the intercalation kinetic of this material, which diffusivity may in general depend on the concentrations in all the sublattices in a non-trivial form. Overcoming this approximation, developing a multi-sublattice diffusion theory is suggested in case the system needs to be optimized for higher current densities.

Finally, the chemical potential obtained from the described free energy is used to calculate the reaction dependence on the overpotential through the modified version of the Butler-Volmer equation<sup>111</sup>, in which the current density depends on the activity of the Li in both the electrolyte and solid phases.

$$i(c_i, x) = y_i \frac{k_0 a_0^{1-\alpha} a_i^\alpha}{\gamma_i^\ddagger} \left( e^{-\frac{\alpha e \eta_i}{k_B T}} - e^{\frac{(1-\alpha) e \eta_i}{k_B T}} \right) \quad (E9)$$

Where  $\alpha$  is the reactor symmetry factor,  $k_0$  is the reaction rate constant per unit area,  $e$  is the elementary charge,  $a_0$  is the activity of the oxidized state (corresponding, in the context of batteries, to the activity of the Li-ions in the electrolyte), which also includes the activity of the electron participating in the reaction,  $a_i = e^{(\mu_i - \mu_i^\ominus)/k_B T}$  is the activity of the ion in the sublattice  $i$ ,  $\eta_i$  is the charge transfer overpotential for the sublattice  $i$  ( $e \eta_i = \mu_i - \mu_0$ ) and  $\gamma_i^\ddagger = \frac{1}{(1-\epsilon_i)}$  is the activity coefficient of the transition state of the sublattice  $i$ . The total reaction rate of a single particle will then be  $R = \int_0^L i(c_i, x) dx$ .

Other than the redox potential and the mixing energy, to implement a phase field model is necessary to quantify the gradient energy term  $\kappa_i$  and the coherency strain  $B_0$ . Following the approach described above for the gradient penalty energy, starting from the know  $\kappa_{LFP} = 9.919 \cdot 10^{-10} J/m$ <sup>44</sup>, and considering the same characteristic length  $\lambda$  for LMP, it is possible to quantify  $\kappa_{LMP} = 17.06 \cdot 10^{-10} J/m$ . To calculate the coherency strain, the values of the

stiffness tensors are taken from the work of Lethole and al.<sup>91</sup>, and applying Eq. E2, the following values are obtained  $B_{0LFP} = 0.2291 \text{ GPa}$ ,  $B_{0LMP} = 0.2038 \text{ GPa}$ .

The developed theory can simulate an electrochemical reaction between a phase separating multi-sublattice particle and an electrolyte. However, for computational reasons, the chemical potential implemented in the open-source code MPET was slightly modified so that the one implemented for a 2 sublattice material becomes

$$\begin{aligned} \mu_i = & 2k_B T \ln \left( \frac{\tilde{c}_i}{1 - \tilde{c}_i} \right) + y_i \Omega_{ii}^* (1 - 2\tilde{c}_i) + y_j \Omega_{ij} (1 - 2\tilde{c}_j) \\ & + \frac{B_0}{c_{max}} (\tilde{c} - \bar{c}) - y_i \kappa_i^* \nabla^2 \tilde{c}_i + \mu_i^\ominus \quad (E10) \end{aligned}$$

The computational necessity, due to the numerical handling of the logarithmic term, to modify the entropic contribution by multiplying it by 2 was compensated by applying a different  $\Omega_{ii}$ , named  $\Omega_{ii}^*$ , that was calculated again, assuring that the voltage hysteresis gap between charge and discharge of the mono-sublattice corresponding material (LFP and LMP) assumed the same value as the one calculated using a coefficient 1 on the entropy. To maintain the same characteristic length of the phase boundary, also  $\kappa_i^*$  was also modified proportionally. The electrolyte parameters are taken from Bernardi and Go 2011<sup>112</sup>.

## Multi-particle simulation

The multi-particle system was simulated using the open-source code MPET<sup>48</sup> considering a half-cell in which the anode is considered as an infinite source of Li at 0 V ( ideal Li metal ), the separator is neglected, and the cathode is composed of a set of particles distributed in different volumes. A good balance between accuracy and computational efficiency was found by simulating 400 particles distributed in 20 different volumes, each of them representing a section of the cathode. Within every volume, the Li ions in the electrolyte have the same electrochemical potential  $\mu_0$  so that the particles in the volume react depending on their size distribution. The electrochemical potential varies so along the thickness of the electrode depending on the reaction rate  $R$  and the transport properties (ambipolar diffusivity of the electrolyte and conductivity).

To model the electrolyte, the Stefan-Maxwell model available in the software was used, and the electrical resistivity of the solid phase was neglected, so the basic set of equations for the multi-particle system is the following:

$$\varepsilon \frac{\partial c_{Li^+}}{\partial t} = -\nabla \cdot \mathbf{F}_{Li^+} + R_{Li^+}, \quad (E11)$$

$$0 = \nabla \cdot \mathbf{i} - eR_{Li^+}, \quad (E12)$$

where  $\mathbf{F}_{Li^+}$  is the Li-ion flux,  $R_{Li^+}$  is the reaction rate from the electrolyte to the particles,  $\mathbf{i}$  is the current density,  $e$  is the electron charge,  $\varepsilon$  is the porosity and  $c_{Li^+}$  is the Li-ion concentration in the electrolyte. The current density is coupled with the reaction rate considering the active area of the particle.

4

The code also allows considering the potential drops coming from the electronic conductivity limitations. Defining  $\mathbf{i}_{e^-}$  as the electronic current the equations modeling this phenomenon are:

$$0 = \nabla \cdot \mathbf{i}_{e^-} - eR_{Li^+}, \quad (E13)$$

where it is assumed that for every Li intercalating an electron is intercalating as well, and

$$\mathbf{i}_{e^-} = -\frac{1-\varepsilon}{\tau} \sigma_s \nabla \phi_s, \quad (E14)$$

in which Ohm's law is assumed to hold in the carbon conductive matrix having an electrical conductivity  $\sigma_s$  and a tortuosity  $\tau$ , such that the current is proportional to the gradient of the electric potential of the solid phase  $\phi_s$ .

The boundary conditions for the transport equations consider no electrical current flowing in the separator, and no ionic current flowing in the current collector.

LFMP parameters		
Enthalpy of mixing ( $\Omega_{Mn}^*$ )	4.705 $10^{-20}$ J/Li	
Gradient penalty ( $\kappa_{Mn}$ )	17.06 $10^{-10}$ J/m	
Coherency strain ( $B_{0Mn}$ )	0.2291 GPa	Ref. <sup>91</sup>
Enthalpy of mixing ( $\Omega_{Fe}^*$ )	2.931 $10^{-20}$ J/Li	Ref. <sup>44</sup>
Gradient penalty ( $\kappa_{Fe}$ )	9.91 $10^{-10}$ J/m	Ref. <sup>44</sup>
Coherency strain ( $B_{0Fe}$ )	0.2891 GPa	Ref. <sup>91</sup>
Charge transfer coefficient ( $\alpha$ )	0.5	
$k_0$	0.5 $A/m^2$	
Morphology		
Particle average length	100 nm	
Particle standard deviation	50 nm	
Cathode thickness (L)	30 $\mu m$ , 80 $\mu m$	
Electrode porosity	60 %, 30 %	
Active material volume loading	70 %	
Number of particles	400	
Bruggeman coefficient	0.5	

Table S1 Parameters used for the multiphase porous electrode theory simulations.

## Conversion from concentration to volume expansion

To compare the evolution of the simulated distribution of the concentration during the charge and discharge process in LFMP with the available refined operando XRD experimental data, we collected the normalized concentration of every finite difference of every particle at every time step in a histogram, creating a probability distribution of the normalized concentration. This distribution is then converted to a volume expansion distribution, as described in this section. Finally, a gaussian broadening is applied to the distribution for visual intent. The obtained result before the conversion to volume is represented in the results section of this document.

To convert from concentration to volume, we define a non-linear relationship between the total normalized concentration in the active particle  $\tilde{c}$  and the normalized volume expansion. A distinction was made between the solid solution state and the single crystalline phase state: if the particle concentration is in a range in which a solid solution transition is expected, we assume that the volume grows linearly with the concentration, if instead, the particle concentration is in a well-defined phase, so before or after the spinodal compositions, we assume that the volume, or at least the refined volume value from X-ray scattering, does not change with the concentration.

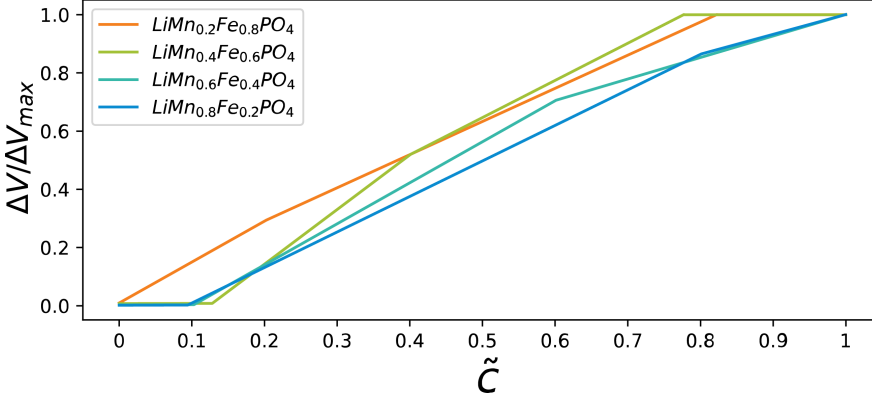


Figure S1. Relationship used to convert the concentration to the volume.

In the case of LFMP, during the lithiation of the Mn sublattice where  $\tilde{c}_1$  will go from 0 to 1, the particles can either be found in a solid solution state if  $y$  is lower than the critical value described in the main text, or they can separate in a bimodal composition. In the latter case, one part of the population can be in a single crystalline phase called  $\alpha$ , which will then give a constant volume, and the remaining is in a solid solution phase. A similar approach can be applied to the Fe plateau, in which  $\tilde{c}_2$  will go from 0 to 1, where all the particles will start from a solid solution state and, during lithiation, some of them may nucleate into the  $\beta$  crystalline phase.

Following this reasoning and considering that the volume expansion during the solid solution transition will depend on the filling Mn or the Fe sublattice, we can create a rectified linear unit function for the evolution of the volume.

Explicitly, we start by finding the spinodal compositions  $\tilde{c}_{i_{minus}}$ ,  $\tilde{c}_{i_{plus}}$

$$\frac{\partial \mu_i}{\partial \tilde{c}_i} \Big|_{\tilde{c}_{i_{minus}}, \tilde{c}_{i_{plus}}} = 0 \quad (E15)$$

The volume of each sublattice,  $V_{Mn}$  and  $V_{Fe}$ , will then be given by

$$\begin{cases} \Delta V_{Mn}(\tilde{c}_1) = 0 & \text{if } \tilde{c}_1 < \tilde{c}_{1_{minus}} \\ \Delta V_{Mn}(\tilde{c}_1) = \Delta V_{LMP} \frac{\tilde{c}_1 - \tilde{c}_{1_{minus}}}{1 - \tilde{c}_{1_{minus}}} & \text{if } \tilde{c}_1 > \tilde{c}_{1_{minus}} \end{cases} \quad (E16)$$

$$\begin{cases} \Delta V_{Fe}(\tilde{c}_2) = \Delta V_{LFP} \frac{\tilde{c}_2}{\tilde{c}_{2plus}} & \text{if } \tilde{c}_2 < \tilde{c}_{2plus} \\ \Delta V_{Fe}(\tilde{c}_2) = \Delta V_{LFP} & \text{if } \tilde{c}_2 > \tilde{c}_{2plus} \end{cases} \quad (E17)$$

Where  $\Delta V_{LFP}$  and  $\Delta V_{LMP}$  are the maximum volume expansions of respectively LFP and LMP.

The total normalized volume expansion will then be

$$\frac{\Delta V(\tilde{c})}{\Delta V_{max}} = \frac{y \Delta V_{Mn}(\tilde{c}_1) + (1-y)\Delta V_{Fe}(\tilde{c}_2)}{y \Delta V_{Mn}(\tilde{c}_1 = 1) + (1-y)\Delta V_{Fe}(\tilde{c}_2 = 1)} \quad (E18)$$

Where  $y$  is the fraction of Mn and  $\tilde{c} = y \tilde{c}_1 + (1-y)\tilde{c}_2$ .

The result of the above calculation will lead to the conversion between volumes plotted in Fig. S4. We want to highlight that this conversion is primarily qualitative, and it was done to explore the correspondence in the phase transition behavior between the simulations and the experiments. A proper conversion will require a complete study of its own.

## Examples of Three-dimensional Energy Path

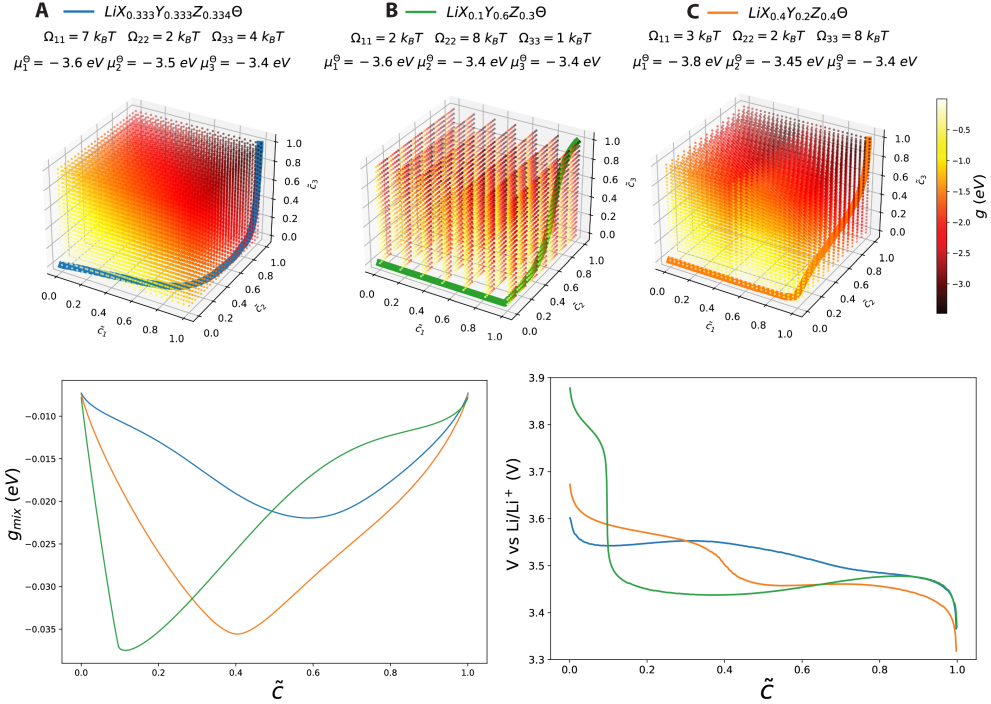


Figure S2. Examples of not-trivial energy paths in three-dimensional energy space of materials A (blue lines), B (green lines), and C (orange lines), the dots represent the free energy at that composition (top). Corresponding minimum mixing free energy path (bottom left) and expected voltage curves for the homogenous system (bottom right).

Taking Eq. 4.4 of the main text and applying it to a 3-sublattice material, we can observe how modifying  $\Omega_{ii}$ ,  $\mu_i^\ominus$  and  $y_i$  it is possible to build non-trivial chemical potentials so that an originally phase-separating material can now behave as a solid solution or vice versa.

For example, material A (in Fig. S1), having similar  $\mu_i^\ominus$  But quite different  $\Omega_{ii}$ , show a shallow phase separation between  $\tilde{c} \approx 0.1$  and  $\tilde{c} \approx 0.6$  even if  $\Omega_{11}$  is much bigger than the  $2 k_B T$  threshold value. Conversely, material B will have  $\tilde{c}_2$  and  $\tilde{c}_3$  reacting simultaneously following a phase separation. Finally, material C is almost following a solid solution path even if most of its components have  $\Omega_{ii} > 2 k_B T$ .

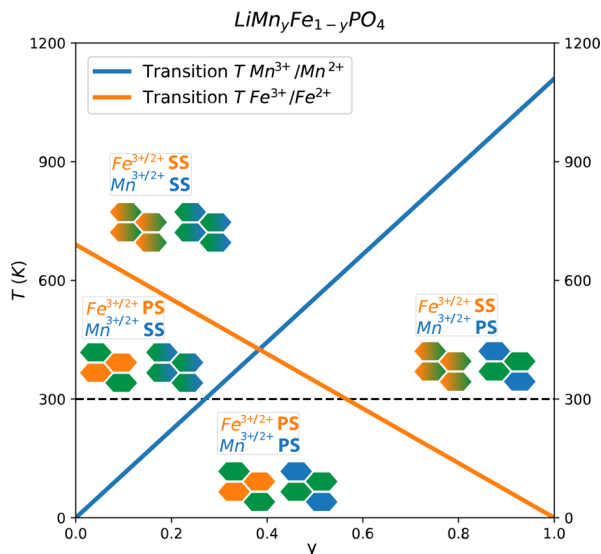
Effect of temperature on the order of phase transition in  $\text{LiMn}_y\text{Fe}_{1-y}\text{PO}_4$ 


Figure S3. Concentration-dependent solid solution temperature of  $\text{LiMn}_y\text{Fe}_{1-y}\text{PO}_4$ . The orange and blue lines show how the temperature in which we observe a solid solution transition of the Fe and the Mn plateaus, respectively, depending on the Mn concentration  $y$ . A schematic representation of the phase transition is added in the four zones arising from these calculations.

Assuming that the calculation for the solid solution composition  $y_{i,ss}(T) < 2k_B T / \Omega_i$  could be done for a wide range of temperatures, the order of phase transition for the two plateaus of  $\text{LiMn}_y\text{Fe}_{1-y}\text{PO}_4$  can be calculated. In Fig. S2 it is possible to observe how the system behaves similarly to a eutectic system, in which at a specific concentration ( $y = 0.38$ ), the temperature required to obtain a solid solution regime in both the plateaus drop considerably. We can find four different zones where the different plateaus have different behaviors.

## Equilibrium voltage profiles

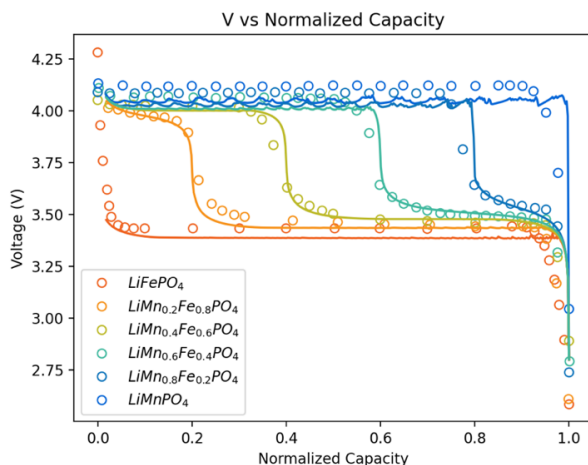


Figure S4. Simulated voltage curves upon a C/100 discharge of  $\text{LiMn}_y\text{Fe}_{1-y}\text{PO}_4$  at various compositions.

As shown in Fig. S3, the model can replicate the experimental voltage curves of  $\text{LiMn}_y\text{Fe}_{1-y}\text{PO}_4$  with high accuracy, confirming what was stated during the comparison between the analytical calculations and the cyclic voltammetry.

The simulations in equilibrium conditions show how the redox shift of the plateau is matched without imposing it for every composition and how the same equation can smoothly replicate the potential at various stoichiometries just by changing the single parameter  $y$ . The voltage curves corresponding to the solid solution behavior are closely reproduced; the ones showing a phase separation instead are slightly different since the simulations focused on the constant current discharge process (for computational efficiency) while the experiments were probably done using different protocols.

## Evolution of the concentration distribution

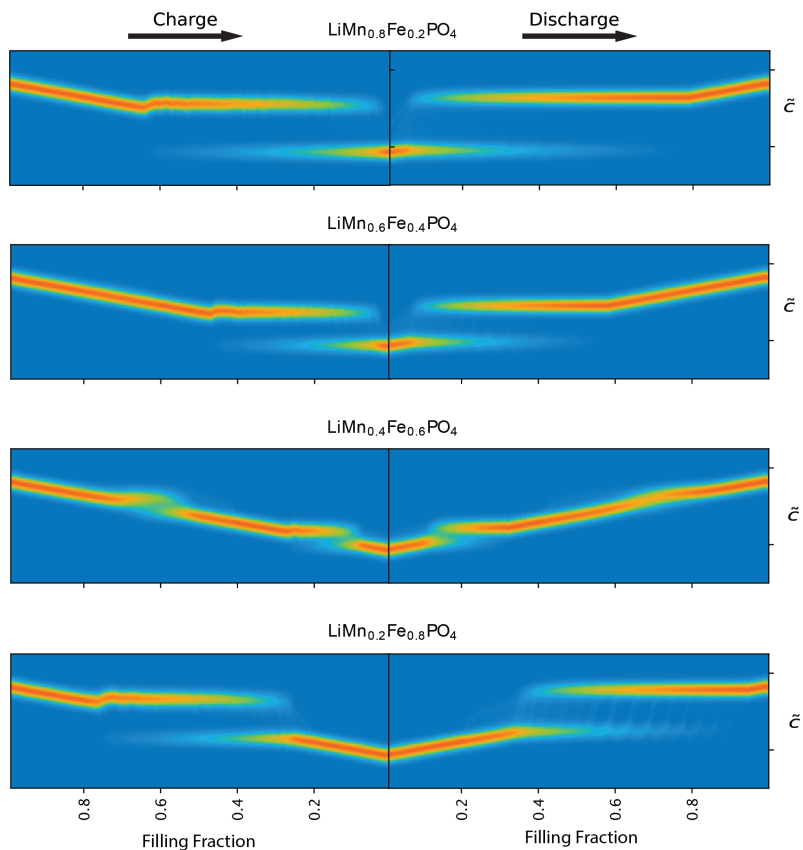


Figure S5. Evolution of the concentration of the C/10 simulations of the main text during charging and discharging.

To further clarify the results in the main text, in Fig. S5 we reported the original evolution of the concentration distribution during charging and discharging at C/10 for the selected compositions of LFMP. The results are similar to Fig. 4.5 of the main text, and it clearly shows phase separation and solid solution behavior in the filling fractions, confirming that the close match with the experiments is not a result of the artificial conversion from concentration to volume. The main difference is in the single-phase regions, where the concentration evolves linearly with time, and the intensity shifts linearly.

## Simulated operando XRD of a 1C cycle

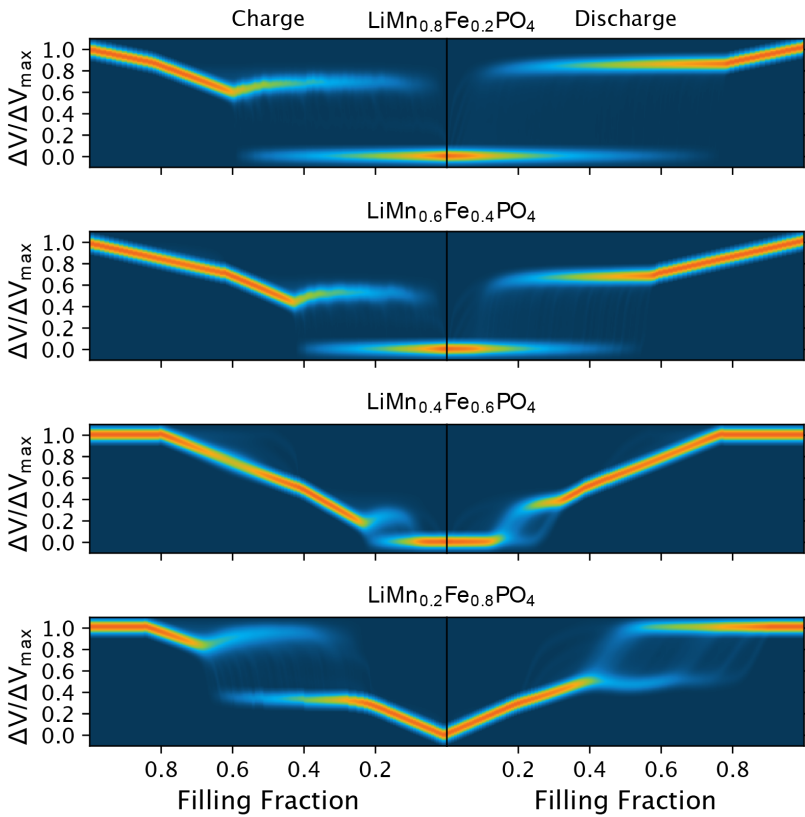


Figure S6: Simulated operando XRD of the particle ensemble studied in the main text for a 1C discharge at different compositions.

To understand more in-depth the collective behavior, the 1C cycle behavior was simulated using the same particle set shown in the main text and described in table S1. The results of the simulated operando XRD in Fig. S6 show how at higher discharge rates, the phase separation is more strongly suppressed even during charge for  $\text{LiMn}_{0.4}\text{Fe}_{0.6}\text{PO}_4$ . This can be explained considering the theory on the auto-inhibitory behavior of a collective particle ensemble<sup>102</sup>. The exchange current density dependence on concentration is, in fact, for both plateaus similar to the one of LFP so that, thanks to the intrinsic low enthalpic term, the phase separation is already suppressed at relatively low rates for the case of  $\gamma = 0.4$ . In the other compositions, the phase separation is still present due to the stronger effective mixing enthalpy of the corresponding plateaus.





# 5 KINETICALLY INDUCED MEMORY EFFECT IN LI-ION BATTERIES

This chapter has been published as: Ombrini P, Wang Q, Vasileiadis A, Wu F, Gao Z, Hu X, van Hulzen M, Li B, Zhao C, Wagemaker M. Kinetically induced memory effect in Li-ion batteries. *EES Batteries*. 2025.

## ABSTRACT

Effective optimization and control of lithium-ion batteries cannot neglect the relation between fundamental physicochemical phenomena and performance. In this work, we apply a multi-step charging protocol to commercially relevant electrodes, such as  $\text{LiNi}_{0.8}\text{Mn}_{0.1}\text{Co}_{0.1}\text{O}_2$  (NMC811),  $\text{LiFePO}_4$  (LFP),  $\text{LiMn}_{1.5}\text{Ni}_{0.5}\text{O}_4$  (LMNO),  $\text{LiMn}_{0.4}\text{Fe}_{0.6}\text{PO}_4$  (LMFP),  $\text{Li}_4\text{Ti}_5\text{O}_{12}$  (LTO) and  $\text{Na}_3\text{V}_2(\text{PO}_4)_3$  (NVP), to investigate how the initial rate affects their kinetic response. Remarkably, electrodes undergoing phase separation exhibit a pronounced counter-intuitive memory effect under high-rate operating conditions. Using operando micro-beam X-ray diffraction, the origin is demonstrated to be embedded in the rate-dependent multi-electrode particle dynamics. Developed phase-field electrochemical models capture the collective behavior of electrode particles underlying the kinetically induced memory effect, establishing how the thermodynamics of the nanoscale (primary particle) level affects macroscopic electrode response under realistic conditions. Building upon these findings, an analytical model is presented, capable of capturing and predicting these effects. These results challenge established battery management strategies, opening the doors for improved characterization and optimization of fast-charging protocols, crucial in minimizing aging and heat production while enhancing energy efficiency and benefitting a wide range of battery-powered applications.

## 5.1 INTRODUCTION

The pursuit of a sustainable future has propelled lithium-ion batteries (LIBs) into a pivotal role across diverse technological realms<sup>1</sup>. Initially confined to consumer electronics, LIBs have become indispensable in electric vehicles, renewable energy storage, off-grid power systems, and grid stabilization applications. A comprehensive understanding of the chemo-physical behavior is essential to unlock the full potential of LIBs within complex and multi-component systems such as electric vehicles and grid storage.

The concept of ‘memory effect’ in batteries has gained widespread recognition in the case of Ni-Cd and Ni-metal-hydride systems, where traces of prior cycling are retained, distorting the voltage profile<sup>2-4</sup>. Interestingly, while this phenomenon has been assumed not to affect LIBs, a pivotal study by Sasaki et al.<sup>5</sup> provided first insights that this may not be true. Researchers<sup>5</sup> redefined the memory effect found in the study as ‘abnormal changes in working voltage’ and provided compelling evidence of its occurrence in materials that undergo phase separation within LIBs. Specifically, they show that when a  $\text{LiFePO}_4$  (LFP) electrode is charged to a designated state of charge (SOC), discharged, and then rapidly recharged, a small voltage peak emerges in its voltage profile. This peak is consistent among different experiments, but it is limited in magnitude and short-lived, making this, aa phenomena of purely fundamental importance, without strong practical implications. Moreover, path-dependent effects on the voltage of phase-separating materials were also notably described by Katrašnik<sup>6</sup> and Deng<sup>7</sup> who focused on the observation of a slight change in open circuit voltage at a given SOC depending on the previous discharge pulse.

The common denominator in the aforementioned studies is the possibility of explaining the phenomena through the lenses of the complex kinetic behaviour of phase-separating active materials. In the active materials that (de)lithiate following a solid-solution path, such as  $\text{LiCoO}_2$  (LCO) and  $\text{LiNi}_x\text{Co}_y\text{Mn}_{1-x-y}\text{O}_2$  (NMC), Li diffuses inside the particles uniformly such that, when the current is stopped, the concentration inside the particles quickly equilibrates, both on crystal and agglomerate levels. Thus, the system evolves without substantial intra or inter-particle heterogeneities, relying solely on the particle’s size distribution and position with respect to the electrode’s depth as a source of heterogeneities. In contrast,  $\text{LiFePO}_4$  (LFP) and  $\text{Li}_4\text{T}_3\text{O}_{12}$  (LTO) undergo phase separation during the (de)lithiation process due to their physio-mechanical properties. At a given state of charge, even under equilibrium conditions, these particles exhibit coexisting Li-poor and Li-rich phases. This fundamental difference in reaction behaviour, evident in a flat voltage plateau and an equilibrium voltage hysteresis<sup>8</sup>, is intricately linked to inter-particle heterogeneities.

The literature consistently reveals that the applied current does not uniformly distribute among all particles in the electrode; rather, a subset of active particles carries the bulk of the current while others remain unaffected in terms of (de)lithiation<sup>9–12</sup>. Moreover, the active particle fraction has been established to be proportionate to the applied rate<sup>9,10</sup>. This phenomenon stems from the size-dependent energy barrier for the nucleation of both the lithium-rich and the lithium-poor phases, favoring the reaction in smaller or nucleated primary particles<sup>13</sup>. Consequently, the reaction dynamics exhibit rate-dependent behaviour, ranging from particle-by-particle lithiation at low rates to collective lithiation at high rates, where the majority of particles are active to sustain the applied current. These dynamic systems can be mathematically described using the regular solution theory<sup>14–17</sup>, and simulated with phase-field modeling, providing a realistic and predictive depiction of the complex dynamics.

Building on this established theory, the acknowledged path dependence of electrode materials<sup>5,18–21</sup>, and previously observed memory effects<sup>5,7,18</sup>, our study reveals the presence and the origin of a strong influence of the initial applied rate on the subsequent cycling performances. Specifically, the discovered phenomenon – hereby addressed as kinetically induced memory effect – presents an increase of 50% in the fast-charging overpotential when a slow charging is applied in the initial step. Further, herein, we demonstrate this to be a general phenomenon in electrodes that exhibit a first-order phase transition upon (dis)charge. Implying operando monitoring of individual electrode crystallites, we reveal the effect of the current on the active particle fraction, while electrochemical phase-field simulations deepen the understanding of the underlying mechanism. Finally, the obtained relation between C-rates and active particles included in an analytical model capable of explain directly the observed results. We conclude by recognizing the pivotal role of preceding applied rates in shaping the voltage profile, and suggest its importance on SOC estimation and fast-charging protocols optimization in large-scale erratic systems coupled with LIBs<sup>22</sup>.

## 5.2 MEMORY EFFECT IN COMMERCIAL BATTERY ELECTRODE MATERIALS

Real-world battery utilization often results in frequent current changes. So, to better understand the behavior of commercial battery electrodes in these scenarios, we designed a protocol that is simple enough to allow interpretation and understanding but can reproduce some of the key features of multi-step charging (Fig. 5.1a). The protocol consists of three distinct steps: the writing step, the resting step, and the reading step. The writing step refers to a partial (dis)charge of the battery to 50% SOC imposed at varying rates, to induce a non-equilibrium state. Subsequently, a 1-hr resting step under open circuit conditions is applied to let the system partially relax and ensure no kinetically-induced gradients exist in the electrolytes. Finally, the

reading step completes the (dis)charge process at a fixed rate to examine the impact of the previously imposed rate on the dynamic behavior of the battery. The cell is then slowly cycled towards full charge and discharge before applying the next protocol, bringing the system to an equilibrium state and erasing the effect.

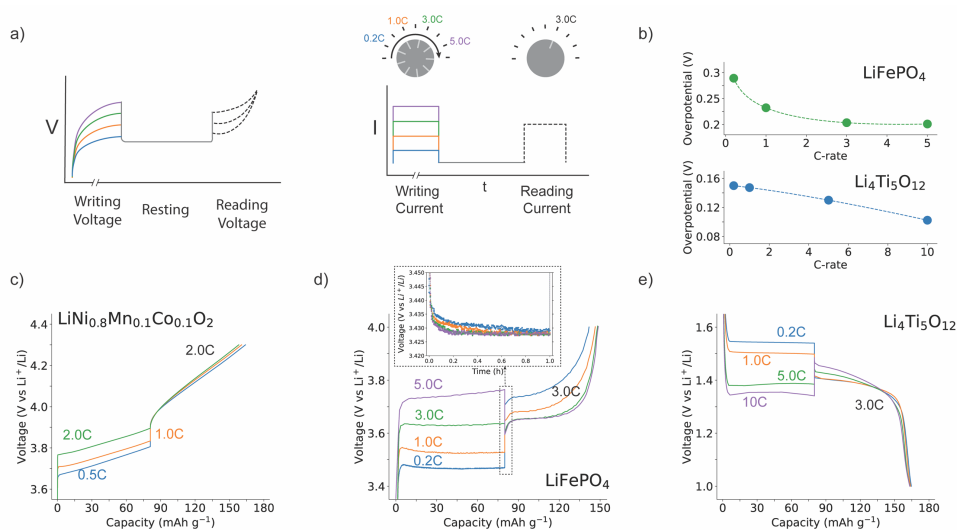


**Figure 5.1. Demonstration of the kinetically induced memory effects in phase-separating electrode materials.** a) Schematic of the memory effect protocol: the depicted colored voltage curves relate to the various currents used in the writing step; zero current is applied during the resting step, and a constant selected current is applied during the reading step. b) Overpotentials in LFP||Li and LTO||Li half-cells, measured 60 seconds into the reading step (voltage plateau) under different writing C-rates. The C-rate refers to the writing step and the equilibrium voltage of LFP and LTO are considered to be 3.42 V and 1.55 V respectively. c) Voltage profile of NMC811||Li half-cells with the charging rate of 0.5C/1.0C/2.0C in the writing step, 2.0C in the reading step (1.0C=180 mA g<sup>-1</sup>). d) Voltage profile of LFP||Li half-cells with the charging rate of 0.2C/1.0C/3.0C/5.0C in the writing step, 3.0C in the reading step (1.0C=150 mA g<sup>-1</sup>). The voltage relaxation during the resting step is also shown. e) Voltage profile of LTO||Li half-cells with the charging rate of 0.2C/1.0C/5.0C/10.0C in the writing step, 3.0C in the reading step (1.0C=175 mA g<sup>-1</sup>).

Fig. 5.1a provides a schematic view of the procedure. The results in Fig. 5.1c-e illustrate typical electrochemical responses recorded from the described writing, relaxation, and reading steps for commonly used electrode materials. Focusing on the voltage curves during the reading steps, a clear distinction emerges between the different electrode materials. As expected, in the case of LiNi<sub>0.8</sub>Co<sub>0.1</sub>Mn<sub>0.1</sub>O<sub>2</sub> (NMC811), in Fig. 5.1c, when a lower charging rate (0.5C) is applied during the writing step, the reading step shows similar overpotential and marginally higher capacity compared to writing steps performed at 1.0C or 2.0C. In contrast, the protocol on LFP||Li cell shows a different behavior (Fig. 5.1b and Fig. S1): when the writing step is conducted at 0.2C,

the reading step presents a 3.75 V plateau, whereas a writing step at 5.0C yields a plateau voltage of 3.63 V. The inverse proportionality between the applied rate and reading step overpotential can be observed clearly in Fig. 5.1b, where it is also noticeable the presence of a saturation current at 3.0C, above which no reduction in overpotential is present. Moreover, an additional 4% capacity can be charged in the 5.0C-3.0C cycle compared to the 0.2C-3.0C case. The LFP electrode, despite starting the 3.0C reading step from the same SOC and at the same open circuit voltage, shows a great difference in overpotential and capacity depending on the previously applied rate. This demonstrates that this material displays a kinetically induced memory effect, that is, it is influenced by the previous cycling history. Notably, the LTO || Li cell shows the same unexpected behavior (Fig. 5.1e) although no saturation current was observed within the range of C-rates tested (Fig. 5.1b). The origin of this difference can be found in the different reaction kinetics between LFP and LTO (Fig. S15 and S22). Moreover, the same behavior can be also observed when a similar protocol is applied in other conditions: applying different reading rates (Fig. S1), during discharge of an LFP || Graphite full cell (Fig. S2), and at various resting times (Fig. S3).

5

The distinguishing factor between LFP, LTO, and NMC is the presence of a first-order phase transition upon (de)lithiation for the first two: materials undergoing a first-order phase separation are susceptible to the kinetically induced memory effect. To confirm this hypothesis, more materials displaying a first-order phase transition, such as  $\text{LiNi}_{0.5}\text{Mn}_{1.5}\text{O}_4$  (LMNO),  $\text{LiMn}_{0.4}\text{Fe}_{0.6}\text{PO}_4$  (LMFP), and  $\text{Na}_3\text{V}_2(\text{PO}_4)_3$  (NVP) were evaluated using similar protocols, also displaying the same phenomenon (Figs. S4-S6). This observation aligns with previously documented memory effects on phase-separating materials<sup>5,6</sup>, here demonstrating the great impact on realistic high-rate conditions. Altogether, these results suggest a broad and general phenomenon that highlights the crucial necessity for more extensive investigations into the dynamic response of these materials under diverse operating conditions.

### 5.3 MONITORING THE PHASE TRANSITION IN INDIVIDUAL GRAINS

In order to better describe the kinetically induced memory effect, we investigated the impact of applied rates on the active particle population throughout different stages of the test protocol. Given the extensive knowledge on it and its relevance as commercial material, LFP was selected as the representative phase-separating material for this study, with the primary objective of quantifying the active particle fraction during variable reading rates. A unique method to monitor the phase transformation of individual crystallites (primary particles) during operando conditions in pouch cells is microbeam X-ray diffraction<sup>10,11</sup>.

MONITORING THE PHASE TRANSITION IN INDIVIDUAL GRAINS

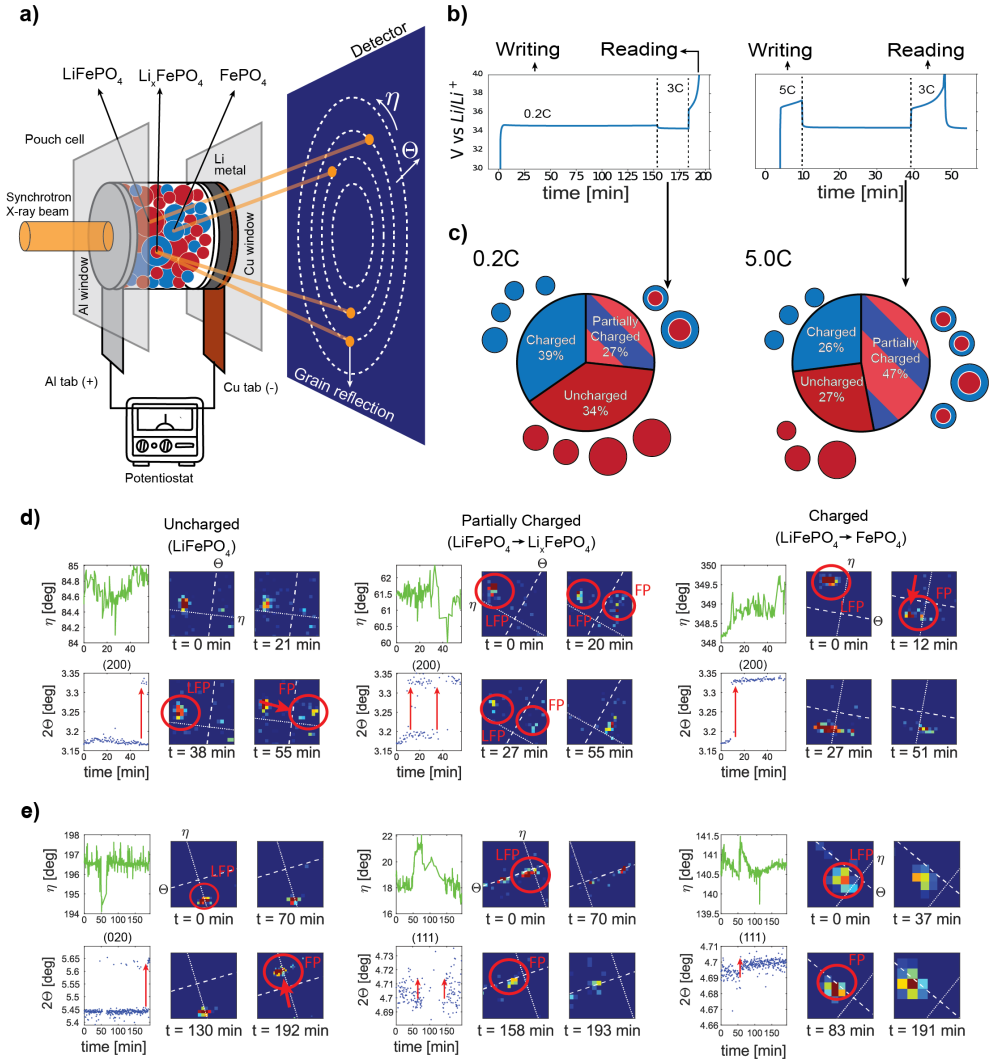


**Figure 5.2. Microbeam x-ray diffraction analysis.** a) Schematic of the microbeam x-ray diffraction experimental setup. b) Measured voltage evolution during the microbeam x-ray diffraction operando experiments: 0.2C-3.0C and 5.0C-3.0C cycles, respectively. c) Fractions of particles uncharged ( $\text{LiFePO}_4$ , red), charged ( $\text{FePO}_4$ , blue) and partially charged ( $\text{Li}_x\text{FePO}_4$ , striped) at the end of the resting writing steps of the 0.2C-3.0C and 5.0C-3.0C cycles, respectively. d) Evolution of the (200) reflection during the 5.0C-3.0C cycle for three different tracked grains. e) Evolution of the (111) and (020) reflections during the 0.2C-3.0C cycle for three different tracked grains. The left graphs show the evolution of the maximum intensity point for the selected grain reflection along the  $2\theta$  and  $\eta$  directions. The heatmaps show the detected grain reflection at different times.

This technique implies an X-ray beam of size comparable to the particle size ( $\sim 1 \mu\text{m}$ ), obtaining single-grain reflections instead of powder averages (Fig. 5.2a). Observing the evolution of their  $2\theta$  values it is possible to identify the crystallite's composition (observing the  $2\theta$  angle) and orientation (monitoring the  $\eta$  values), during operando conditions. Approximately 100 reflections, representing an equal amount of  $\text{LiFePO}_4$  crystallites, were tracked during the electrochemical protocol with the same methodology applied by van Hulzen<sup>10,11</sup>. From hereon we refer to one crystallite as one particle. The anticipated first-order phase transition between  $\text{LiFePO}_4$  (LFP) and  $\text{FePO}_4$  (FP) is observed through the disappearance of the LFP reflection and the appearance of the FP reflection at a different  $2\theta$  (Fig. 5.2d-e). Particle categorization is established on the observed shift of the  $2\theta$  reflections at the conclusion of the writing step. As shown in Figs 5.2d-e, charged particles are identified based on the exclusive presence of the peak associated with the FP phase during the resting step; partially charged particles exhibit both the FP and LFP peaks, indicating partial delithiation; uncharged particles retain an unaffected LFP phase and are activated only during the subsequent reading step. The sudden shift in  $2\theta$  value indicates a fast delithiation, while the presence of two parallel  $2\theta$  values at the same  $\eta$  indicates a slow delithiation, occurring through phase separation.

Two different charging protocols were applied to the same battery: a protocol where the writing step was conducted at a high charging rate (5.0C) and one where it was conducted at a low charging rate (0.2C). In both cases, the battery was rested for 30 minutes, and the charging was completed at 3.0C (Fig. 5.2b). After both protocols a 0.1C memory-erasing discharge was conducted, so that the batteries differ only in the charge rate during the writing step. Analyzing the microbeam results provides direct insights into the role of the active particle population in the kinetically induced memory effect under operando conditions (Fig. 5.2d). Specifically, under a 0.2C charge rate (writing step), a particle-by-particle lithiation mechanism is observed, where few particles are rapidly delithiating at each given time. Focusing on the electrode's state after the completion of resting step, we found 39% of the particles being charged (full phase transition from LFP to FP) and 27% nucleating the lithium-poor phase without completing the charge (i.e., the coexistence of LFP and FP phases), while the rest remain uncharged (LFP phase). This is in line with the expected mosaic arrangement composed by either lithiated or delithiated crystals. Subsequently, during the 3.0C reading step, the remaining particles (61%) are charged by the imposed current. In contrast, when subjected to a 5.0C rate during the writing step, a lower fraction of particles (26%) achieves full charge during this step, while the majority (47%) enter the resting period partially charged, in a phase-separated state. The subsequent 3.0C current can then be sustained by a higher fraction of particles (74%) being either partially charged or uncharged. These findings, summarized graphically in Fig. 5.2c, underscore the complex relationship between charging rates of the active particle population, shedding light on the dynamics of (de)lithiation processes within the electrode.

The kinetically induced memory effect can so be explained by the difference in multi-particle dynamics during the initial step. Specifically, under high applied rates, the current is supported by a greater number of particles (increased active population), resulting in a higher fraction of nucleated (phase-separated) particles at the 50% SOC. These nucleated particles result more accessible to the system during the subsequent reading step, having already surmounted the nucleation energy barrier. Notably, the phase separation persists during the resting period.

Conversely, under low applied writing rates the electrode reaches 50% SOC following a particle-by-particle delithiation, so the majority of the particles result either uncharged (lithiated) or completely charged (delithiated). In the subsequent reading step, the applied current is sustained by a reduced number of particles, i.e. the particles that are either partially charged or uncharged. Moreover, the uncharged particles need to overcome the nucleation barrier. The combination of these factors leads the higher overpotentials as shown in Fig 5.1b.

Previous work<sup>10,11,23</sup> described the formation of a metastable solid solution phase transition in LFP, such that, during a fast (dis)charge, the particle cannot proceed toward phase separation due to the mismatch in characteristic times between reaction and diffusion kinetics. In contrast, no solution phase transition at 5C was observed within this study, which can be attributed to a fundamental distinction in particle shape. Specifically, leveraging the b crystalline direction for 1D fast diffusion kinetics, platelet-shaped LFP particles demonstrate a reaction-limited behavior. On the other hand, the spheroidal commercial particles employed in this work (Figs. S7-S9), characterized by higher defect concentrations and, consequently, quasi-isotropic diffusivity, exhibit an effectively diffusion-limited behavior resulting in a more favorable phase separation. Moreover, the presence of the kinetically induced memory effect in a wide set of phase-separating materials (Fig. 5.1e and Figs. S4-S6) shows that the presence of a metastable solid solution transition in LFP is not a decisive factor in explaining the observed memory effect.

## 5.4 ELECTROCHEMICAL MODELING OF THE MEMORY EFFECT

To further unravel and quantify the underlying mechanisms responsible for the kinetically induced memory effect, we implied electrochemical porous electrode models extended to encompass the thermodynamics of phase-separating active particles through phase-field modeling<sup>14</sup>. Traditional models<sup>24</sup> consider uniform diffusion and fit the open circuit voltage from experimental data, on the contrary phase-field models account for size-dependent nucleation barriers<sup>25–27</sup> and derive the chemical potential from the free energy landscape<sup>17</sup>. This technique can predict the behavior of phase-separating active battery materials at both the single-particle and multi-particle levels under various operating conditions<sup>7,9,15,17,28–34</sup>.

## 5 | KINETICALLY INDUCED MEMORY EFFECT IN LI-ION BATTERIES

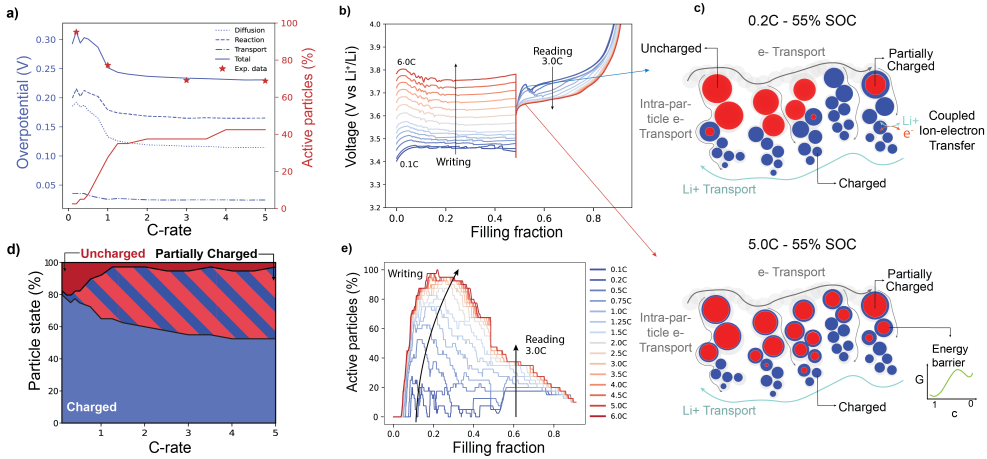


**Figure 5.3. Electrochemical modeling results.** a) Deconvoluted average overpotentials and active particle population at the onset of the reading step vs. writing rate (see Method section for further details). b) Simulated voltage profiles for the memory protocols of LFP at writing rates varying from 0.1C to 6.0C and fixed reading rate of 3.0C. c) Li-ion distribution in a randomly selected set of representative particles of the phase-field simulation at 55% SOC during the reading step for the case of 0.2C and 5.0C writing rates. Blue corresponds to the FP phase, and red corresponds to the LFP phase. The transport phenomena considered in the model are also shown. d) Fraction of particles in the charged ( $\text{FePO}_4$ ), partially charged ( $\text{Li}_x\text{FePO}_4$ ), and discharged ( $\text{LiFePO}_4$ ) states at 55% SOC at different writing rates. e) Evolution of the active particle population during the memory protocols for the simulation presented in b. A particle is considered active if its average lithiation state is between 15% and 85%.

The coupling between phase-field and electrochemical modeling can also fit experimental voltage curves<sup>30,35</sup>, provide an accurate picture of the active particle population<sup>9</sup>, and generate realistic operando X-ray diffractograms<sup>17</sup>. Considering the capabilities of this modeling technique, we utilize the software MPET<sup>14</sup> to build an LFP electrode model capable of reproducing the experimental results. In particular, we consider spherical diffusion-limited particles that react with the surrounding electrolyte following the couple ion-electron transfer theory<sup>36</sup>, and account for electronic transport losses between the particles (see Method section and Supplementary information for further details).

The simulated results for LFP in Fig. 5.3 unfold the kinetics of the system during the memory protocol, revealing the effect of a range of writing rates on the reading overpotentials. The voltage curves in Fig. 5.3b are in good agreement with the experimental results (Fig. S11), showing the correct voltage at the onset of the reading steps, the kinetically induced capacity losses, and plateauing at high rates. It is noteworthy to specify that the model does not consider the evolution of the charge transfer resistance of the Li metal electrode or self-discharge

mechanisms. The simulations, by matching the experiments solely considering the phase separation mechanism, also confirm it to be the main responsible of the memory effect.

By analyzing the simulation data, the origin of the total overpotential can be separated into its components (Fig. 5.3a): both the reaction and diffusion overpotentials at the onset of the reading step, are inversely proportional to the applied writing rate, whereas the transport overpotential is marginally affected by the writing rate due to the low loading of the tested sample ( $2 \text{ mAh cm}^{-2}$ ).

Fig. 5.3e illustrates the complete multi-particle dynamics by showing the evolution of the active particle population during the memory protocol. At low rates, the system maintains a low active particle population during the writing step, following a particle-by-particle lithiation scheme, reaching the reading step with a few particles which are internally phase-separated. The system is then forced to overcome the nucleation barrier with a reduced available reactive area. As the writing rate increases, the system reacts more homogeneously, accommodating higher currents towards more particles. Due to the wide difference in particle sizes (Figs. S8-S9), the smaller particles will be delithiated faster such that the active particle population starts to decrease before reaching 50% SOC. The kinetic is therefore dominated by the larger-sized particles, which are the system's major current drivers. This imposes a limit on the maximum active particle population achievable during a (dis)charge and explains the saturation of the kinetically induced memory effect at rates higher than 3.0C. After the resting step, where we observe a small drop in active particle fraction due to intra-particle Li exchange (Fig. 5.3e), the available surface area of the phase-separated particles will accommodate the reading step current. Additionally, in the supplementary results we explore the effect of the resting step on the active particle population (Fig. S20). It is important to note that while the overpotential saturation occurs at 3.0C for LFP, the LTO electrode does not exhibit saturation even at 10.0C (Fig. S13). Despite the similar particle size, the maximum active particle population, and its related saturation current, depend on both particle size and exchange current density. The significant difference in reaction kinetics between the two materials accounts for the distinct behavior (Fig. S22). This highlights the capability of the memory protocol to provide insights into charge transfer resistance in phase-separating materials. To further clarify this relationship, in the supplementary results, we present the influence of particle size distribution and exchange current density on active particle population dynamics (Fig. S15) and saturation current (Fig. S16).

Fig. 5.3d depicts the dynamics of the system in the same fashion as described for the micro-beam data, i.e. an increase in writing rate leads to a greater fraction of particles being phase-separated at the onset of the reading step. In particular, the 5.0C writing rate leads to 46% of the particles being phase-separated and only 2% of them being fully delithiated, while the 0.2C writing rate only achieves 5% and 12% of phase-separated and delithiated particles, respectively. Finally, Fig. 5.3b visually shows the particle concentration at the beginning of the reading step for the two C-rates explored: 0.2C and 5.0C. The former presents a mosaic lithiation scheme

where most particles are found either completely uncharged or charged due to the particle-by-particle lithiation dynamics. In particular, smaller particles are completely charged due to their lower energy barrier for nucleation and faster diffusion times, while bigger particles are mostly uncharged. The 5.0C case is instead mostly composed of phase-separated particles, with only a minority of smaller particles being completely charged.

The thermodynamic interpretation of the phenomenon also clarifies why solid solution materials cannot experience a kinetically induced memory effect. As the electrochemical model demonstrates (Fig. S14), the combination of Fickian diffusion and monotonic chemical potential of solid solution materials impose a fast relaxation of the system: the single particle is rapidly homogenized by internal diffusion, and the difference between the surface concentrations, induced by the previous fast kinetics, drives an inter-particle reaction that quickly homogenizes the system. In phase-separating materials, instead, once the particle is nucleated, both phases will be characterized by similar chemical potentials, and the driving force for multi-particle equilibration is strongly reduced. The origin of this kinetic response is also shown to be general and reproducible in other phase-separating materials as shown by the simulation performed with the  $\text{Li}_4\text{Ti}_5\text{O}_{12}$  model<sup>15</sup> (Fig. S13).

## 5.5 ANALYTICAL APPROXIMATION

Although a complete description of the phenomenon requires solving a set of partial differential equations, this approach is often impractical. Here, we present an analytical approximation that captures the key trends using simplified relationships. For a uniform particle size distribution, the reactive surface area is proportional to both the fraction of active particles during the reading step ( $f$ ) and the total reactive area ( $S$ ). Given the exchange current density at the particle surface ( $j_0$ ), the reaction overpotential ( $\eta_{rxn}$ ) can be expressed as a function of  $f$  and imposed reading current  $i_R$ . Assuming Butler-Volmer reaction kinetics we obtain:

$$\eta_{rxn} \cong \frac{k_B T}{e} \sinh^{-1} \left( \frac{i_R}{2 j_0 S f} \right) \quad (5.1)$$

In addition to reaction overpotential, the diffusion overpotential ( $\eta_{diff}$ ) can be approximated by the Nernst relation  $\eta_{diff} \sim \ln(c_s/c_{eq})$ , where  $c_s$  and  $c_{eq}$  are the surface and equilibrium concentration of the delithiated phase, respectively. Approximating the ionic diffusion with a mass transfer coefficient  $k_m$ , we can also obtain a relation between  $f$  and  $\eta_{diff}$ :

$$\eta_{diff} \cong \frac{k_B T}{e} \ln \left( 1 + \frac{i_R}{e k_m c_0 S f} \right) \quad (5.2)$$

These equations hold under the assumption that the current regime during the reading step activates all remaining particles (see Method section of Supplementary Information). Finally, an empirical relation, based on a sigmoid function, is used for linking  $f$  to the writing C-rate:

$$f \approx \frac{f_{max}}{1 + e^{-w*(C_{rate}-b)}} \quad (5.3)$$

where the maximum active particle fraction  $f_{max}$ , the weight  $w$  and the bias  $b$ , are fitted based on the phase-field results. This relation is admittedly difficult to obtain analytically, since it depends on particle size distribution, exchange current density and the state of charge.

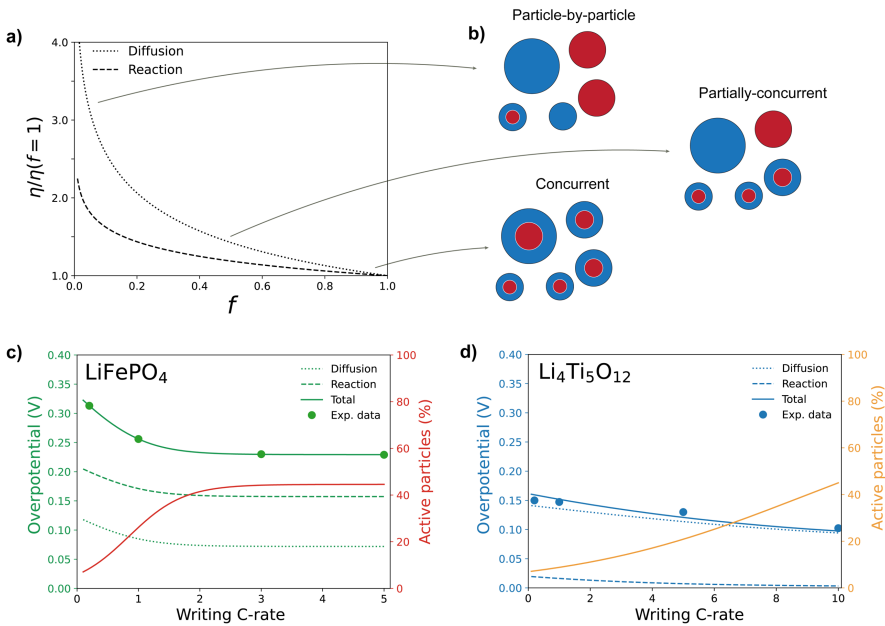


**Figure 5.4.** Analytical solution for the relation between the writing C-rate and reaction and diffusion overpotentials. a) Scaling of the reaction and diffusion overpotentials as a function of active particle fraction. The overpotentials are normalized w.r.t. the values at  $f = 1$ . Arbitrary parameters were chosen within reasonable values (close to fitted values). b) Schematic of different phase arrangements of particles corresponding to varying active particle fractions. c) Fit of the experimental overpotential for the  $\text{LiFePO}_4$  | Li half-cell. d) Fit of the experimental overpotential for the  $\text{Li}_4\text{Ti}_5\text{O}_{12}$  | Li half-cell.

When plotted (Fig. 5.4a), the resulting relations show the significant importance of the active particle population on reaction and diffusion overpotentials. For instance, the diffusion overpotential can increase by a factor of four if the active particle population is reduced. The analytical model is then used to fit the experimental data presented in Fig. 5.1. By allowing  $w$  and  $b$  to vary within realistic bounds (informed by the phase-field model), the relation between the writing C-rate and active particle fraction can be captured accurately.

The precision in the fitting, of both the LFP and LTO cases (Fig. 5.4c,d), showcase the use of the derived approximation for predicting and understanding the kinetically induced memory effect. The effective diffusivity of LTO and LFP are comparable, as well as their particle size, resulting in similar activation-induced overpotential. The slower reaction kinetics of LFP is the primary reason for its larger overpotential difference between slow and fast charging. Moreover, the fit also predict the relation between active particle population and C-rate in good agreement with the phase-field results. This and the possibility itself to fit the data with the provided analytical model, further validates the conclusion that the previously activated particles are responsible for the difference in overpotentials.

## 5.6 CONCLUSIONS

This study shows and explains a general phenomenon affecting all phase-separating electrode materials: a strong inverse correlation between the initial applied (dis)charging rate and the resulting overpotential during a subsequent step, thus a kinetically induced memory effect. The origin of this behavior is herein described from a thermodynamic perspective (Fig. 5.5).

If lower rates are employed during the writing step of the protocol (e.g. 0.2C) the reaction primarily occurs for smaller particles, characterized by faster kinetics and a lower nucleation barrier. The electrode results so composed mostly of either fully lithiated or fully delithiated particles. Greater overpotential is so required to activate bigger-size particles during the reading step. Higher charging rates (e.g. 5.0C) spread the current to multiple particles, leading to a set of phase-separated metastable particles. The inter-particle lithium exchange is delayed by the coexistence of the same chemical potential of the two phases and, when the reading current is applied, the phase-separated particles are electrochemically more active since the nucleation barrier has vanished. This allows the system to achieve the same reading rate (e.g. 3.0C) with lower overpotentials. From an energy perspective, part of the additional energy supplied to the system during a high-rate writing step is stored within the phase boundaries. Consequently, less additional energy is required to drive the current during the reading step. This nuanced interplay between current rates and phase-separation dynamics sheds light on the crucial role of activation barriers and population dynamics in governing the electrochemical behavior of these systems.

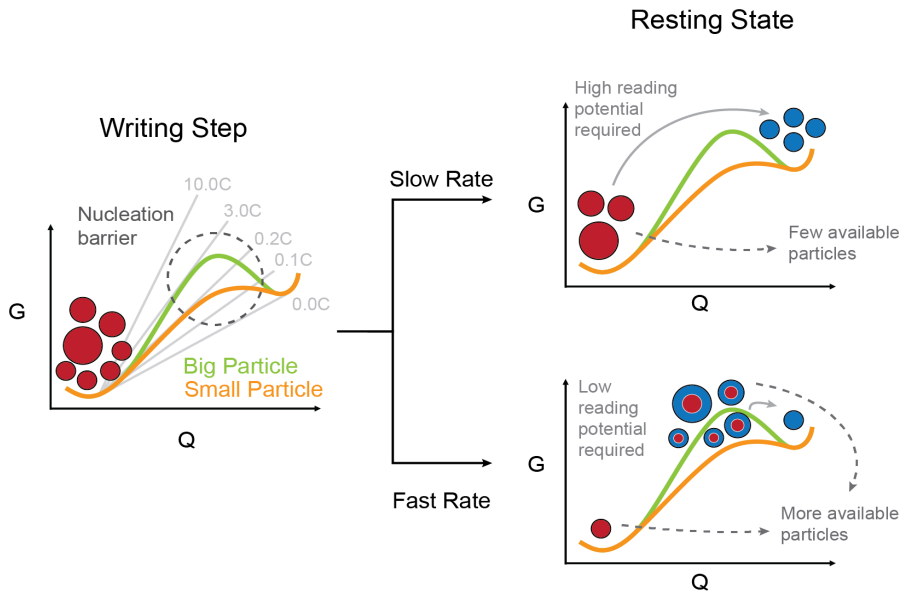


**Figure 5.5. Schematic summary of the origin of the kinetically induced memory effect.** The thermodynamic origin of the memory effect in terms of free energy ( $G$ ) evolution during slow and fast writing steps is described. The size-dependent energy barriers are considered<sup>26</sup>. The common energy tangent is followed at low rates, increasing the rate manifest in a deviation from the minimum energy path. Lower rates are so capable of overcoming the energy barrier for small particles, while higher rates allow particles of greater size to reach a metastable higher energy configuration. The resulting difference in energy landscape is represented with red particles as fully lithiated (low energy), blue particle as fully delithiated (high energy) and bi-colored particles as phase separated. Energy and capacity ( $Q$ ) are purely representative and not at scale.

Multiple studies, primarily focusing on LFP, assessed the non-trivial multi-particle and single-particle reaction path that phase-separating materials follow during (de)intercalation<sup>38–42</sup>. Early descriptions relied on a domino-cascade model, suggesting a particle-by-particle (de)lithiation process<sup>42</sup>. However, subsequent experimental<sup>9,10</sup> and computational<sup>9,15</sup> studies have provided compelling evidence that the active particle population is intricately linked to the applied rate, challenging the initial univocal interpretation. Building on these findings, other works focused on the investigation of the metastable solid solution<sup>25,26,28,29</sup> (characteristic of LFP but not universal to all phase-separating materials) and the relaxation behavior<sup>7,43,44</sup>, providing a foundation for the understanding of current-induced phenomena. Specifically, Deng and coworkers<sup>7</sup> characterized the unexpected change in overpotential during quasi-equilibrium discharge of LFP following a high-rate current pulse, revealed by the study of Katrašnik et al.<sup>6</sup>, through X-ray microscopy and phase-field modeling on reaction-limited micro-platelet particles. Notably, offering valuable insights, they did not quantitatively assess the strong consequences of these pulses on the subsequent high-rate operating conditions.

Our protocol, closer to commercially relevant rates, reveals the impact of these non-equilibrium phenomena on typical battery operations. The thermodynamic interpretation of it (Fig. 5.5), obtained by combining modeling and operando monitoring of individual particles, opens the doors to improved protocol design for both deeper fundamental understating and battery management strategies.

Robust indication of the multi-particle dynamics can be obtained by combining the multi-step protocol and the developed analytical model (Eq. 5.1-5.3). By collecting data from a set of writing currents, we use the presented relations to obtain the active particle population as function of C-rate. This offers valuable insights into optimal charging rates able to activate the majority of particles within the electrode.

While this study focuses on half-cells charging for better fundamental understanding, we also prove the described memory effect in commercially relevant LFP | Graphite full cells (Fig. S2). Similarly, the previous applied current influence the subsequent overpotential, but the role of the Graphite hinders its presence when a higher rate is applied during the reading step. The kinetically induced memory effect in full cells is so dependent on the kinetically limiting electrode and therefore on a wide range of manufacturing parameters. Based on these results, we also speculate the presence of the memory effect in an LTO | NMC cell. In fact, LTO electrodes reliably show the kinetically induced memory effect, while NMC's kinetics is not influence by the previous current rate. The combination of these materials, important in high-power applications, is therefore a candidate for the exploitation of the discovered phenomenon. Since the discovered effect arises from the particle-level heterogeneities, its magnitude can be reduced in high-capacity electrodes, where the ionic or electronic transport along the electrode thickness are the limiting factors (Fig. S19). In the case of next-generation battery materials, such as LMNO, LMFP and NVP<sup>45</sup>, the kinetically induced memory effect can instead become a tool for characterizing specific regions of the capacity that exhibit phase separation (Fig. S4-S6).

Moreover, our study underlines the significant implications that may arise from oversimplifying the treatment of phase-separating materials, both computationally and experimentally. Although single-particle models have demonstrated their ability to predict constant current kinetic<sup>46</sup>, they fall short in capturing behaviors intrinsically linked to the active particle population and phase separation. In fact, the relation between SOC and kinetic properties is not univocally definable. At the same SOC the electrode can be composed of different ratios of phase-separated and homogenous particles depending on the previous applied rate. As shown here, these phenomena have a significant effect on the voltage profile. So that its prediction and the subsequent management and optimization of battery operations can be misled by oversimplified models<sup>24,47-49</sup>. It becomes so critical, when modeling phase-separating materials, to account for multi-particle dynamics and phase-separation kinetics to correctly predict voltage and current responses in complex protocols (Fig. S17-S18). Thus, this study proves the necessity of phase-field methods

for improving state-of-the-art battery management strategies<sup>50</sup>. We also speculate SOC estimation algorithms could be misled by these memory effects, if not properly included in the equivalent circuit representation. To apply these findings to fast control-oriented numerical tools, we suggest coupling phase-field models and advanced equivalent resistors. The former would be initially used to capture the relation between C-rate, SOC and active particle population (Eq. 3), the latter can then be modelled based on the analytical equations provided in this work (Eq. 1, 2). Furthermore, it is shown how multi-step protocols can maximize the active particle population. This can directly translate into the reduction of intra-particle stresses, side reactions, heat generation, and energy consumption. To fully deploy this effect in real-world scenarios, future studies should focus on exploiting this phenomenon via numerical optimization and clarifying its impact at multiple SOC, temperatures, and rates.

Finally, we show how the continual pursuit of fundamental knowledge in the field of batteries can have direct implications on current technology, leading to better protocols for battery management systems, improving battery performance, energy efficiency, and lifespan, ultimately contributing to advancing battery technologies and the broader field of energy storage systems.

## MATERIALS AND METHODS

### Materials

LiFePO<sub>4</sub>, composed by single crystal particles, was obtained from Leneng Technology for which the cathodes were prepared by mixing LiFePO<sub>4</sub> material, poly(vinylidene difluoride) (PVDF, MTT) binder and Super P (Alfa Aesar) conductive carbon in a weight ratio of 92:4:4. The resulting slurry was cast on the Al foil then dried at 60 °C for 6 h, followed by drying overnight at 120 °C in a vacuum oven. Li<sub>4</sub>Ti<sub>5</sub>O<sub>12</sub> anode and LiNi<sub>0.5</sub>Mn<sub>1.5</sub>O<sub>4</sub> were purchased from MTT Corporation and used as received. LiNi<sub>0.8</sub>Co<sub>0.1</sub>Mn<sub>0.1</sub>O<sub>2</sub> (NMC811) was synthesized using coprecipitation method: A certain amount of alkaline aqueous solution (NH<sub>4</sub>OH and NaOH) was poured into deionized water (1.5 L) to form the base solution in a tank reactor under continuous stirring. Then, a 2 M solution of NiSO<sub>4</sub>·6H<sub>2</sub>O, CoSO<sub>4</sub>·7H<sub>2</sub>O, and MnSO<sub>4</sub>·H<sub>2</sub>O with a molar ratio of 8:1:1 and an aqueous solution of 5 M NH<sub>4</sub>OH and 10 M NaOH were added into the base solution in the tank reactor with a steady rate of 8 mL min<sup>-1</sup>. The coprecipitation temperature was controlled at 50 °C, and the pH value was maintained at approximately 11 by NH<sub>4</sub>OH with a stirring speed of 500 rpm under nitrogen atmosphere. The coprecipitated Ni<sub>0.8</sub>Co<sub>0.1</sub>Mn<sub>0.1</sub>(OH)<sub>2</sub> precursor was prepared, which was subsequently washed by deionized water and ethanol for four times and dried in a vacuum at 120 °C for 24 h. The apparent and tap density of Ni<sub>0.8</sub>Co<sub>0.1</sub>Mn<sub>0.1</sub>(OH)<sub>2</sub> precursors were measured at 1.88 g cm<sup>-3</sup> and 2.06 g cm<sup>-3</sup>, respectively. For preparation of NMC811 materials, the as-obtained precursor was mixed with LiOH·H<sub>2</sub>O at a molar ratio of 1:1.03; then heated to 500 °C for 5 h and subsequently calcined at 780 °C for 12 h in oxygen atmosphere. After cooling naturally, the material was immediately placed into an Ar-filled glovebox to prevent being exposed to moisture. The NMC811 electrodes were prepared by mixing active material, Super P and PVDF binder in the mass ratio of 90: 5: 5 in N-methyl-2-pyrrolidone (NMP) solvent and cast on Al foil and then dried at 60 °C for 6 h, followed by drying in a vacuum oven at 120 °C overnight. X-ray diffraction pattern demonstrates the pure phase of this prepared NMC811 material. Battery-grade lithium hexafluorophosphate (LiPF<sub>6</sub>), ethylene carbonate (EC), diethyl carbonate (DEC), fluoroethylene carbonate (FEC) were purchased from E-Lyte innovations, and subsequently dehydrated using a 4 Å molecular sieve (Sigma-Aldrich).

### Electrochemical measurements

Electrochemical cycling tests of all batteries were based on CR2032 coin cells assembled in an Ar-filled glove box (H<sub>2</sub>O < 0.1 ppm, O<sub>2</sub> < 0.1 ppm) with Celgard 2500 separators and tested at room temperature, unless stated otherwise. The electrolyte used consisted of 1M LiPF<sub>6</sub> in EC/DEC (1:1 in volume) with 5% FEC. 70 μL electrolytes were injected into each coin cell for

comparison. All coin cells were tested using multi-channel battery testing systems (Land CT2001A or Lanhe G340A). 15.6 mm diameter lithium metal foils with 250  $\mu\text{m}$  thickness were used as both the working and counter electrodes. Electrochemical cycling performance of the electrodes (12 mm diameter) are all tested with an areal capacity of 2  $\text{mAh cm}^{-2}$  with lithium metal foils as counter electrode. All the cells underwent to a formation cycle composed by two 0.1C (0.2  $\text{mA cm}^{-2}$ ) charge-discharge cycles.

## Materials characterization

Morphologies of electrodes were measured on a cold field scanning electron microscope (SEM, HITACH-S4800, SU8010). XRD was performed using a Bruker D8 Advance diffractometer equipped with a Cu  $K\alpha$  radiation source ( $\lambda_1 = 1.54060 \text{ \AA}$ ,  $\lambda_2 = 1.54439 \text{ \AA}$  at 40 kV and 40 mA). Rietveld refinement of the XRD was carried out using the General Structure Analysis System software with the EXPGUI software interface. TEM experiments were performed on a STEM (JEM-ARM300F, JEOL) operated at 300 kV with a cold field emission gun and double Cs correctors. The microscope was equipped with Gatan OneView and K2 cameras for image recording. STEM images were taken with an electron dose rate of 50–500  $\text{e}^- \text{ \AA}^{-2} \text{ s}^{-1}$  with an exposure time of several seconds for each image, with a built-in drift correction function in GMS3 using the OneView and K2 camera.

## Micro-beam diffraction experiments

For the LFP microbeam diffraction experiment, a similar setup was used as described in van Hulzen et al.<sup>10</sup>. The LFP || Li half-cells were prepared as pouch cells and fixed in a clamp with a conic opening on both sides to allow the X-ray beam to pass through. A monochromatic X-ray beam with wavelength 0.2852  $\text{ \AA}$  (energy 43.47 keV) and spot size of  $\sim 1$  micron was used to register the diffraction patterns on an Eiger2 X CdTe 4M detector with 2068 x 2162 pixels. To increase the number of grains in Bragg condition the sample was rotated along the z-axis (perpendicular to the beam). For all measurements the total rotation was  $5^\circ$  with a step size of  $0.05^\circ$  and an exposure time of 0.05 seconds, collecting 101 frames in about 6 seconds. To mitigate beam damage four locations were probed by rotation resulting in a time resolution of about 30 seconds per location. A detailed description of the provided data can be found in Supplementary information. The raw data were analyzed following the methodology outlined in the Methods section of van Hulzen et al.<sup>10</sup>.

## Electrochemical phase-field modeling

The physics-based electrochemical model was developed by expanding on the open-source software MPET<sup>14</sup>. The single particle of LFP was simulated by considering diffusion-limited spherically symmetric one-dimensional particle axis so that the local Li concentration  $c$  evolves accordingly to

$$\frac{dc}{dt} = \nabla \cdot \left( \frac{D}{k_B T} c \nabla \mu \right) \quad (5.4)$$

where  $D$  is the concentration-dependent diffusivity and  $\mu$  is the phase-field chemical potential. The particle's reaction rate  $R$  between the particle of concentration  $c$ , and the electrolyte of concentration  $c_{Li^+}$  is modeled through the Coupled Ion Electron Transfer Theory<sup>36,51</sup>, specifically the electron-coupled ion transfer approximation:

$$R = k_0 \left( 1 - \frac{c}{c_{max}} \right) \left( \frac{c_{Li^+}}{1 + e^{\eta_f/k_B T}} - \frac{c/c_{max}}{1 + e^{-\eta_f/k_B T}} \right) \operatorname{erfc} \left( \frac{\frac{\lambda}{k_B T} - \sqrt{\left( \frac{\eta_f}{k_B T} \right)^2 + 1} + \sqrt{\frac{\lambda}{k_B T}}}{2 \sqrt{\frac{\lambda}{k_B T}}} \right) \quad (5.5)$$

where  $k_0$  is the exchange current density,  $\eta_f$  is the formal overpotential and  $\lambda$  is the reorganization energy for the electron transfer. The electrode is discretized into sub-volumes, each consisting of 8 particles of varying sizes following the experimental particle size distribution. The electrode-level ionic and electronic losses were modeled implying porous electrode theory<sup>16</sup>. Moreover, wiring losses within the sub-volume were considered, similar to the work of Li et al.<sup>9</sup>. A more detailed description of the model can be found in Supplementary information.

The analysis of the overpotentials was defined as follows: the reaction overpotential of a single particle is the overpotential driving the reaction, and it corresponds to the difference between the surface chemical potential of the particle and the electrolyte chemical potential at a specific electrode depth; the diffusion overpotential is defined as the difference between the surface chemical potential and the equilibrium potential of the material at the that average composition; the transport overpotential is the difference between the electrochemical potential of Li ions at the Li-metal electrolyte interface and the electrochemical potential at the current collector. The total overpotential is the difference between the equilibrium chemical potential of the LFP plateau and the potential at 55% SOC.

## REFERENCES

1. Goodenough, J. B. & Park, K.-S. The Li-Ion Rechargeable Battery: A Perspective. *J. Am. Chem. Soc.* **135**, 1167–1176 (2013).
2. Barnard, R., Crickmore, G. T., Lee, J. A. & Tye, F. L. The cause of residual capacity in nickel oxyhydroxide electrodes. *J. Appl. Electrochem.* **10**, 61–70 (1980).
3. Huggins, R. Mechanism of the memory effect in “Nickel” electrodes. *Solid State Ion.* **177**, 2643–2646 (2006).
4. Sato, Y., Takeuchi, S. & Kobayakawa, K. Cause of the memory effect observed in alkaline secondary batteries using nickel electrode. *J. Power Sources* (2001).
5. Sasaki, T., Ukyo, Y. & Novák, P. Memory effect in a lithium-ion battery. *Nat. Mater.* **12**, 569–575 (2013).
6. Katrašnik, T. *et al.* Entering Voltage Hysteresis in Phase-Separating Materials: Revealing the Electrochemical Signature of the Intraparticle Phase-Separated State. *Adv. Mater.* 2210937 (2023) doi:10.1002/adma.202210937.
7. Deng, H. D. *et al.* Beyond Constant Current: Origin of Pulse-Induced Activation in Phase-Transforming Battery Electrodes. *ACS Nano* **18**, 2210–2218 (2024).
8. Dreyer, W. *et al.* The thermodynamic origin of hysteresis in insertion batteries. *Nat. Mater.* **9**, 448–453 (2010).
9. Li, Y. *et al.* Current-induced transition from particle-by-particle to concurrent intercalation in phase-separating battery electrodes. *Nat. Mater.* **13**, 1149–1156 (2014).
10. van Hulzen, M., Ooms, F. G. B., Wright, J. P. & Wagemaker, M. Revealing Operando Transformation Dynamics in Individual Li-ion Electrode Crystallites Using X-Ray Microbeam Diffraction. *Front. Energy Res.* **6**, 59 (2018).
11. Zhang, X. *et al.* Direct view on the phase evolution in individual LiFePO<sub>4</sub> nanoparticles during Li-ion battery cycling. *Nat. Commun.* **6**, 8333 (2015).
12. Bai, P. & Tian, G. Statistical kinetics of phase-transforming nanoparticles in LiFePO<sub>4</sub> porous electrodes. *Electrochimica Acta* **89**, 644–651 (2013).
13. Cogswell, D. A. & Bazant, M. Z. Size-dependent phase morphologies in LiFePO<sub>4</sub> battery particles. *Electrochem. Commun.* **95**, 33–37 (2018).
14. Smith, R. B. & Bazant, M. Z. Multiphase Porous Electrode Theory. *J. Electrochem. Soc.* **164**, E3291–E3310 (2017).
15. Vasileiadis, A. *et al.* Toward Optimal Performance and In-Depth Understanding of Spinel Li<sub>4</sub>Ti<sub>5</sub>O<sub>12</sub> Electrodes through Phase Field Modeling. *Adv. Funct. Mater.* **28**, 1705992 (2018).
16. Ferguson, T. R. & Bazant, M. Z. Nonequilibrium Thermodynamics of Porous Electrodes. *J. Electrochem. Soc.* **159**, A1967–A1985 (2012).
17. Ombrini, P., Bazant, M. Z., Wagemaker, M. & Vasileiadis, A. Thermodynamics of multi-sublattice battery active materials: from an extended regular solution theory to a phase-field model of LiMnyFe<sub>1-y</sub>PO<sub>4</sub>. *Npj Comput. Mater.* **9**, 148 (2023).
18. Katrašnik, T. *et al.* Entering Voltage Hysteresis in Phase-Separating Materials: Revealing the Electrochemical Signature of the Intraparticle Phase-Separated State. *Adv. Mater.* **35**, 2210937 (2023).
19. Guo, X. *et al.* Size-Dependent Memory Effect of the LiFePO<sub>4</sub> Electrode in Li-Ion Batteries. *ACS Appl. Mater. Interfaces* **10**, 41407–41414 (2018).
20. Srinivasan, V. & Newman, J. Existence of Path-Dependence in the LiFePO<sub>4</sub> Electrode.
21. Jia, J., Tan, C., Liu, M., Li, D. & Chen, Y. Relaxation-Induced Memory Effect of LiFePO<sub>4</sub> Electrodes in Li-Ion Batteries. *ACS Appl. Mater. Interfaces* **9**, 24561–24567 (2017).

22. Shi, W. *et al.* Influence of memory effect on the state-of-charge estimation of large-format Li-ion batteries based on LiFePO<sub>4</sub> cathode. *J. Power Sources* **312**, 55–59 (2016).
23. Lim, J. *et al.* Origin and hysteresis of lithium compositional spatiodynamics within battery primary particles. *Science* **353**, 566–571 (2016).
24. Duan, X. *et al.* Electrochemical Modeling of Fast Charging in Batteries. *Adv. Energy Mater.* 2400710 (2024) doi:10.1002/aenm.202400710.
25. Wagemaker, M., Mulder, F. M. & Van der Ven, A. The Role of Surface and Interface Energy on Phase Stability of Nanosized Insertion Compounds. *Adv. Mater.* **21**, 2703–2709 (2009).
26. Wagemaker, M. *et al.* Dynamic Solubility Limits in Nanosized Olivine LiFePO<sub>4</sub>. *J. Am. Chem. Soc.* **133**, 10222–10228 (2011).
27. Cogswell, D. A. & Bazant, M. Z. Theory of Coherent Nucleation in Phase-Separating Nanoparticles. *Nano Lett.* **13**, 3036–3041 (2013).
28. Bai, P., Cogswell, D. A. & Bazant, M. Z. Suppression of Phase Separation in LiFePO<sub>4</sub> Nanoparticles During Battery Discharge. *Nano Lett.* **11**, 4890–4896 (2011).
29. Cogswell, D. A. & Bazant, M. Z. Coherency Strain and the Kinetics of Phase Separation in LiFePO<sub>4</sub> Nanoparticles. *ACS Nano* **6**, 2215–2225 (2012).
30. Galuppini, G. *et al.* Nonlinear identifiability analysis of Multiphase Porous Electrode Theory-based battery models: A Lithium Iron Phosphate case study. *J. Power Sources* **573**, 233009 (2023).
31. Koo, B. *et al.* Dynamic surface phases controlling asymmetry of high-rate lithiation and delithiation in phase-separating electrodes. *Energy Environ. Sci.* 10.1039/D3EE00341H (2023) doi:10.1039/D3EE00341H.
32. Bazant, M. *et al.* *Learning Heterogeneous Reaction Kinetics from X-Ray Movies Pixel-by-Pixel.* <https://www.researchsquare.com/article/rs-2320040/v1> (2022) doi:10.21203/rs.3.rs-2320040/v1.
33. Schwietert, T. K. *et al.* Phase-Field Computational Framework for Addressing Challenges in Solid-State Batteries. *PRX Energy* **2**, 033014 (2023).
34. Karanth, P. *et al.* A phase inversion strategy for low-tortuosity and ultrahigh-mass-loading nickel-rich layered oxide electrodes. *Cell Rep. Phys. Sci.* 101972 (2024) doi:10.1016/j.xcrp.2024.101972.
35. Zhang, Y. *et al.* Towards better Li metal anodes: Challenges and strategies. *Mater. Today* **33**, 56–74 (2020).
36. Bazant, M. Z. Unified quantum theory of electrochemical kinetics by coupled ion-electron transfer. *Faraday Discuss.* 10.1039/D3FD00108C (2023) doi:10.1039/D3FD00108C.
37. Ferguson, T. R. & Bazant, M. Z. Phase Transformation Dynamics in Porous Battery Electrodes. *Electrochimica Acta* **146**, 89–97 (2014).
38. Malik, R., Abdellahi, A. & Ceder, G. A Critical Review of the Li Insertion Mechanisms in LiFePO<sub>4</sub> Electrodes. *J. Electrochem. Soc.* **160**, A3179–A3197 (2013).
39. Brunetti, G. *et al.* Confirmation of the Domino-Cascade Model by LiFePO<sub>4</sub>/FePO<sub>4</sub> Precession Electron Diffraction. *Chem. Mater.* **23**, 4515–4524 (2011).
40. Chueh, W. C. *et al.* Intercalation Pathway in Many-Particle LiFePO<sub>4</sub> Electrode Revealed by Nanoscale State-of-Charge Mapping. *Nano Lett.* **13**, 866–872 (2013).
41. Laffont, L. *et al.* Study of the LiFePO<sub>4</sub>/FePO<sub>4</sub> Two-Phase System by High-Resolution Electron Energy Loss Spectroscopy. *Chem. Mater.* **18**, 5520–5529 (2006).
42. Delmas, C., Maccario, M., Croguennec, L., Le Cras, F. & Weill, F. Lithium deintercalation in LiFePO<sub>4</sub> nanoparticles via a domino-cascade model. *Nat. Mater.* **7**, 665–671 (2008).
43. Liu, H. *et al.* Capturing metastable structures during high-rate cycling of LiFePO<sub>4</sub> nanoparticle electrodes. *Science* **344**, 1252817 (2014).
44. Li, Y. *et al.* Fluid-enhanced surface diffusion controls intraparticle phase transformations. *Nat. Mater.* **17**, 915–922 (2018).
45. Deng, Y. *et al.* Recent Advances of Mn-Rich LiFe<sub>1-y</sub>Mn<sub>y</sub>PO<sub>4</sub> (0.5 ≤ y < 1.0) Cathode Materials for High Energy Density Lithium Ion Batteries. *Adv. Energy Mater.* **7**, 1601958 (2017).

46. Pozzato, G. *et al.* Core-Shell Enhanced Single Particle Model for lithium iron phosphate Batteries: Model Formulation and Analysis of Numerical Solutions. *J. Electrochem. Soc.* **169**, 063510 (2022).
47. Azimi, V., Allam, A. & Onori, S. Extending life of Lithium-ion battery systems by embracing heterogeneities via an optimal control-based active balancing strategy. Preprint at <http://arxiv.org/abs/2203.04226> (2022).
48. Galuppini, G. *et al.* *Efficient Computation of Safe, Fast Charging Protocols for Multiphase Lithium-Ion Batteries: A Lithium Iron Phosphate Case Study*. <https://www.ssrn.com/abstract=4392427> (2023) doi:10.2139/ssrn.4392427.
49. Rivera-Barrera, J., Muñoz-Galeano, N. & Sarmiento-Maldonado, H. SoC Estimation for Lithium-ion Batteries: Review and Future Challenges. *Electronics* **6**, 102 (2017).
50. Habib, A. K. M. A. *et al.* Lithium-Ion Battery Management System for Electric Vehicles: Constraints, Challenges, and Recommendations. *Batteries* **9**, 152 (2023).
51. Fraggedakis, D. *et al.* Theory of coupled ion-electron transfer kinetics. *Electrochimica Acta* **367**, 137432 (2021).
52. Zhuang, D. & Bazant, M. Z. Scaling analysis of mosaic phase separation in Li-ion batteries. *Phys. Rev. E* **110**, 064142 (2024).
53. Zhao, H. *et al.* Learning heterogeneous reaction kinetics from X-ray videos pixel by pixel. *Nature* **621**, 289–294 (2023).
54. McClelland, I. *et al.* Direct Observation of Dynamic Lithium Diffusion Behavior in Nickel-Rich, LiNi<sub>0.8</sub>Mn<sub>0.1</sub>Co<sub>0.1</sub>O<sub>2</sub> (NMC811) Cathodes Using *Operando* Muon Spectroscopy. *Chem. Mater.* **35**, 4149–4158 (2023).
55. Bai, P. & Bazant, M. Z. Charge transfer kinetics at the solid–solid interface in porous electrodes. *Nat. Commun.* **5**, 3585 (2014).
56. Fraggedakis, D. *et al.* A scaling law to determine phase morphologies during ion intercalation. *Energy Environ. Sci.* **13**, 2142–2152 (2020).
57. Malik, R., Burch, D., Bazant, M. & Ceder, G. Particle Size Dependence of the Ionic Diffusivity. *Nano Lett.* **10**, 4123–4127 (2010).

## SUPPLEMENTARY INFORMATION

## Electrochemical experiments

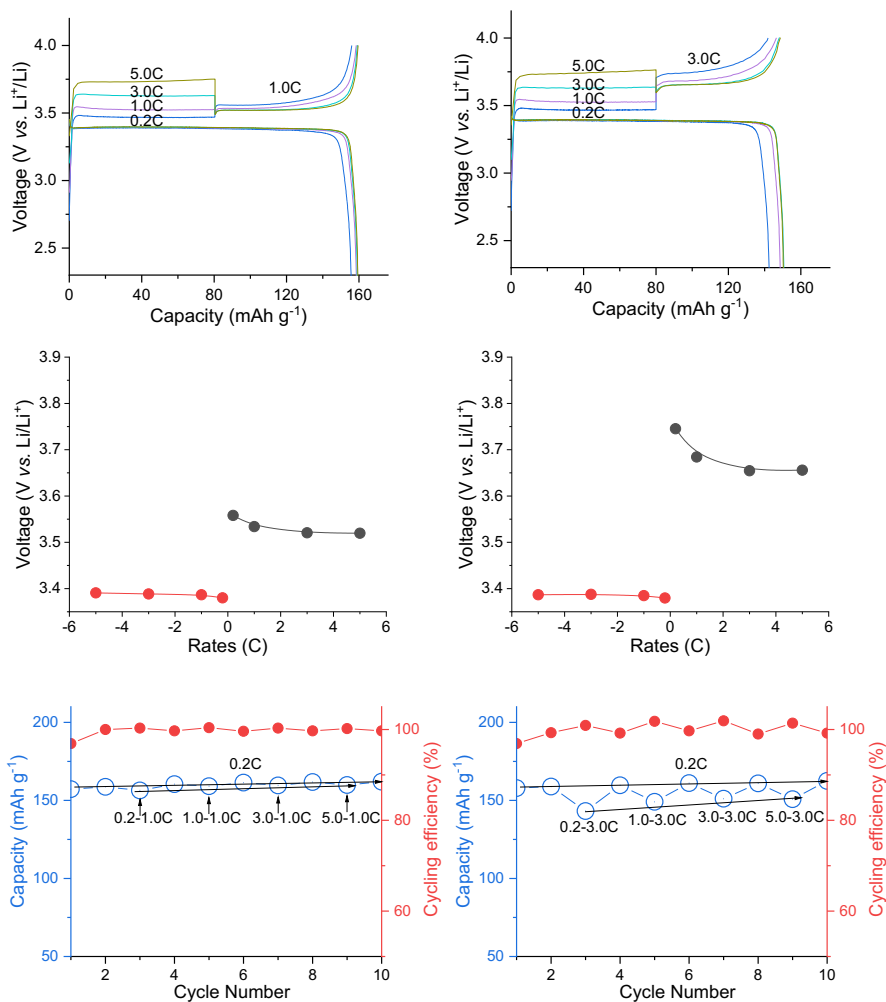


Figure S1. Voltage vs capacity evolution of an LFP | Li cell during the memory protocol. The voltage profile for LFP at 1.0C in the reading step (left column), and 3.0C in the reading step (right column), respectively (1.0C=150 mA g<sup>-1</sup>). The overpotential tends to decrease with an increased charging rate in the writing step (center figures), while the capacity tends to increase. The difference between the plateau potentials is reduced if the reading step is executed at a lower rate (lower figure).

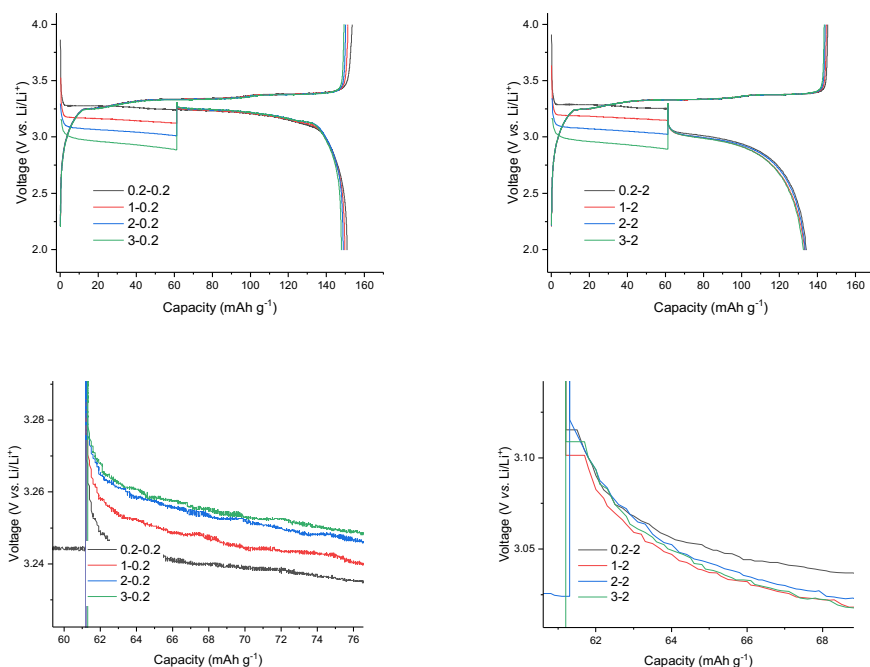


Figure S2. Voltage vs capacity evolution of an LFP | Graphite cell during a discharge memory protocol. The voltage profile of LFP | Graphite at 0.2C in the reading step (left column), and 2.0C in the reading step (right column), respectively (1.0C=150 mA g<sup>-1</sup>). Corresponding enlarged figures of initial overpotentials (lower figures).

The memory protocol applied to an LFP | Graphite full cell during discharge shows the presence of the kinetically induced memory effect. In particular, if the reading step is performed at low rates (0.2C) a reduced overpotential is visible, while performing a 2.0C reading step do not show a specific trend. The origin of this discrepancy can be found in the counteracting effect of LFP and Graphite heterogeneities. Low reading rates can show the reduced reaction overpotential, originating from the higher LFP active particle population (Fig. S21). The overpotential of higher rates is instead dependent on multiple factors, such as uneven Li distribution in the graphite particles. This hinders the LFP's memory effect and does not allow the full cell voltage to significantly change. A full cell's behavior is so dependent on the kinetic limitations of both electrodes, and it is therefore not possible to generalize the phenomenon. The experiment was performed during discharge to allow for high rates, since high charging rates might initiate Li plating on graphite particles and significantly change the electrode's properties.

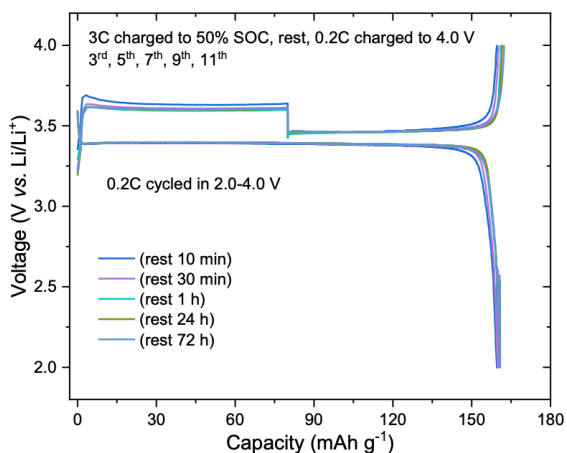


Figure S3. Voltage vs capacity evolution of LFP || Li cells during the memory protocol cycle at different resting times. The charging rate is 3.0C during the writing step and 0.2C during the reading step. No relevant differences can be found at different resting times indicating that the long-lasting effect of particle-level heterogeneities created during the writing step.

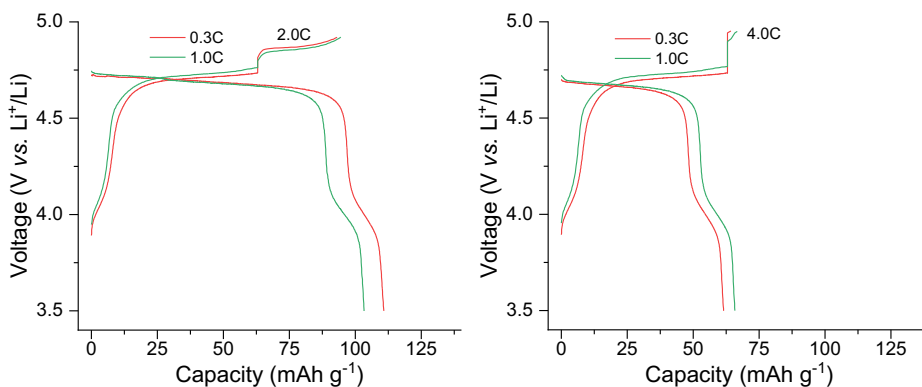


Figure S4. Voltage profile of  $\text{LiNi}_{0.5}\text{Mn}_{1.5}\text{O}_4$  || Li cells during the memory protocol. The charging rate is 0.3C/1.0C in the writing step, 0.2C/2.0C/4.0C in the reading step, and 0.1C in the discharge (1.0C=147  $\text{mA g}^{-1}$ ). The kinetically induced memory effect is also present in  $\text{LiNi}_{0.5}\text{Mn}_{1.5}\text{O}_4$ , being a phase-separating material, but due to the smaller miscibility gap it is less pronounced.

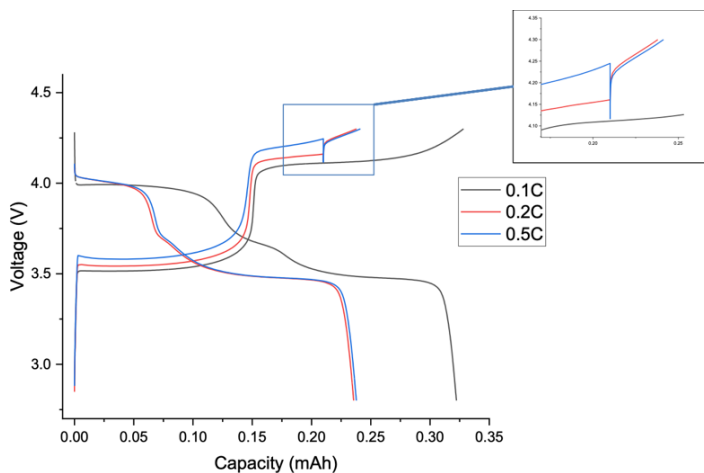


Figure S5. Voltage profile of  $\text{LiMn}_{0.4}\text{Fe}_{0.6}\text{PO}_4 \mid \text{Li}$  cells during the memory protocol. The charging rates are 0.2C and 0.5C in the writing step, and 0.3C in the reading step ( $1.0\text{C}=150 \text{ mA g}^{-1}$ ). The kinetically induced memory effect is also present in  $\text{LiMn}_{0.4}\text{Fe}_{0.6}\text{PO}_4$ , in particular, the Mn plateau of this composition is phase-separating<sup>17</sup> with a reduced miscibility gap.

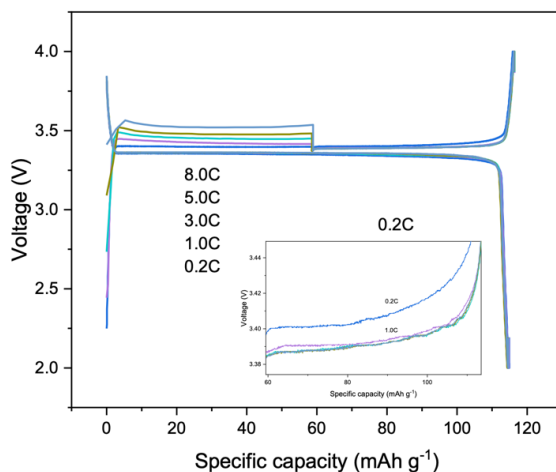


Figure S6. Voltage profile of  $\text{Na}_3\text{V}_2(\text{PO}_4)_3 \mid \text{Na}$  cells during the memory protocol. The charging rates are 0.2C/8.0C in the writing step, and 0.2C in the reading step ( $1.0\text{C}=110 \text{ mA g}^{-1}$ ). The kinetically induced memory effect is shown to be general to every phase separating insertion compound for rechargeable batteries beyond the Li-ion batteries.

## Material characterization

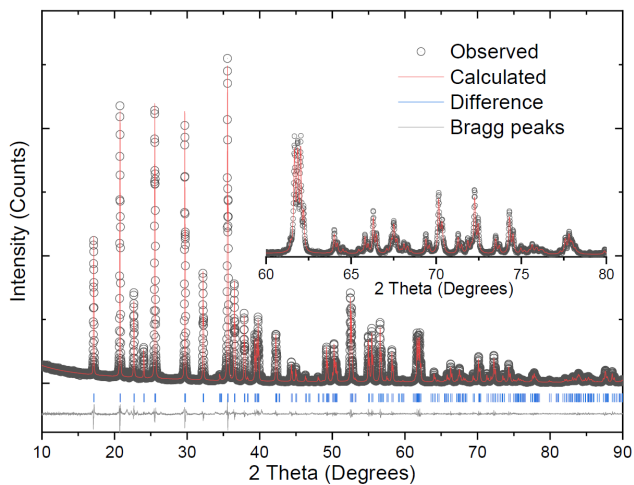


Figure S7. The XRD Rietveld refinement of  $\text{LiFePO}_4$  material used in this study. The patterns of the sample show the formation of orthorhombic  $\text{LiFePO}_4$  crystal structure (space group:  $Pnma$ ), commonly known as olivine type phase.

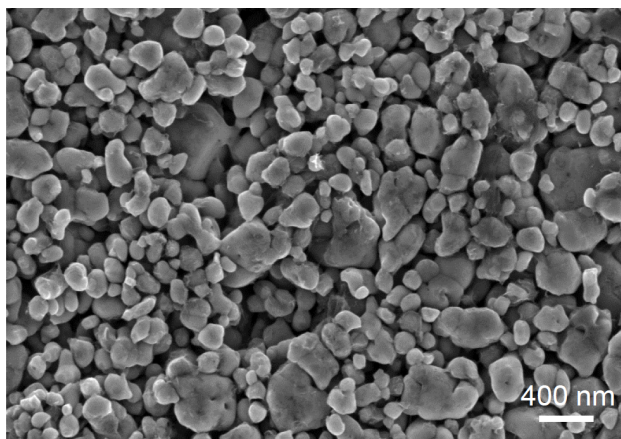


Figure S8. SEM image of  $\text{LiFePO}_4$  material used in this study. According to the SEM images of the  $\text{LiFePO}_4$  material, the particle size is in the range of 100-500 nm.

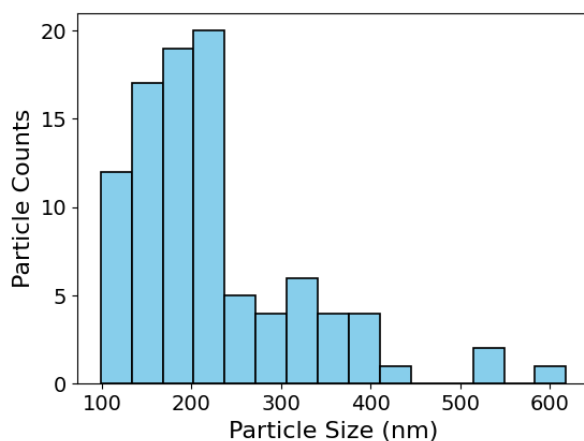


Figure S9. Particle size distribution  $\text{LiFePO}_4$  material used in this study. According to the SEM images of the  $\text{LiFePO}_4$  material, the particle size distribution is a lognormal distribution with an average of 200 nm.

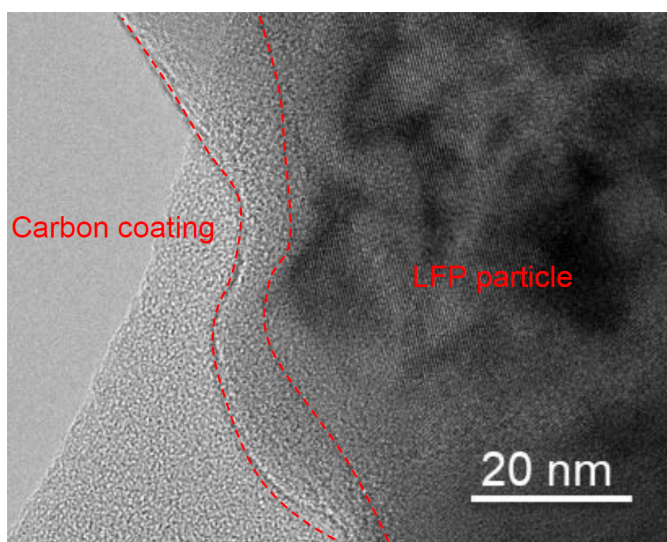


Figure S10. TEM image of  $\text{LiFePO}_4$  material used in this study. The  $\text{LiFePO}_4$  particle is coated with an amorphous carbon layer with a thickness around 10 nm.

## Simulation results

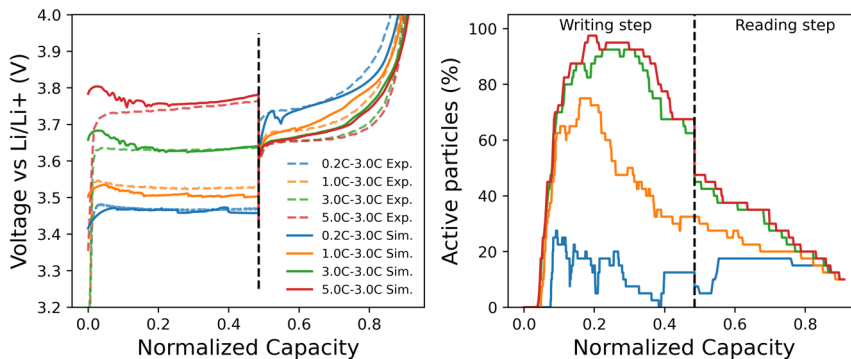


Figure S11. Comparison between the experimental and the simulated voltage curves for the memory cycles on  $\text{LiFePO}_4$  (left) and evolution of the active particle population during the application of the memory cycles on  $\text{LiFePO}_4$  (right).

5

The electrochemical phase-field simulation can reproduce the kinetically induced memory effect and the capacity loss for the LFP case. The model can so be considered the first one capable of fitting the voltage curves of a complex protocol by incorporating the phase separation mechanism and the relevant sources of overpotential with a purely physics-based approach. The resulting active particle population dynamics also shows how the increased active particles at the beginning of the readings step is responsible for the lower overpotential.

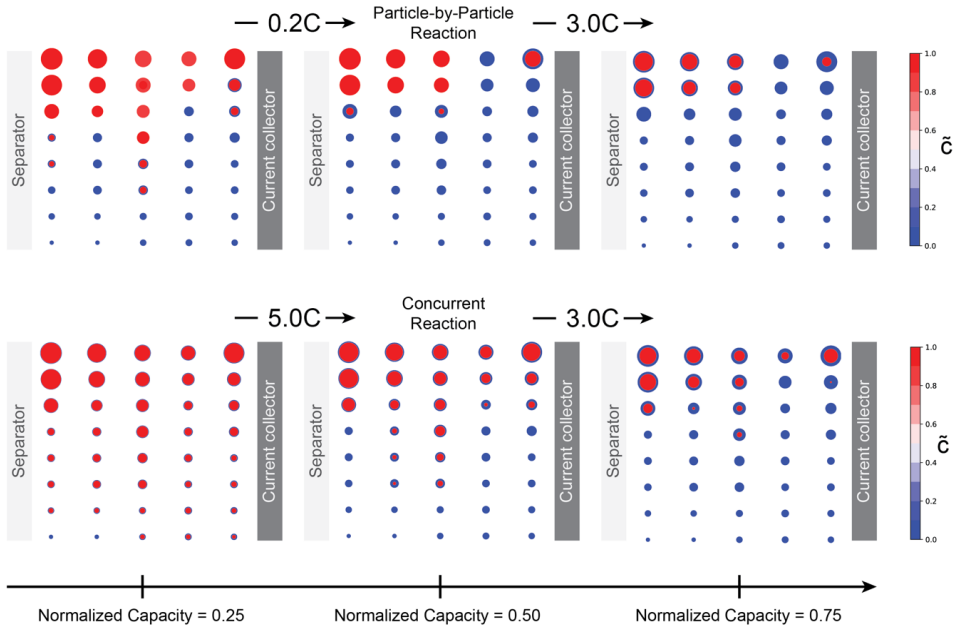


Figure S12. Evolution of the concentration inside the simulated particles during the 0.2C-3.0C (upper) and 5.0C-3.0C (lower) memory protocols. 0.2C and 5.0C rates refer to the writing rates, the reading rate was set to 3.0C.

The simulations can also show the evolution of the concentration inside each particle. We can observe the particle-by-particle reaction taking place at 0.2C leading to a mosaic state at 50%SOC, while the 5.0C case proceeds by utilizing most of the available particles. The phase-field simulation is capable of obtaining a shrinking core mechanism without the imposition of any sudden phase change leading to a realistic result.

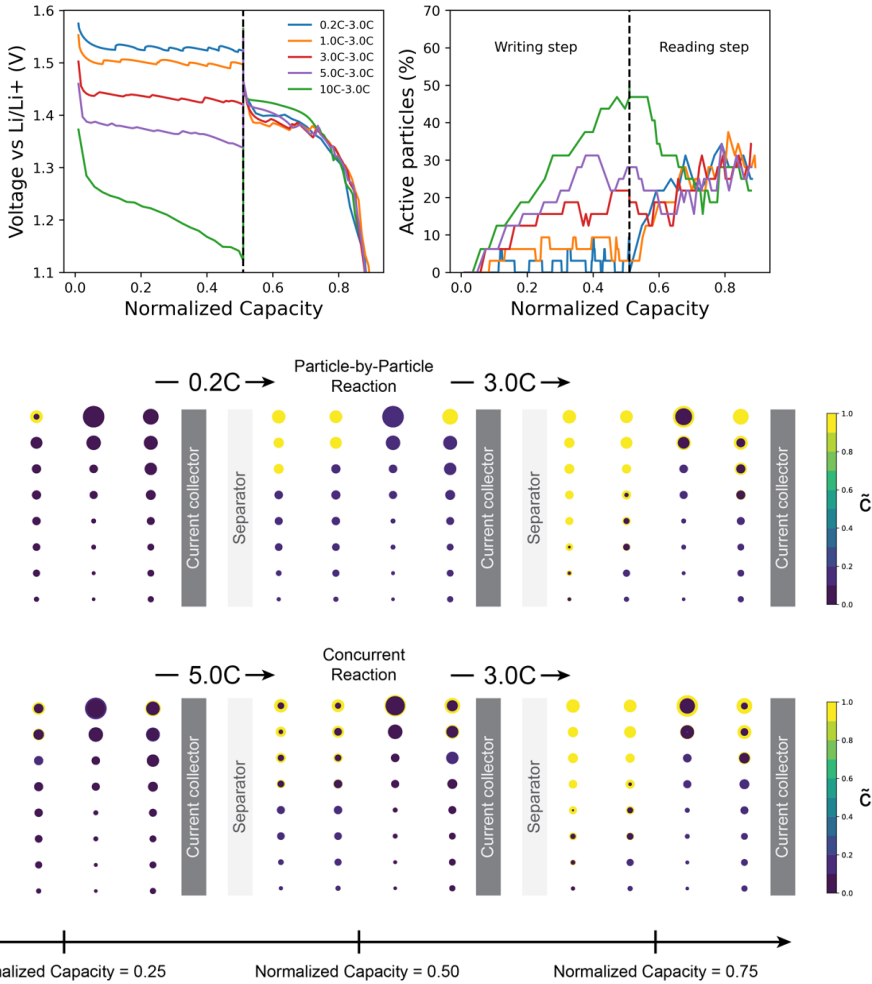


Figure S13. Simulation of the kinetically induced memory effect on  $\text{Li}_4\text{Ti}_5\text{O}_{12}$ . Voltage responses during to the memory protocols (upper left), active particle population dynamics (upper right), evolution of the solid concentration during the 0.2C-3.0C and 5.0C-3.0C memory protocols (bottom).

The model developed by Vasileiadis et al.<sup>15</sup> was adapted by considering wiring effects and used to investigate the effect of the memory protocol the lithiation of  $\text{Li}_4\text{Ti}_5\text{O}_{12}$ . The numerical results, in line with the experiments, prove the presence of this effect being general for phase-separating materials, and being regulated by the same phenomena. The active particle population is following the same trend observed in the LFP case. The absence of a saturation current is explained by the higher exchange current density of  $\text{Li}_4\text{Ti}_5\text{O}_{12}$  which limits the active particle population. The simulations are capable of showing the mosaic lithiation for the case of 0.2C writing step in comparison to the collective intercalation for the 5.0C case.

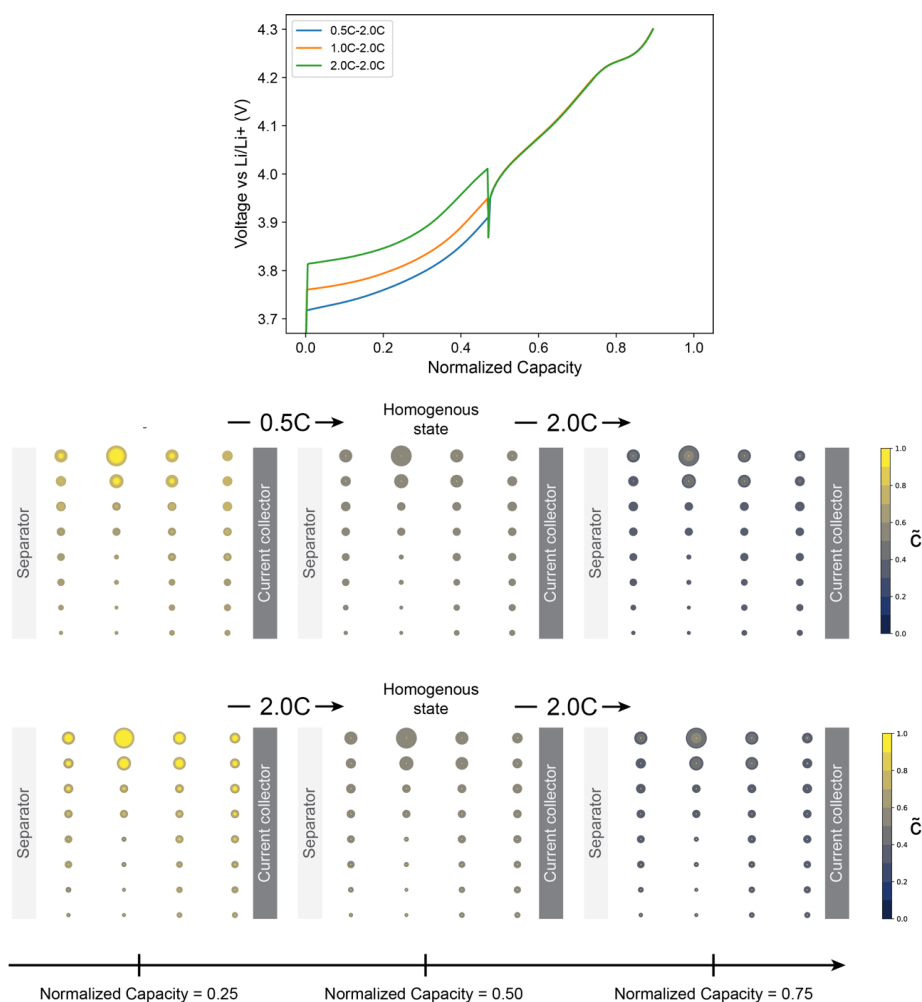


Figure S14. Simulation of the effects of the memory protocol on  $\text{LiNi}_{0.8}\text{Mn}_{0.1}\text{Co}_{0.1}\text{O}_2$ . Voltage responses during to the memory protocols (upper), evolution of the solid concentration during the 0.2C-3.0C and 5.0C-3.0C memory protocols (bottom).

By implying a validated model of NMC811<sup>34</sup> to simulate the electrochemical behavior under the effect of the memory protocol, we observe how the different rates hardly influence the collective dynamics in a diffusion-limited solid-solution system. After the relaxation, the particles equilibrate internally and exchange lithium with each other, resulting in the same state despite the writing rate. This naturally leads to the same voltage response to the subsequent applied current.

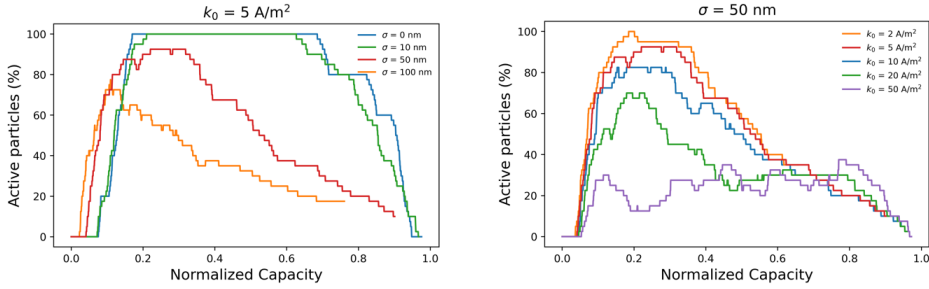


Figure S15. Active particle population dynamics of the LFP electrode, for various standard deviation of the particle size distribution  $\sigma$  (left) and exchange current densities  $k_0$  (right), during a 3.0C constant current charge.

5

Our findings indicate that variations in the standard deviation of the particle size distribution ( $\sigma$ ) significantly affect the symmetry of the active particle population evolution. Smaller particles tend to initiate the phase transition earlier, and because they also complete the delithiation process before larger particles, the system struggles to sustain a high active particle fraction throughout the reaction. In contrast, a narrower particle size distribution promotes a more synchronized reaction across particles, as they exhibit similar nucleation barriers and kinetic properties. As a result, the active particle population remains more stable during the charging process. The exchange current density ( $k_0$ ), on the other hand, primarily acts as a scaling factor that governs the balance between the overall electrode reaction time and the reaction time of individual particles<sup>52</sup>. Higher  $k_0$  values enable the system to sustain the current by activating fewer particles at the same rate, effectively reducing the required active particle fraction. This behavior is illustrated in Fig. S15, which shows how increased  $k_0$  shifts the burden of charge transfer onto fewer particles while maintaining the same applied current. Ultimately, while the evolution of the active particle population is strongly influenced by the particle size distribution, the maximum active population at a given rate scales proportionally with the charge transfer resistance. These findings highlight the intricate interplay between particle-level kinetics and macroscopic electrochemical response, reinforcing the importance of considering both parameters when modeling and optimizing phase-separating battery materials.

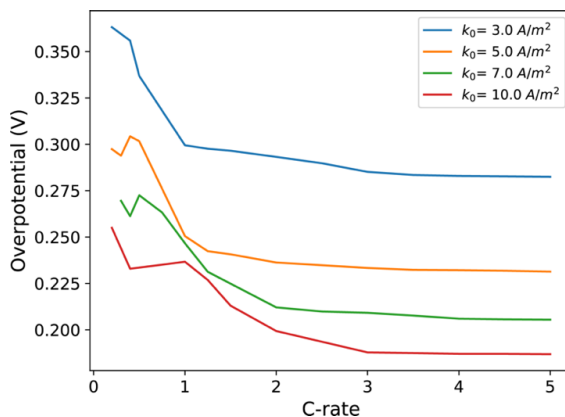
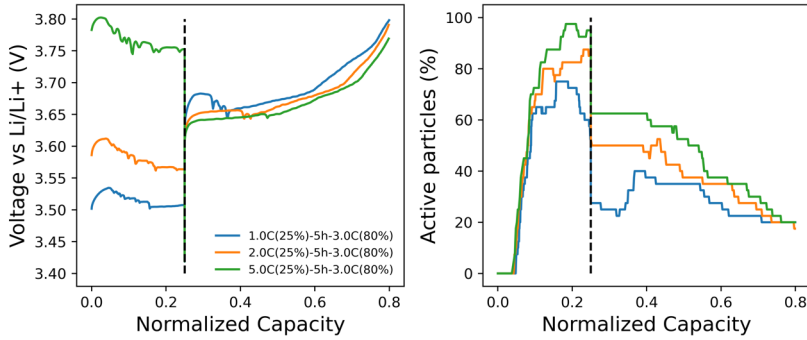


Figure S16. Effect of LFP exchange current density ( $k_0$ ) on the initial overpotential of the reading step. The x-axis refers to the writing rate, the reading rate was set to 3.0C.

5

By changing the exchange current density and applying the memory cycle on the same model utilized previously we observe how the saturation current is strongly dependent on this parameter. We can in fact observe how increasing this parameter, not only the overpotential is reduced, but also the saturation current is driven towards higher rates. While the change in overpotential can be unidentifiable since it is possible to compensate for it by changing other limiting factors such as electrical conductivity or tortuosity, the saturation current is instead strongly related to  $k_0$ . This underlines the use of this protocol for the parameter estimation of this usually unidentifiable parameter<sup>30</sup>.

## LFP



## LTO

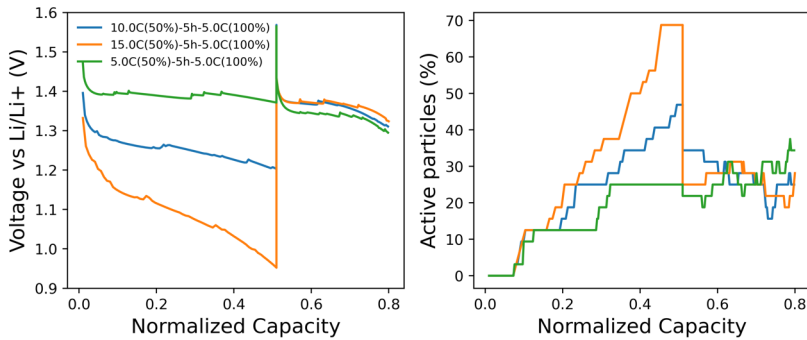


Figure S17. Examples of voltage and active particle populations during optimize protocols for LFP (upper figure) and LTO (lower figure) electrodes.

Optimized protocols for battery charging, have the multi-objective goals, such as minimizing the energy expenditure and ensuring correct heat management. To explore the implications of the kinetically induced memory effect in practical battery operation scenarios, we employed our validated electrochemical model to simulate realistic charging strategies for LFP and LTO electrodes, focusing on coupling battery operation with electricity pricing. Specifically, we examined scenarios where batteries are integrated within energy storage systems, and charging schedules are strategically aligned with variable electricity prices.

We considered the following scenario: a battery initially at 0% SOC is first partially charged and subsequently brought to 80% SOC, five hours later. Such a scenario commonly occurs in practice, as batteries cannot remain fully discharged for prolonged periods without experiencing degradation. Consequently, the operator of the energy storage system must perform an initial

partial charge step to protect battery longevity, followed by a later charging step that can be strategically aligned with favorable electricity prices or grid conditions. While it is intuitive that the reached SOC and charging rate influence the energy expended during the initial charging, our findings highlight that—due to the kinetically induced memory effect—these initial parameters also significantly influence the overpotential observed during the subsequent charging step, five hours later.

For the LFP electrode, we observe that the active particle fraction peaks at approximately 25% SOC (Fig. 5.3). Therefore, it can be advantageous to initially charge the battery to around 25% SOC, maximizing particle activation. However, the initial charging rate significantly influences subsequent charging efficiency due to the memory effect. For example, an initial 2.0C charging step consumes slightly more energy than a 1.0C step but results in lower overpotentials and higher efficiency during the subsequent high-rate (3.0C) step, as illustrated by the simulations (Fig. S17). Specifically, an initial charge at 2.0C consumes approximately 0.04 mWh cm<sup>-2</sup> more energy compared to a 1.0C step, but this initial energy investment reduces subsequent overpotentials, recovering approximately 0.03 mWh cm<sup>-2</sup> during the later charging stage. To quantify these energy differences, we assumed a fully charged battery capacity of approximately 6.8 mWh cm<sup>-2</sup> (calculated as 3.4 V × 2 mAh cm<sup>-2</sup>). Notably, this trade-off between initial and subsequent charging efficiency depends on the relative electricity pricing during each charging phase. If energy prices are substantially lower during the initial charging step, a higher initial rate could be economically favorable despite higher initial energy consumption. Importantly, we observe that excessively high initial rates (e.g., above 3.0C) yield diminishing returns, as the maximum particle activation saturates, and additional energy input is lost primarily due to transport limitations rather than stored as useful boundary energy. Conversely, moderate initial rates (around 1.0–2.0C) partially store the additional invested energy within the system as boundary energy, which can be subsequently utilized to reduce later overpotentials.

For LTO electrodes, despite particle sizes similar to those of LFP, we do not observe saturation even at high currents (15.0C). This is because the active particle population—and consequently the saturation current—depends not only on particle size but also on the exchange current density. The substantially lower charge-transfer resistance of LTO compared to LFP (Fig. S22) means that fewer particles are activated even at high rates (Fig. S17), making solid-state diffusion the predominant source of overpotential. Additionally, the faster inter-particle lithium exchange in LTO significantly reduces the active particle population during the 5-hour resting period. Consequently, employing higher initial rates does not enhance efficiency during the subsequent charging steps for LTO, limiting the potential for revenue-driven optimization that was demonstrated with LFP electrodes.

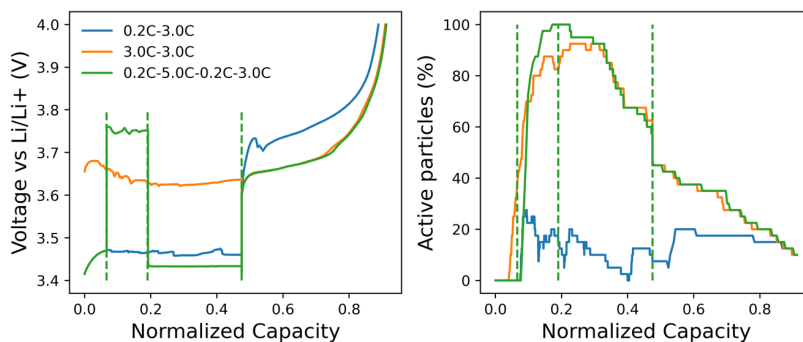


Figure S18. Comparison between the previously validated memory protocols (0.2C-1h\_rest-3.0C, 3.0C-1h\_rest-3.0C) and a multi-step protocol (0.2C-5.0C-0.2C-1h\_rest-3.0C). The dashed vertical lines correspond the changes in the multi-step protocol current.

5

To further demonstrate the model's capability for protocol optimization, we simulated a multi-step charging protocol consisting of:

- 0.2C charge up to 10% SOC
- 5.0C charge from 10% to 20% SOC
- 0.2C charge from 20% to 50% SOC
- 1 hour rest
- 3.0C charge up to cutoff voltage of 4.0 V.

This protocol was designed to assess whether a brief high-current pulse could activate a greater fraction of particles and influence the subsequent overpotential. As shown in Fig. S18, the active particle population rapidly increases upon application of the 5.0C pulse. Interestingly, despite the subsequent return to a low charging rate (0.2C), the phase-separated particles do not undergo lithium exchange and remain in an active state. As a result, when the 3.0C reading step is applied, the electrode follows a voltage profile similar to that of the 3.0C-3.0C protocol rather than the 0.2C-3.0C protocol. This leads to a lower overpotential during the high-rate step, demonstrating that short current pulses can effectively nucleate a large fraction of particles and enhance the electrode's kinetic response. These findings suggest that strategically incorporating brief high-rate pulses into charging protocols could serve as a tool for improving phase-separating battery materials' efficiency, particularly in fast-charging applications.

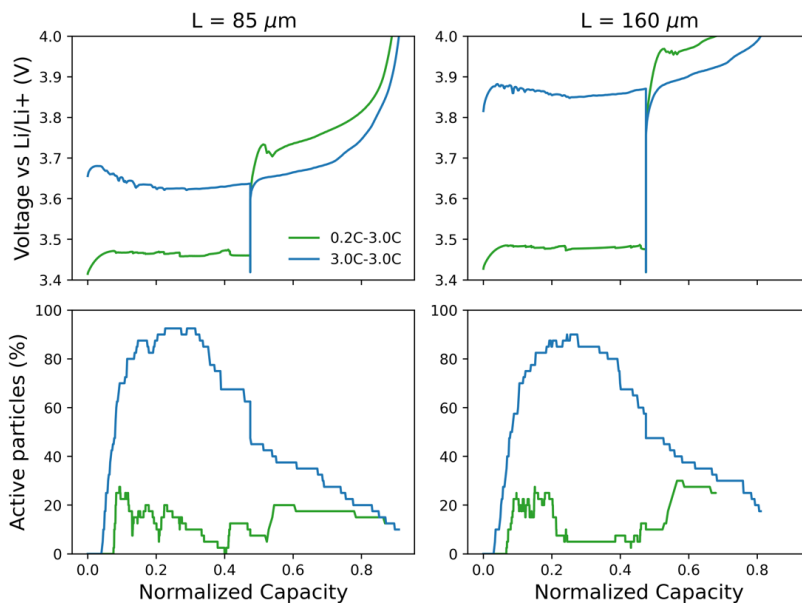


Figure S19. Comparison between the LFP model results of the 0.2C-3.0C and 3.0C-3.0C protocols for the validated scenario (left) and the thicker electrode (right).

Comparing a thicker electrode ( $L = 160 \mu\text{m}$ ) to the base case ( $L = 85 \mu\text{m}$ ), we find that the kinetically induced memory effect remains evident. While the overall voltage increases due to the higher current density, the active particle population dynamics remain fundamentally unchanged, continuing to drive the memory effect. Additionally, we observe a slight reduction in the maximum active particle population for the 3.0C-3.0C protocol in the thicker electrode. This is attributed to greater localization of reactions toward the separator side, driven by increased electrolyte polarization within the electrode. However, this effect is relatively minor, as the dominant contributors to overpotential in this system are the diffusion and reaction limitations at the particle level.

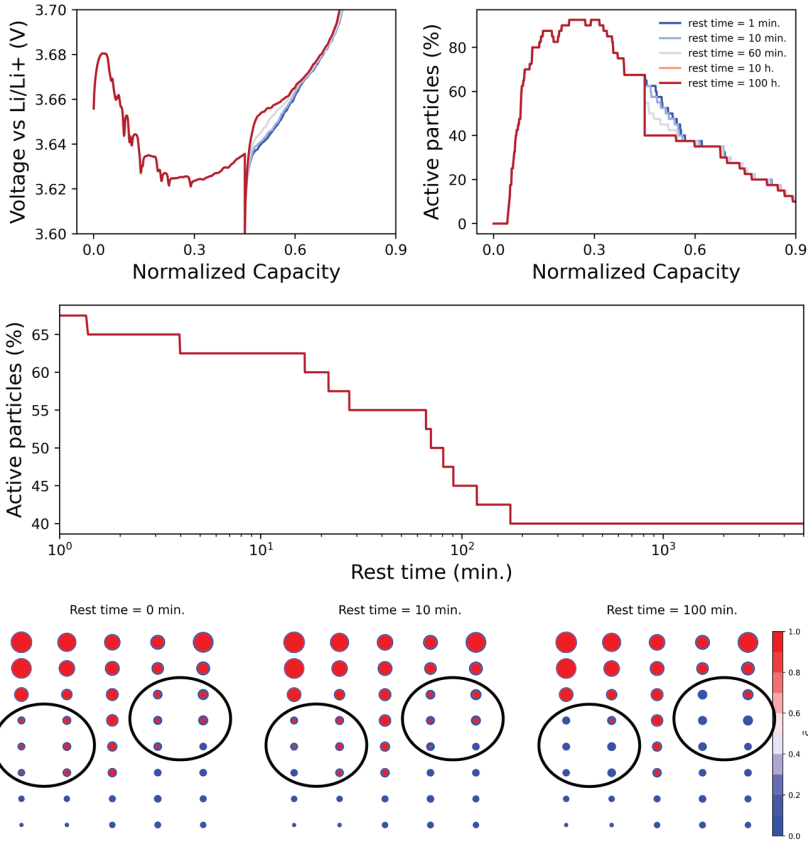


Figure S20. Effect of resting time on the LFP subsequent voltage response and active particle population. Comparison between voltage profiles and active particle population at varying resting times during a 3.0C-3.0C protocol (upper figure). Active particle population evolution during resting after a 3.0C charge to 50% SOC (central figure). Solid particle concentration during resting after a 3.0C charge to 50% SOC (lower figure).

We employed the validated model to simulate the effect of a variation of the rest time. The simulations in Fig. S20 show that the voltage overpotential at the beginning of the reading step increases proportionally to the resting time. Under open-circuit conditions, inter-particle lithium exchange gradually drives the system towards a mosaic state, reducing the active particle population. This reduction follows an exponential trend, eventually saturating after approximately 200 minutes at a stable value of 40%. The reason relies on the effect of the phase boundary energy on the different particle sizes. In smaller particles the relative energy increase due to the presence of a phase boundary is greater than in bigger particles, and consequently the drive towards a homogenous state. Combining this effect with the faster kinetics allows Li

exchange between smaller particles, while the similar energies and the slower kinetics inhibit the relaxation of bigger particles.

These results further validate our interpretation that the kinetically induced memory effect is directly linked to the stability of phase-separated particles. While relaxation does occur, the relatively slow redistribution kinetics in spheroidal particles preserves the effect over experimentally relevant timescales, highlighting the importance of particle morphology in dictating the timescales of these phenomena.

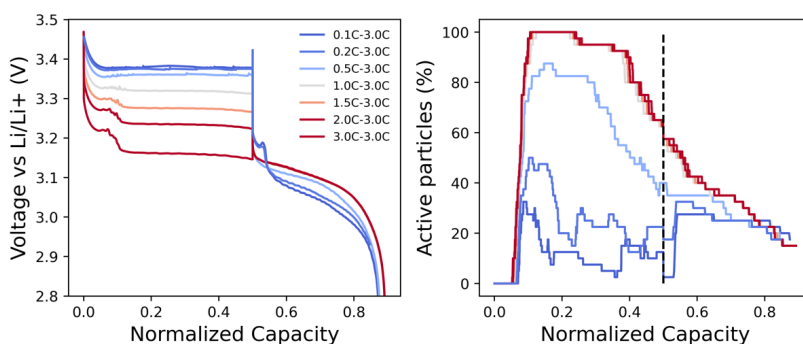


Figure S21. Examples of voltage and active particle populations during discharge memory protocols for an LFP electrode.

To investigate the difference between charge and discharge on the kinetically induced memory effect, we simulated discharge memory protocols using the same model and parameters described in table T3. The results are in line with the experimental observation (Fig. S2) and allow for decoupling of the LFP effect from the Graphite behaviour. Specifically, higher writing C-rates during the initial discharge step activate a larger fraction of particles, subsequently resulting in lower overpotentials during the reading step. This behaviour mirrors the previously observed charging process. However, one notable distinction arises due to differences in lithiation and delithiation kinetics, attributable to asymmetric charge-transfer behaviour (Fig. S22). As shown in literature<sup>9</sup>, during lithiation, the autoinhibitory reaction kinetics forces the system to activate a larger particle population to sustain the same current, thus increasing the active particle fraction. Consequently, the memory effect remains observable, but the limiting current is decreased, in line with the results of Fig. S2. We can conclude that kinetic limitations originating from the Graphite electrode are responsible for the hindering of the memory effect on the voltage a full cell.

## Microbeam X-ray diffraction data analysis

The raw data were analyzed following the methodology outlined in the Methods section of Ref 10. This analysis provided two datasets: the “LabeledGrainsTable” and the “EnrichedFramesTable”, which store the evolution of all detected grains throughout the 0.2C–3.0C and 5.0C–3.0C memory protocols, along with the corresponding electrochemical data. The description tables legend is hereby provided.

Column name	Description
exp_name	ESRF experiment name.
exp_nr	ESRF experiment number.
snapshot	Internal reference.
grainnr	Number of the grain. Changing for each grain and timestep.
labelnr	Number of the labelled grain. Changing for each grain, remaining constant during time.
framenr	Number of the timestep.
point	Point of the pouch cell under the beam.
eta	Value of the grain's $\eta$ at the given timestep.
omega	Value of the cell's $\omega$ at the given timestep.
twotheta	Value of the grain's $2\theta$ at the given timestep.
deviation	Deviation from the initial $2\theta$ value
dspace	Plane distance
hkl	Grain's reflection and phase (LFP or FP).
xmin, xmax, ymin, ymax	Values of the pixel frame for plotting.
intensity	Integral of the total intensity in the frame.
grain	2D matrix showing the intensity in the frame.

Table T1 Legend of LabeledGrainsTable

Column name	Description
Time	Date-time of the experiment
ESRFCurrent	Energy of the ring
Exposure	Data collection time in seconds
rot_angle	$\omega$ angle. Indicates z-axis rotation.
rot_angle_step	$\omega$ step angle.
sample_y	y-coordinate of the sample (indicates which location of the sample is lit)
sample_z	z-coordinate of the sample (indicates which location of the sample is lit)
FrameNr	Sequential frame number
CellNr	Number reference to the electrochemical pouch cell that was used
ExperimentNr	Number reference to the cycling experiment
CapAh	Capacity in Ah
EnWh	Energy in Wh
I	Current running through the cell
V	Voltage of the cell
Mode	Electrochemical mode: C for Charge, D for Discharge and R for Rest
ECTime	Time the current and voltage were measured. Closest available data point w.r.t. frame time

Table T2 Legend of EnrichedFramesTable

To ensure robust analysis, we selected and tracked all labelled grains that were consistently detected from the beginning to the end of the protocol and appeared in at least 35 frames. This post-processing step was necessary due to grain rotation. When a grain rotates—often as a result of contact with expanding or contracting neighboring particles—it may fall out of the Bragg condition, preventing further detection of its reflection.

For the selected grains, we tracked their  $\eta, \theta$  values and plotted their reflections in a 2D space across all protocol steps, as shown in Fig. 5.2. By analysing the number of peaks and their evolution in  $\theta$  over time, we classified the grains into three categories as described in the main text, based on when they exhibit FP, LFP, or both reflections during the various protocol steps.

## Electrochemical phase-field model

A physics-based electrochemical model was implied to fully characterize the thermodynamic origin of the kinetically induced memory effect.

The particle behavior was modeled by considering a Cahn-Hilliard phase-field formalism so that, given a normalized concentration  $\tilde{c} = \frac{c}{c_{max}}$ , the chemical potential of a particle with maximum concentration  $c_{max}$  is determined by the regular solution theory including the gradient energy penalty  $\kappa$  and the regular solution parameter  $\Omega$ :

$$\mu = \mu^\ominus + k_B T \ln \left( \frac{\tilde{c}}{1 - \tilde{c}} \right) + \Omega(1 - 2\tilde{c}) - \frac{\kappa}{c_{max}} \nabla^2 \tilde{c} \quad (E1)$$

where  $\mu^\ominus$  is the difference in chemical potential between the Li/Li<sup>+</sup> redox potential and the chemical potential of the material.

The solid concentration within the particle evolves according to linear irreversible thermodynamics:

$$\frac{dc}{dt} = \nabla \cdot \left( \frac{D}{k_B T} \nabla \mu \right) \quad (E2)$$

where  $D = D_0 c (1 - \tilde{c})$  is the lattice diffusivity with tracer diffusivity  $D_0$ .

For the case of LFP the reaction rate  $R$  at the particle surface is calculated by using the electro-limited case of Coupled Ion Electron Transfer Theory<sup>36,51</sup>

$$R(c, \eta) = k_0 (1 - \tilde{c}) \left( \frac{c_{Li^+}}{1 + e^{\frac{\eta_f}{k_B T}}} - \frac{\tilde{c}}{1 + e^{-\frac{\eta_f}{k_B T}}} \right) \operatorname{erfc} \left( \frac{\frac{\lambda}{k_B T} - \sqrt{\left( \frac{\eta_f}{k_B T} \right)^2 + 1} + \sqrt{\frac{\lambda}{k_B T}}}{2 \sqrt{\frac{\lambda}{k_B T}}} \right) \quad (E3)$$

which consider an exchange current density  $k_0$ , electrolyte concentration  $c_{Li^+}$ , reorganization energy  $\lambda$ , and formal overpotential  $\eta_f$ , to naturally reproduce the overpotential dependence and the concentration dependence of the reaction rate for LFP<sup>53</sup>. The formal overpotential is defined as

$$\eta_f = \eta + \frac{k_B T}{e} \ln \left( \frac{c_{Li^+}}{c} \right) \quad (E4)$$

where the overpotential is calculated, considering the solid phase electrical potential  $\phi_s$ , as  $\eta = \frac{\mu - \mu_{Li^+}}{e} + \phi_s$ . Finally, we clarify here some differences in the modeling for the cases of LTO and NMC811.

Given the good electrical conductivity of LTO<sup>15</sup> we speculate the correct approximation for the reaction rate to be the ion-couple electron transfer<sup>36</sup>:

$$R = k_0(1 - \tilde{c})\sqrt{\tilde{c} c_{Li^+}} \left( e^{\frac{1}{2} \frac{e\eta}{k_B T}} - e^{-\frac{1}{2} \frac{e\eta}{k_B T}} \right) \quad (E5)$$

Moreover, NMC811 was simulated following the more common approach to electrochemical modeling given its efficacy in the simulation of solid solution materials.

The mass conservation is considered to follow Fick's law

$$\frac{dc}{dt} = \nabla \cdot (D(\tilde{c})\nabla c) \quad (E6)$$

and the reaction rate is approximated by the Butler-Volmer equation

$$R = k_0(\tilde{c})\sqrt{c_{Li^+}} \left( e^{\frac{1}{2} \frac{e\eta}{k_B T}} - e^{-\frac{1}{2} \frac{e\eta}{k_B T}} \right) \quad (E7)$$

Where the diffusion and the exchange current density dependence on concentration and the open circuit voltage are fitted from the work of McClelland, et al.<sup>34,54</sup>:

$$D(\tilde{c}) = D_0 10^{(-66631.56 \tilde{c}^9 + 317224.13 \tilde{c}^8 + -647127.91 \tilde{c}^7 + 740625.61 \tilde{c}^6 + -522889.49 \tilde{c}^5 + 235652.79 \tilde{c}^4 + -67638.171 \tilde{c}^3 + 11887.013 \tilde{c}^2 + -1155.894 \tilde{c} + 37.601)},$$

$$k_0(\tilde{c}) = k_0(87.15 \tilde{c}^5 - 445.05 \tilde{c}^4 + 815.43 \tilde{c}^3 - 669.95 \tilde{c}^2 + 236.09 \tilde{c} - 23.67),$$

$$\begin{aligned} \mu = & -k_B T \left( -0.8090 \tilde{c} + 4.4875 - 0.0428 \tanh(18.5138 (\tilde{c} - 0.5542)) \right. \\ & \left. - 17.7326 \tanh(15.7890 (\tilde{c} - 0.3117)) \right. \\ & \left. + 17.5842 \tanh(15.9308 (\tilde{c} - 0.3120)) \right). \end{aligned}$$

Both ionic and electronic losses along the thickness of the electrode are simulated by the commonly implied porous electrode theory. The ionic flux is considered to respect electroneutrality so that the mass and charge conservation are formalized as:

$$\varepsilon \frac{dc_{Li^+}}{dt} = \nabla \cdot (\varepsilon D_{amb} \nabla c) - \nabla \cdot \left( \frac{t^i \mathbf{i}}{e} \right) - e R_V, \quad (E8)$$

$$0 = \nabla \cdot \mathbf{i}_i - e R_V, \quad (E9)$$

Where  $R_V$  is the volume-average reaction rate from the reaction occurring in the volume,  $\mathbf{i}_i$  is the ionic current density,  $\varepsilon$  is the porosity and  $e$  is the electron charge. Specifically, the current is calculated according to the Stefan-Maxwell model for concentrated solution theory.

The electrical conductivity along the depth of the electrode is also simulated by considering charge conservation and Ohm's law:

$$0 = -\nabla \cdot \mathbf{i}_e - e R_V \quad (E10)$$

$$\mathbf{i}_e = -\frac{1 - \varepsilon}{\tau} \sigma \nabla \varphi_s \quad (E11)$$

$\mathbf{i}_e$  is the electrical current,  $\tau$  is the tortuosity,  $\sigma$  is the electrical conductivity of the mixture of carbon black and LFP and  $\varphi_s$  is the electrical potential of the solid phase.

In addition to the standard porous electrode theory model, due to the known limited electrical conductivity of LFP particles, we considered a wiring model along the volume for the LFP simulations. In particular, the particles in the volume are randomly generated having sizes following the experimental particle size distribution. The list of particles in the specific volume is then sorted by decreasing size and considered aligned along the discrete volume. This is done to account for the better electrical connection of bigger particles. The first particle in the volume at depth  $x$  will then be in contact with the carbon black having so electrical potential  $\varphi_s(x)$ . The rest of the particles are wired to it, following a transmission line model, as previously adopted<sup>9</sup>,

so that, given a particle conductance  $G$  and being  $\Delta\phi_{k,k+1}$  the potential difference between particle  $k$  and  $k + 1$  the local charge conservation requires

$$G(\Delta\phi_{k-1,k} - \Delta\phi_{k,k+1}) = -eR_k \quad (E12)$$

for the particle  $k$  having a reaction rate  $R_k$ .

This addition, while increasing the fitting capabilities of the model, does not modify sensibly the kinetic of the system and does not influence the conclusion on the role of diffusion and reaction overpotentials in the appearance of the kinetically induced memory effect. In fact, the good carbon coating of the particles under exam guarantees high intra-particle conductivity and generates negligible overpotentials.

Finally, for numerical reasons, the homogenous part of the chemical potential  $\mu_{homog}$  was approximated by:

$$\mu_{homog} = k_B T \left\{ -3.405 - 15 \exp\left(-\frac{\tilde{c} - 0.02}{0.02}\right) + (1.5 - 4.3\tilde{c}) \left[ \frac{1}{2} \tanh\left(\frac{\tilde{c} - 0.03}{0.05}\right) \right] + 20 \left[ \frac{1}{2} \tanh\left(\frac{\tilde{c} - 1}{0.06}\right) \right] \right\} \quad (E13)$$

This closely follows the regular solution chemical potential defined above but avoids logarithmic terms which are detrimental to the numerical stability of the simulation.

The remaining set of equations is described in the work defining the software MPET<sup>14</sup> used for the simulations.

## Parameters of the electrochemical phase-field model

The exchange current density is of primary importance in determining the saturation current for the kinetically induced memory effect. It is therefore important to elaborate on the different functional forms assumed by the model describing its relationship with concentration and overpotential.

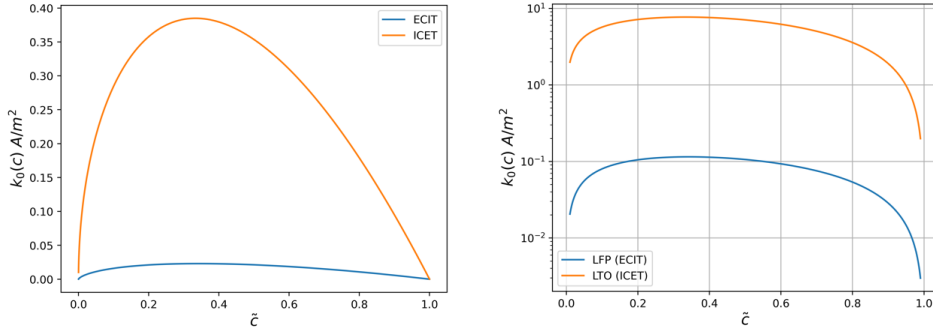


Figure S22. Comparison between Electron-limited (ECIT) and Ion-limited (ICET) formalism. Comparison between ECIT and ICET for the case of  $k_0 = 1 \text{ A m}^{-2}$  (left). Comparison between the exchange current densities of LFP and LTO used in this study (right).

5

Given the different approximations used the real values assumed by the exchange current densities differ significantly. If the same pre-factor  $k_0$  is used, ICET predicts a maximum exchange current density 16 times greater than ECIT. Using then the values obtained by fitting the memory protocols for LFP and LTO we can see how the real implied values differ by 2 orders of magnitude in line with the known low exchange current density of LFP<sup>55</sup>.

Given the known low electrical conductivity of bulk LFP and the fundamental role of carbon coating in enhancing this feature, we approximated the inter-particle conductance as proportional to the amorphous carbon conductivity and coating thickness  $G = \sigma_{carbon} t_{coating}$ . Considering  $\sigma_{carbon} \sim 10^{-2} \text{ S m}^{-1}$  and  $t_{coating} = 10 \text{ nm}$  we obtain  $G \sim 10^{-10} \text{ S}$ . This value was then used as a reference value for the parameter estimation.

In LFP, the fast single-file diffusion along the [010] direction can only be properly exploited in platelet-shaped particles. On the contrary, in spheroidal commercial particles, we can expect a shirking core behavior<sup>56</sup> and a greater amount of defects<sup>57</sup> leading to an effective low tracer diffusivity.

<b><i>Material parameters</i></b>		
Enthalpy of mixing ( $\Omega$ )	$1.85 \cdot 10^{-20}$ J/Li	Ref <sup>14</sup>
Gradient penalty ( $\kappa$ )	$10 \cdot 10^{-10}$ J/m	Ref <sup>14</sup>
Tracer diffusivity ( $D_0$ )	$0.75 \cdot 10^{-16}$ m <sup>2</sup> /s	Best-fit
Exchange current density ( $k_0$ )	5 A/m <sup>2</sup>	Best-fit
Reorganization Energy ( $\lambda$ )	$3.4 \cdot 10^{-20}$ J	Ref <sup>55</sup>
<b><i>Electrode parameters</i></b>		
Average particle radius	100 nm	Measured
Standard deviation particle radius	50 nm	Measured
Electrode thickness	85 $\mu$ m	Measured
Electrode porosity	55%	Measured
Active material volume loading	85 %	Measured
Number of particles	40	
Bruggeman exponent	1.8	Best-fit
Electrical conductivity ( $\sigma$ )	0.4 S/m	Best-fit
Inter-particle conductance ( $G$ )	$0.8 \cdot 10^{-10}$ S	Best-fit

Table T3 Parameters used for the electrochemical model of LiFePO<sub>4</sub>.

<b><i>Material parameters</i></b>		
Enthalpy of mixing ( $\Omega$ )	$1.43 \cdot 10^{-20}$ J/Li	Ref <sup>14</sup>
Gradient penalty ( $\kappa$ )	$2.5 \cdot 10^{-10}$ J/m	Ref <sup>15</sup>
Tracer diffusivity ( $D_0$ )	$4 \cdot 10^{-16}$ m <sup>2</sup> /s	Ref <sup>15</sup>
Exchange current density ( $k_0$ )	20 A/m <sup>2</sup>	Arbitrary
<b><i>Electrode parameters</i></b>		
Average particle radius	100 nm	Measured <sup>15</sup>
Standard deviation particle radius	50 nm	Measured <sup>15</sup>
Electrode thickness	85 $\mu$ m	Measured
Electrode porosity	30%	Measured
Active material volume loading	57 %	Measured
Number of particles	32	
Bruggeman exponent	0.5	Ref <sup>15</sup>
Electrical conductivity ( $\sigma$ )	1 S/m	Arbitrary
Inter-particle conductance ( $G$ )	$1 \cdot 10^{-11}$ S	Arbitrary

Table T4 Parameters used for the electrochemical model of Li<sub>4</sub>Ti<sub>5</sub>O<sub>12</sub>.

<b>Material parameters</b>		
Diffusivity perfector ( $D_0$ )	10	Arbitrary
Exchange current density ( $k_0$ )	3 A/m <sup>2</sup>	Arbitrary
<b>Electrode parameters</b>		
Average particle radius	10 $\mu\text{m}$	Arbitrary
Standard deviation particle radius	5 $\mu\text{m}$	Arbitrary
Electrode thickness	65 $\mu\text{m}$	Measured
Electrode porosity	30%	Measured
Active material volume loading	57 %	Measured
Number of particles	80	
Bruggeman exponent	0.5	Ref <sup>15</sup>
Electrical conductivity ( $\sigma$ )	1 S/m	Arbitrary

Table T5 Parameters used for the electrochemical model of  $\text{LiNi}_{0.8}\text{Mn}_{0.1}\text{Co}_{0.1}\text{O}_2$ .

## Analytical model

The analytical formula presented in the main text was obtained by considering the following approximations. The electrochemical phase-field model showed the minimal impact of the long-range ionic and electronic transport on the total overpotential. This is due to the high porosity and low mass loading of the electrode under examination. We can so neglect these phenomena and assume that the electrode reacts uniformly along the thickness direction.

The geometrical parameters of the electrode can be used to compute its surface area, key parameter determining its performance. Assuming all the particles having spherical shape and radius  $R$ , we compute the total number of particles as

$$N_p = \frac{A t (1 - \varepsilon) v}{\frac{4}{3} \pi R^3} \quad (E14)$$

Where we considered the electrode area  $A$ , thickness  $t$ , porosity  $\varepsilon$  and volume fraction of active material  $v$ . The total surface area will so be  $S = N_p 4 \pi R^2$ .

Despite the full model implying CIET theory for the reaction kinetics, that formalism does not allow a direct solution of the reaction overpotential ( $\eta_{rxn}$ ). To avoid iterative procedures and obtain a purely analytical solution we approximate the reaction kinetics with the symmetric form of the Butler-Volmer equation:

$$i_R = S_r j_0 \left( e^{\alpha \frac{e\eta_{rxn}}{k_B T}} - e^{-(1-\alpha) \frac{e\eta_{rxn}}{k_B T}} \right) \quad (E15)$$

Where  $i_R$  is the total current at a given C-rate,  $S_r$  is the reactive surface area,  $j_0$  is the exchange current density, and  $\alpha$  is the charge transfer coefficient that is approximated to be 0.5 in this solution. Assuming that all the available active particles are utilized by the reading current, the reaction overpotential ( $\eta_{rxn}$ ) can be so expressed as

$$\eta_{rxn} \cong \frac{k_B T}{e} \sinh^{-1} \left( \frac{i_R}{2 j_0 S_r} \right) \quad (E16)$$

The exchange current density is, generally, a function of the concentration, and thus it is evolving during the reaction process. Nevertheless, for phase-separated particles, after a relaxation process the appearing core-shell structure expose reliably a consistent (de)lithiated phase. Since our goal is to compute the initial overpotential we can consider  $j_0$  assuming the value at the corresponding equilibrium concentration. Considering now the reactive surface area will so be proportional to total surface area  $S$  and the active particle fraction  $f$  we arrive at Eq. 1 of the main text.

The diffusion overpotential ( $\eta_{diff}$ ) can also be computed considering a similar framework. The relaxed structure of a phase-separated particle present on the outer surface a single phase having an equilibrium concentration  $c_{eq}$ . Considering small deviation from  $c_{eq}$  the diffusion overpotential can be approximated by knowing the surface concentration  $c_s$  as  $\eta_{diff} = \frac{k_B T}{e} (\ln c_s - \ln c_{eq})$ . The relation between  $c_s$  and  $c_{eq}$  is given by a mass transfer coefficient  $k_m$  so that

$$c_s = c_{eq} + \frac{j_p}{e k_m} \quad (E17)$$

where the specific current on the particle  $j_p$  relates to the total surface area and active particle fraction:

$$j_p = \frac{i_R}{S f} \quad (E18)$$

Combining these equations, we reach to Eq. 2 of the main text. The mass transfer coefficient can be related to the diffusion coefficient by approximating the flux as 1D and planar so that  $k_m = D/L$  where  $L$  is the diffusion length. Assuming  $R$  as diffusion length we can relate the

diffusivity and the active particle fraction with the diffusion overpotential. It must be noted that, being a phase-separating material, the effective diffusivity used in this approximation does not necessarily coincide with the tracer diffusivity used for the phase field model. However, it is safe to assume it should have the same order of magnitude.

The analytical approximation was to the experimental data fitted by using a differential evolution algorithm. The algorithm was chosen to assure a wide exploration of the parameter space and obtain a reliable set of parameters that could minimize the error. The initial guess was given based on the parameters of the electrochemical phase-field model and the values of diffusivity ( $D$ ) and exchange current density ( $j_0$ ) were bounded to be within the same order of magnitude as the electrochemical parameters.

Effective Diffusivity ( $D$ )	$0.16 \cdot 10^{-16} \text{ m}^2/\text{s}$	Best-fit
Exchange current density ( $j_0$ )	$0.594 \cdot 10^{-3} \text{ A/m}^2$	Best-fit
Maximum active particle fraction ( $f_{max}$ )	0.424	From phase-field
$w$	2.24	Best-fit
$b$	0.844	Best-fit
Particle radius ( $R$ )	200 nm	From phase-field
Electrode thickness ( $t$ )	85 $\mu\text{m}$	Measured
Electrode porosity ( $\epsilon$ )	55%	Measured
Active material volume loading ( $v$ )	85 %	Measured

Table T6 Parameters used for the overpotential approximation of  $\text{LiFePO}_4$ .

Effective Diffusivity ( $D$ )	$0.647 \cdot 10^{-17} \text{ m}^2/\text{s}$	Best-fit
Exchange current density ( $j_0$ )	$1 \text{ A/m}^2$	Best-fit
Maximum active particle fraction ( $f_{max}$ )	0.796	Best-fit
$w$	0.26	Best-fit
$b$	8.98	Best-fit
Particle radius ( $R$ )	200 nm	From phase-field
Electrode thickness ( $t$ )	85 $\mu\text{m}$	Measured
Electrode porosity ( $\epsilon$ )	30%	Measured
Active material volume loading ( $v$ )	57 %	Measured

Table T7 Parameters used for the overpotential approximation of  $\text{Li}_4\text{Ti}_5\text{O}_{12}$ .





# 6 THE IMPEDANCE RESPONSE OF PHASE SEPARATING ELECTRODES

## ABSTRACT

Electrochemical impedance spectroscopy (EIS) is a powerful technique for rapidly and reliably characterizing the performance and state of battery electrodes. Its full potential is realized when the data are interpreted through a physics-based framework. By mapping impedance spectra to physically meaningful quantities, EIS becomes not only a tool for data-driven analysis but also a valuable aid in the research and development of electrode materials and architectures. Current state-of-the-art methods are well suited for homogeneous systems under equilibrium conditions. However, many practical electrode materials, such as  $\text{LiFePO}_4$  (LFP), graphite, and  $\text{Na}_3\text{V}_2(\text{PO}_4)_3$  (NVP), undergo phase separation into regions with distinct solid-state concentrations, even at equilibrium. This complexity has limited the applicability of conventional EIS interpretation techniques, hindering efforts to assess their performance, degradation mechanisms, and state of charge. To address this gap, we employ advanced phase-field electrochemical models to investigate the impedance response of phase-separating materials. Our results reveal previously unexplained features, such as charge–discharge asymmetries and anomalous low-frequency behavior, as natural consequences of phase separation dynamics. These findings lay the groundwork for a physics based interpretation of the impedance of multi-phase materials. By bridging the gap between rich physical behavior and impedance signatures, this work opens the door to accurate, predictive, and material-specific uses of EIS in battery research and engineering.

## 6.1 INTRODUCTION

The impedance response of battery electrodes is a key nondestructive technique that provides insight into the transport and reaction phenomena occurring within a battery<sup>1</sup>. As a result, electrochemical impedance spectroscopy (EIS) has been widely used to assess various aspects of electrode behavior, including power output prediction and degradation monitoring<sup>2</sup>. EIS measurements are relatively accessible and, when supported by the appropriate instrumentation, can also be performed *in situ* during battery operation<sup>3–5</sup> to yield valuable diagnostic information in a compact data framework<sup>2</sup>.

Impedance spectra consist of real and imaginary components of impedance and can be interpreted using different approaches. One of the most common is the use of equivalent circuit models (ECMs), which allow fitting of experimental data and translation into semi-physical parameters such as charge-transfer resistance<sup>6</sup>, double-layer capacitance, solid diffusivities<sup>7,8</sup>, and ionic and electronic conductivities in the electrolyte and composite electrode<sup>9</sup>. These circuits are constructed as analogs of the electrochemical system<sup>10</sup>. For instance, a reactive interface may be modeled as an RC element, with a resistor and capacitor in parallel representing the charge-transfer resistance and double-layer capacitance, respectively<sup>1</sup>. If solid-state diffusion is present, a Warburg-type impedance element can be incorporated<sup>8</sup>. These basic components can be extended and arranged in series or parallel to represent more complex systems with interacting phases<sup>7</sup>. For example, transmission-line models, with or without charge-transfer elements, are often used to describe transport processes within porous electrodes where reactions and double-layer formation occur throughout the electrode thickness<sup>1,9</sup>.

This approach is grounded in the linearization of the underlying physical phenomena: although electrochemical processes are inherently nonlinear, at sufficiently small perturbation amplitudes their behavior can be linearized, enabling the derivation of circuit elements that represent the system's impedance response and yield physically meaningful parameters when fitting EIS data<sup>6,11,12</sup>.

However, relying on analytically solvable ECMs imposes limitations, requiring the assumption of homogeneity within the system. Alternatively, physics-based nonlinear models can simulate the behavior of porous electrodes by solving coupled partial differential equations that describe the transport and reaction processes<sup>13–18</sup>, delivering also valuable information on the coupling between phenomena. These models vary in fidelity, from fully three-dimensional<sup>19–21</sup> to pseudo-two-dimensional (P2D), with corresponding differences in computational cost. They can be used to simulate impedance spectra by applying small voltage or current perturbations in a virtual experiment (the brute-force, time-domain method)<sup>22,23</sup>. A noteworthy example of this procedure

is the prediction of an inductive behavior of phase-separated  $\text{LiFePO}_4$  particles<sup>23</sup>. This method can, in fact, capture any electrochemical system; however, it is computationally intensive.

Recent works provide a middle ground: computing the impedance directly from P2D models using their linearized, frequency-domain response obtained from the Jacobian of the governing equations<sup>24,25</sup>. In practice, the discretized equations are linearized at a chosen operating point, and the complex response to sinusoidal perturbations is evaluated without time-stepping. This frequency-domain method, made openly accessible by the symbolic framework offered by PyBaMM<sup>17</sup>, reproduces brute-force simulations closely while reducing the computational cost by orders of magnitude. Being applicable across any electrochemical model, it was used in previous works to clarify which parameters control distinct spectral features, with the goal of enabling parameter estimation from impedance data with improved identifiability<sup>11,22</sup>. This methodology has been shown to extrapolate reliably to the time domain, predicting dynamic load profiles with high fidelity.

In this work, we apply those methods to characterize the impedance response of phase-separating electrodes and to guide future experiments on this important class of battery materials. Unlike conventional solid-solution materials (e.g., layered oxides), phase-separating materials, such as  $\text{LiFePO}_4$ ,  $\text{LiMn}_x\text{Fe}_{1-x}\text{PO}_4$ ,  $\text{Li}_4\text{Ti}_5\text{O}_{12}$ ,  $\text{LiMn}_2\text{O}_4$ , graphite, and  $\text{Na}_3\text{V}_2(\text{PO}_4)_3$ , exhibit markedly different dynamics<sup>19,26–34</sup>. Due to their thermodynamic tendency to separate into Li-rich and Li-poor phases, both inter-particle and intra-particle phase separation can occur during (de)lithiation. The specific mode depends on multiple factors, including particle size, electrode thickness, and applied rate<sup>28,35–39</sup>. Moreover, their dynamic response can be characterized by the presence of different phases between external and internal layers, and these structures can evolve in a path-dependent manner.

To model these systems, conventional Doyle–Fuller–Newman (DFN) models<sup>13–15,40</sup> have been extended to account for phase separation by embedding phase-field methods within the particle description, creating the multiphase porous electrode theory (MPET)<sup>16,18,41,42</sup>. By coupling phase-field formulations with thermodynamically consistent chemical potentials, it is possible to capture the complex response of phase-separating materials across multiple conditions and to explain a broad set of experimental observations, including memory effects<sup>28,36</sup>, thermodynamic hysteresis<sup>27,42</sup>, and rate-dependent ensemble dynamics<sup>37</sup>.

Given their inherently complex dynamics and the presence of multiple phases, the impedance of phase-separating electrodes becomes excessively complex to be comprehensively captured using ECMs. The assumptions of homogeneity and symmetry break down, rendering analytical solutions unfeasible and obscuring parameter identifiability. To overcome these challenges, we use an MPET-based model representative of an archetypical phase-separating material, akin to

$\text{LiFePO}_4$ . We then compute its impedance response using both the linearized frequency-domain method and the brute-force time domain method, preserving rigor while maintaining computational tractability<sup>24</sup>.

We could elucidate the impedance response of phase-separating systems under different operating and design conditions (state of charge, electrode thickness, and history). The results indicate that phase-separating materials exhibit rate-dependent and path-dependent impedance with uncommon low-frequency features that arise from the kinetics of phase-boundary motion. We discuss how these signatures should be interpreted, how they differ from solid-solution electrodes. The results suggest how these features can be leveraged to design informative impedance experiments on phase-separating materials.

## 6.2 CAHN-HILLIARD REACTION MODEL

To capture the impedance of phase-separating electrodes within a porous-electrode framework, we start from the standard Doyle–Fuller–Newman (DFN) model and modify the particle description. In the standard DFN formulation, each particle is assumed to obey Fick’s law<sup>13</sup>. This is applicable to solid-solution materials, but cannot capture the internal dynamics of a phase-separating electrode, where Li-rich and Li-poor phases can coexist inside a single particle. To describe this behavior, we replace the Fickian solid-state transport equation with a Cahn–Hilliard–reaction (CHR) model<sup>28,32,42,43</sup>.

By adopting this formulation, we implicitly assume that the active material particles are diffusion-limited and that a shrinking-core mechanism is triggered during (de)lithiation<sup>44</sup>. This assumption will not always hold: in some materials the rate-limiting step is not solid-state transport but the interfacial reaction. In such cases, alternative descriptions, such as the Allen–Cahn–reaction (ACR) model, may be more appropriate<sup>20,26,41</sup>. While the ACR approach has been successfully applied to interpret experimental data<sup>26,29,37,45,46</sup>, it neglects diffusion entirely. Therefore, as shown in the work of Zelič et al.<sup>23</sup>, it cannot reproduce the low-frequency tail originating from solid diffusion, while still capturing phase separation. A complete description of reaction-limited systems would require a fully two-dimensional or three-dimensional particle model<sup>47</sup>. The computational cost of such simulations, however, is currently beyond what is practical for systematic impedance calculations.

In the CHR description, the dependent variable  $\tilde{c}(r, t)$  is the normalized lithium concentration in the solid. The lithium chemical potential is given by a regular solution model<sup>27,48</sup>

$$\mu(\tilde{c}) = \mu_0 + k_B T \ln\left(\frac{\tilde{c}}{1-\tilde{c}}\right) + \Theta(1-2\tilde{c}) - \kappa \nabla^2 \tilde{c} \quad (6.1)$$

where  $\mu_0 = -V_0 e$  sets the reference potential relative to Li/Li<sup>+</sup>,  $k_B$  is the Boltzmann constant,  $T$  is the absolute temperature,  $\Theta$  is the regular solution interaction parameter controlling the miscibility gap, and  $\kappa$  is the gradient-energy term that penalizes concentration gradients and sets the interface width, providing a natural description of the phase boundary. Solid transport then follows

$$\frac{\partial \tilde{c}}{\partial t} = \nabla \cdot \left[ D \tilde{c}(1-\tilde{c}) \nabla \left( \frac{\mu}{k_B T} \right) \right] \quad (6.2)$$

in spherical symmetry, with  $\partial_r |_{r=0} \tilde{c} = 0$  at  $r = 0$  and constant surface energy at  $r = R$  ( $\partial_r |_{r=R} \tilde{c} = \partial \gamma / \partial \tilde{c} = 0$ ). The diffusive flux at the surface couples directly to the interfacial reaction current density  $j$ .

The open circuit potential  $U(\tilde{c})$  comes directly from the surface chemical potential:

$$U(\tilde{c}) = -\frac{\mu(\tilde{c})}{e} \Big|_{r=R} \quad (6.3)$$

so that

$$\eta = \phi_s - \phi_e - U(\tilde{c}) \quad (6.4)$$

where  $\phi_s$  is the solid-phase potential in the active material, and  $\phi_e$  is the electrolyte potential in the adjacent pore. In the DFN framework, both  $\phi_s$  and  $\phi_e$  are obtained by solving the porous-electrode charge-conservation equations.

For the interfacial kinetics, we use the ion-coupled electron transfer approximation (ICET)<sup>49</sup>:

$$j = j_0(\tilde{c}) \left( e^{-\alpha \frac{e\eta}{k_B T}} - e^{(1-\alpha) \frac{e\eta}{k_B T}} \right) \quad (6.5)$$

with

$$j_0 = k_0 \tilde{c}_e^{1-\alpha} \tilde{c}^\alpha (1-\tilde{c}) \quad (6.6)$$

where  $\tilde{c}_e$  is the dimensionless electrolyte concentration and  $k_0$  is the prefactor that depends on the properties of the electrode-electrolyte interface. Notably, also for  $\alpha = 0.5$ , the factor  $\tilde{c}^\alpha(1 - \tilde{c})$  makes  $j_0$  intrinsically asymmetric. Moreover, a constant double-layer specific capacitance  $C_{dl}$  is assigned to each particle surface. By embedding the presented particle dynamics into a porous electrode model, we arrive at the MPET framework: the DFN's physics is preserved, but each particle can now phase-separate internally. Within this framework, we study three cases.

Single particle model (SPM-CHR): a single particle evolving according to CHR dynamics, in contact with an electrolyte reservoir at fixed concentration and potential. In this limit, the electrolyte potential is set to  $\phi_e = 0$ , and the solid-phase potential  $\phi_s$  is simply the applied particle voltage. This isolates the intrinsic impedance features that arise purely from intra-particle phase dynamics, without electrode-scale effects.

DFN-CHR: a porous electrode resolved along its thickness where all particles are identical spheres evolving according to CHR dynamics. This adds electrolyte and electronic transport through the porous structure, showing how electrode-level phase separation manifests in the impedance.

Multi-particle DFN-CHR: the most general case, in which each electrode control volume contains a particle size distribution. Given particles of surface  $S_i$  and volume  $V_i$ , occurring with a number density  $n_i$  ( $\sum_i n_i = 1$ ), the local reaction term ( $R$ ) and the specific surface area ( $a$ ) are weighted according to  $f_i$  and their surface-to-volume ratio:

$$R = \frac{\varepsilon_s \sum_i n_i S_i j_i}{e \sum_i n_i V_i} \quad (6.7)$$

$$a = \varepsilon_s \frac{\sum_i n_i S_i}{\sum_i n_i V_i} \quad (6.8)$$

This level captures the combined effects of particle-size heterogeneity, spatial variations in reactivity, and phase separation.

For all cases discussed in this work, the impedance response was computed as follows: the electrode is initialized at a filling fraction of 0.01 (or 0.99 for delithiation) and (de)lithiated at constant current until a target filling fraction is reached. The system is then held under open-circuit conditions for 4 hours. At this point, the impedance is computed using the final solution, with 200 logarithmically spaced frequencies ranging from  $10^{-4}$  to  $10^3$  Hz. In our simulations, an ideal reference electrode is placed inside the separator, positioned 5  $\mu\text{m}$  away from the porous

electrode surface. This configuration lets us compute the half-cell impedance as it would be measured experimentally, while removing most of the electrolyte ohmic drop in the separator and the counter electrode response. Importantly, during the impedance computation, the frequency-based solver linearizes about the fixed state, effectively “freezing” the system variables<sup>24</sup>.

### 6.3 CHARGE TRANSFER RESISTANCE IN PHASE-SEPARATING MATERIALS

The thermodynamically consistent framework hereby employed constrains the particles to a defined set of states. As shown in Fig. 6.1, with  $\Theta = 80$  meV, the spinodal limits (onset of instability of a homogeneous particle) occur at  $\tilde{c}_{\text{spin}}^{\text{poor}} = 0.2$  and  $\tilde{c}_{\text{spin}}^{\text{rich}} = 0.8$ . When the concentration overcomes this point, the phase separation begins, and the surface composition jumps to the opposite binodal side ( $\tilde{c}_{\text{bin}}^{\text{rich}}$  for lithiation,  $\tilde{c}_{\text{bin}}^{\text{poor}}$  for delithiation). Specifically, the binodal concentrations correspond to the values on either side of the gap having the same potential, i.e.  $U(\tilde{c}_{\text{bin}}^{\text{poor}}) = U(\tilde{c}_{\text{bin}}^{\text{rich}}) = V_0$ . After the jump, a core-shell structure forms, and the reaction forces the interface to migrate towards the center. During this two-phase stage, the surface composition stays near the binodal. Only once the interface annihilates at the center, the particle returns to a single phase<sup>43</sup>. If the current is interrupted during this sequence, the particle ensemble might relax towards a metastable state with multiple particles remaining phase separated<sup>28,35,36</sup>, with higher rates leading to a higher fraction of phase separated particles<sup>28</sup>. The resulting open circuit potential is therefore influenced by the previous rate and results in between the reference value ( $V_0$ ) and the hysteresis value ( $U(\tilde{c}_{\text{spin}}^{\text{poor}})$  for lithiation, or  $U(\tilde{c}_{\text{spin}}^{\text{rich}})$  for delithiation). In other words, high rates can induce the voltage to enter the hysteresis window<sup>35</sup>.

If instead the electrode evolves close to equilibrium (at extremely low rates) the energy of the system is minimized by maintaining homogenous particles, so that each particle will quickly equilibrate to the same potential<sup>50</sup>. This is usually referred to as particle-by-particle insertion<sup>37</sup>, with the voltage tracing the familiar hysteresis branches (lithiation vs. delithiation). When the current is halted, the system will be composed of either fully lithiated or fully delithiated particles, and the equilibrium potential will correspond to  $U(\tilde{c}_{\text{spin}}^{\text{poor}})$  for lithiation or  $U(\tilde{c}_{\text{spin}}^{\text{rich}})$  for delithiation.

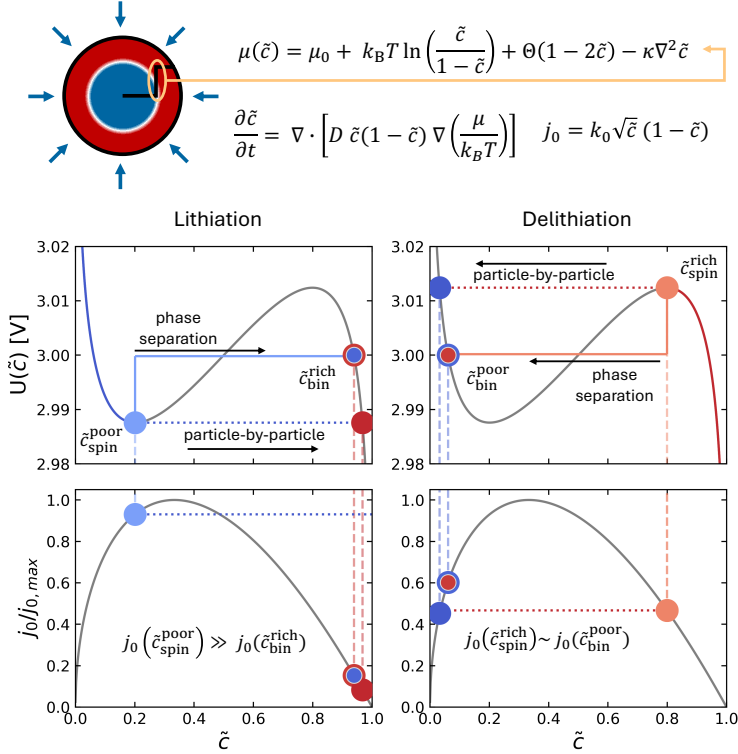


Figure 6.1. Schematic representation of the Cahn–Hilliard–reaction (CHR) model and ICET exchange current density. The open-circuit potential ( $U(\tilde{c})$ ) and normalized exchange current density ( $j_0/j_{0,max}$ ) profiles are compared during lithiation and delithiation with the corresponding values of  $U$  and  $j_0$  at the binodal and spinodal points.

Because of the asymmetric relation between the exchange current density and the solid concentration ( $j_0 \propto \tilde{c}^{0.5} (1 - \tilde{c})$ ), these limited surface compositions have a profound impact on the charge-transfer resistance. As illustrated in Fig. 6.1, both in case particle-by-particle lithiation and intra-particle phase separation, the Li-rich and Li-poor surfaces present drastically different charge transfer resistances. On the contrary, during delithiation, the exchange current densities of the Li-rich and the Li-poor phases result almost identical, suggesting no visible changes in charge transfer resistance in these conditions. While this result originates from the specific choice of  $\Omega$  and  $\alpha$ , CIET theory and experimental results confirm  $j_0$  having a similar trend to the one we included in the model<sup>26,49</sup>. Therefore, we expect generally to observe greater evolution of charge transfer resistance during lithiation than during delithiation, leading to a strong path dependence, severely affecting the impedance of phase-separating porous electrodes.

## 6.4 THE IMPEDANCE OF THE SPM-CHR MODEL

To understand the impedance of electrodes composed of phase-separating materials, we begin by evaluating the impedance response of a single particle surrounded by an electrolyte held at fixed concentration and electrochemical potential, i.e., using the SPM-CHR model. The chosen parameters, representative of a realistic phase-separating electrode, can be found in the supplementary Information. The qualitative trends hereby described are general for SPM-CHR models, while the quantitative response might vary with the chosen parameters.

Fig. 6.2 shows the evolution of the impedance spectra for an SPM-CHR at various filling fractions. When the particle remains homogeneous, i.e. before entering the spinodal region, the Nyquist plot displays the typical features of a single reactive particle with solid-state diffusion: a high-frequency semicircle associated with charge transfer, followed by a diffusion tail that begins at  $45^\circ$  and transitions into a finite-length Warburg approaching capacitive limit<sup>8</sup>. This behavior is observed during both lithiation and delithiation at low (0.1) and high (0.9) filling fractions, respectively. It is consistent with analytical approximations for single-particle impedance, where the high-frequency region shows the charge transfer process, and the low-frequency regime depicts a diffusion process with reflective boundaries; since, under spherical symmetry, concentration oscillations cannot propagate beyond the particle center<sup>8</sup>.

Once the particle undergoes spinodal decomposition, i.e. within the miscibility gap, a sharp transition in the concentration profile occurs. Within this stoichiometric window, the system minimizes its free energy by forming a Li-rich and a Li-poor phase. Given the imposed spherical symmetry and the one-dimensional CHR approximation, the particle phase-separates radially. Depending on the lithiation direction, this results in a core-shell structure with either a Li-rich or Li-poor phase at the outer boundary.

As expected from the sudden shift in solid concentration at the particle–electrolyte interface, the high-frequency semicircle exhibits a discontinuous change alongside the impedance magnitude. Due to the asymmetry in the exchange current density, the sudden concentration jumps lead to an increased charge transfer resistance, while a reduction is observed following delithiation. Notably, since the surface concentration remains constant until the particle overcomes the miscibility gap at the end of (de)lithiation, the size of the charge transfer process remains effectively unchanged throughout the intermediate filling fractions. Therefore, the charge transfer resistance becomes path-dependent, as it is governed by the phase exposed at the surface, which varies with the reaction direction. The marked difference between lithiation and delithiation is also shown in Fig. S1.

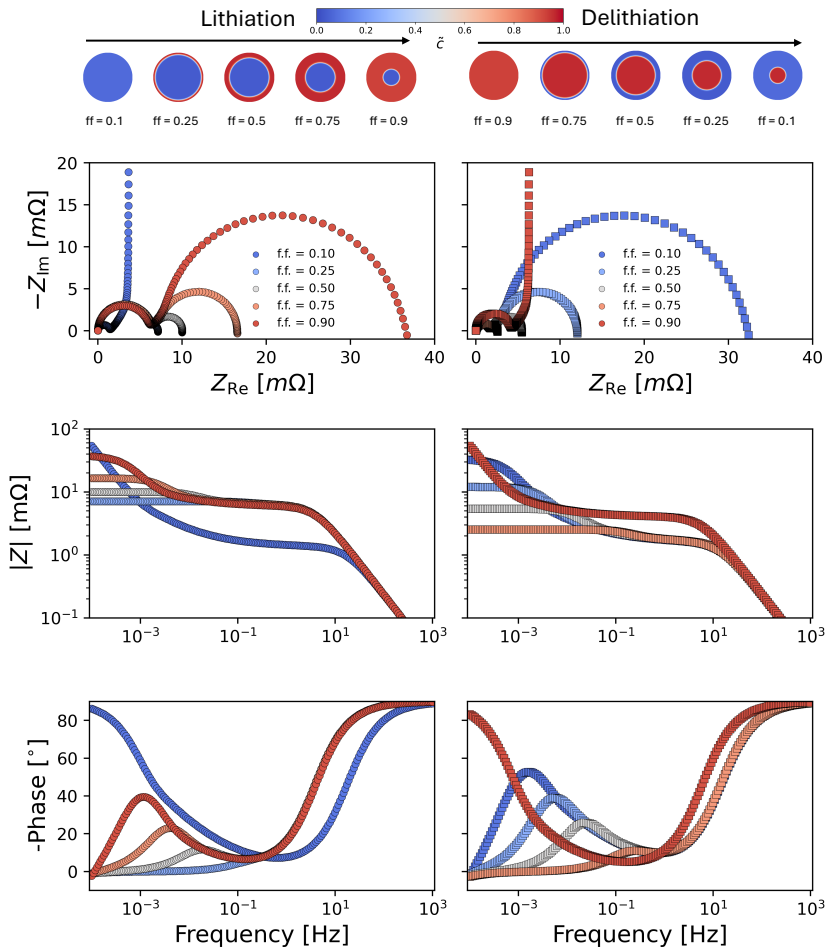


Figure 6.2. The impedance response of an SPM-CHR model. Above, the particle concentration profile at varying filling fractions. Below, the computed Nyquist and Bode plots at varying filling fractions following lithiation and delithiation. The SPM-CHR model was applied to an electrode of  $30\ \mu\text{m}$  in thickness and  $1\ \text{mAh cm}^{-2}$  loading.

More intriguing is the behavior at low frequencies. After the  $45^\circ$  slope in the mid-frequency region, the Nyquist plot exhibits a downward-bending arc instead of the conventional vertical diffusion line, and the Bode plot shows a flat magnitude plateau. This shift results from a change in boundary behavior: from reflective to effectively transmissive<sup>1</sup>. As concentration flux moves from the surface toward the center, it partially penetrates the phase boundary, producing a transmission-like effect. Consistent with analytical models for transmissive boundary diffusion<sup>1</sup>, the size of this secondary feature increases proportionally to the shift of the phase boundary

position, reflecting the longer timescales required for diffusion to reach the phase interface. The particle's impedance is so growing with the motion of the phase boundary.

These results suggest that an atypical feature may appear in diffusion-limited phase-separating material that evolves as shrinking-cores: the Nyquist plot may exhibit a second semicircle, potentially misleading interpretation by suggesting a secondary reaction process<sup>51</sup>. This feature might instead stem from the effects of intra-particle phase separation. Moreover, the second arc reaches negative values in the Nyquist and Bode plots, suggesting inductive behavior. These unexpected features were already predicted by Zelič et al.<sup>23</sup> for reaction-limited particles. Here, we show its presence in diffusion-limited core-shell structures, helping in the explanation of experimental results in diffusion-limited graphite particles<sup>52</sup>.

Finally, to further confirm the origin of these spectral features, we repeated the simulations with modified diffusion and reaction coefficients. In Supplementary Fig. S2, we observed that the high-frequency semicircle is sensitive to changes in the exchange current density prefactor ( $k_0$ ), while the low-frequency pseudo-semicircle depends solely on the diffusion coefficient and the position of the phase boundary.

## 6.5 THE IMPEDANCE OF THE DFN-CHR MODEL

The SPM-CHR yields intra-particle concentration profiles that depend solely on the filling fraction and the direction from which it is reached. By adopting a DFN-CHR framework, it becomes possible to explore how the impedance response varies based on electrode configuration, state of lithiation, reaction direction, and the influence of electrolyte transport within the porous electrode. We examine these effects on a 30  $\mu\text{m}$ -thick electrode, analyzing the system at various degrees of lithiation under pseudo-equilibrium conditions (after reaching the target filling fraction at a C-rate of 0.01C). Under these conditions, the electrode comprises either fully lithiated or delithiated particles, depending on their location relative to the separator.

Fig. 6.3 shows the evolution of the impedance spectra at different filling fractions and reaction directions. In the early stages, when the electrode remains homogeneous, the high-frequency region displays a squashed semicircle typical of transmission line behavior characteristic of porous electrode kinetics. At lower frequencies, an additional impedance component emerges, associated with electrolyte transport. To verify this, in Fig. S4, we show how this second feature vanishes when the electrode is extremely thin, while in Fig. S5 we present its dependence on the cation transference number. The low-frequency regime instead presents a diffusion tail, consistent with a uniform concentration profile across the electrode.

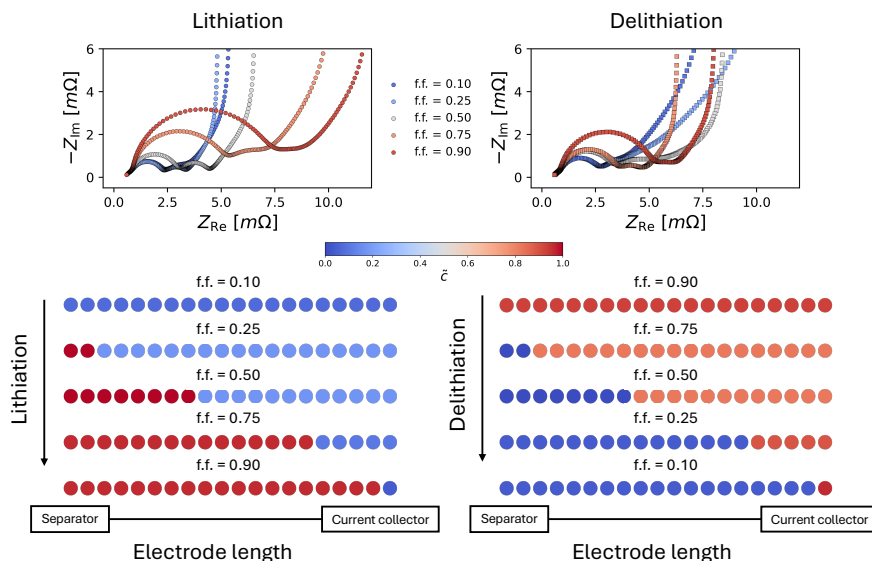


**Figure 6.3.** The impedance response of a CHR-DFN model. Above, the computed Nyquist plots at varying filling fractions following lithiation and delithiation. Below, the particle concentrations along the electrode length at varying filling fractions. The Bode plots are shown in Fig. S3.

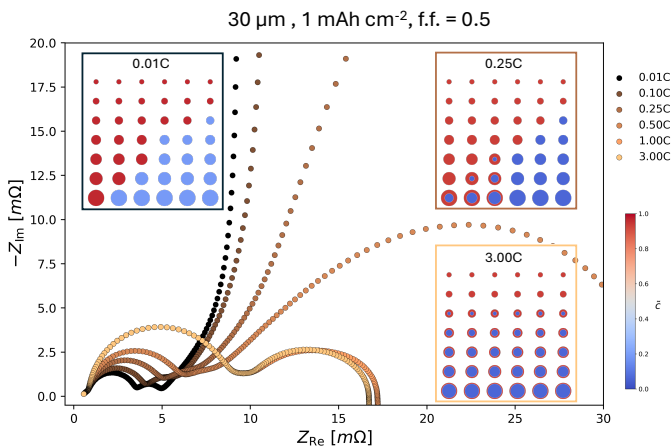
More compelling is the impedance evolution across various states of lithiation. During lithiation, the high-frequency semicircle grows with increasing filling fraction. This occurs because particles at higher lithiation exhibit reduced exchange current density, thereby increasing the overall charge transfer resistance. In contrast, during delithiation, the high-frequency semicircle remains unchanged within the miscibility gap of the particle ensemble. This is due to the limited difference between the charge transfer resistance of the Li-rich and Li-poor phases when the delithiation hysteresis branch is followed (Fig. 6.1). A change in the high-frequency component is therefore only observed when the system is outside the miscibility gap (f.f. = 0.10 and f.f. = 0.90).

This asymmetric behavior has been reported in experimental studies but remains insufficiently explained in literature<sup>33,53–58</sup>. Notably, in the work of Rue et al.<sup>53</sup> the charge transfer component of the spectra suddenly changes upon charging, also not showing any change with the progression of the charging protocol. Our findings provide a potential mechanistic explanation for this observation: the change in current direction pushes the voltage, and therefore the concentration, towards the upper part of the hysteresis loop (Fig. 6.1), where the charge transfer resistance of Li-rich and Li-poor phases converges to similar values. Notably, this behavior is now connected to the intrinsic thermodynamic hysteresis of phase separating multi-particle electrodes<sup>50</sup>, even when fully relaxed at spinodal concentrations.

## 6.6 THE IMPEDANCE OF THE MULTI-PARTICLE DFN-CHR MODEL

Having examined the effects of lithium distribution occurring under pseudo-equilibrium conditions, we now turn to the impact of introducing a particle size distribution using the multi-particle DFN-CHR model. When a population of particles is considered, both intra-particle and inter-particle phase separation can be observed<sup>28,32</sup>. The ionic distribution in the solid phase depends on the applied rate, with higher rates promoting a more uniform reaction across particles<sup>28,36</sup>. Consequently, even after prolonged open-circuit relaxation, the electrode retains a memory of the preceding current, with the fraction of phase-separated particles scaling with the prior rate<sup>28</sup>. A higher fraction of phase separated particles is so able to respond to subsequent currents producing lower overpotentials due to the more efficient distribution of the current.

To understand the effect of this phenomenon on the electrode's impedance we applied a protocol composed by three steps: the electrode is (de)lithiated to a filling fraction of 0.5 at a defined rate (from 0.01C to 3.0C), the system is kept under open circuit condition for 4 hours, finally, the impedance response is computed on the resulting state using the frequency-domain method.



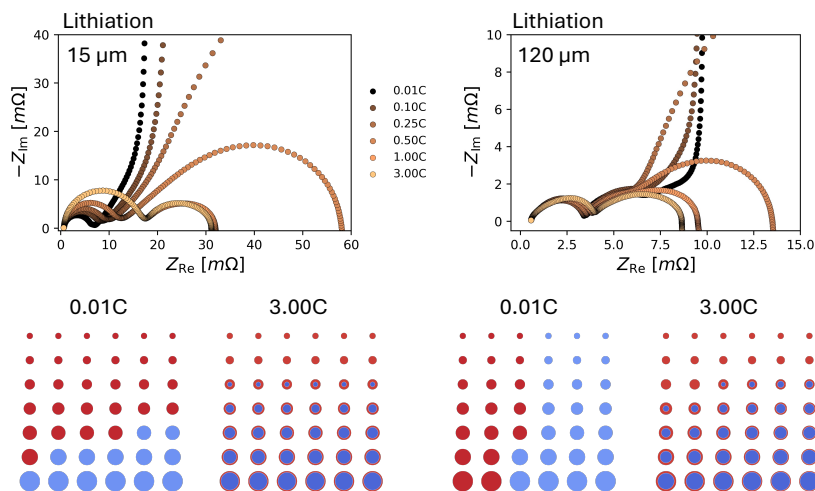
**Figure 6.4.** Impedance of a multi-particle CHR-DFN model of a thick electrode following a lithiation memory protocol. The Nyquist plot shows the impedance spectra computed at a filling fraction of 0.5 after applying different lithiation rates. Panels display the ionic concentration distribution for the 0.01C, 0.25C, and 3.0C cases, with the separator on the left and the current collector on the right.

Fig. 6.4 presents the results for a 30  $\mu\text{m}$  multi-particle electrode, where both electrolyte transport and particle dynamics influence the response. Under quasi-equilibrium conditions (0.01C), the electrode reaches a filling fraction of 0.5 with all particles remaining homogeneous, producing a mosaic-like inter-particle phase separation. In this state, small lithiated particles are distributed throughout the electrode, while larger lithiated particles appear closer to the separator. As the rate increases, more particles are phase-separated, exhibiting a core-shell structure. At moderate rates (0.25C), only a few large particles are phase-separated, whereas at high rates (3.0C), all particles participate in the reaction, resulting in small fully lithiated particles and large phase-separated ones.

This rate-dependent ionic distribution is mirrored in the impedance response, revealing a clear memory effect. Both the high-frequency and low-frequency regions of the spectrum vary significantly depending on the previously applied rate. At low rates, the spectrum displays the typical charge-transfer and electrolyte-transport arcs, followed by a diffusion tail, consistent with homogeneous particle filling. Notably, differences are already apparent between the 0.01C and 0.10C spectra, suggesting that extremely low rates might be necessary to assure homogenous particles when probing the SOC-dependent impedance of phase-separating materials. This behavior is consistent with the reported experimental results of phase-separating materials<sup>33,51,53–58</sup>. In fact, these results are often acquired after reaching the required filling fraction at a low rate, usually 0.1C, assuring homogenous particle-by-particle reactions.

At higher rates, the spectra change substantially. With more particles developing Li-rich surfaces, the high-frequency charge-transfer resistance increases. At the same time, the low-frequency region transitions from a vertical (reflective) tail to a broader, transmissive-like arc. As seen in the SPM-CHR case, this arises when phase boundaries permit partial transmission of concentration waves. In a multi-particle electrode, this effect is distributed: particles have phase boundaries at different depths, each contributing uniquely to the impedance. The result is a composite low-frequency response reflecting the variety of phase boundary positions across the population. While these observations are now extended to more realistic electrodes, to the best of our knowledge, no experiments have been reported where the electrode was (de)lithiated at high rates prior to the acquisition of the impedance data. The only partial exception is the work of Zhuang and Wei<sup>34</sup> where, despite having only applied 0.1C, the larger-sized  $\text{LiMn}_2\text{O}_4$  particles (8  $\mu\text{m}$ ) might still undergo intra-particle phase separation, explaining the presented third arching feature at intermediate lithiation degrees.

When comparing thinner (15  $\mu\text{m}$ ) and thicker (120  $\mu\text{m}$ ) electrodes, the manifestation of the memory effect becomes clearer (Fig. 6.5). In the thin electrode, particle size dominates the solid concentration distribution under quasi-equilibrium conditions: smaller particles complete lithiation, while larger ones remain unreacted, almost independently of their position. The resulting spectra are similar to the 30  $\mu\text{m}$  case, but without the electrolyte-transport feature.



**Figure 6.5.** Effect of electrode thickness on impedance following a lithiation memory protocol. The left panel shows a thin electrode ( $15\ \mu\text{m}$ ,  $0.5\ \text{mAh cm}^{-2}$ ) and the right panel a thick electrode ( $120\ \mu\text{m}$ ,  $4\ \text{mAh cm}^{-2}$ ). Both spectra are taken at a filling fraction of 0.5, with corresponding particle concentration maps for 0.01C and 3.0C shown below.

6

In thick electrodes, particle position plays a larger role. At any rate, particles near the separator fully lithiate, while those further away remain partially filled or totally empty. The low-frequency part of the spectrum still transitions from a vertical tail to transmissive-like arcs, but these arcs become more extended because they combine contributions from both phase-separated and homogeneous particles at different depths and with varying phase boundary positions. The high-frequency region shows the skewed semicircle characteristic of porous electrodes, but its size no longer changes noticeably with prior rate: at high frequencies, the perturbation only penetrates the region near the separator, which consistently presents a Li-rich surface. This could change, however, if electronic transport through the electrode cannot be neglected, in which case reacted particles might appear on both sides of the electrode with consequences on its impedance response.

A similar relation between the prior rate and the electrode's impedance is found during delithiation. Supplementary Fig. S6 shows a predictable consistency in the high-frequency feature, given by similar exchange current densities following delithiation (Fig. 6.1). The lower frequencies instead reproduce the rate-induced transition towards a diffusive arc.

## 6.7 BRUTE FORCE METHOD

To finalize the work, we place our attention on the system of equations hereby used, since they are inherently nonlinear<sup>6</sup>. While the reaction kinetics can typically be considered linear under small perturbations, this assumption cannot be made a priori for the diffusion process. In particular, the CHR formulation introduces a nonlinear coupling between the concentration and the chemical potential, which includes a boundary energy term<sup>43</sup>. As a result, the equation for the mass conservation becomes fourth order in space, further complicating the linearity assumption.

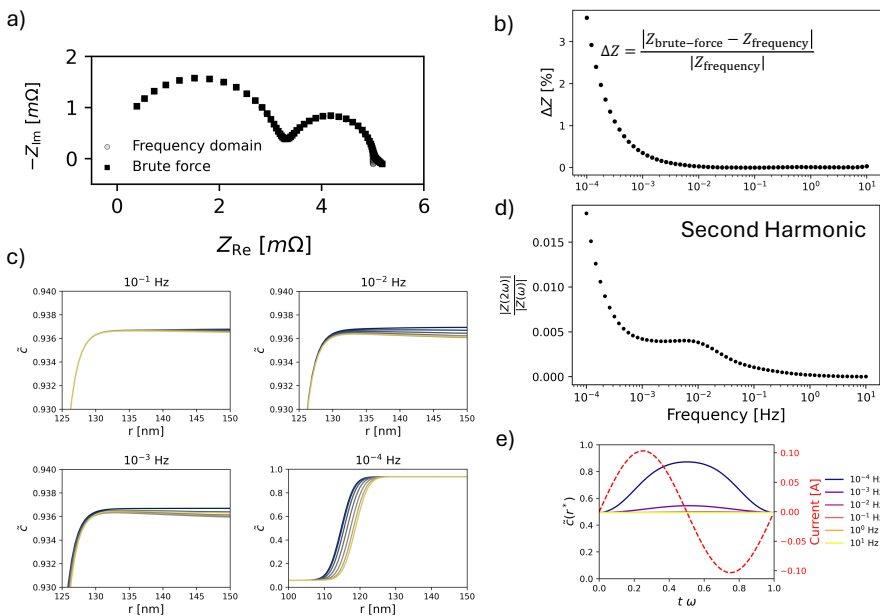


**Figure 6.6. Brute-force impedance.** a) Comparison between the impedance spectra obtained from the frequency-domain method and the brute-force (time-domain) simulation of the SPM-CHR at a filling fraction of 0.5 after lithiation. b) Relative difference in the impedance modulus between the two methods. c) Evolution of the particle concentration profile during the last half-cycle of the sinusoidal perturbation in the brute-force simulation, shown for various frequencies. d) Ratio between the first and second harmonic magnitudes, computed via FFT of the time-domain response. e) Evolution of boundary concentration during sinusoidal current perturbations at different frequencies and corresponding applied currents.  $\tilde{c}(r^*)$  is the concentration at the phase boundary median point where, in equilibrium,  $\tilde{c}(r^*) = 0.5$ .

Despite this, the frequency-domain method used here implicitly assumes linear system behavior. To verify whether this assumption holds, we performed a brute-force time-domain simulation

by applying a small sinusoidal current (0.05C) to the SPM-CHR model at a filling fraction of 0.5 following lithiation. The Fourier components of the resulting voltage responses, presenting 1 mV of stationary perturbation amplitude (Fig. S7), were then analyzed, replicating how impedance would be measured in an experimental setting.

Fig. 6.6a compares the frequency-domain and brute-force impedance spectra for frequencies ranging from 10 to  $10^{-4}$  Hz. The limited frequency range is selected to assure numerical accuracy. Good agreement is observed at mid and high frequencies, but discrepancies emerge at low frequencies; particularly below  $10^{-3}$  Hz (Fig. 6.6b). To better understand this divergence, we analyzed the time evolution of the internal concentration profile under sinusoidal current excitation (Fig. 6.6c). At high frequencies, the perturbation remains confined to the outer layer of the particle, resulting in a predominantly linear response. However, at low frequencies, the current oscillation induces motion of the phase boundary, a highly nonlinear effect that is not captured by the linearized frequency-domain method. This behavior is further confirmed in Fig. 6.6e, which shows that the amplitude of the oscillation at the boundary increases as frequency decreases.

6

To further quantify the degree of nonlinearity, we examined the harmonic content of the time-domain response. Fig. 6.6d shows the ratio between the magnitudes of the second and first harmonics. As the system transitions from a reaction-dominated regime to one dominated by diffusion, the second harmonic becomes more pronounced. Still, the ratio remains relatively small (under 2%), indicating that the response is only weakly nonlinear under the tested conditions.

These results highlight the importance of carefully considering the results of the frequency-domain method when used on phase-field models. While the method computes the inherent linear response, in experimental settings, this might not be achievable, since it might require imposing extremely small voltage perturbations ( $\sim 0.1$  mV). As a result, while the Fourier results do not show dominant nonlinear distortion, the frequency-domain method may still fail to reproduce low-frequency experimental data. This occurs at extremely low frequencies, hardly reached experimentally due to their impractical acquisition time (10 hours). However, it is recommended to verify the linearity when interpreting experimental EIS data of a phase-separating electrode, since different sizes and diffusivities might introduce non-linearities also at higher frequencies.

## 6.8 CONCLUSIONS

In this work, we applied a multiphase porous electrode modeling framework to analyze the impedance response of diffusion-limited phase-separating battery electrodes. Spanning from SPM-CHR to multi-particle DFN-CHR models, this approach shows the capabilities of the direct computation of impedance spectra from physically consistent models. By doing so we also reveal several insights that advance the interpretation of impedance for phase-separating materials.

One of the most important findings is the emergence of a low-frequency feature in the spectra of the SPM-CHR, which resembles a second semicircle. Conventionally, such features are attributed to the presence of multiple reaction processes. However, our analysis shows that this apparent second arc can also arise from the dynamics of radially phase-separated particles that introduce a transmissive diffusion pathway. This result challenges common interpretations and highlights how phase separation alone can produce complex impedance features.

Furthermore, we demonstrate that the impedance response can generally be path dependent. Even at identical overall lithium content, the impedance can differ depending on whether, prior to the acquisition of the spectra, the electrode was undergoing lithiation or delithiation. In the case of an SPM-CHR, this asymmetry originates from the surface phase exposed during reaction since Li-rich and Li-poor phases present different charge transfer resistance. For multi-particle systems that evolve in quasi-equilibrium conditions, the impedance depends on the ratio between lithiated and delithiated particles and the hysteresis branch followed by the electrode. Such direction-dependent impedance has been observed experimentally<sup>53,54</sup> but often lacked a clear mechanistic explanation. Our work provides a physical rationale grounded in population dynamics.

When extending the analysis to varying rates, we observe a pronounced kinetically induced memory effect<sup>28</sup> on the impedance response. Higher C-rates lead to a more uniform reaction across particles, increasing the number of phase-separated particles, manifesting in a broadened and distributed low-frequency response. The impedance spectrum becomes, therefore, a complex combination of transmissive and reflective diffusion elements, reflecting the diverse internal states of the particle population. However, the assumed core-shell structure, generating this feature, can be hard to obtain experimentally, since multiple phase morphologies can be obtained depending on the material and electrode properties<sup>19</sup>. Therefore, experiments on a range of phase-separating materials, particle morphologies, and electrode designs are needed to verify these claims.

Finally, our brute-force time-domain simulations confirm that, while the system behaves mostly linearly under small perturbations, deviations from linearity become relevant at low frequencies where the phase boundary is oscillating. However, within the utilized parameters, this occurs at extremely low frequencies ( $10^{-4}$  Hz) that are rarely utilized in experimental setups since they necessitate extremely long acquisition times ( $> 10$  hours).

These findings demonstrate that impedance, when computed from advanced physical models, can become a powerful probe of internal states of battery electrodes. While equivalent circuits cannot always meaningfully explain complex spectra, advancements in electrochemical models can extend their interpretability. In general, the developed methodology, coupled with further advancements in physics-based battery modeling, can extend the use of EIS in building next-generation diagnostic techniques and electrode designs.

## REFERENCES

1. Lazanas, A. Ch. & Prodromidis, M. I. Electrochemical Impedance Spectroscopy—A Tutorial. *ACS Meas. Sci. Au* **3**, 162–193 (2023).
2. Iurilli, P., Brivio, C. & Wood, V. On the use of electrochemical impedance spectroscopy to characterize and model the aging phenomena of lithium-ion batteries: a critical review. *J. Power Sources* **505**, 229860 (2021).
3. Halleman, N. *et al.* Operando electrochemical impedance spectroscopy and its application to commercial Li-ion batteries. *J. Power Sources* **547**, 232005 (2022).
4. Zhu, X. *et al.* Operando odd random phase electrochemical impedance spectroscopy as a promising tool for monitoring lithium-ion batteries during fast charging. *J. Power Sources* **544**, 231852 (2022).
5. Sihvo, J. *et al.* Pseudo-random sequences for low-cost operando impedance measurements of Li-ion batteries. Preprint at <https://doi.org/10.48550/arXiv.2506.07519> (2025).
6. Halleman, N. *et al.* Electrochemical impedance spectroscopy beyond linearity and stationarity—A critical review. *Electrochimica Acta* **466**, 142939 (2023).
7. Zhu, X., Soult, M. C., Wouters, B. & Mamme, M. H. Study of Solid-State Diffusion Impedance in Li-Ion Batteries Using Parallel-Diffusion Warburg Model. *J. Electrochem. Soc.* **171**, 060539 (2024).
8. Song, J. & Bazant, M. Z. Effects of Nanoparticle Geometry and Size Distribution on Diffusion Impedance of Battery Electrodes. *J. Electrochem. Soc.* **160**, A15–A24 (2013).
9. Bumberger, A. E., Nenning, A. & Fleig, J. Transmission line revisited – the impedance of mixed ionic and electronic conductors. *Phys. Chem. Chem. Phys.* **26**, 15068–15089 (2024).
10. Lagnoni, M., Scarpelli, C., Lutzemberger, G. & Bertei, A. Critical comparison of equivalent circuit and physics-based models for lithium-ion batteries: A graphite/lithium-iron-phosphate case study. *J. Energy Storage* **94**, 112326 (2024).
11. Kirk, T. L., Lewis-Douglas, A., Howey, D., Please, C. P. & Jon Chapman, S. Nonlinear Electrochemical Impedance Spectroscopy for Lithium-Ion Battery Model Parameterization. *J. Electrochem. Soc.* **170**, 010514 (2023).
12. Ji, Y. & Schwartz, D. T. Second-Harmonic Nonlinear Electrochemical Impedance Spectroscopy: Part II. Model-Based Analysis of Lithium-Ion Battery Experiments. *J. Electrochem. Soc.* **171**, 023504 (2024).
13. Brosa Planella, F. *et al.* A continuum of physics-based lithium-ion battery models reviewed. *Prog. Energy* **4**, 042003 (2022).
14. Doyle, M., Fuller, T. F. & Newman, J. Modeling of Galvanostatic Charge and Discharge of the Lithium/Polymer/Insertion Cell. *J. Electrochem. Soc.* **140**, 1526–1533 (1993).
15. Fuller, T. F., Doyle, M. & Newman, J. Simulation and Optimization of the Dual Lithium Ion Insertion Cell. *J. Electrochem. Soc.* **141**, 1–10 (1994).
16. Ferguson, T. R. & Bazant, M. Z. Nonequilibrium Thermodynamics of Porous Electrodes. *J. Electrochem. Soc.* **159**, A1967–A1985 (2012).
17. Sulzer, V., Marquis, S. G., Timms, R., Robinson, M. & Chapman, S. J. Python Battery Mathematical Modelling (PyBaMM). *J. Open Res. Softw.* **9**, 14 (2021).
18. Smith, R. B. & Bazant, M. Z. Multiphase Porous Electrode Theory. *J. Electrochem. Soc.* **164**, E3291–E3310 (2017).
19. Lu, X. *et al.* Multiscale dynamics of charging and plating in graphite electrodes coupling operando microscopy and phase-field modelling. *Nat. Commun.* **14**, 5127 (2023).
20. Daubner, S. *et al.* Multiphase-field modeling of spinodal decomposition during intercalation in an Allen-Cahn framework. *Phys. Rev. Mater.* **5**, 035406 (2021).
21. Daubner, S. *et al.* Simulation of intercalation and phase transitions in nano-porous, polycrystalline agglomerates. *Npj Comput. Mater.* **11**, 211 (2025).

22. Wimarshana, B., Bin-Mat-Arishad, I. & Fly, A. A multi-step parameter identification of a physico-chemical lithium-ion battery model with electrochemical impedance data. *J. Power Sources* **580**, 233400 (2023).
23. Zelič, K., Mele, I., Bhowmik, A. & Katrašnik, T. Phase separating electrode materials - chemical inductors? *Energy Storage Mater.* **56**, 489–494 (2023).
24. Halleman, N. *et al.* Physics-Based Battery Model Parametrisation from Impedance Data. *J. Electrochem. Soc.* **172**, 060507 (2025).
25. Zhu, H. *et al.* Extracting and Interpreting Electrochemical Impedance Spectra (EIS) from Physics-Based Models of Lithium-Ion Batteries. *J. Electrochem. Soc.* **171**, 050512 (2024).
26. Zhao, H. *et al.* Learning heterogeneous reaction kinetics from X-ray videos pixel by pixel. *Nature* **621**, 289–294 (2023).
27. Ombrini, P., Bazant, M. Z., Wagemaker, M. & Vasileiadis, A. Thermodynamics of multi-sublattice battery active materials: from an extended regular solution theory to a phase-field model of  $\text{LiMnyFe}_{1-y}\text{PO}_4$ . *Npj Comput. Mater.* **9**, 148 (2023).
28. Ombrini, P. *et al.* Kinetically induced memory effect in Li-ion batteries. *EES Batter.* 10.1039/D5EB00014A (2025) doi:10.1039/D5EB00014A.
29. Ombrini, P. *et al.* Modeling Single-Crystal Electrodes as a Network of Primary Particles.
30. Lian, H. & Bazant, M. Z. Modeling Lithium Plating Onset on Porous Graphite Electrodes Under Fast Charging with Hierarchical Multiphase Porous Electrode Theory. *J. Electrochem. Soc.* **171**, 010526 (2024).
31. Wang, Z. *et al.* Phase stability and sodium-vacancy orderings in a NaSICON electrode. *J. Mater. Chem. A* **10**, 209–217 (2022).
32. Vasileiadis, A. *et al.* Toward Optimal Performance and In-Depth Understanding of Spinel  $\text{Li}_4\text{Ti}_5\text{O}_{12}$  Electrodes through Phase Field Modeling. *Adv. Funct. Mater.* **28**, 1705992 (2018).
33. Subasinghe, L. U. *et al.* A study on heat generation characteristics of  $\text{Na}_3\text{V}_2(\text{PO}_4)_3$  cathode and hard carbon anode-based sodium-ion cells. *J. Therm. Anal. Calorim.* **147**, 8631–8649 (2022).
34. Zhuang, Q.-C. *et al.* An Electrochemical Impedance Spectroscopic Study of the Electronic and Ionic Transport Properties of Spinel  $\text{LiMn}_2\text{O}_4$ . *J. Phys. Chem. C* **114**, 8614–8621 (2010).
35. Katrašnik, T. *et al.* Entering Voltage Hysteresis in Phase-Separating Materials: Revealing the Electrochemical Signature of the Intraparticle Phase-Separated State. *Adv. Mater.* **35**, 2210937 (2023).
36. Deng, H. D. *et al.* Beyond Constant Current: Origin of Pulse-Induced Activation in Phase-Transforming Battery Electrodes. *ACS Nano* **18**, 2210–2218 (2024).
37. Li, Y. *et al.* Current-induced transition from particle-by-particle to concurrent intercalation in phase-separating battery electrodes. *Nat. Mater.* **13**, 1149–1156 (2014).
38. van Hulzen, M., Ooms, F. G. B., Wright, J. P. & Wagemaker, M. Revealing Operando Transformation Dynamics in Individual Li-ion Electrode Crystallites Using X-Ray Microbeam Diffraction. *Front. Energy Res.* **6**, 59 (2018).
39. Zhang, X. *et al.* Direct view on the phase evolution in individual  $\text{LiFePO}_4$  nanoparticles during Li-ion battery cycling. *Nat. Commun.* **6**, 8333 (2015).
40. Srinivasan, V. & Newman, J. Discharge Model for the Lithium Iron-Phosphate Electrode. *J. Electrochem. Soc.* **151**, A1517 (2004).
41. Bai, P., Cogswell, D. A. & Bazant, M. Z. Suppression of Phase Separation in  $\text{LiFePO}_4$  Nanoparticles During Battery Discharge. *Nano Lett.* **11**, 4890–4896 (2011).
42. Ferguson, T. R. & Bazant, M. Z. Phase Transformation Dynamics in Porous Battery Electrodes. *Electrochimica Acta* **146**, 89–97 (2014).
43. Zeng, Y. & Bazant, M. Z. Cahn-Hilliard Reaction Model for Isotropic Li-ion Battery Particles. *MRS Proc.* **1542**, mrss13-1542-g02-01 (2013).

44. Fraggedakis, D. *et al.* A scaling law to determine phase morphologies during ion intercalation. *Energy Environ. Sci.* **13**, 2142–2152 (2020).
45. Deng, H. D. *et al.* Correlative image learning of chemo-mechanics in phase-transforming solids. *Nat. Mater.* **21**, 547–554 (2022).
46. Li, Y. & others. Fluid-enhanced surface diffusion controls intraparticle phase transformations. *Nat. Mater.* **17**, 915–922 (2018).
47. Nadkarni, N. *et al.* Interplay of phase boundary anisotropy and electro-auto-catalytic surface reactions on the lithium intercalation dynamics in Li X FePO<sub>4</sub> 4 plateletlike nanoparticles. *Phys. Rev. Mater.* **2**, 085406 (2018).
48. Zelič, K. & Katrašnik, T. Thermodynamically consistent derivation of chemical potential of a battery solid particle from the regular solution theory applied to LiFePO<sub>4</sub>. *Sci. Rep.* **9**, 2123 (2019).
49. Bazant, M. Z. Unified quantum theory of electrochemical kinetics by coupled ion–electron transfer. *Faraday Discuss.* **246**, 60–124 (2023).
50. Dreyer, W. *et al.* The thermodynamic origin of hysteresis in insertion batteries. *Nat. Mater.* **9**, 448–453 (2010).
51. Holzapfel, M. *et al.* First lithiation and charge/discharge cycles of graphite materials, investigated by electrochemical impedance spectroscopy. *J. Electroanal. Chem.* **546**, 41–50 (2003).
52. Thapa, A. & Gao, H. Low-frequency Inductive Loop and Its Origin in the Impedance Spectrum of a Graphite Anode. *J. Electrochem. Soc.* **169**, 110535 (2022).
53. Rue, A. L. *et al.* State-of-Charge Estimation of LiFePO<sub>4</sub>–Li<sub>4</sub>Ti<sub>5</sub>O<sub>12</sub> Batteries using History-Dependent Complex-Impedance. *J. Electrochem. Soc.* **166**, A4041–A4046 (2019).
54. Moazzen, E., Scipioni, R., Ma, M. & Barnett, S. Interpretation and Modelling of the Electrochemical Impedance of LiFePO<sub>4</sub>/Li<sub>4</sub>Ti<sub>5</sub>O<sub>12</sub> Batteries. *J. Electrochem. Soc.* **168**, 050519 (2021).
55. Kurzweil, P. & Scheuerpflug, W. State-of-Charge Monitoring and Battery Diagnosis of Different Lithium Ion Chemistries Using Impedance Spectroscopy. *Batteries* **7**, 17 (2021).
56. Zhu, Y. & Wang, C. Strain accommodation and potential hysteresis of LiFePO<sub>4</sub> cathodes during lithium ion insertion/extraction. *J. Power Sources* **196**, 1442–1448 (2011).
57. Hong, J., Wang, C. & Kasavajjula, U. Kinetic behavior of LiFeMgPO<sub>4</sub> cathode material for Li-ion batteries. *J. Power Sources* **162**, 1289–1296 (2006).
58. Tang, K., Yu, X., Sun, J., Li, H. & Huang, X. Kinetic analysis on LiFePO<sub>4</sub> thin films by CV, GITT, and EIS. *Electrochimica Acta* **56**, 4869–4875 (2011).
59. Nyman, A., Behm, M. & Lindbergh, G. Electrochemical characterisation and modelling of the mass transport phenomena in LiPF<sub>6</sub>–EC–EMC electrolyte. *Electrochimica Acta* **53**, 6356–6365 (2008).

## SUPPLEMENTARY INFORMATION

<i>Particle parameters</i>	
Regular solution parameter ( $\Theta$ )	80 meV
Phase boundary energy ( $\kappa$ )	10 J m <sup>-1</sup>
Reference potential ( $V_0$ )	3.0 V
Solid diffusivity ( $D$ )	5 10 <sup>-7</sup> m <sup>2</sup> s <sup>-1</sup>
Maximum concentration ( $c_{max}$ )	22261 mol m <sup>-3</sup>
Exchange current density prefactor ( $k_0$ )	2 A m <sup>-2</sup>
Mean particle radius	200 nm
Standard deviation of particle radius	100 nm
Particle size distribution	Lognormal
<i>Electrode parameters</i>	
Electrode porosity	0.4
Active material volume fraction	0.55
Bruggeman coefficient	0.5
Bulk electrical conductivity ( $\sigma_{bulk}$ )	10 S m <sup>-1</sup> (negligible)
Initial electrolyte concentration	1 M
Electrolyte properties	Nyman <sup>59</sup>
Separator thickness	5 $\mu$ m
Separator porosity	0.4

Table S1. Model's parameters. The arbitrarily selected parameters are representative of a phase separating electrode material, akin to LiFePO<sub>4</sub>, but similar trends and effects are generalizable to multiple materials and parameter sets.

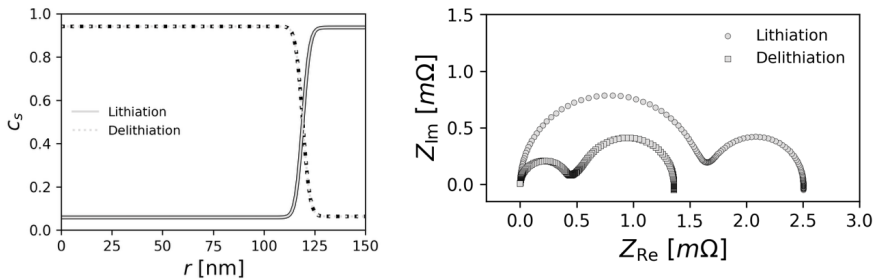


Figure S1. Comparison between the concentration profiles and impedance of the SPM-CHR model after lithiation and delithiation at a filling fraction of 0.5.

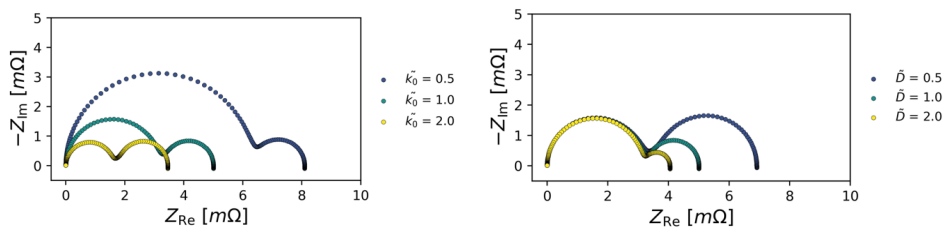


Figure S2. Effect of the exchange current density prefactor ( $\tilde{k}_0 = k_0/k_{0,std}$ ) (left) and solid diffusivity ( $\tilde{D} = D/D_0$ ) (right) on the impedance results of the SPM-CHR model at a filling fraction of 0.5, following lithiation.

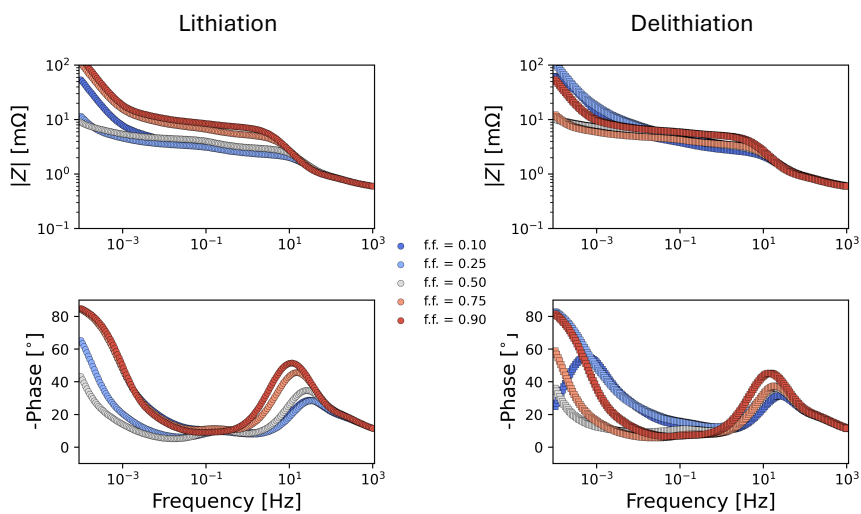


Figure S3. The impedance response of a CHR-DFN model. Computed Bode plots at varying filling fraction following lithiation and delithiation.

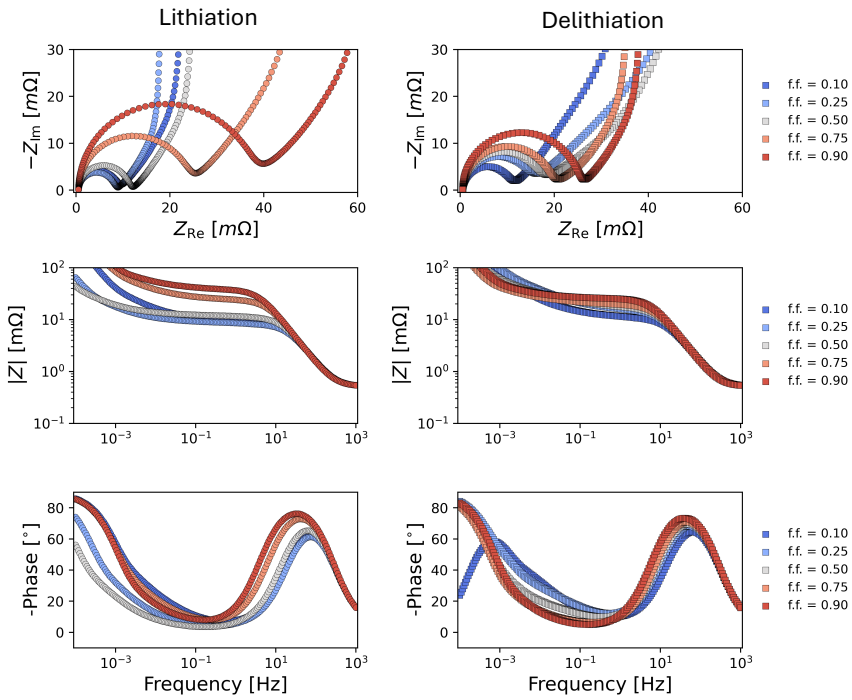


Figure S4. Nyquist and Bode plots at varying filling fractions (f.f.) for the case of an extremely thin DFN-CHR model ( $5 \mu\text{m}$ ) (de)lithiated in quasi-equilibrium conditions (0.01C).

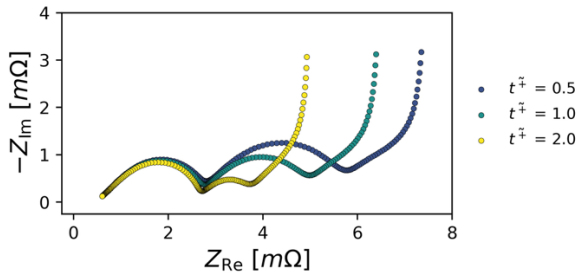


Figure S5. Effect of the transference number ( $t^+$ ) on the impedance of the DFN-CHR model lithiated in quasi-equilibrium conditions (0.01C) to a filling fraction of 0.5.

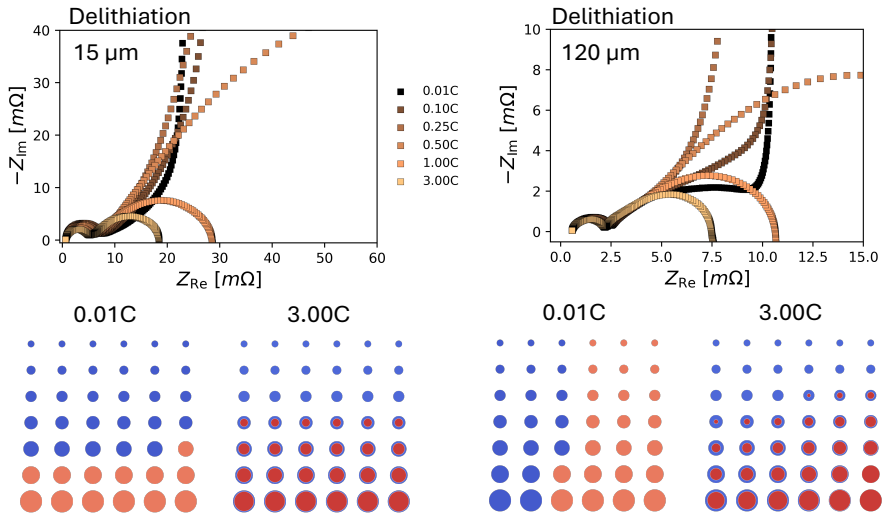


Figure S6. Effect of electrode thickness on impedance following a delithiation memory protocol. The left panel shows a thin electrode ( $15\ \mu\text{m}$ ,  $0.5\ \text{mAh cm}^{-2}$ ) and the right panel a thick electrode ( $120\ \mu\text{m}$ ,  $4\ \text{mAh cm}^{-2}$ ). Both spectra are taken at a filling fraction of 0.5, with corresponding particle concentration maps for 0.01C and 3.0C shown below.

6

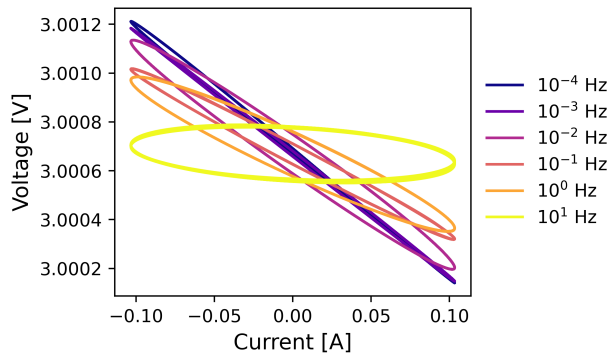


Figure S7. Current-voltage relation during the last five periods of the brute-force time domain simulations at varying frequencies. The stationarity is verified, and the voltage perturbation is  $\sim 1\ \text{mV}$ .



# 7 MODELING SINGLE-CRYSTAL ELECTRODES AS A NETWORK OF PRIMARY PARTICLES

This chapter has been published as: Ombrini P, Pathak S, Ntagkras D, Pal SK, Karanth P, Mulder FM, Wagemaker M, Bazant MZ, Vasileiadis A. Modeling Single-Crystal Electrodes as a Network of Primary Particles. *Energy and Environmental Science*. 2025.

## ABSTRACT

Predicting lithium-ion battery behavior is critical for advancing next-generation energy storage. Conventional Doyle–Fuller–Newman models can simulate many materials, but they fail in phase-separating single-crystal systems, such as lithium iron phosphate ( $\text{LiFePO}_4$ , LFP), where the electrical connectivity of primary particles limits charge transport. We redefine the electrode as a network of reactive primary particles, each governed by validated electrochemical kinetics and interconnected through tomographic-informed contact resistances. Without empirical tuning, the model predicts voltage responses of LFP electrodes across temperatures, rates, loadings, and dynamic load conditions using a single fitted physical parameter. It also captures and explains charge-discharge asymmetries and hysteresis. By bridging particle-scale physics up to cell-level performance, while retaining computational efficiency, this physics-based framework provides a foundation for the design, and control of single-crystal electrode systems.

## 7.1 INTRODUCTION

Over the past decade, Li-ion batteries have rapidly evolved. Advancements in every scale – from electrode to pack – have significantly boosted the energy and power densities of these batteries<sup>1</sup>, as exemplified by the emergence of lithium iron phosphate (LFP)-based batteries, now dominating the battery market<sup>2</sup>. At the electrode scale, architectures such as graded porosity<sup>3</sup> and multi-layered structures<sup>4</sup> have been exploited for improving long-range ion transport. At the particle scale, electrodes can be manufactured with secondary agglomerated particles or single-crystal primary particles<sup>5</sup>, here termed single-crystal electrodes (SCEs). Secondary agglomerates minimize the internal surface area, thereby reducing electrolyte-induced degradation<sup>6</sup>, but they are prone to fracture<sup>7</sup>; In contrast, SCEs can avoid cracking-induced degradation<sup>8</sup>, thereby improving cycle life and power densities. Active materials with low ionic diffusivity, such as LFP, are typically manufactured as nanometric single crystals, achieving diffusion times on the scale of milliseconds<sup>9</sup> and resulting in a reaction-limited process<sup>10,11</sup>.

Yet commercial SCEs fall short of these rate capabilities, indicating the presence of additional limiting factors. Ionic transport in the electrolyte can limit high-loading electrodes ( $> 3 \text{ mAh cm}^{-2}$ )<sup>12</sup>, but thin high-power electrodes mitigate this issue. For the latter case, the performance of SCEs composed of insulating materials are impacted by the inter-particle *electrical connectivity*<sup>13</sup>. This is evident by their ability to reach 9-seconds discharge when very high (63%) carbon loading is used<sup>14</sup> and by the significant improvements of LFP performances when carbon coating is applied<sup>15</sup>. The work of Li et al.<sup>13</sup> shows that the reaction initiates from particles connected to the carbon black (CB) and propagates then towards the unconnected ones, demonstrating that inter-particle electron transport, coupled with local reactions with the electrolyte, is at the core of the reaction mechanism. Additional evidence is provided by the significant performance losses of LFP electrodes in cold conditions<sup>16</sup>, compared to layered oxide electrodes. The reason lies in the electrical conductivity of the carbon coating decreasing sharply at low temperatures<sup>17</sup>, since the electrons hopping between metallic  $sp^2$  and insulating  $sp^3$  domains introduce a macroscopic energy barrier<sup>17</sup>.

Considering the growing importance of SCEs, especially those based on LFP, it is necessary to develop reliable numerical models to operate them in control-oriented tasks<sup>18</sup>. While data-driven approaches can be employed<sup>19</sup>, they cannot extrapolate beyond the data and provide little physical insight. Physics-based modeling, in contrast, can predict battery performances under new condition and accelerate electrode development<sup>20</sup> by optimizing CB content, thickness, and porosity<sup>21</sup>. However, despite advances in the characterization of SCEs<sup>5,13</sup>, these systems have not been comprehensively modeled.

## 7 | MODELING SINGLE-CRYSTAL ELECTRODES AS A NETWORK OF PRIMARY PARTICLES

Doyle-Fuller-Newman models (DFN)<sup>12,22</sup> can achieve precise results with limited computational cost<sup>23</sup>, making them attractive for practical applications. Ionic transport in the electrolyte is captured by adjusting diffusivity and conductivity base on porosity and tortuosity<sup>12,22</sup>. Similarly, electron transport through the solid phase is modeled using Ohm's law<sup>24</sup>. The electrode is divided into discretized volumes, containing a set of independent particles and having uniform electrolyte and electrical potential. The local reaction rate depends on the specified reaction kinetics and solid-state diffusivities. DFN models perform reasonably well when applied to single-phase diffusion-limited materials such as transition metal oxide, especially if concentration-dependent diffusivities and reactivities are considered<sup>3</sup>.

Thomas-Alyea<sup>25</sup> and Safari<sup>26</sup>, expanded DFN models by considering the limited electrical conductivity of LFP and the role of CB-connectivity, enabling them to capture both constant current and path-dependent voltage profiles of an LFP electrode. However, empirical relations were necessary to fit the data, and phase-separation kinetics was entirely neglected. Materials such as  $\text{LiFePO}_4$ <sup>27</sup>,  $\text{LiMn}_y\text{Fe}_{1-y}\text{PO}_4$ <sup>28</sup>,  $\text{Li}_4\text{Ti}_5\text{O}_{12}$ <sup>29</sup>, and graphite<sup>30</sup> have instead a thermodynamic driving force to separate into Li-rich and Li-poor phases. Capturing this mechanism is essential to capture the electrode-scale behavior. For this scope, multiphase porous electrode theory (MPET)<sup>31</sup> has been developed by combining DFN and phase-field models, i.e., computing the chemical potential starting from the free energy functional and accounting for the energy penalty of phase boundaries<sup>24</sup>. Using this method, one can model charge-discharge asymmetries in reaction kinetics<sup>32</sup>, voltage hysteresis<sup>33</sup>, active particle population dynamics<sup>34</sup>, and Li-plating on graphite<sup>30</sup>. However, key morphological descriptions are necessary, as exemplified by the case of graphite electrodes, where hierarchical structures<sup>30</sup> were considered necessary to achieve an accurate fit of MPET simulations to experimental data. Similarly, for LFP, the electrical connectivity of primary particles must be considered, as it plays a critical role in shaping the electrode's behavior.

In response to these challenges, this study proposes a new paradigm for modeling SCEs: instead of treating the electrode as a collection of particles governed by Fickian diffusion, it is modeled as a network of electrically connected nanoparticles governed by Kirchhoff's law. Reconstructing a commercial electrode with focused ion beam scanning electron microscopy (FIB-SEM)<sup>35</sup>, followed by segmentation and particle identification, we abstracted the three-dimensional microstructures into a network. The model incorporates inter-particle connectivity<sup>36</sup>, which governs the local voltage drop and, consequently, the single-particle reaction rate. Furthermore, individual particles are modeled using validated approaches<sup>24</sup>, including coupled ion-electron transfer kinetics (CIET)<sup>37</sup> and phase-field modeling<sup>38</sup>, all integrated into a consistent modeling framework.

This fast and scalable approach is here applied to LFP, due to its growing importance in the battery market<sup>39</sup>. However, it is adaptable to a broad range of single-crystal, reaction-limited electrochemical systems. The resulting model bridges diverse electrochemical protocols, including imposed current (CC) and galvanostatic intermittent titration technique (GITT), across varying temperatures, using only one fitting parameter, thereby delivering both accuracy and versatility. Finally, by being firmly rooted in physics and devoid of empirical equations, the model effectively captures the internal mechanisms of SCEs, making it a valuable tool for advancing electrochemical modeling.

## 7.2 THE ELECTRODE AS A NETWORK OF CONNECTED REACTIVE PARTICLES

Tomographic information of a commercial LFP electrode was obtained using FIB-SEM (Fig. 7.1a). After segmentation<sup>43</sup>, the stack was divided in cubic sub-volumes, and the individual particles were identified (Fig. 7.1b). Each sub-volume was abstracted as network, by processing the particle-particle and the particle-CB contact areas in adjacency matrices where each pixel records the contact area between two particles or between the particle and the CB phase (Fig. 7.1c). Using these matrices, we constructed a set of *graphs*<sup>42</sup> where each node stores the information on the particle's size and active surface area. Each edge represents relative contact areas, with CB treated as a source node (Fig. 7.1d). The segmentation details and their statistics are provided in the Supplementary Information.

The resulting networks can simulate the reaction kinetics of the microstructure by enforcing current conservation at each node (Fig. 7.1g). Assuming that the primary electrical potential losses occur at contact interfaces and that the particle's surface is equipotential, the inter-particle and CB contact conductance ( $G_{ij}$  and  $G_{i-cb}$ ) are taken proportional to the contact areas<sup>44,45</sup>. Considering the inter-particle contact areas remain constant during cycling, the constitutive law of the discretized sub-volume can be expressed for each particle  $i$  as:

$$I_i(\varphi_i, \mu_{surf_i}, \mu_{elyte}) - G_{i-cb}(\varphi_i - \varphi_{cb}) - \sum_{i \neq j} G_{ij}(\varphi_i - \varphi_j) = 0$$

where the  $I_i$  is the current consumed by the reaction, the second term is the current delivered by the CB, and the summation accounts for the current exchanged with adjacent particles. In this framework, the electrical potential driving a particle's reaction ( $\varphi_i$ ) reflects the influence of the surrounding particle network and the CB potential ( $\varphi_{cb}$ ). The electrical and ionic potentials ( $\varphi_{cb}$  and  $\mu_{elyte}$ ) depend on electron and ion transport along the electrode thickness, where

## 7 | MODELING SINGLE-CRYSTAL ELECTRODES AS A NETWORK OF PRIMARY PARTICLES

percolation is assumed, integrating information about the depth of the simulated sub-volume and the electrode's porosity and tortuosity<sup>46</sup>.

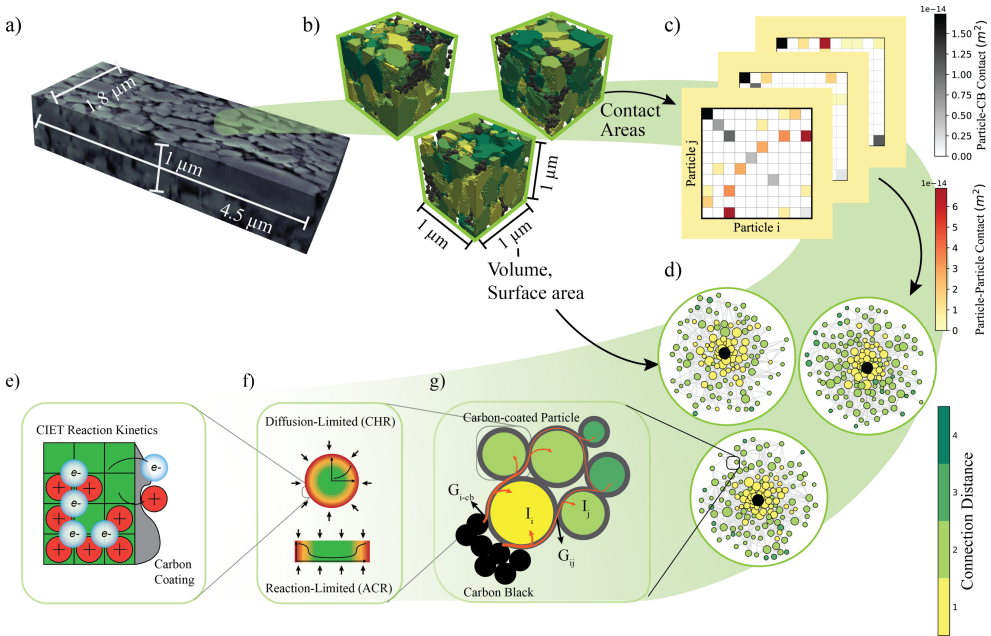


**Figure 7.1. Multiscale model of single-crystal electrodes.** a) Volume reconstructed from FIB-SEM scans. b) Segmented sub-volumes. Black particles correspond to the reconstructed<sup>40</sup> spherical nanoparticles of the CB particle phase, the green scale particles correspond to labeled LFP particles. c) Example of adjacency matrix. The copper scale refers to the inter-particle contact and the greyscale to the particle-CB contact. d) Networks obtained from the sub-volumes: node size is proportional to the particle volume and the color represents the connection distance. e) Schematic of the coupled ion-electron transfer model used to simulate the reaction kinetics. f) Schematic representation of two limiting models that can be used to simulate single-particle reaction kinetics. g) Schematic representation of the network conductance paths. The particle  $i$  with connection distance 1 is connected to the carbon black through a conductance  $G_{i-cb}$  and to the particle  $j$  with connection distance 2 through a conductance  $G_{ij}$ . The particles react with the electron and electrolyte reservoir with currents  $I_i$  and  $I_j$ , respectively. The electric current originating from the carbon black, is consumed by the particles as expressed in the Kirchhoff's law.

This framework can be combined with validated single particle models to compute their surface chemical potentials ( $\mu_{surf_i}$ ): 0D homogeneous particles<sup>33</sup>; 1D diffusion-limited particles<sup>29</sup> (Cahn-Hilliard approach<sup>29</sup>) or 1D reaction-limited particles<sup>28,38</sup> (Allen-Chan formalism<sup>38</sup>) (Fig. 1f). This follows established multiphase porous electrode theory models<sup>31</sup>. Considering chemo-mechanical effects, which tend to suppress phase separation within submicron-sized

particles<sup>38,47–49</sup>, we adopted the 0D approximation which reduces the computational cost, while still capturing inter-particle phase separation<sup>33</sup> (Fig. S28). Furthermore, we describe the reaction kinetics  $I_i$  using models validated by direct imaging of lithium intercalation dynamics in both LFP single-crystal particles<sup>32</sup> and LFP porous electrodes<sup>34</sup>, i.e. using the electron-transfer-limited version of CIET<sup>37,48</sup> (Fig. 7.1e). The complete mathematical formulation appears in Supplementary Methods.

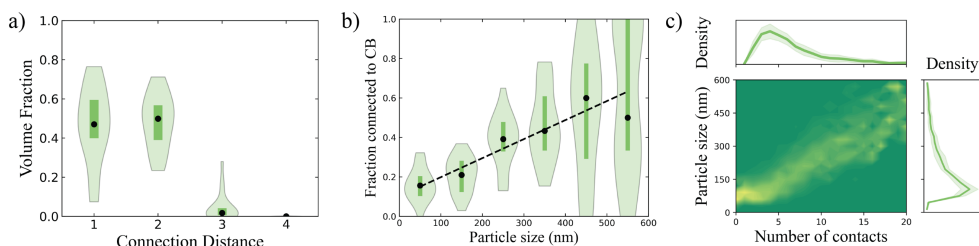


**Figure 7.2.** a) Distribution of volume fraction as a function of connection distance. The width of the violin represents the density of the specific volume fraction across the sub-volumes. b) Fraction of directly connected particles as a function of particle size with 100 nm bin size. The width of the violin represents the probability density for the given size range (100 nm). c) The contour plot shows the relation between particle size and number of contacts. The line plots illustrate the probability density for the number of contacts and particle size distributions across various sub-volumes. The shaded areas (or error bars) represent confidence intervals of  $\pm 1$  standard deviation.

The generated networks reveal the electrode’s microstructural properties (Fig. 7.2). Computing the shortest path from each particle to the CB node defines its *connection distance*, i.e., the minimal number of edges separating it from CB. Most particles lie one or two edges away (i.e., having a connection distance of 1 or 2), while a few require three or four (Figs. 7.1d, 7.2a). Particle size distribution plays a significant role in shaping these statistics. Larger particles are more likely to directly contact the CB phase (Fig 7.2b) and exhibit more inter-particle contacts (Fig 7.2c). Therefore, they enhance the network’s connectivity and ensure uniform current distribution. Hence, despite relying solely on small particles, which might appear advantageous for faster particle-level kinetics, they increase the connection distance, thereby diminishing the electrode’s rate capability. While a more uniform CB distribution might mitigate this, achieving it in practice is challenging and risks disrupting the percolation network, which is essential for electronic conductivity. This analysis, further detailed in the Supplementary Methods, helps justify the choice of using a bimodal particle size distribution, where smaller particles can fill the larger voids of the larger particles and explores the connectivity statistics of the SCEs, which must be considered in careful electrode engineering.

### 7.3 INTERCALATION DYNAMICS IN SINGLE-CRYSTAL ELECTRODES

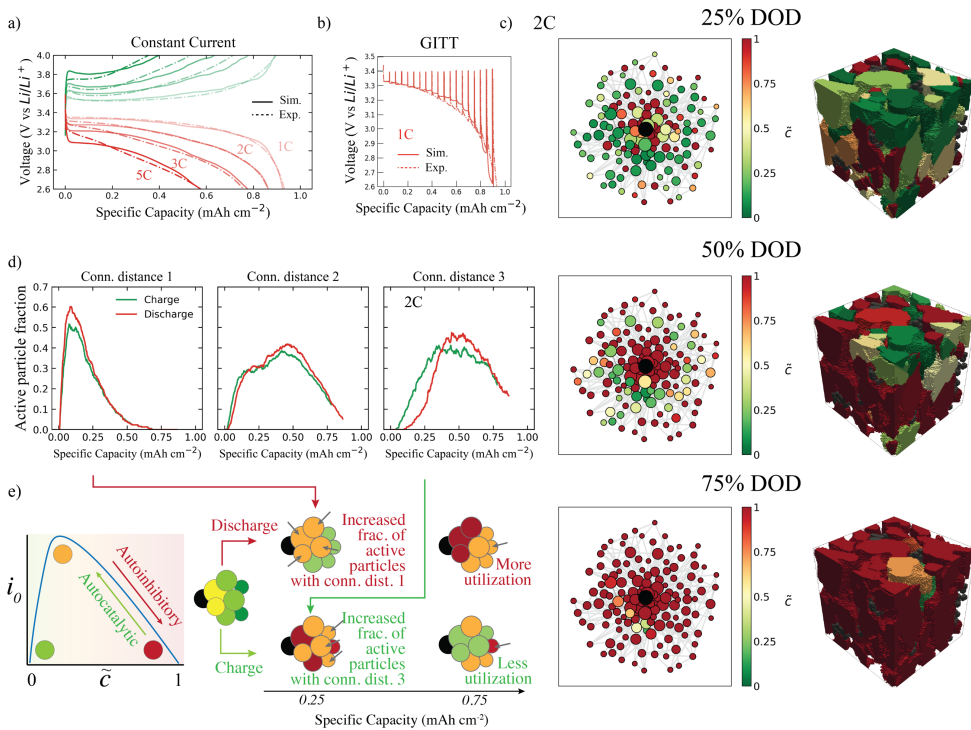


**Figure 7.3. Dynamics of lithium intercalation in a single-crystal electrode.** a) Comparison between the experimental and simulated voltage curves for 1C, 2C, 3C, and 5C for discharge (red) and charge (green). (1C = 1 mA cm<sup>-2</sup>). b) Comparison between the experimental and simulated voltages for the GITT protocol. Each pulse delivered 1C current and lasted 3 minutes. The resting time is 30 minutes. c) Evolution of the particle network and its corresponding microstructure during 2C discharge at different depths of discharge (DOD). The color scale shows the degree of lithiation of the particles. d) Evolution of the active particle population during a 2C discharge (red) and charge (green), divided by connection distance. Each percentage is calculated based on the population having the corresponding connection distance. e) Schematic representation of the autocatalytic/autoinhibitory reaction kinetics and its effects on the active particle population dynamics.

To verify the model’s accuracy in predicting the electrochemical response of real porous electrodes, we compared it with a set of experimental measurements conducted on the sample characterized in this work. As a result of the precise characterization, the model requires only *one fitted parameter*: the inter-particle conductivity  $\sigma$ . This parameter determines the utilizable

capacity and is highly sensitive to the synthesis path and carbon coating quality. The reduction to a single fitted parameter enhances model identifiability, allowing for precise estimation that only *requires one cycle* as a dataset. Finding  $\sigma$  by solely fitting the 2C discharge cycle of the 1 mAh cm<sup>-2</sup> sample, the model replicates constant current (CC) charge and discharge across multiple C-rates (Fig. 7.3a), including the ones of a higher-loading sample (2 mAh cm<sup>-2</sup>) (Fig. S18). This also further confirms the kinetically limiting factor lies in the local particle wiring. All parameterization details, including porosity and tortuosity implementation based on microstructural characterization, are provided in the Supplementary Information (Supplementary Table 1-3).

Beyond reproducing voltage responses, the model allows for a detailed investigation of the internal dynamics. In agreement with experiments<sup>13</sup> the system initiates with full (de)lithiation of the particles directly connected with the CB and gradually expands deeper into the network (Fig. 7.3c). By defining as *active particles* those within the spinodal range (0.15–0.85 filling fraction), we observed the active particle population evolving in distinct waves (Fig. 7.3d): first the particles having a connection distance of one or two, only after most of these particles complete their reaction, the poorly connected particles are activated. High-potential electrons from the CB are consumed by the (de)lithiation of the nearest particles, preventing the particles deeper in the network from participating.

By integrating the network framework with CIET<sup>32,48</sup> reaction kinetics, the model captures *charge–discharge asymmetry* at the electrode level (Fig. 7.3a) and explains its origin through the lens of electro-autocatalysis<sup>34,50</sup>. The asymmetry arises from the concentration dependence of the exchange current density,  $i_0(c)$ <sup>37</sup> (Fig. 7.3e). During delithiation (charging), lithium removal increases  $i_0(c)$ , accelerating ion extraction; an *autocatalytic* effect. During lithiation (discharging), lithium insertion decreases  $i_0(c)$ , slowing the reaction; an *autoinhibitory* effect. During charging, the autocatalytic feedback accelerates the delithiation of particles directly connected to the CB. As fewer particles are needed to sustain the current (Fig. 7.3d) and are depleted, they become inactive early in the charge process. Consequently, the system is forced to rely on more distant particles (e.g., connection distance three) earlier than it otherwise would. These deeper particles are then less available in later stages, requiring higher overpotentials, and thus limiting overall charge capacity (Fig. 7.3d). In contrast, during discharge, the autoinhibitory effect slows the lithiation reaction, and the reduced local current demand allows electrons to bypass front-line particles and reach deeper ones with limited potential losses, enabling greater capacity. These predictive insights emerge only through the combined use of quantum-informed reaction kinetics and the network-based transport formalism. As such, the model offers a physically grounded explanation for charge–discharge asymmetry and provides a foundation for optimizing operational protocols.

## 7 | MODELING SINGLE-CRYSTAL ELECTRODES AS A NETWORK OF PRIMARY PARTICLES

Our model also clarifies the poor correlation between particle size and degree of lithiation. Both nucleation theory<sup>47</sup> and the increased surface-area-to-volume ratio should improve the rate capabilities of smaller particles. Despite this, both experimental observation<sup>51</sup> and our model show little correlation between particle size and filling fraction (Fig. S29). The higher average connectivity of bigger particles offset their kinetics and thermodynamic disadvantages, leading to a more equilibrated lithiation profile.

The uncovered mechanism is also key to understanding the response observed under the GITT protocol (Fig. 7.3b). Despite 30-minute rest periods, a steadily increasing potential drop is observed after each pulse. Our model explains this behavior by capturing the interplay between phase separation and electronic connectivity. The phase separation induces a *mosaic* arrangement of fully lithiated and fully delithiated particles. Early in the protocol, the lithiated particles coincide with those having stronger connectivity to the CB, allowing for low overpotentials. As the reaction front progresses deeper into the network, activating poorly connected particles requires increasingly higher overpotentials. The same model properties are responsible for capturing the thermodynamic hysteresis between charge and discharge (Fig. S21) and the kinetically induced memory effect<sup>52</sup> (Fig. S23), without specialized algorithms<sup>53</sup>.

Finally, the advantage of our network formalism becomes particularly clear when compared to a conventional DFN model<sup>54</sup>. This model can be tuned by adjusting diffusivity and bulk electrical conductivity to match capacity retention under constant-current conditions (Fig. S24). However, significant changes in bulk conductivity are required to account for the performance difference between the 1 mAh cm<sup>-2</sup> and 2 mAh cm<sup>-2</sup> electrodes. Due to the missing physical consistency, the DFN model lacks predictive transferability for guiding electrode design. Assuming Fickian diffusion and neglecting phase separation, this approach also prevents it from capturing the system's response under GITT protocols; a critical feature for battery control under dynamic operating conditions<sup>55</sup>. In contrast, our model naturally captures these phenomena, enabling mechanism-based predictions. This highlights the need for physically grounded approaches that go beyond blind parameter fitting and provide robust insights into performance-limiting mechanisms.

### 7.4 THE EFFECT OF TEMPERATURE

Temperature-dependent tests provide a final validation for our model. This is obtained by including an Arrhenius-like temperature dependence of the electrical conductivity ( $\sigma(T) \sim e^{-E_\sigma/k_B T}$ ), originating from the conduction mechanism of the amorphous carbon coating<sup>17</sup>. Adjusting the previously measured activation energy<sup>17</sup> to 0.32 eV, by fitting the 2C

discharge at 10 °C, the model closely matches the experimental data for multiple C-rates at 10 °C and extrapolates the -5 °C behavior (Fig. 7.4a). Moreover, the difference between the GITT response at 25 °C and -5 °C is also captured, further supporting the model's validity (Fig. 7.4b). Although electrolyte conductivity already varies with temperature<sup>56</sup>, we show in the Supplementary Information (Fig. S17) how accounting for  $\sigma(T)$  is necessary to reproduce the low-temperature data.

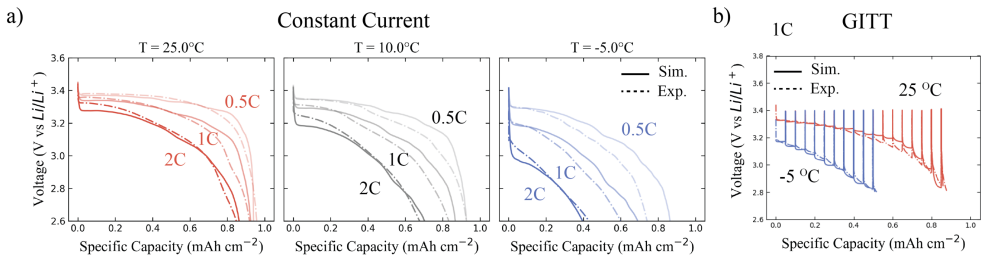


**Figure 7.4.** Effect of temperature on the kinetics of single crystal electrodes. a) Comparison between the experimental and simulated voltage curves for 0.5C, 1C and 2C discharges at 25°C, 10°C and -5°C. b) Comparison between the experimental and simulated voltage curves for the GITT protocol. Each pulse delivered 1C current and lasted 3 minutes. The resting time is 30 minutes.

Moreover, we show the active particle population is not significantly affected by the temperature change (Fig. S30). Two counteracting factors, the increase in charge transfer resistance and the decrease of electrical conductivity, play opposite roles. Finally, the obtained activation energy is distant from that of the LFP bulk conductivity ( $\sim 0.5$  eV)<sup>57</sup> further proving the contact resistance to be the limiting factor. While electrolyte engineering is still important, these findings direct the attention to enhancing carbon coatings or introducing carbon nanotubes to improve low-temperature performance of SCEs<sup>58</sup>.

## 7.5 CONCLUSIONS

Modeling of Li-ion batteries can play a crucial role in optimizing their performance and lifespan<sup>2</sup>. Despite its importance, existing porous electrode theories have deficiencies that render them unreliable for SCE. Unifying microstructural imaging, network science, and first-principles kinetics, we present a framework that integrates the microstructural information into a reduced-order formalism. After abstracting the microstructure into a network of electrically interconnected particles, we found that the relationship between the particle size distribution and the CB volume fraction can shape the network's properties.

## 7 | MODELING SINGLE-CRYSTAL ELECTRODES AS A NETWORK OF PRIMARY PARTICLES

Moreover, validated models describing single-particle behavior are integrated with the network framework, creating a robust, physics-based simulation. By grounding the model on the system's physics, the unknown parameters can be accurately found using a limited dataset, enabling reliable predictions. The resulting model demonstrates exceptional generalization across various experimental conditions, including varying protocols, temperatures, and electrode loadings. The critical role of integrating both network abstraction and phase separation into the model becomes particularly evident in intermittent current scenarios, such as GITT, where conventional DFN models fail to predict the electrode's dynamics. By accounting for phase separation, the model preserves inter-particle heterogeneity during open-circuit conditions, while the network ensures that the multi-particle lithiation sequence is faithfully respected. This physics-informed approach allows the model to accurately predict voltage responses based on both state of charge (SOC) and prior cycling history. Combined with its limited computational cost, these capabilities make the model highly effective in predicting voltage responses under real-world, dynamic input conditions.

Better accuracy and predictivity are coupled with a deeper fundamental understanding. Beyond long-range electron transport, the CB spatial distribution has a drastic influence on the local dynamics and the low-temperature performance of LFP electrodes. This framework, when coupled with microstructure generation<sup>40,59</sup>, can also predict and optimize the effects of porosity, particle size, and CB volume fractions. For example, an increase in porosity, if leading to a decrease in inter-particle connectivity, might result in unexpected performance losses. Additionally, in future studies, the concept of a particle network could be used to investigate degradation mechanisms by including dynamic detachment<sup>36</sup> of particles during cycling.

In conclusion, this modeling approach holds broad application potential, spanning solid-state batteries, emerging chemistries, and, more generally, reaction-limited electrochemical systems. Through this study, we have laid a strong foundation for the development of more efficient and reliable energy storage solutions, addressing the increasing demands of modern technology and advancing sustainable energy applications.

## METHODS

**Coin cell preparation and cell cycling.** The single-crystal  $\text{LiFePO}_4$  coated electrodes were acquired from CustomCells<sup>®</sup> in two loadings:  $1 \text{ mAh cm}^{-2}$  and  $2 \text{ mAh cm}^{-2}$ . The electrodes were cut into disks of 12.7 mm diameter and dried under vacuum at  $80 \text{ }^\circ\text{C}$  overnight prior to cell assembly. The coin cells were assembled in an Argon glovebox using the LFP electrodes, a  $25 \text{ }\mu\text{m}$  thick Celgard 2500<sup>®</sup> separator, and a  $250 \text{ }\mu\text{m}$  thick, 15.4 mm diameter Li metal counter electrode. 1 M Lithium Hexafluorophosphate ( $\text{LiPF}_6$ ) in ethylene carbonate (EC): dimethyl carbonate (DMC) (1:1 vol%) was used as the electrolyte. The assembled coin cells were cycled using a LANHE<sup>®</sup> battery tester inside a climate-controlled climate chamber. Prior to testing, the cells underwent two formation charge-discharge cycles at 0.1C, where 1C corresponds to either  $1 \text{ mA cm}^{-2}$  or  $2 \text{ mA cm}^{-2}$ , depending on the electrode. The rate performance was evaluated as follows: the cells were charged and discharged at the target C-rate until reaching the cutoff voltage (4.0 V for charge and 2.6 V for discharge), followed by a 1-hour rest period. Subsequently, the cells were charged and discharged at 0.5C until the cutoff voltage was reached, and then they were held at this voltage until the current decreased to C/20. This second step ensured that the electrodes reached fully (de)lithiated states, facilitating parameterization of the simulations. The same protocol was applied at all tested temperatures. The GITT protocol also followed the same procedure, with 20 pulses at 1C ( $1 \text{ mAh cm}^{-2}$ ) lasting 3 minutes, followed by a 30-minute rest.

**Electrode characterization.** The electrode's weights and thicknesses were measured by scraping a region of the electrode, flattening the remaining Al, and measuring their weights and thicknesses. The values were subtracted from the weight and thickness of the coated sample. The thickness was found to vary from  $28 \text{ }\mu\text{m}$  to  $31 \text{ }\mu\text{m}$  across the samples and the weight was found to vary accordingly. The  $1 \text{ mAh cm}^{-2}$  LFP electrode as used to acquire the scanning electron microscopy (SEM) and the focus ion beam scanning electron microscopy (FIB-SEM) images. SEM images were acquired using a JEOL JSM-IT700HR FE-SEM setup in backscattered electron detection mode (acceleration voltage: 5 kV). 3d volumes were created using a dual beam FIB-SEM (FEI Helios G4 CX). To insure a smooth sliced surface, a thin ( $0.5 \text{ }\mu\text{m}$ ) Pt layer was deposited on the top surface using Pt-GIS installed in the FIB-SEM. An auto slice & view software (ThermoFisher Scientific) was used to automate the aligning, slicing and acquisition of the high-resolution SEM images. For the FIB-SEM characterization, two different regions of the electrode were scanned to ensure local inhomogeneities could be captured. Volumes of  $4.5 \text{ }\mu\text{m} \times 1.8 \text{ }\mu\text{m} \times 1 \text{ }\mu\text{m}$  and  $4.5 \text{ }\mu\text{m} \times 2.7 \text{ }\mu\text{m} \times 1.7 \text{ }\mu\text{m}$  were scanned by slicing different parts of the electrode material and a slicing distance of 50 nm. Details about the segmentation<sup>43</sup>, microstructure characterization<sup>46</sup>, particle identification algorithms<sup>40</sup>, sub-volume post-processing and relative statistics can be found in the Supplementary Information.

**Computational methods.** The model's equations were implemented expanding upon the existing MPET software<sup>31</sup> and can be found in the Supplementary Information.

## REFERENCES

1. Ziegler, M. S. & Trancik, J. E. Re-examining rates of lithium-ion battery technology improvement and cost decline. *Energy Environ. Sci.* 14, 1635–1651 (2021).
2. Birol, D. F. Batteries and Secure Energy Transitions. *IEA* (2024).
3. Karanth, P. *et al.* A phase inversion strategy for low-tortuosity and ultrahigh-mass-loading nickel-rich layered oxide electrodes. *Cell Rep. Phys. Sci.* 101972 (2024) doi:10.1016/j.xcrp.2024.101972.
4. Tredenick, E. C. *et al.* A Multilayer Doyle-Fuller-Newman Model to Optimise the Rate Performance of Bilayer Cathodes in Li Ion Batteries. *J. Electrochem. Soc.* 171, 060531 (2024).
5. Min, J., Suk, W., Wong, S. C. Y. & Li, Y. Single-Particle Electrochemical Cycling Single-Crystal and Polycrystalline NMC Particles. *Adv. Funct. Mater.* 2410241 (2024) doi:10.1002/adfm.202410241.
6. Lee, S., Su, L., Mesnier, A., Cui, Z. & Manthiram, A. Cracking vs. surface reactivity in high-nickel cathodes for lithium-ion batteries. *Joule* 7, 2430–2444 (2023).
7. Samantaray, Y., Cogswell, D. A., Cohen, A. E. & Bazant, M. Z. Electrochemically Resolved Acoustic Emissions from Li-ion Batteries. Preprint at <https://doi.org/10.26434/chemrxiv-2025-r7vwq> (2025).
8. Min, J., Gubow, L. M., Hargrave, R. J., Siegel, J. B. & Li, Y. Direct measurements of size-independent lithium diffusion and reaction times in individual polycrystalline battery particles. *Energy Environ. Sci.* 16, 3847–3859 (2023).
9. Malik, R., Burch, D., Bazant, M. & Ceder, G. Particle Size Dependence of the Ionic Diffusivity. *Nano Lett.* 10, 4123–4127 (2010).
10. Fraggedakis, D. *et al.* A scaling law to determine phase morphologies during ion intercalation. *Energy Environ. Sci.* 13, 2142–2152 (2020).
11. Gaberscek, M., Dominko, R. & Jamnik, J. Is small particle size more important than carbon coating? An example study on LiFePO<sub>4</sub> cathodes. *Electrochem. Commun.* 9, 2778–2783 (2007).
12. Tredenick, E. C. *et al.* Bridging the Gap between Microstructurally Resolved Computed Tomography-Based and Homogenised Doyle-Fuller-Newman Models for Lithium-Ion Batteries. *J. Electrochem. Soc.* 172, 030503 (2025).
13. Li, Y. *et al.* Effects of Particle Size, Electronic Connectivity, and Incoherent Nanoscale Domains on the Sequence of Lithiation in LiFePO<sub>4</sub> Porous Electrodes. *Adv. Mater.* 27, 6591–6597 (2015).
14. Kang, B. & Ceder, G. Battery materials for ultrafast charging and discharging. *Nature* 458, 190–193 (2009).
15. Doeff, M. M., Hu, Y., McLarnon, F. & Kostecki, R. Effect of Surface Carbon Structure on the Electrochemical Performance of LiFePO<sub>4</sub>.
16. Zhang, N. *et al.* Critical Review on Low-Temperature Li-Ion/Metal Batteries. *Adv. Mater.* 34, 2107899 (2022).
17. Seid, K. A. Multiscale electronic transport mechanism and true conductivities in amorphous carbon–LiFePO<sub>4</sub> nanocomposites. *J Mater Chem* 22, 2641–2649 (2012).
18. Azimi, V., Allam, A. & Onori, S. Extending Life of Lithium-Ion Battery Systems by Embracing Heterogeneities via an Optimal Control-Based Active Balancing Strategy. *IEEE Trans. Control Syst. Technol.* 1–15 (2022) doi:10.1109/TCST.2022.3215610.
19. Li, W. *et al.* Online capacity estimation of lithium-ion batteries with deep long short-term memory networks. *J. Power Sources* 482, 228863 (2021).
20. Xu, L., Cooper, J., Allam, A. & Onori, S. Comparative Analysis of Numerical Methods for Lithium-Ion Battery Electrochemical Modeling. *J. Electrochem. Soc.* 170, 120525 (2023).

21. Haverkort, J. W. A theoretical analysis of the optimal electrode thickness and porosity. *Electrochimica Acta* 295, 846–860 (2019).
22. Doyle, M., Fuller, T. F. & Newman, J. Modeling of Galvanostatic Charge and Discharge of the Lithium/Polymer/Insertion Cell. *J. Electrochem. Soc.* 140, 1526–1533 (1993).
23. Berliner, M. D., Cogswell, D. A., Bazant, M. Z. & Braatz, R. D. Methods—PETLION: Open-Source Software for Millisecond-Scale Porous Electrode Theory-Based Lithium-Ion Battery Simulations. *J. Electrochem. Soc.* 168, 090504 (2021).
24. Ferguson, T. R. & Bazant, M. Z. Nonequilibrium Thermodynamics of Porous Electrodes. *J. Electrochem. Soc.* 159, A1967–A1985 (2012).
25. Thomas-Alyea, K. E. Modeling Resistive-Reactant and Phase-Change Materials in Battery Electrodes. *ECSS Trans.* 16, 155–165 (2008).
26. Safari, M. & Delacourt, C. Mathematical Modeling of Lithium Iron Phosphate Electrode: Galvanostatic Charge/Discharge and Path Dependence. *J. Electrochem. Soc.* 158, A63 (2011).
27. Deng, H. D. *et al.* Beyond Constant Current: Origin of Pulse-Induced Activation in Phase-Transforming Battery Electrodes. *ACS Nano* 18, 2210–2218 (2024).
28. Ombrini, P., Bazant, M. Z., Wagemaker, M. & Vasileiadis, A. Thermodynamics of multi-sublattice battery active materials: from an extended regular solution theory to a phase-field model of  $\text{LiMnyFe}_{1-y}\text{PO}_4$ . *Npj Comput. Mater.* 9, 148 (2023).
29. Vasileiadis, A. *et al.* Toward Optimal Performance and In-Depth Understanding of Spinel  $\text{Li}_4\text{Ti}_5\text{O}_{12}$  Electrodes through Phase Field Modeling. *Adv. Funct. Mater.* 28, 1705992 (2018).
30. Lian, H. & Bazant, M. Z. Modeling Lithium Plating Onset on Porous Graphite Electrodes Under Fast Charging with Hierarchical Multiphase Porous Electrode Theory. *J. Electrochem. Soc.* 171, 010526 (2024).
31. Smith, R. B. & Bazant, M. Z. Multiphase Porous Electrode Theory. *J. Electrochem. Soc.* 164, E3291–E3310 (2017).
32. Zhao, H. *et al.* Learning heterogeneous reaction kinetics from X-ray videos pixel by pixel. *Nature* 621, 289–294 (2023).
33. Ferguson, T. R. & Bazant, M. Z. Phase Transformation Dynamics in Porous Battery Electrodes. *Electrochimica Acta* 146, 89–97 (2014).
34. Li, Y. *et al.* Current-induced transition from particle-by-particle to concurrent intercalation in phase-separating battery electrodes. *Nat. Mater.* 13, 1149–1156 (2014).
35. Ender, M., Joos, J., Carraro, T. & Ivers-Tiffée, E. Quantitative Characterization of  $\text{LiFePO}_4$  Cathodes Reconstructed by FIB/SEM Tomography. *J. Electrochem. Soc.* 159, A972–A980 (2012).
36. Li, J. *et al.* Dynamics of particle network in composite battery cathodes. *Science* 376, 517–521 (2022).
37. Bazant, M. Z. Unified quantum theory of electrochemical kinetics by coupled ion–electron transfer. *Faraday Discuss.* 246, 60–124 (2023).
38. Bai, P., Cogswell, D. A. & Bazant, M. Z. Suppression of Phase Separation in  $\text{LiFePO}_4$  Nanoparticles During Battery Discharge. *Nano Lett.* 11, 4890–4896 (2011).
39. Rostami, H., Valio, J., Tynjälä, P., Lassı, U. & Suominen, P. Life Cycle of  $\text{LiFePO}_4$  Batteries: Production, Recycling, and Market Trends. *ChemPhysChem* 25, e202400459 (2024).
40. Usseglio-Viretta, F. L. E. *et al.* MATBOX: An Open-source Microstructure Analysis Toolbox for microstructure generation, segmentation, characterization, visualization, correlation, and meshing. *SoftwareX* 17, 100915 (2022).
41. Jacomy, M., Venturini, T., Heymann, S. & Bastian, M. ForceAtlas2, a Continuous Graph Layout Algorithm for Handy Network Visualization Designed for the Gephi Software. *PLoS ONE* 9, e98679 (2014).
42. Hagberg, A. A., Schult, D. A. & Swart, P. J. Exploring Network Structure, Dynamics, and Function using NetworkX. in 11–15 (Pasadena, California, 2008). doi:10.25080/TCWV9851.

## 7 | MODELING SINGLE-CRYSTAL ELECTRODES AS A NETWORK OF PRIMARY PARTICLES

43. Berg, S. *et al.* ilastik: interactive machine learning for (bio)image analysis. *Nat. Methods* 16, 1226–1232 (2019).
44. Kuo, J. J., Kang, S. D. & Chueh, W. C. Contact Resistance of Carbon–Li<sub>x</sub> (Ni,Mn,Co)O<sub>2</sub> Interfaces. *Adv. Energy Mater.* 12, 2201114 (2022).
45. Becker, V., Birkholz, O., Gan, Y. & Kamlah, M. Modeling the Influence of Particle Shape on Mechanical Compression and Effective Transport Properties in Granular Lithium-Ion Battery Electrodes. *Energy Technol.* 9, 2000886 (2021).
46. Cooper, S. J., Bertei, A., Shearing, P. R., Kilner, J. A. & Brandon, N. P. TauFactor: An open-source application for calculating tortuosity factors from tomographic data. *SoftwareX* 5, 203–210 (2016).
47. Cogswell, D. A. & Bazant, M. Z. Theory of Coherent Nucleation in Phase-Separating Nanoparticles. *Nano Lett.* 13, 3036–3041 (2013).
48. Zhang, Y. *et al.* Lithium-ion intercalation by coupled ion-electron transfer. Preprint at <https://doi.org/10.26434/chemrxiv-2024-d00cp> (2024).
49. Cogswell, D. A. & Bazant, M. Z. Size-dependent phase morphologies in LiFePO<sub>4</sub> battery particles. *Electrochem. Commun.* 95, 33–37 (2018).
50. Bazant, M. Z. Thermodynamic stability of driven open systems and control of phase separation by electro-autocatalysis. *Faraday Discuss.* 199, 423–463 (2017).
51. Chueh, W. C. *et al.* Intercalation Pathway in Many-Particle LiFePO<sub>4</sub> Electrode Revealed by Nanoscale State-of-Charge Mapping. *Nano Lett.* 13, 866–872 (2013).
52. Ombriani, P. *et al.* Kinetically induced memory effect in Li-ion batteries. *EES Batter.* 10.1039/D5EB00014A (2025) doi:10.1039/D5EB00014A.
53. Wycisk, D., Oldenburger, M., Stoye, M. G., Mrkonjic, T. & Latz, A. Modified Plett-model for modeling voltage hysteresis in lithium-ion cells. *J. Energy Storage* 52, 105016 (2022).
54. Afshar, S., Morris, K. & Khajepour, A. Fully dynamical representation of a LFP battery cell. in *2017 American Control Conference (ACC)* 499–504 (IEEE, Seattle, WA, USA, 2017). doi:10.23919/ACC.2017.7963002.
55. Geslin, A. *et al.* Dynamic cycling enhances battery lifetime. *Nat. Energy* (2024) doi:10.1038/s41560-024-01675-8.
56. Valøen, L. O. & Reimers, J. N. Transport properties of LiPF<sub>6</sub>-based Li-ion battery electrolytes. *J. Electrochem. Soc.* 152, A882 (2005).
57. Delacourt, C., Laffont, L., Bouchet, R. & Wurm, C. Toward Understanding of Electrical Limitations (Electronic, Ionic) in LiMPO<sub>4</sub> (M = Fe, Mn) Electrode Materials. *J. Electrochem. Soc.*
58. Wu, X. *et al.* Carbon-Nanotube-Decorated Nano-LiFePO<sub>4</sub> @C Cathode Material with Superior High-Rate and Low-Temperature Performances for Lithium-Ion Batteries. *Adv. Energy Mater.* 3, 1155–1160 (2013).
59. Kench, S. *et al.* Li-ion battery design through microstructural optimization using generative AI. *Matter* S2590238524004466 (2024) doi:10.1016/j.matt.2024.08.014.
60. Schneider, C. A., Rasband, W. S. & Eliceiri, K. W. NIH Image to ImageJ: 25 years of image analysis. *Nat. Methods* 9, 671–675 (2012).
61. Usseglio-Viretta, F. L. E. *et al.* Quantitative Relationships Between Pore Tortuosity, Pore Topology, and Solid Particle Morphology Using a Novel Discrete Particle Size Algorithm. *J. Electrochem. Soc.* 167, 100513 (2020).
62. Bazant, M. Z. Unified quantum theory of electrochemical kinetics by coupled ion-electron transfer. *Faraday Discuss.* 10.1039/D3FD00108C (2023) doi:10.1039/D3FD00108C.
63. Morgan, M. Electrical conduction in amorphous carbon films. *Thin Solid Films* 7, 313–323 (1971).

64. Ombrini, P. *et al.* Kinetically Induced Memory Effect in Li-ion Batteries. Preprint at <https://doi.org/10.26434/chemrxiv-2024-ctxkm> (2024).
65. Pozzato, G. *et al.* Core-Shell Enhanced Single Particle Model for lithium iron phosphate Batteries: Model Formulation and Analysis of Numerical Solutions. *J. Electrochem. Soc.* 169, 063510 (2022).
66. Galuppini, G. *et al.* Efficient computation of safe, fast charging protocols for multiphase lithium-ion batteries: A lithium iron phosphate case study. *J. Power Sources* 580, 233272 (2023).
67. Zeng, Y. & Bazant, M. Z. Cahn-Hilliard Reaction Model for Isotropic Li-ion Battery Particles. *MRS Proc.* 1542, mrss13-1542-g02-01 (2013).
68. Bai, P. & Bazant, M. Z. Charge transfer kinetics at the solid–solid interface in porous electrodes. *Nat. Commun.* 5, 3585 (2014).

## SUPPLEMENTARY INFORMATION

### Particle size distribution

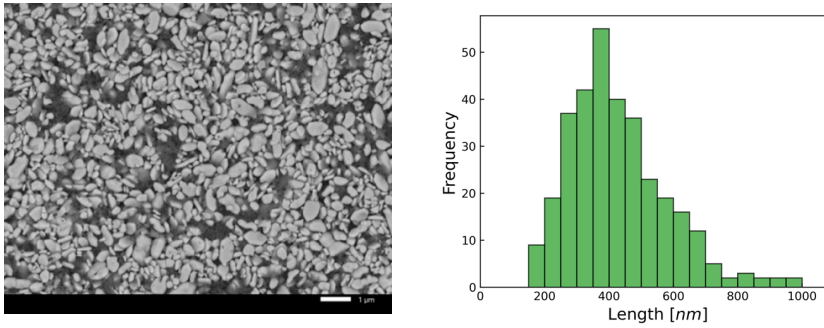
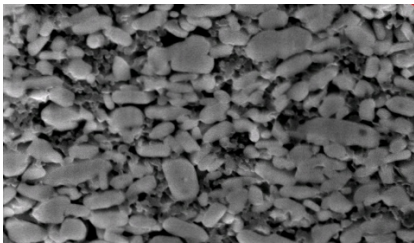


Figure S1. Particle size distribution. a) SEM top-view of the 1 mAh cm<sup>-2</sup> LFP electrode. b) Particle size distribution.

7 The SEM top-view image (Fig. S1a) was analyzed to determine the particle size distribution by measuring the longest dimension of individual particles. The resulting size distribution (Fig. S1b) follows a lognormal trend, with a peak at 350 nm.

### Segmentation

a)



b)

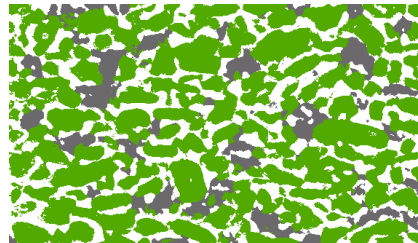


Figure S2. Segmentation procedure. a) FIB-SEM view image of the electrode microstructure. b) Segmented image highlighting the three phases: porosity (white), CB (gray), and LFP phase (green).

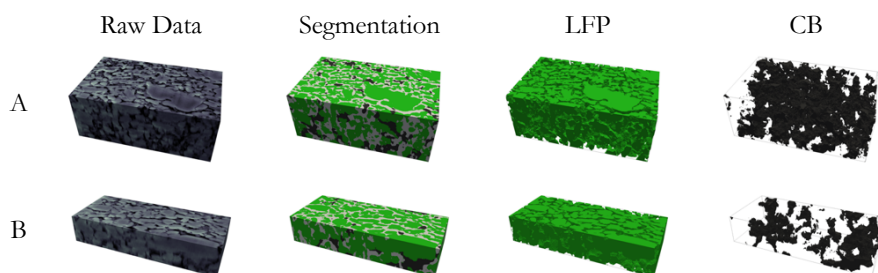


Figure S3. Segmentation of samples A and B. Raw data in grayscale of the two analyzed electrode volumes. Segmented data, LFP phase, and CB phase.

The three-dimensional stack was reconstructed using the ImageJ interpolation tool<sup>60</sup> to ensure cubic voxels. The reconstructed volumes were then segmented into three distinct phases: porosity, carbon black (CB), and the LFP phase. The binder was assumed to be homogeneously distributed, and its volume fraction was considered negligible.

Segmentation was performed using a convolutional neural network (CNN) implemented in ilastik<sup>43</sup>. The process involved manual labeling of the different phases, followed by iterative updates of the CNN until a satisfactory visual agreement was achieved. Due to the overlap in grayscale values between carbon black and particle shading, both grayscale intensity and pattern recognition features were incorporated into the CNN. This approach enabled the differentiation of carbon black from shading artifacts by leveraging its characteristic structural features (Fig. S2b).

### Microstructure characterization

The segmented microstructures were analyzed using the open-source software MATBOX<sup>40</sup>. Feature extraction is necessary to obtain realistic microstructural parameters for the pseudo-2-dimensional model. For instance, the porosity and the tortuosity determine the ionic transport properties.

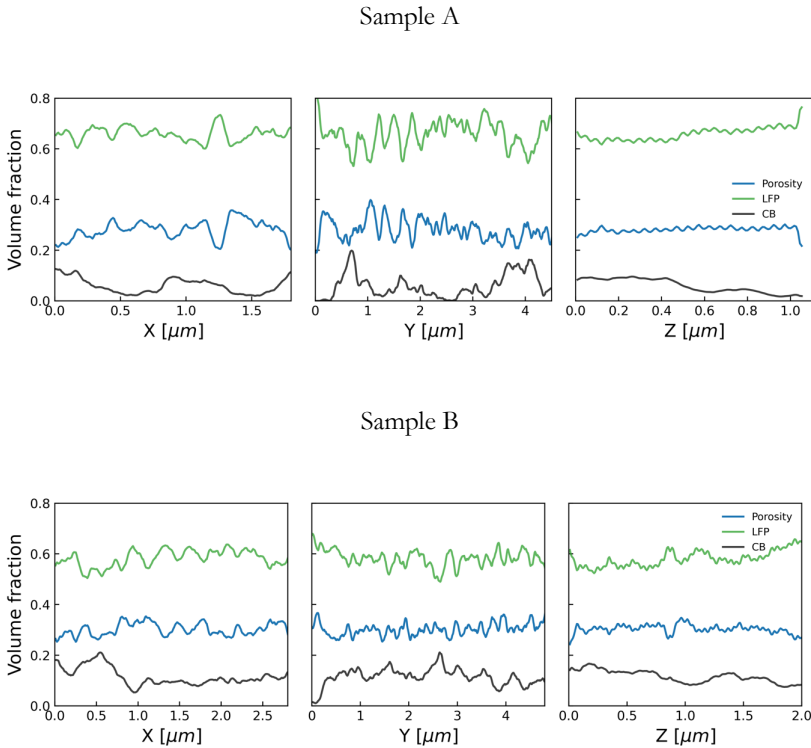


Figure S4. Volume fraction of porosity, LFP, and CB phase along the x, y, and z direction, respectively.

The volume fraction of LFP results homogenous along the various directions of the three-dimensional structure. The carbon phase is instead unevenly distributed (Fig. S4).

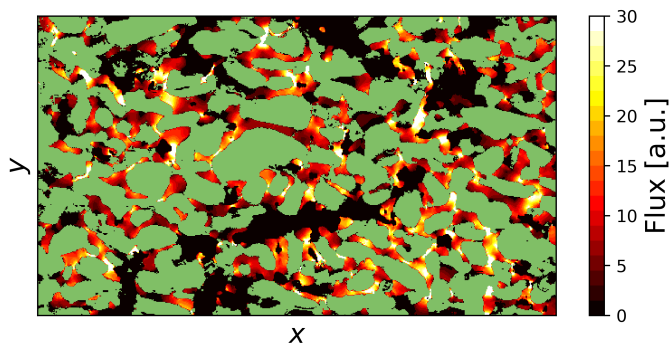


Figure S5. Example of flux calculation of a slice of the segmented volume.

The tortuosity was analyzed with TauFactor<sup>46</sup> to obtain effective ionic conductivities (Fig. S5). The results indicate that the electrode exhibits strongly anisotropic transport properties. Excluding the z-direction, which may be influenced by slicing and interpolation, a difference is observed between the y-direction (perpendicular to the current collector) and the x-direction (parallel to the current collector), having tortuosity of 5.46 and 3.02, respectively. This anisotropy is likely a consequence of the drying and calendaring processes. The higher tortuosity along the y-direction reduces the through-plane ionic conductivity. So, considering the relation between tortuosity  $\tau$  and porosity  $\varepsilon$ ,  $\tau = \varepsilon^\beta$ , the Bruggeman exponent results  $\beta = -1.49$ . Nevertheless, the limited electrode thickness ensures that ionic diffusion is not a limiting factor (Fig. S15).

## Particle identification

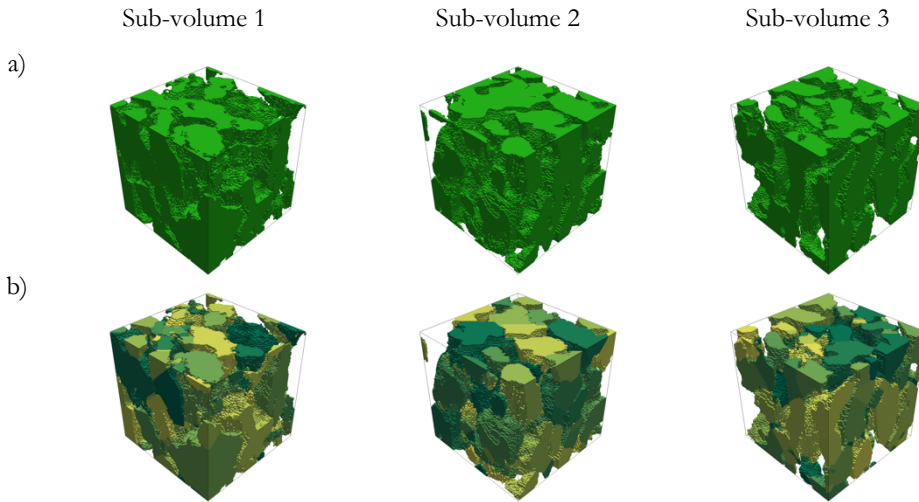


Figure S6. Particle identification. Examples of segmented LFP phase (a) and corresponding particle labeling after particle identification (b). The colors of the labelled particles correspond to different label numbers.

7

The mesoscopic (electrode-level) properties guarantee a precise reduced-order description of the long-range transport phenomena. The microscopic (agglomerate-level) properties are instead necessary to fully characterize the connectivity of the system and abstract it into a network. To analyze these properties, the segmented volumes were divided in 20 cubic sub-volumes of 1  $\mu\text{m}$  side length. The Pseudo-Coulomb Repulsive field (PCRf) method<sup>61</sup> was employed to distinguish and label each particle in the sub-volumes. This method was chosen due to its effectiveness in identifying particles with non-spherical shapes, which are commonly observed in LFP single-crystal systems (Fig. S6). The same approach was applied to label carbon particles. The resulting volumes are composed of  $\sim 150$  particles, suitable for optimizing the simulation time without compromising accuracy.

## Sub-volume post-processing

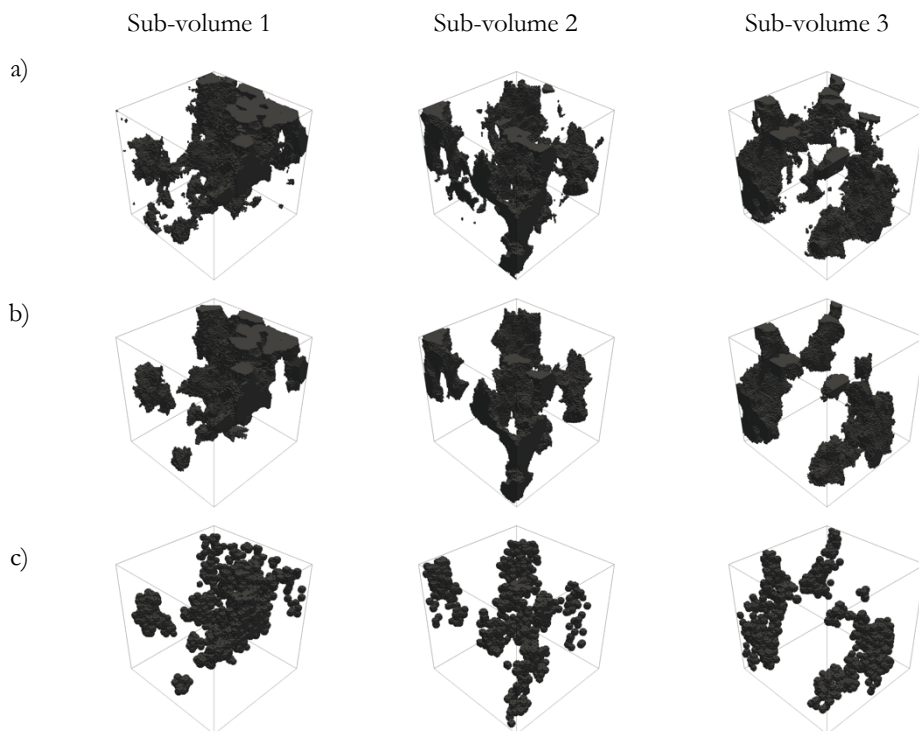


Figure S7. Carbon phase reconstruction. Examples of segmented carbon phase (a), corresponding post-processed carbon phase (b) and reconstructed carbon nanoparticles (c).

Post-processing algorithms were applied to remove artifacts originated during segmentation and particle identifications. Specifically, a particle size threshold was defined to exclude carbon and LFP particles with sizes smaller than  $10^6 \text{ nm}^3$  and  $10^5 \text{ nm}^3$ , respectively. After these adjustments, the resulting sub-volumes are composed of  $\sim 150$  LFP particles (Fig. S7b), and the particle size distribution (Fig. 7.2) is in line with the one manually obtained by particle counting (Fig. S1). Additionally, the carbon phase was considered to consist of agglomerated nanoparticles smaller than 50 nm in size, with intrinsic nanoporous structures. Accurate representation of carbon-particle contact is critical for the model, necessitating precise retrieval of these features. The segmented carbon phase does not resolve nanoscale details but instead captures the tap density of the carbon black (CB). For the remainder of this document, the term “CB volume fraction” refers to the tap volume fraction, i.e., the volume fraction determined prior to nanoparticle generation. This approach allows a direct relationship between manufacturing parameters and electrode performance.

## 7 | MODELING SINGLE-CRYSTAL ELECTRODES AS A NETWORK OF PRIMARY PARTICLES

To generate a realistic nanoporous structure, MATBOX<sup>40</sup> was employed to create 50 nm-wide carbon nanoparticles in the regions corresponding to the segmented carbon phase (Fig. S7c). Based on the difference between the tap density and the bulk density of the carbon black, 50% of the segmented carbon black regions were filled with these nanoparticles. This reconstruction significantly improved the precision of the structural analysis. It was observed that the contact area between LFP particles and the carbon phase was reduced, on average, by an order of magnitude, resulting in substantial differences in carbon-LFP conductivity.

### Networks construction

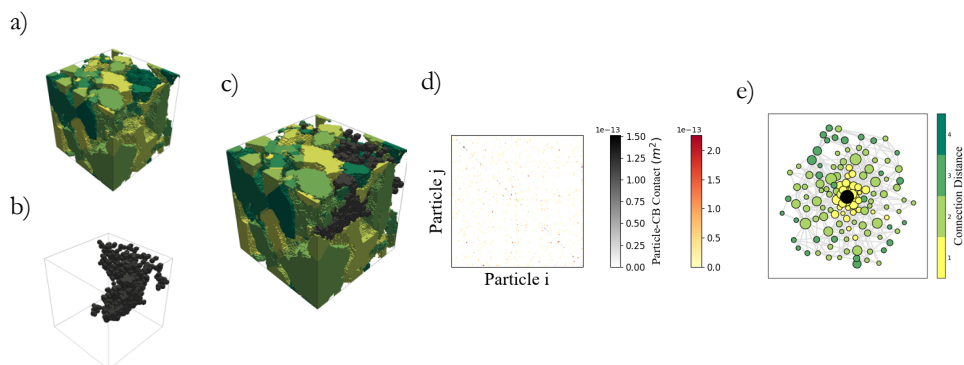


Figure S8. Network construction. Example of a three-dimensional reconstruction of LFP (a) and CB particles (b). c) Fully reconstructed three-dimensional sub-volume. d) Example of an adjacency matrix, where copper intensity is proportional to the particle-particle contact area, and the grayscale of diagonal elements represents the particle-CB contact area. (e) Resulting network representation, where node size is proportional to particle size, and color indicates the connection distance from the CB.

Each sub-volume was abstracted into a network of reactive particles. For each particle within the sub-volume, the following features were extracted: volume, surface area, thickness, and width. Principal component analysis was employed to identify the direction of minimal variance, enabling the extraction of particle thickness and width. The contact areas with the electrolyte (reactive surface area), adjacent particles, and the carbon phase were determined by counting the number of shared voxel surfaces between a particle and the neighboring phase. Periodic boundary conditions were considered, i.e. the voxels at the edge of the tensor were considered neighbors with the ones on the opposite side. This was done to avoid drastically reducing the number of contacts of bigger particles at the edge of the curve.

Using the contact information, an adjacency matrix was constructed (Fig. S8d). The diagonal elements of the matrix represent the particle-carbon contact area (if present), while the off-diagonal elements store the particle-particle contact areas. The network was then built by

assigning extracted particle features (e.g., volume, surface area, reactive surface area, thickness, and width) to each node. If the particle-particle contact area was non-zero, an edge was created between the corresponding nodes, with the relative contact area as the edge weight. Similarly, if a particle-carbon contact was present, an edge connecting the particle to an external "carbon node" was added (Fig. S8e).

## Sub-volume statistics

Due to computational limitations, the obtained 20 sub-volumes, each containing  $\sim 150$  particles cannot be fully incorporated into the abstracted network model. To address this, it was necessary to identify a representative subset of sub-volumes. To balance computational efficiency with physical accuracy, a statistical analysis of the sub-volumes was conducted to select those that are most representative of the overall system.

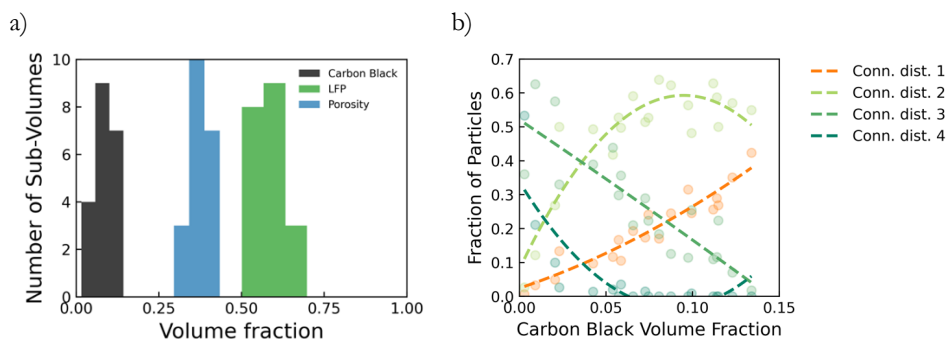


Figure S9. Distribution of phase fractions. a) Distribution of phases among sub-volumes. b) Relation between the sub-volume's carbon black volume fraction and the connection distances.

The sub-volumes exhibit a median porosity of approximately 32%, a carbon black (CB) volume fraction of  $\sim 8.5\%$ , and an LFP volume fraction of  $\sim 59\%$ . The distributions of these properties, with comparable standard deviations for all phases, suggest a uniform microstructure (Fig. S9a). This uniformity is particularly evident for the LFP volume fraction and porosity, as small variations in these parameters do not significantly affect the electrode's performance.

However, the distribution of the CB volume fraction is a critical factor. Analyzing the connectivity within the sub-volumes reveals a strong correlation between the CB volume fraction and the distribution of connection distances (Fig. S9b). Specifically, the fraction of particles with a connection distance of 1 is directly proportional to the CB fraction, whereas connection distances of 3 and 4 are inversely proportional. Consequently, even small variations in the CB fraction can lead to substantial differences in the connection distance distribution.

## 7 | MODELING SINGLE-CRYSTAL ELECTRODES AS A NETWORK OF PRIMARY PARTICLES

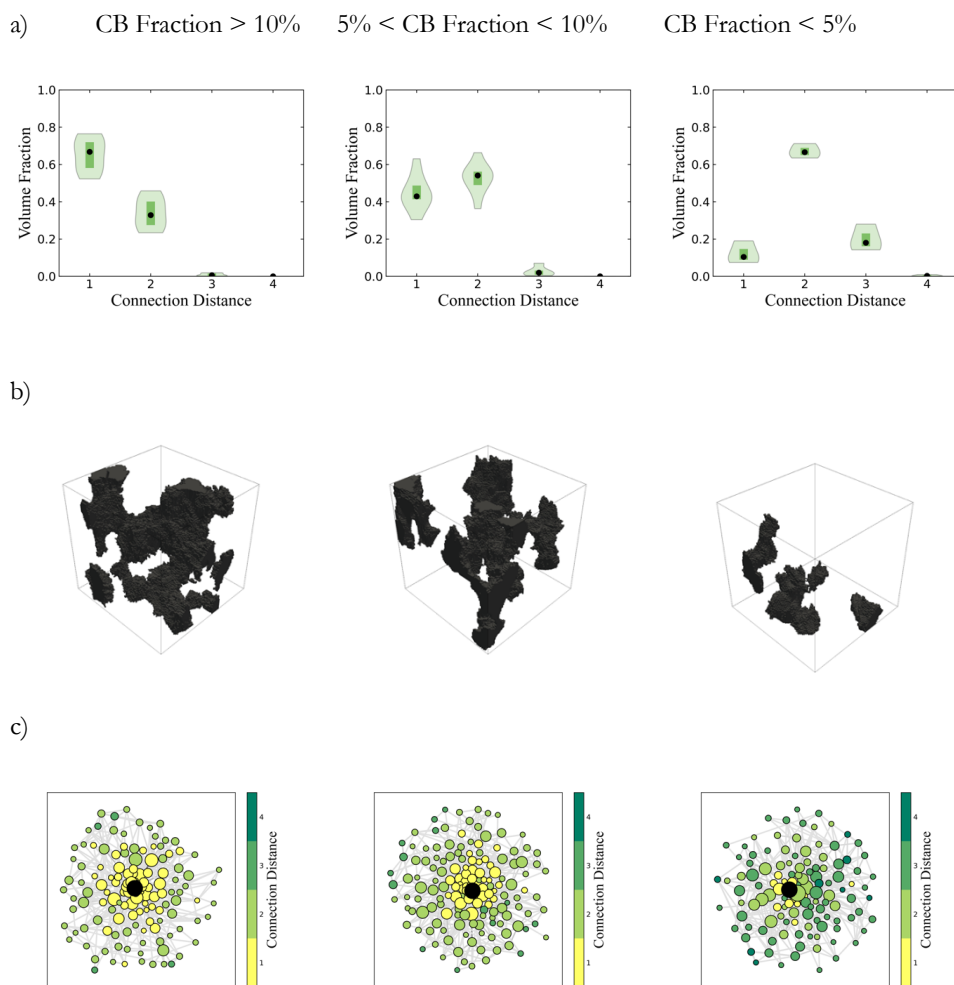


Figure S10. Sub-volumes sets. a) Volume fraction distribution as a function of connection distance. b) Segmented CB phase in the volume. c) Network obtained from the volume analysis.

Sub-volumes with a CB fraction greater than 10% are capable of sustaining fast reaction kinetics due to the high fraction of particles with a connection distance of 1. In contrast, sub-volumes with a CB fraction below 5% experience a drastic reduction in connectivity, with the majority of particles exhibiting a connection distance of 3. Based on this observation, the sub-volumes were categorized into three sets: those with CB fractions greater than 10%, between 5% and 10%, and below 5%. Analyzing these three sets revealed distinct differences in their connection distance distributions (Fig. S10a). The set with median CB volume fraction displayed a

distribution similar to that of the entire sub-volume ensemble (Fig. 7.2). In contrast, sub-volumes with CB fractions greater or lower than the median showed distributions skewed towards connection distances of 1 or 3, respectively.

Furthermore, two of the 20 sub-volumes were identified with CB fractions as low as 1.5% and 1.7%. When included in the simulations (Fig. S19), these sub-volumes deliver very limited capacity even at a every tested rate. This result led to the conclusion that approximately 5% of the LFP material remains inactive due to insufficient surrounding carbon black. While a full multi-network model may consider these heterogeneities, we account for this effect with a 5% reduction in active material volume fraction in the simulation parameters. In the way we could maintain a limited number of sub-volumes for each simulation.

This adjustment ensures that the pseudo-2-dimensional model captures an intrinsic 3-dimensional characteristic of the electrode. This approximation also explains the discrepancy between the delivered capacity at C/10 and the theoretical capacity calculated based on the electrode's thickness, porosity, and weight fractions of CB, LFP, and binder.

## Mathematical model

The presented model was implemented as an expansion of multiphase porous electrode theory (MPET) already implemented by previous studies<sup>31</sup> by including the network connectivity within the discretized volumes. Here we elucidate the model's novel equations, for a description of MPET, the reader is referred to reference<sup>31</sup>.

In each a discretized sub-volume, the charge conservation for each node results in

$$\begin{cases} I_i(\eta_i) - G_{i-cb}(\varphi_i - \varphi_{cb}) - \sum_{i \neq j} G_{ij}(\varphi_i - \varphi_j) = 0 \text{ if } G_{i-cb} \neq 0 \\ I_i(\eta_i) - \sum_{i \neq j} G_{ij}(\varphi_i - \varphi_j) = 0 \text{ if } G_{i-cb} = 0 \end{cases} \quad (\text{E1})$$

we consider a particle  $i$ , at potential  $\varphi_i$ , reacting with the electrolyte. The particle acts as a source (or sink) of current  $I_i$  and exchanges current with the carbon black ( $cb$ ), having potential  $\varphi_{cb}$ , and with the particles  $j$  in contact with  $i$  (if  $G_{ij} \neq 0$ ), having potential  $\varphi_j$ . Finally, the reaction current  $I_i$  depends on the local reaction overpotential  $\eta_i$ .

The particle-carbon conductance  $G_{i-cb}$  is calculated based on the spreading resistance model<sup>44,45</sup>:

$$G_{i-cb} = \sigma_c 2 \sqrt{A_{i-cb}/\pi} \quad (\text{E2})$$

where  $A_{i-cb}$  is the obtained contact area, stored in the adjacency matrix (Fig. S8) in location  $(i, i)$ . The same approximation is chosen for the particle-particle conductance  $G_{ij}$ , so that

$$G_{ij} = \sigma_c 2 \sqrt{A_{ij}p/\pi} \quad (\text{E3})$$

where  $A_{ij}$  is the particle-particle contact area, stored in the adjacency matrix in location  $(i, j)$ . Moreover, a penalty factor  $p = 0.01$  is added to consider the difference between the apparent contact area and the roughness effect<sup>44</sup>. More complex methodologies can be used<sup>45</sup>, but for the sake of clarity and effectiveness, we adopted the spherical contact assumption<sup>44</sup>.

The contact conductivity ( $\sigma_c$ ) depends on the material under study. For the LiFePO<sub>4</sub> case, we consider it as the conductivity of the carbon coating, thus independent of the particle concentration. If instead an uncoated material is used, e.g. LiCoO<sub>2</sub>, where the conductivity mainly comes from bulk conduction, a concentration dependence might be considered. Moreover, the model assumes the contact area as the main source of resistance, while the potential of the particle's surface is assumed uniform. Given the temperature dependence of the carbon coating conductivity, we incorporate an Arrhenius relation for the electronic conductivity:

$$\sigma_c = \sigma_{c_0} e^{-\frac{E_\sigma}{k_B T} \left(1 - \frac{T}{T_{amb}}\right)} \quad (\text{E4})$$

Where  $\sigma_{c_0}$  is the conductivity at room temperature ( $T_{amb} = 298 \text{ K}$ ),  $E_\sigma$  is the activation energy for the electrical conductivity,  $k_B$  is the Boltzmann constant, and  $T$  the temperature.

The reaction overpotential is defined as  $\eta_i = \mu_{surf_i} - \mu_{elyte} - \varphi_i$ , depending so on the electrolyte chemical potential in the discretized sub-volume ( $\mu_{elyte}$ ), considered uniform within the network, and the surface chemical potential of the reacting specie  $\mu_{surf_i}$ . The surface chemical potential will depend on the chosen kinetic model and the thermodynamic properties of the material. The particle kinetics can be approximated with Fickian diffusion<sup>3</sup>, Cahn Hillard<sup>24,29</sup>, or Allen Cahn<sup>38</sup>. The open circuit potential can either be fitted from experimental data or derived based on the regular solution theory<sup>24,28,31</sup>. For solid solution materials (e.g. LiCoO<sub>2</sub>, LiNi<sub>x</sub>Mn<sub>y</sub>Co<sub>1-x-y</sub>O<sub>2</sub>) the first option is effective so that:

$$\mu_{solid} = -eV(c) \quad (\text{E5})$$

where  $V(c)$  is the fitted open circuit potential, dependent on the solid concentration  $c$ . For phase separating materials (e.g. LiFePO<sub>4</sub>, LiFe<sub>x</sub>Mn<sub>1-x</sub>PO<sub>4</sub>, Na<sub>3</sub>V<sub>2</sub>(PO<sub>4</sub>)<sub>3</sub>, Graphite) is fundamental to consider the free energy functional<sup>24,32</sup>  $G(c)$ , comprehensive of the phase boundary penalty and wetting energies. Approximating the homogenous bulk free energy with the regular solution theory<sup>24,28</sup>, and considering the phase gradient energy penalty from phase-field modeling, we obtain

$$\mu_{solid} = -eV_0 + k_B T \ln\left(\frac{\tilde{c}}{1 - \tilde{c}}\right) + \Omega (1 - 2\tilde{c}) - \nabla \cdot (\kappa \nabla \tilde{c}) \quad (\text{E6})$$

## 7 | MODELING SINGLE-CRYSTAL ELECTRODES AS A NETWORK OF PRIMARY PARTICLES

where  $\tilde{c} = c/c_{max}$ ,  $V_0$  is the standard reaction potential,  $T$  the temperature,  $\Omega$  the regular solution parameter (regulating the phase separation<sup>24,28</sup>) and  $\kappa$  the specific gradient energy.

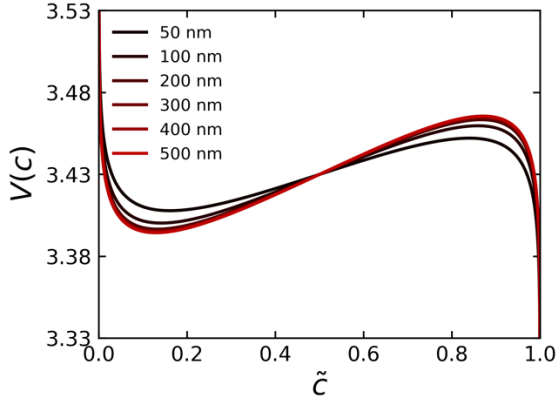


Figure S11. Size dependent open circuit potential of LFP.

To consider the effect of wetting and phase boundary energy in the reduced order formalism, the regular solution parameter ( $\Omega$ ) can be described as size dependent<sup>33,47</sup>. This method allows the use of 0-dimensional particle model, leading to faster computation with almost identical results. A result comparison is presented in Fig. S28.

The particle's current  $I_i(\eta_i)$  is defined as the integral over the reactive surface area  $S_i$ :

$$I_i(\eta_i) = \int_{S_i} j_i(\eta_i) dS \quad (E7)$$

where the functional form of  $j(\eta)$  depends on the limiting factor<sup>48,62</sup>. Based on Coupled Ion Electron Transfer theory (CIET), in case of electron-transfer-limited reaction kinetics we can express  $j(\eta)$  as a function of the exchange current density  $k_0$ , activation energy  $E_A$ , normalized electrolyte concentration  $\tilde{c}_{Li^+} = c_{Li^+}/c_{elyte_0}$  and normalized reorganization energy  $\tilde{\lambda} = \lambda/k_B T$ .

$$j(\eta) = k_0 e^{-\frac{E_A}{k_B T} \left(1 - \frac{T}{T_{amb}}\right)} \left(\frac{1 - \tilde{c}}{2}\right) \left(\frac{\tilde{c}_{Li^+}}{1 + e^{\eta_f/k_B T}} - \frac{\tilde{c}}{1 + e^{-\eta_f/k_B T}}\right) \operatorname{erfc}\left(\frac{\tilde{\lambda} - \sqrt{1 + \tilde{\lambda}} + \left(\frac{\eta_f}{k_B T}\right)^2}{2\sqrt{\tilde{\lambda}}}\right) \quad (\text{E8})$$

where we consider the formal overpotential  $\eta_f = \eta + \frac{k_B T}{e} \ln\left(\frac{\tilde{c}_{Li^+}}{\tilde{c}}\right)$ .

In the case of ion-transfer-limited reaction kinetics, we can instead use

$$j(\eta) = k_0 e^{-\frac{E_A}{k_B T} \left(1 - \frac{T}{T_{amb}}\right)} \tilde{c}_{Li^+}^{1-\alpha} \tilde{c}^\alpha (1 - \tilde{c}) \left(e^{-\alpha \frac{e\eta}{k_B T}} - e^{(1-\alpha) \frac{e\eta}{k_B T}}\right) \quad (\text{E9})$$

In general, the ionic surface concentration  $c_{Li^+}$  is a function of the electrolyte concentration  $c_{elyte}$ . The relation between the two depends on the adsorption energy and the activity electrolyte activity. These values, difficult to obtain experimentally, typically lead to  $c_{Li^+} \sim c_{elyte}/3$  in concentrated organic electrolytes<sup>32,48,62</sup>. We so adopted this approximation to model our reaction kinetics.

The average particle filling fraction  $\bar{c}_i$  evolves depending on the particle's reaction current  $I_i$  and its volume  $V_i$ :

$$\frac{d\bar{c}_i}{dt} = -\frac{I_i(\eta_i)}{e V_i c_{max}} \quad (\text{E10})$$

For the case of 0-dimensional approximation, the current is so given by  $I_i(\eta_i) = j_i(\eta_i) S_i$ . The surface to volume ratio  $S_i/V_i$  is thus the dominant factor governing the particle's reaction kinetics.

The total current density in the sub-volume is thus

$$I_V = -\varepsilon_{AM} e c_{max} \sum_i \frac{V_i}{V_{tot}} \frac{d\bar{c}_i}{dt} \quad (\text{E11})$$

## 7 | MODELING SINGLE-CRYSTAL ELECTRODES AS A NETWORK OF PRIMARY PARTICLES

where  $\epsilon_{AM}$  is the active material volume fraction and  $V_{tot}$  is the total volume of all the particles in the sub-volume. The electrolyte and carbon black potentials depend on the long-range transport properties of the electrode and are described by Stefan-Maxwell concentrated solution theory and Ohm's law, respectively<sup>31</sup>. The electrolyte parameters are taken from reference<sup>56</sup>.

### Model parametrization

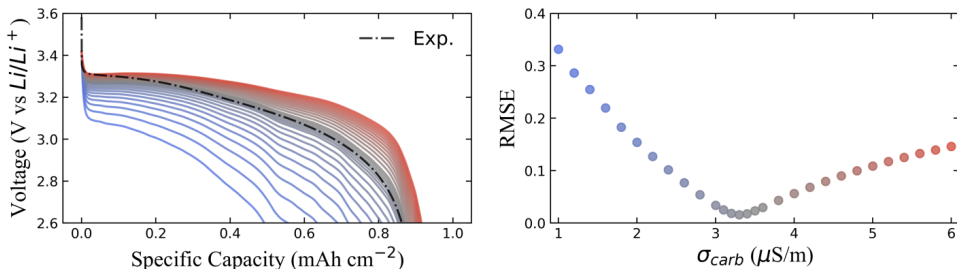


Figure S12. Effect of  $\sigma_c$  on the ambient temperature 2C discharge voltage curve at of the  $1 \text{ mAh cm}^{-2}$  sample (left). Corresponding root mean square error (right).

7

Due to the extensive characterization of the electrode, the parameter estimation for the system results straightforward. Having only one unknown parameter, the inter-particle conductivity  $\sigma_c$ , we necessitate only one dataset. We selected the 2C discharge voltage curve of the  $1 \text{ mAh cm}^{-2}$  sample, choosing a thin electrode to minimize electron transport limitations along its thickness, thereby eliminating the need to estimate  $\sigma_{bulk}$ . Moreover, the 2C protocol, which delivers 86% of the capacity, highlights kinetic limitations while avoiding intra-particle diffusion constraints, ensuring the current remains within the model's validity range. Regarding the cell's series resistance and the Li-metal reaction overpotential, we analytically determine their combined upper bound. The overpotential at the start of the 1C discharge curve is approximately 50 mV. Given a current density of  $1 \text{ mA cm}^{-2}$ , this corresponds to an upper bound for the series resistance,  $R_{series}$ , of  $5 \text{ m}\Omega \text{ m}^2$ . Since the cathode is the primary contributor to the overpotential, we assign a conservative value of  $R_{series} = 10^{-2} \text{ m}\Omega \text{ m}^2$  to ensure its contribution remains negligible. The complete parameter set is provided in Table T1.

As shown in Fig. S12, we varied  $\sigma_c$  from  $1 \mu\text{S m}^{-1}$  to  $6 \mu\text{S m}^{-1}$  in increments of  $0.2 \mu\text{S m}^{-1}$  and then refine the fitting around the minimum of the root mean square error (RMSE), obtaining  $\sigma_c = 3.3 \mu\text{S m}^{-1}$ . The RMSE between the experimental and simulate voltage  $V$  and  $\hat{V}$  is defined as:

$$RMSE = \sqrt{\frac{\sum_{i=1}^N (V_i - \widehat{V}_i)^2}{N}} \quad (\text{E12})$$

The resulting model successfully extrapolates to higher and lower rates for both charge and discharge (Fig. 7.3). Discrepancies between the model and experimental results primarily occur at the initial stage of the curve and at higher rates. These deviations can be attributed to the assumption of a zero-dimensional, reaction-limited particle model. Since the whole particle reacts simultaneously, the initial activation overpotential is higher, leading to an initially elevated overpotential. Despite this limitation, the model accurately captures capacity retention even at high rates, as the primary source of overpotential—inter-particle connectivity—is well represented.

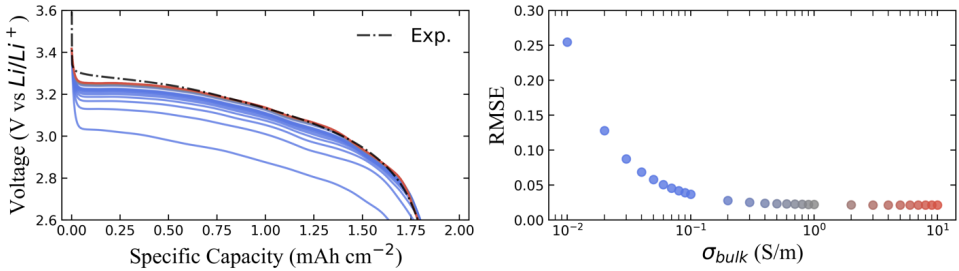


Fig. S13. Effect of  $\sigma_{bulk}$  on the ambient temperature 2C discharge voltage curve at of the 2 mAh cm<sup>-2</sup> sample (left). Corresponding root mean square error (right).

Simulations reproducing the behavior of the 2 mAh cm<sup>-2</sup> sample were also parametrized based on the 2C discharge cycle. Due to the higher loading and increased electrode thickness, sensitivity to  $\sigma_{bulk}$  was more pronounced. An optimal fit was achieved when  $\sigma_{bulk}$  was set above 0.5 S m<sup>-1</sup>, consistent with literature values<sup>54</sup>. Below this threshold, the error increased significantly. Thus, we concluded that bulk electronic conductivity can also be neglected for the 2 mAh cm<sup>-2</sup> sample, as inter-particle electron transfer remains the dominant factor even at higher loadings. Consequently, the thicker electrode could be accurately fitted by solely adjusting the electrode thickness parameter based on the measured thickness (Fig. S18).

## 7 | MODELING SINGLE-CRYSTAL ELECTRODES AS A NETWORK OF PRIMARY PARTICLES

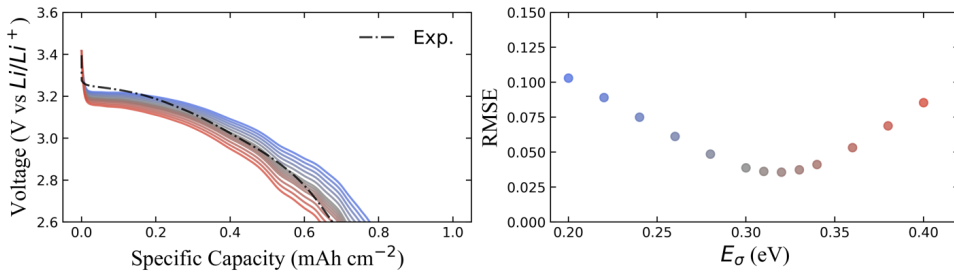


Figure S14. Effect of  $E_\sigma$  on the 2C discharge voltage curve at  $-10$  °C (left). Corresponding root mean square error (right).

Lower-temperature simulations were conducted using the derived model and parameters, with the activation energy of inter-particle conductivity,  $E_\sigma$ , as the only additional fitted parameter. The minimum error for the 2C discharge cycle at  $10$  °C was found at  $E_\sigma = 0.32$  eV, consistent with previously reported values for carbon-coated LFP particles<sup>17,63</sup>. With these parameters, the model accurately predicts capacity retention across various temperatures and rates (Fig. 7.4). Under extreme conditions, such as  $-5$  °C at a 2C rate, the model estimates higher overpotentials than those observed experimentally, while at 0.5C and  $-5$  °C, it predicts higher capacity retention. These discrepancies likely stem from limited understanding of the effects of low temperatures on reaction kinetics and electrolyte transport, highlighting the need for further research to improve model reliability and enhance low-temperature performance control.

## Variable evolution along electrode thickness

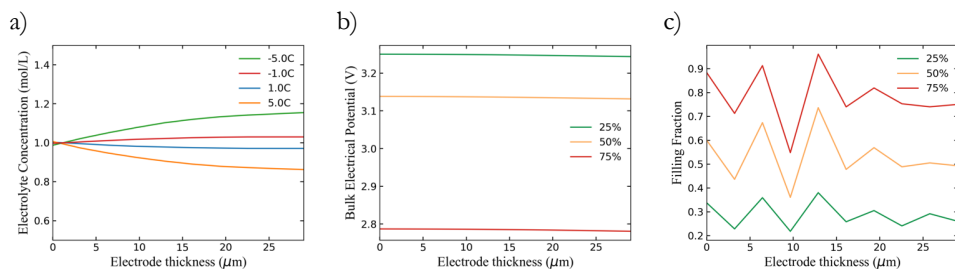


Figure S15. Depth-wise heterogeneities a) Electrolyte concentration as a function of electrode's depth, during the last simulation timestep (cutoff voltage) for the 1 mAh cm<sup>-2</sup> simulations, at ambient temperature, at various C-rates. b) Electrical potential of the bulk phase (carbon black backbone) as a function of electrode depth, at various DOD for the 2C discharge cycle of the 1 mAh cm<sup>-2</sup> simulation. c) Volume-average filling fraction as a function of electrode's depth, at various DOD for the 2C discharge cycle of the 1 mAh cm<sup>-2</sup> simulation.

Despite the relatively high tortuosity obtained from the microstructure characterization ( $\tau = \epsilon^{-1.49}$ ), the electrolyte diffusion maintains the electrolyte concentration close to the initial value (1 mol/L) (Fig. S15a). This stability is attributed to the limited electrode thickness (30 μm) and the low current densities, which do not exceed 5 mA cm<sup>-2</sup>. For similar reasons, the bulk potential exhibits minimal variation along the electrode thickness (Fig. S15b).

In contrast, the filling fraction shows variability along the electrode depth (Fig. S15c). This arises from the use of different sub-volumes, each with slightly varying CB volume fractions, to represent the electrode's heterogeneity. In our modeling approach, these sub-volumes are arranged in series along the electrode thickness. This approximation is appropriate for the system, as both the electrolyte concentration and bulk electrical potential remain relatively uniform across the thickness. This setup ensures that each network receives consistent boundary conditions for bulk potential and reaction kinetics while maintaining a computational time of less than one minute per simulation.

## 7 | MODELING SINGLE-CRYSTAL ELECTRODES AS A NETWORK OF PRIMARY PARTICLES

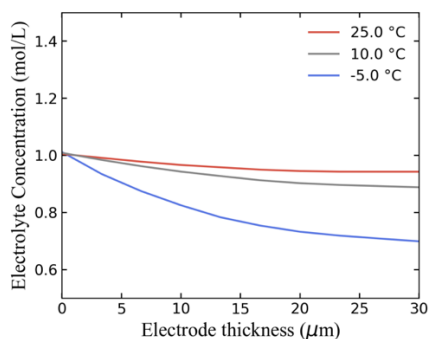


Figure S16. Electrolyte concentration as a function of electrode's depth, during the last simulation timestep (cutoff voltage) for the  $1 \text{ mAh cm}^{-2}$  simulations, during a 2C discharge at various temperatures.

In the case of low-temperature simulations, the electrolyte concentration exhibits greater polarization effects due to the reduced electrolyte diffusivity (Fig. S16). However, this variation is not responsible for the performance drop, as simulating the electrode without incorporating temperature-dependent intra-particle conductivity fails to capture the expected capacity retention (Fig. S17).

7

### The role of the temperature-dependent electrolyte kinetics

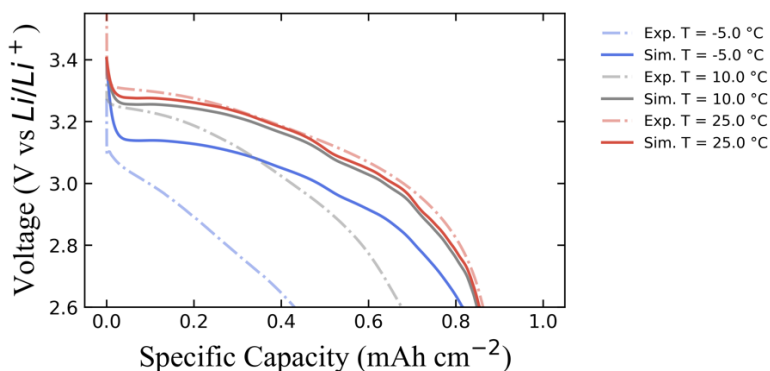


Figure S17. Comparison between the experimental and the simulated voltage profiles at 2C discharge rate in case the inter-particle electrical conductivity is not temperature dependent.

The model accounts for various sources of temperature dependence, including inter-particle electrical conductivity, reaction kinetics, and electrolyte ionic conductivity and diffusivity. To isolate the effects of these factors, Fig. S17 presents the simulated voltage response when only

typical temperature dependencies—electrolyte properties and reaction kinetics—are considered. The simulation results indicate increased overpotential at lower temperatures, primarily due to limitations in electrolyte transport and charge transfer kinetics. However, the electrode's low thickness and high reactive surface area prevent these factors from becoming the dominant bottleneck. This finding underscores the necessity of incorporating the temperature dependence of electronic conductive pathways to achieve a predictive and reliable model.

### Comparison between simulations and experiments of the 2 mAh cm<sup>-2</sup> sample

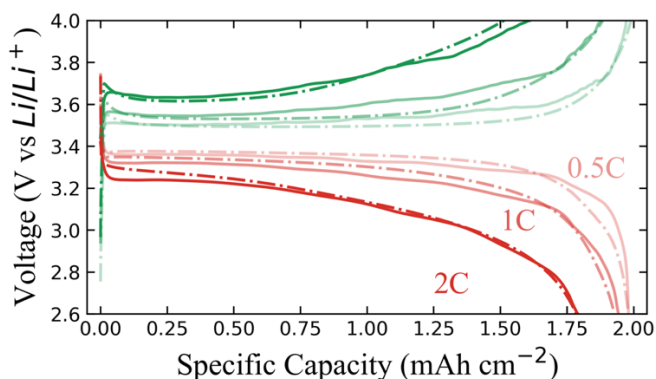


Figure S18. Comparison between the experimental and the simulated voltage profiles for the 2 mAh cm<sup>-2</sup> sample at various C-rates. The charge is represented in green, the discharge in red.

Using the parameters obtained from fitting the 1 mAh cm<sup>-2</sup> sample, and solely doubling the electrode thickness, the model accurately reproduces the experimental results for the 2 mAh cm<sup>-2</sup> electrode (Fig. S18). This further confirms that electronic connectivity is the primary limiting factor, while ionic transport in the electrolyte has a minimal impact on this electrode configuration.

The strong extrapolation capability of the model demonstrates its suitability for optimizing electrode properties without requiring extensive experimental datasets, making it a valuable tool for electrode design and performance enhancement.

## Effect of the carbon black volume fraction

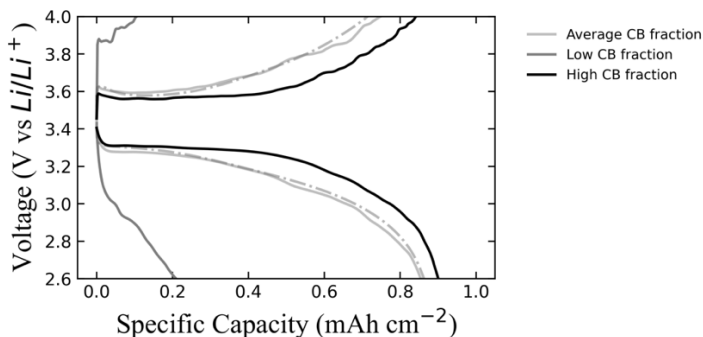


Figure S19. Simulated voltage curves for 4 different sub-volumes groups presenting difference active material and carbon black volume fractions.

Previous studies<sup>13,44</sup> have investigated the impact of carbon black (CB) volume fraction on the performance and kinetics of single-crystal LFP electrodes. To assess the model's ability to reproduce these experimental trends, we utilized the obtained sub-volume sets, each characterized by a different CB fraction (Fig. S9), to simulate the response of an electrode with a modified active material ratio. This approach enables the quantification of the role of connectivity and conductive additives in commercial electrodes without the need to prepare multiple slurries and coatings.

The results (Fig. S19) reveal a strong correlation between performance and CB content. For instance, during a 2C discharge, the sub-volume set with a CB volume fraction greater than 10% delivers 6% more capacity than the set containing 5–10% CB. In contrast, the set representing CB fractions below 5% is severely constrained by inter-particle contact resistance, exhibiting significantly slower kinetics and delivering 76% less capacity at the same rate. Furthermore, charge-discharge asymmetry decreases with increasing CB content and is more pronounced in simulations with low CB fractions.

These findings highlight the highly nonlinear relationship between CB fraction and electrode kinetics. A moderate increase in CB content can lead to a substantial improvement in performance. However, once the CB fraction is optimized for the target current rate, further increases do not provide significant kinetic benefits. Additionally, this methodology offers valuable insights into the role of conductive additives, enabling the optimization of electrode composition without the need for extensive experimental testing.

## Effect of exchange current density and inter-particle conductivity

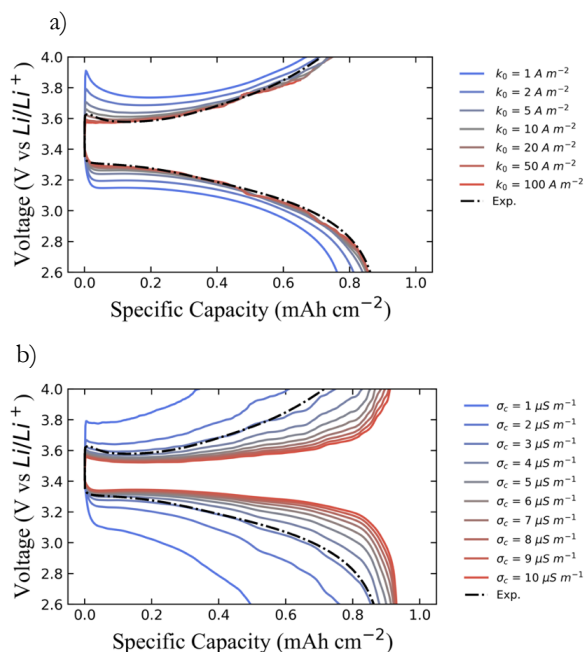


Figure S20. Comparison between the experimental and simulated voltage curve of a 2C discharge and 2C charge at varying  $k_0$  (a) and  $\sigma_c$  (b).

To illustrate the role of the inter-particle conductivity  $\sigma_c$  and the exchange current density  $k_0$ , and clarify the main kinetic limiting factor of the system, in Fig. S20 we show their effect on the 2C charge-discharge voltage curves on a wide range. The effects of small  $k_0$  variations are negligible (Fig. S20a), showing its difficult identifiability and relative lower importance of electrode kinetics. Solely when changing the order of magnitude,  $k_0$  mainly affects the initial overpotential in both the charging and discharging process. The charging process is more severely affected due to the asymmetric concentration dependence of the exchange current density<sup>62</sup>. However, capacity retention is not substantially impacted. This behavior arises from the phase-separating nature of the particle ensemble, which compensates for a lower  $k_0$  by increasing the number of active particles, leading to a more uniform current distribution. When  $k_0$  drops significantly the system activates instead all the available particles, exhibiting a distinctly reaction-limited behavior.

In contrast, variations in  $\sigma_c$  have a pronounced effect on the delivered capacity for both charge and discharge (Fig. S20b). Since electronic resistance is the primary source of overpotential, even small changes in  $\sigma_c$  within the same order of magnitude lead to substantial capacity differences.

## 7 | MODELING SINGLE-CRYSTAL ELECTRODES AS A NETWORK OF PRIMARY PARTICLES

These results highlight the critical importance of optimizing electrode connectivity and minimizing the contact resistance, as these factors have a more significant impact on electrode performance compared to reducing charge transfer resistance.

### Charge-discharge hysteresis

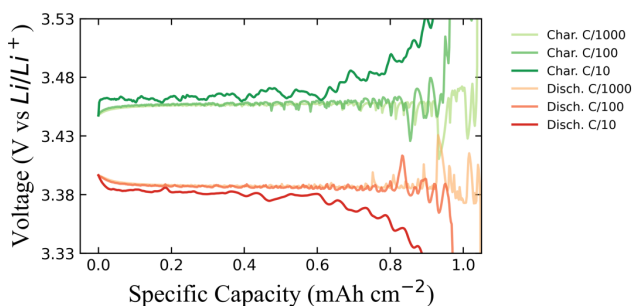


Figure S21. Simulated charge (blue) and discharge (red) voltage curves at C/10, C/100, C/1000.

7 The physics-based approach used in this work comprehend the use of regular solution theory for describing the energy landscape governing LFP thermodynamics. This framework results in a non-monotonic chemical potential that describe the open circuit voltage of LFP (Eq. 6). This intrinsic property allows the model to naturally capture the charge-discharge hysteresis of the electrode, across arbitrary C-rates. Consequently, the relationship between current direction and voltage is inherently reproduced without the need for additional empirical models<sup>53</sup>.

## Kinetically induced memory effect

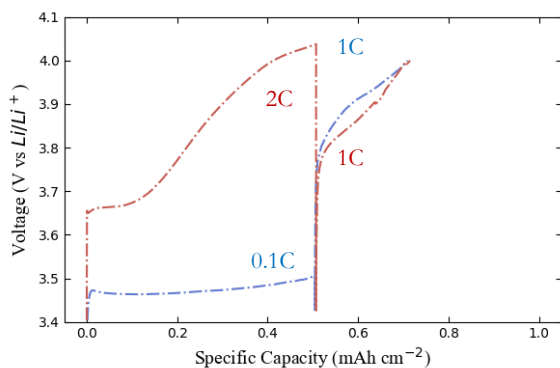


Figure S22. Experimental voltage response to the memory protocol of the 1 mAh cm<sup>-2</sup> sample.

We evaluated the electrochemical response of the 1 mAh cm<sup>-2</sup> sample under a memory protocol<sup>64</sup>, designed to investigate the effect of charging history on subsequent electrochemical behavior. The protocol consisted of the following steps:

- The electrode was first charged to 50% SOC at C/10, followed by a 1-hour open-circuit rest and then charged to a cutoff voltage of 4V at 1C.
- Afterward, the electrode was discharged to 0% SOC at C/10 to restore its initial lithiation state.
- A second charging sequence was performed, where the electrode was brought to 50% SOC at 2C, rested for 1 hour, and then fully charged at 1C.

As shown in our previous work<sup>27,64</sup>, different charging rates induced a different thermodynamic state on the system, which endures also after open-circuit relaxation. A higher initial charging rate increases the fraction of particles that reach 50% SOC in a phase-separated state, leading to a larger population of active particles in the subsequent charging step. In contrast, lower charging rates promote a mosaic state, where most particles are either fully lithiated or fully delithiated. This difference is reflected in the overpotential observed during the second charging step, where higher initial rates result in lower overpotentials.

To assess the model's predictive capability under arbitrary input conditions, we compared its response during the memory protocol. Our previous works<sup>27,64</sup> demonstrated the significance of surface diffusion in the relaxation behavior of platelet-like LFP particles. To capture this

## 7 | MODELING SINGLE-CRYSTAL ELECTRODES AS A NETWORK OF PRIMARY PARTICLES

phenomenon, we extended the model accordingly. This modification leveraged the model's flexibility and the capabilities of the MPET software<sup>31</sup>. Specifically, we employed a 1D reaction-limited (ACR) model for individual particles, replacing the 0D reduced-order model used in the simulations presented in the main text. Due to the increased computational demand, the simulation was rescaled to three sub-volumes to prevent memory overflow.

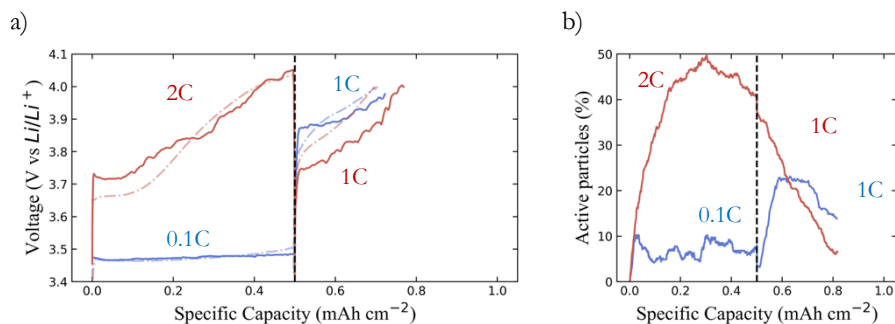


Figure S23. Kinetically induced memory effect. a) Comparison between the experimental and simulated voltage curves for 0.1C-1C and 2C-1C memory protocols for the 1 mAh cm<sup>-2</sup> sample. b) Evolution of the active particle population during the 0.1C-1C and 2C-1C memory protocols.

7

The integration of the network model with the reaction-limited surface diffusion model successfully predicts the onset of the kinetically induced memory effect (Fig. S23a). Although the limited number of simulated particles prevents a precise quantitative match with experimental data, the underlying phenomenon is well captured and explained through active particle population dynamics (Fig. S23b). This result further confirms the critical role of charging history in determining subsequent electrochemical behavior and highlights the model's capability to describe these effects.

## Results of the DFN model

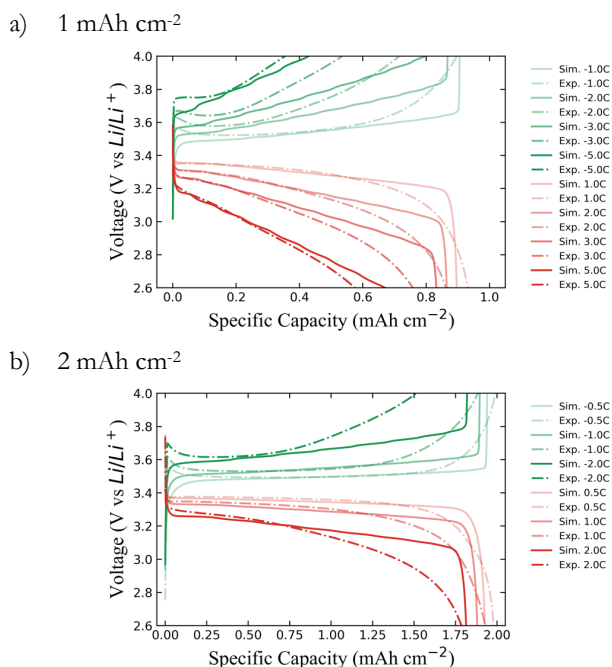


Figure S24. Constant current results of the DFN model. a) Comparison between the experimental and simulated voltage curves for 1C, 2C, 3C, and 5C for charge and discharge for the  $1 \text{ mAh cm}^{-2}$  sample. b) Comparison between the experimental and simulated voltage curves for 0.5, 1C, and 2C for charge and discharge for the  $2 \text{ mAh cm}^{-2}$  sample.

Conventional approaches, which assume Fick's diffusion as the limiting factor, fail to reproduce the experimental results (Fig. S24). The DFN model can correctly approximate the rate-dependent capacity retention for the discharge curves of both samples (Fig. S24a,b). This property explains their successful application in full LFP-Graphite batteries, especially when Graphite is the limiting kinetic factor<sup>65,66</sup>. However, it does not accurately capture the full voltage response, particularly during charging.

Additionally, parametrizing the DFN models led to unphysically low bulk electrical conductivity for the in-depth electron transport. Specifically, the  $1 \text{ mAh cm}^{-2}$  sample required  $\sigma_{bulk} = 3.87 \cdot 10^{-3} \text{ S m}^{-1}$ . In contrast, the  $2 \text{ mAh cm}^{-2}$ , despite having the same composition and only differing in thickness ( $30 \text{ }\mu\text{m}$  vs.  $60 \text{ }\mu\text{m}$ ), required a significantly higher value  $\sigma_{bulk} = 1.83 \cdot 10^{-2} \text{ S m}^{-1}$ . The complete parameter set can be found in Table T2. The large discrepancy between these values indicates that the model lacks predictive accuracy, undermining its use in microstructural optimization.

## 7 | MODELING SINGLE-CRYSTAL ELECTRODES AS A NETWORK OF PRIMARY PARTICLES

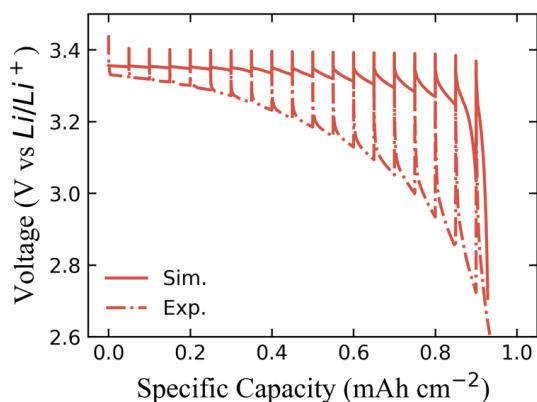


Figure S25. Comparison between the experimental and simulated GITT results for the DFN model. Each pulse delivered 1C current and lasted 3 minutes. The resting time is 30 minutes.

We evaluate the results of the DFN under the GITT protocol (Fig. S25). The model is incapable of reproducing the GITT experiment<sup>54</sup>. The assumption of Fickian diffusion and the absence of phase separation leads to fast equilibration of the particle concentration in open circuit conditions. The subsequent discharge pulses are so uncorrelated and the lithiation proceeds without memory of the previous state, only depending on the state of charge. This guarantees similar overpotentials for each pulse, substantially deviating from the experimental results. These findings indicate that DFN models are not suitable for simulating single-crystal electrodes, particularly under real-world conditions where battery operation involves multiple unpredictable inputs.

## Results of the CHR model

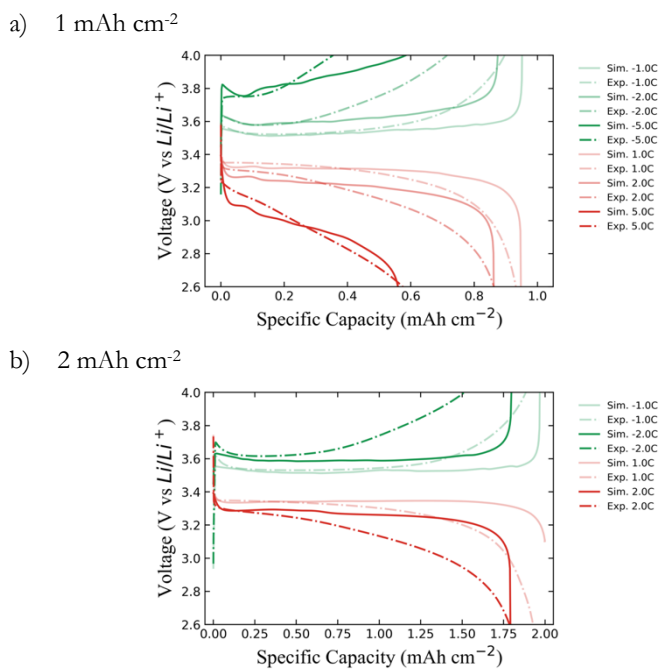


Figure S26. Results of the CHR model. a) Comparison between the experimental and simulated voltage curves for 1C, 2C, and 5C for charge and discharge for the  $1 \text{ mAh cm}^{-2}$  sample. b) Comparison between the experimental and simulated voltage curves for 1C, and 2C for charge and discharge for the  $2 \text{ mAh cm}^{-2}$  sample.

Even considering more advanced approaches, such as the Cahn-Hillard Reaction model (CHR)<sup>29,64,67</sup>, assuming a diffusion-limited system does not apply to the electrode under investigation (Fig. S26). The developed CHR model can predict the capacity retention of the discharge protocols, but it fails to predict the voltage curves and the charging behavior. Despite including the phase separation kinetics, the diffusion-limited system can only evolve as a core-shell. As a result, drastic voltage drops occur when the surface concentration approaches the fully (de)lithiated states. Moreover, similar to the DFN model, the CHR model presents unphysical adjustments to the bulk electrical conductivity between the  $1 \text{ mAh cm}^{-2}$  and  $2 \text{ mAh cm}^{-2}$  samples. The  $1 \text{ mAh cm}^{-2}$  electrode requires  $\sigma_{bulk} = 5 \cdot 10^{-3} \text{ S/m}$ , while the  $2 \text{ mAh cm}^{-2}$  is fitted with  $\sigma_{bulk} = 6 \cdot 10^{-2} \text{ S/m}$ . The complete parameter set can be found in Table 3.

Results of the ACR model without inter-particle connectivity

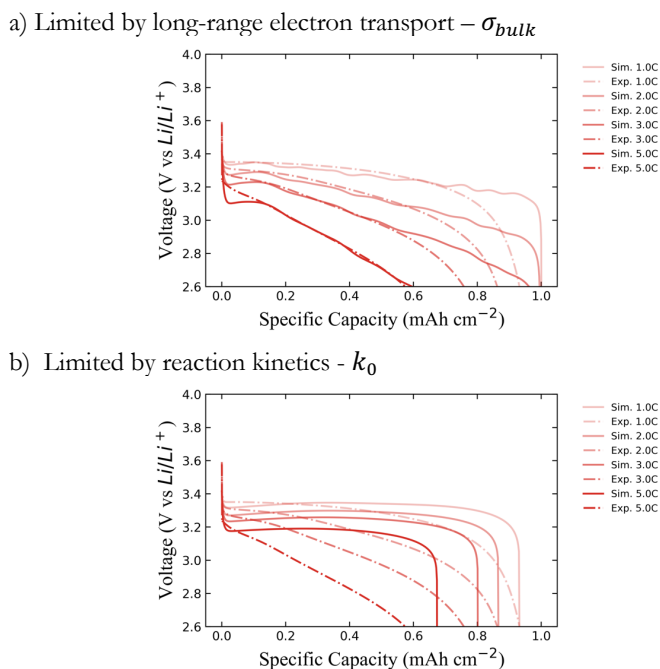


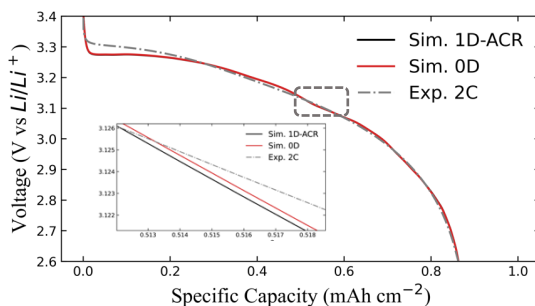
Figure S27. Results of the ACR model without network effects. a) Comparison between the experimental and simulated voltage curves for 1C, 2C, 3C, and 5C discharge for the 1 mAh cm<sup>-2</sup> sample, considering long-range electron transport as a limiting factor. b) Comparison between the experimental and simulated voltage curves for 1C, 2C, 3C, and 5C discharge for the 1 mAh cm<sup>-2</sup> sample, considering reaction kinetics as a limiting factor.

To further clarify the necessity of the inter-particle connectivity in modeling a single-crystal electrode we show the results of a phase-field electrochemical model that employs the 1D-ACR formalism without considering other sources of overpotentials. Given the known electrode structure and electrolyte properties, the only unknown sources of overpotential are the long-range electron transport – governed by  $\sigma_{bulk}$  – and the reaction overpotential – governed by  $k_0$ . If only  $\sigma_{bulk}$  is modified (Fig. S27a), the model reaches the best fit at  $\sigma_{bulk} = 3.2 \cdot 10^{-3}$  S m<sup>-1</sup>, similarly to the DFN model in Fig. S24. Compared to the DFN model, the ACR model can better describe the inter-particle and intra-particle phase-separation kinetics<sup>34,38</sup>, but it lacks of the ability to predict capacity losses at high rates. Being in fact solely reaction limited, only an unphysically low bulk electrical conductivity can assure a relevant overpotential and fit the 5C discharge curve.

Modifying instead the exchange current density pre-factor ( $k_0$ ) to low values ( $1 \text{ A m}^{-2}$  in the CIET formalism) can lead to particle-induced capacity losses, since the system reaches the limiting current predicted by CIET<sup>62</sup>. Despite this, the purely reaction limited model cannot predict the voltage curve with reasonable error margin (Fig. S27b). These results show the necessity of considering the inter-particle connectivity when modeling a single-crystal electrode.

### Comparison between the 0D and 1D ACR models

a)



b)

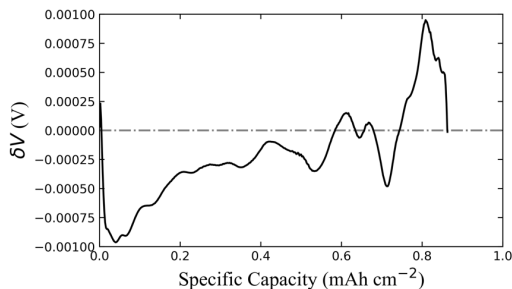


Figure S28. Comparison between the full 1D-ACR model and the 0D reduced model. a) Comparison between simulated and experimental voltage curves for the 2C discharge of the  $1 \text{ mAh cm}^{-2}$  sample using the 1D-ACR model and the reduced 0D model. b) Potential difference between the 1D-ACR model and the 0D reduced model during the 2C discharge.

When employing the 0-dimensional approximation<sup>33</sup> it is crucial to determine its precision in modeling the particles under investigation. To do so we compared the results of the 1D ACR particle model with its corresponding 0D approximation. The results in Fig. S28 show negligible differences between the two approaches. Specifically, the results present less than 1 mV of difference (Fig. S28b). This is due to the chemo-mechanical coupling that regulates the phase transformation dynamics of nanoparticles of LFP<sup>47</sup>. Due to the limited particle size, the 1D ACR

## 7 | MODELING SINGLE-CRYSTAL ELECTRODES AS A NETWORK OF PRIMARY PARTICLES

model predicts a quasi-homogenous reaction within the particles and mainly shows inter-particle phase separation. This is in line with experimental findings that attribute intra-particle phase separation to incoherent domains<sup>13,34</sup>, neglected by the ACR model. We concluded that the 0D approximation, reducing the computational time by 10 times (30 s vs 300 s), is a suitable reduced-order model that guarantees the correct simulation of the electrode's kinetic properties.

### Effect of particle size on filling fraction

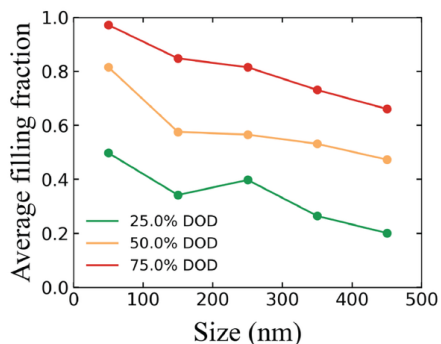


Figure S29. Average filling fraction as a function of particle size during the 2C discharge at 25%, 50%, and 75% DOD.

7

### Effect of temperature on population dynamics

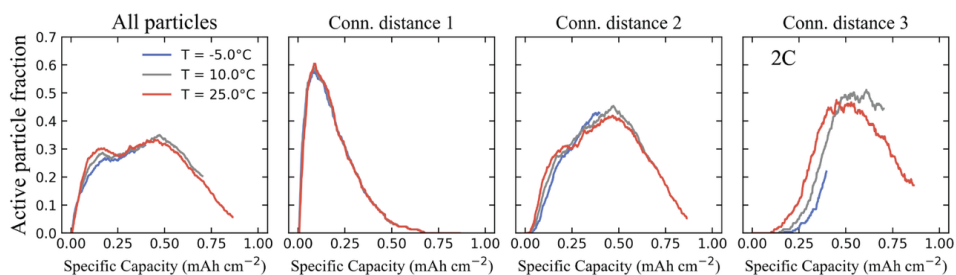


Figure S30. Evolution of the active particle population during a 2C discharge at 25°C, 10°C and -5°C, respectively. The population is divided by connection distance.

Slower charge transfer kinetics forces the system to utilize more particles, while the reduced electron mobility confines the reaction to better-connected particles. This results in slightly different active population dynamics where poorly connected particles are activated in later

stages of the discharge process. Considering the inter-particle connectivity and its temperature dependence, provides a clearer view of the electrode dynamics, aiding in protocol optimization.

Supplementary Table 1 Parameters of the network model.

<b><i>Material parameters</i></b>		
Enthalpy of mixing ( $\Omega$ )	$1.85 \cdot 10^{-20} \text{ J Li}^{-1}$	Ref <sup>38</sup>
Exchange current density prefactor ( $k_0$ ) (CIET)	$15 \text{ A m}^{-2}$	Ref <sup>68</sup>
Reorganization Energy ( $\lambda$ )	$212 \text{ meV}$	Ref <sup>68</sup>
Exchange current density activation energy ( $E_A$ )	$114 \text{ meV}$	Ref <sup>68</sup>
<b><i>Electrode parameters</i></b>		
Series resistance ( $R_{series}$ )	$10^{-2} \text{ m}\Omega \text{ m}^2$	Best-fit
Electrode thickness ( $1 \text{ mAh cm}^{-2}$ )	$30 \mu\text{m}$	Measured
Electrode thickness ( $2 \text{ mAh cm}^{-2}$ )	$63 \mu\text{m}$	Measured
Electrode porosity	$32 \%$	Measured
Active material volume loading	$82 \%$	Measured
Bruggeman exponent	$-1.49$	Measured
Inter-particle electrical conductivity ( $\sigma_{c_0}$ )	$3.3 \mu\text{S m}^{-1}$	Best-fit
Inter-particle $\sigma_c$ activation energy ( $E_\sigma$ )	$320 \text{ meV}$	Best-fit
Initial electrolyte concentration	$1 \text{ M}$	Measured
Separator thickness	$25 \mu\text{m}$	Measured
Separator porosity	$55 \%$	Ref <sup>29</sup>

## 7 | MODELING SINGLE-CRYSTAL ELECTRODES AS A NETWORK OF PRIMARY PARTICLES

Supplementary Table 2 Parameters of the DFN model.

<b>Material parameters</b>		
Open circuit potential	Afshar 2017	Ref <sup>54</sup>
Diffusion coefficient ( $D_0$ )	$3.95 \cdot 10^{-17} \text{ m}^2 \text{ s}^{-1}$	Best-fit
Exchange current density prefactor ( $k_0$ ) (BV)	$0.62 \text{ A m}^{-2}$	Best-fit
<b>Electrode parameters</b>		
Particle radius	100 nm	Measured
Series resistance ( $R_{series}$ )	$10^{-2} \text{ m}\Omega \text{ m}^2$	Best-fit
Electrode thickness (1 mAh $\text{cm}^{-2}$ )	30 $\mu\text{m}$	Measured
Electrode thickness (2 mAh $\text{cm}^{-2}$ )	63 $\mu\text{m}$	Measured
Electrode porosity	32 %	Measured
Active material volume loading	82 %	Measured
Bruggeman exponent	-1.49	Measured
Bulk electrical conductivity ( $\sigma_{bulk}$ )(1 mAh $\text{cm}^{-2}$ )	$3.87 \cdot 10^{-3} \text{ S m}^{-1}$	Best-fit
Bulk electrical conductivity ( $\sigma_{bulk}$ )(2 mAh $\text{cm}^{-2}$ )	$1.83 \cdot 10^{-2} \text{ S m}^{-1}$	Best-fit
Initial electrolyte concentration	1 M	Measured
Separator thickness	25 $\mu\text{m}$	Measured
Separator porosity	55 %	Ref <sup>29</sup>

Supplementary Table 3 Parameters of the CHR model.

<b>Material parameters</b>		
Enthalpy of mixing ( $\Omega$ )	$1.85 \cdot 10^{-20} \text{ J Li}^{-1}$	Ref <sup>38</sup>
Diffusion coefficient ( $D_0$ )	$2.1 \cdot 10^{-17} \text{ m}^2 \text{ s}^{-1}$	Best-fit
Exchange current density prefactor ( $k_0$ ) (CIET)	$5 \text{ A m}^{-2}$	Ref <sup>68</sup>
Reorganization Energy ( $\lambda$ )	212 meV	Ref <sup>68</sup>
<b>Electrode parameters</b>		
Particle radius	100 nm	Measured
Series resistance ( $R_{series}$ )	$10^{-2} \text{ m}\Omega \text{ m}^2$	Best-fit
Electrode thickness (1 mAh $\text{cm}^{-2}$ )	30 $\mu\text{m}$	Measured
Electrode thickness (2 mAh $\text{cm}^{-2}$ )	63 $\mu\text{m}$	Measured
Electrode porosity	32 %	Measured
Active material volume loading	82 %	Measured
Bruggeman exponent	-1.49	Measured
Bulk electrical conductivity ( $\sigma_{bulk}$ )(1 mAh $\text{cm}^{-2}$ )	$5 \cdot 10^{-3} \text{ S m}^{-1}$	Best-fit
Bulk electrical conductivity ( $\sigma_{bulk}$ )(2 mAh $\text{cm}^{-2}$ )	$6 \cdot 10^{-2} \text{ S m}^{-1}$	Best-fit
Initial electrolyte concentration	1 M	Measured
Separator thickness	25 $\mu\text{m}$	Measured
Separator porosity	55 %	Ref <sup>29</sup>





# 8

## MULTISCALE MODELING OF LITHIUM IRON PHOSPHATE ELECTRODES COMPOSED BY NANOPOROUS SECONDARY PARTICLES

## ABSTRACT

The development and deployment of Li-ion batteries strongly rely on predictive and accurate modeling. Such models must capture the thermodynamic and morphological characteristics of the electrodes. In this work, we focus on lithium iron phosphate (LFP) electrodes composed of secondary nanoporous particles and extend the conventional Doyle–Fuller–Newman framework by incorporating phase separation, electron-limited reaction kinetics, and hierarchical electronic and ionic transport. We begin with three-dimensional simulations of a single LFP secondary particle to investigate the influence of conductive binder domain (CBD) distribution on its surface. These insights are then used to parametrize a reduced-order one-dimensional model, which is embedded into a multi-particle porous electrode framework. The resulting simulations not only reproduce experimental data for both thin and thick electrodes with high accuracy, but also elucidate key transport phenomena and limiting factors. Finally, the validated model is applied to identify optimal electrode loadings for targeted applications. This multiscale approach establishes a robust framework able to use electrode physics to inform electrode design, paving the way to physics-based optimization of current and next-generation electrodes.

## 8.1 INTRODUCTION

Li-ion batteries, essential for electrification and the energy transition<sup>1,2</sup>, can be manufactured using different electrode materials. While the most common material for the negative electrode (anode) is graphite, multiple competing materials are available on the market for the positive electrode (cathode). The most widespread are layered oxides, such as  $\text{LiCoO}_2$  (LCO),  $\text{LiNi}_x\text{Mn}_y\text{Co}_{1-x-y}\text{O}_2$  (NMC), or  $\text{LiNi}_x\text{Co}_y\text{Al}_{1-x-y}\text{O}_2$  (NCA), and lithium iron phosphate (LFP)<sup>2</sup>. The former were initially the most adopted chemistries due to their high operating potentials ( $\sim 4$  V), good specific capacity ( $\sim 200$  mAh  $\text{g}^{-1}$ ), and fast kinetic performance<sup>3</sup>. The latter, instead, has a lower specific capacity ( $\sim 160$  mAh  $\text{g}^{-1}$ ) and lower operating voltage ( $\sim 3.43$  V)<sup>4</sup>. Despite these apparent disadvantages, it is rapidly gaining market share thanks to recent materials improvements, lower manufacturing costs, and excellent durability<sup>1</sup>.

These improvements have been driven by careful electrode and particle design choices aimed at mitigating LFP's limitations. Specifically, primary crystallites are synthesized at nanoscopic sizes to shorten the lithium diffusion path and reduce the impact of the one-dimensional diffusion kinetics that limit LFP performance<sup>5-7</sup>. Additionally, to address its low intrinsic electrical conductivity, the particles are coated with a layer of amorphous carbon that facilitates electron mobility<sup>8</sup>. This ensures that electrons can more effectively reach the particle surface and participate in electrochemical reactions with the ions in the electrolyte<sup>9,10</sup>.

Depending on the synthesis method, LFP electrodes can adopt different morphologies<sup>11,12</sup>. They may remain as dispersed single-crystal primary particles or form agglomerated secondary particles. The former configuration provides a large contact area with the electrolyte, while it can lead to decreased packing density. These particles are often synthesized in platelet form to align the diffusion and reaction pathways, enabling fast single-particle kinetics<sup>7</sup>. However, single-crystal electrodes can suffer from poor inter-particle contact, which limits electronic conductivity between them<sup>9,13</sup>. Careful engineering of the conductive additive network in the electrode composition is therefore necessary to ensure that a sufficient fraction of particles have access to electrons and are effectively wired to the conductive matrix.

In contrast, secondary particles composed of primary nanoparticles offer more reliable inter-particle contact. This morphology is widely adopted in layered oxides, where crystals are densely packed to ensure good solid-state diffusion between particles and fast overall kinetics<sup>14-16</sup>. However, LFP's one-dimensional lithium diffusion mechanism makes solid-state diffusion across grain boundaries inefficient, as diffusion channels must align perfectly<sup>4</sup>. To address this, secondary LFP particles are synthesized as nanoporous structures<sup>17,18</sup>. In this configuration, lithium-ion transport occurs primarily through the electrolyte within the nanopores<sup>19</sup>. Once inside, the ions react locally with the primary particles, based on the local electrolyte and electrical

potentials. These structures are often referred to as *hierarchically structured*<sup>17,18,20,21</sup>, as the electrodes display two levels of porosity: microscopic inter-particle porosity, which enables long-range ionic transport across the electrode thickness, and nanoscopic intra-particle porosity, which governs local ion access to the primary particles.

The limiting transport factor in hierarchical microstructures depends on the choice of the active material. Due to their good electronic conductivity and large primary particle size, layered oxides and graphite-based hierarchical particles are typically limited by ionic transport within the nanopores<sup>21</sup> or by solid-state diffusion within the primary particles<sup>19,20</sup>. In contrast, LFP nanoporous particles are more likely to be limited by electron transport<sup>22</sup>. This results from their inherently low electrical conductivity and the presence of nanosized primary particles that mitigate solid-state diffusion limitations. Consequently, electron transport through the electrode relies predominantly on the conductive binder domain (CBD)<sup>23</sup>. The particle's kinetics is instead regulated by local electric transport. The ions and electrons reach the outer surface of the secondary particles through the CBD and the electrode macropores. The ions diffuse within the nanopores, the electrons migrate within the bulk and along the carbon-coated surfaces of the primary particles, reacting then locally on the internal surface of the secondary particles.

Moreover, the kinetics of LFP electrodes sensibly differ from those of layered oxides. Specifically, layered oxides equilibrate at any ionic filling fraction, while olivine phosphates tend to separate into Li-rich and Li-poor phases<sup>24,25</sup>. The phase separation modifies both the electrode-scale and particle-scale behaviors<sup>24,26,27</sup>, exacerbating local reaction rates and driving the system towards heterogeneous states.

8

Reliable and accurate physics-based models are necessary to optimize LFP-based hierarchical morphologies, both in terms of design and operation. The most widely used electrochemical models are those based on the work of Doyle, Fuller, and Newman (DFN), which assume Fickian diffusion as the primary particle-scale limiting mechanism<sup>28–30</sup>. However, previous studies have highlighted the need to carefully account for the microstructural and thermodynamic characteristics of electrodes. Specifically, including effects such as electrical wiring limitations<sup>13,31–33</sup>, contact losses<sup>27</sup>, phase separation<sup>34–36</sup>, or nanoporous structures<sup>19–21</sup> has been essential to accurately reproduce and explain experimental observations across various materials and morphologies.

Building on prior work, we develop a multiscale framework to quantify and predict the behavior of LFP electrodes composed of hierarchical secondary particles. The nanoporous secondary particles are represented by a homogeneous porous electrode model, coupled with a thermodynamically derived chemical potential<sup>24</sup>, capturing phase separation as well as nanoscale

wetting and mechanical effects<sup>34,37,38</sup>. Interfacial reaction kinetics is described by Coupled Ion-Electron Transfer (CIET) theory, which explicitly captures the roles of both ionic and electronic transport<sup>39–41</sup>.

Observing the importance of the conductive binder domain (CBD)<sup>13,31–33</sup>, especially in poorly conductive LFP electrodes, we speculate that spherical secondary particles might display largely heterogeneous reaction. Therefore, we first model a single nanoporous LFP particle with fully resolved three-dimensional simulations. This allows us to investigate not only the impact the CBD distribution on the particle surface, which may vary significantly depending on the manufacturing parameters. The insights gained from this three-dimensional model inform a reduced-order, one-dimensional single-particle description with surface constriction resistance and a size-dependent effective conductivity, which reproduces the three-dimensional behavior at a far lower computational cost. Including this particle model within a multi-particle DFN framework, we validate it against both thin and thick LFP electrodes. The parametrized model is then used to analyze electrode-scale heterogeneities and, ultimately, to map optimal electrode loadings for specific power and energy targets, providing practical guidance for next-generation Li-ion architectures.

## 8.2 MODEL OVERVIEW

To build the multiscale framework, we begin with one-dimensional and three-dimensional homogenized hierarchical models of single nanoporous particles (denoted as 1D-SPHM and 3D-SPHM). The two formulations share the same physics and material parameters; they differ only in boundary conditions and symmetry. We consider a spherical nanoporous secondary particle of radius  $R_p$  containing electrolyte-filled nanopores and a percolating solid phase. Transport in the electrolyte and solid domains is described using porous-electrode theory<sup>30,42</sup>: the electrolyte, with concentration  $c_e$  and potential  $\phi_e$ , is characterized by conductivity  $\kappa$  and diffusivity  $D_e$ ; the solid phase, with potential  $\phi_s$ , is characterized by conductivity  $\sigma$ . The conductivity  $\sigma$  is here considered as a mesoscopic property, depending so on both bulk and carbon-coating conductivities. Both phases are modulated by their respective volume fractions and tortuosities. The full governing equations are provided in the Supplementary Information.

A key modeling choice concerns the primary crystallites. Hierarchical models often resolve both solid diffusion and surface reactions within the primary particles embedded in the secondary particles<sup>19–21</sup>, which adds a pseudo-dimension and increases computational cost. Here, we adopt a zero-dimensional approximation at the primary level. Although LFP is a phase-separating material, its nanoparticles can be treated as undergoing a homogeneous solid-solution transition<sup>34,37,38</sup>. This assumption is supported by kinetics (solid diffusion timescales are much

## 8 | MULTISCALE MODELING OF LITHIUM IRON PHOSPHATE ELECTRODES COMPOSED BY NANOPOROUS SECONDARY PARTICLES

shorter than interfacial reaction times<sup>34,43,44</sup>, and thermodynamics (wetting and mechanical coherency suppress concentration gradients and stabilize the solid solution<sup>37,38,45</sup>). While this may not hold for all LFP morphologies, the particle sizes considered here justify the approximation. Each primary particle is therefore modeled as homogeneous (i.e.  $c_{surf}^{primary} = c_{bulk}^{primary}$ ), which reduces cost while retaining the essential physics.

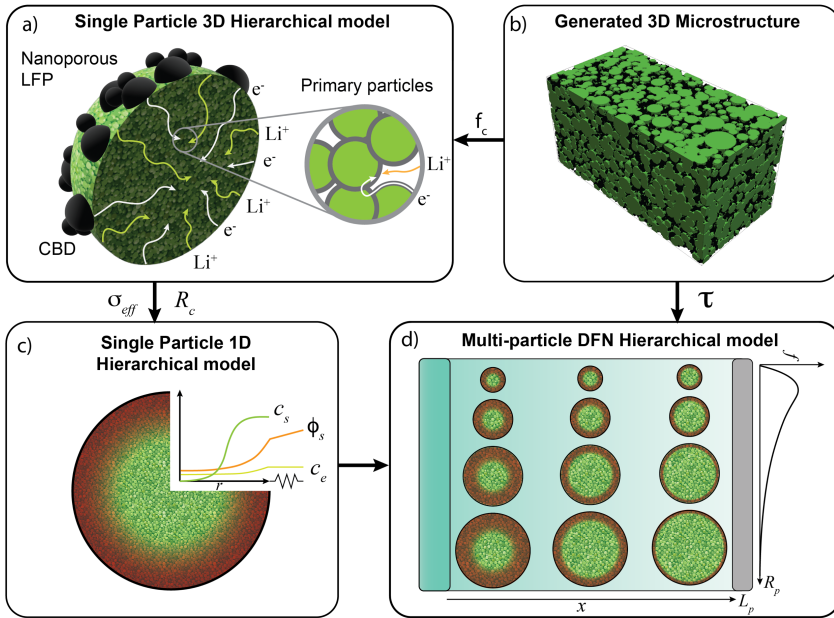


**Figure 8.1. Multiscale modeling.** a) Schematic representation of the 3D-SPHM. The surface is surrounded by CBD caps; ion and electron transport occur within the nanopores. b) Generated three-dimensional microstructure composed of secondary particles (green), CBD (black), and electrolyte-filled porous phase (transparent). c) Schematic representation of the 1D-SPHM comprehending the bulk transport along the radial direction and the constriction resistance on the surface. d) Schematic of the multi-particle DFN model composed of a set of representative particles, each having a specified occurrence based on the size distribution. The same particle distribution is repeated along the electrode thickness to simulate macroscopic transport.

As a result, the normalized solid concentration  $\tilde{c}_s = c_s/c_{max}$ , evolves solely according to the local reaction overpotential  $\eta = \phi_s - \phi_e - U(\tilde{c}_s)$ . Interfacial reaction kinetics is described using the ECIT formalism<sup>39</sup> of CIET theory, which accounts for coupled ion–electron transfer at the particle surface. The open circuit potential  $U(\tilde{c}_s)$ , conventionally approximated based on

experimental data of the open circuit voltages<sup>30</sup>, is instead defined from its thermodynamic origin, i.e., related to the derivative of the specific free energy  $g$  with respect to the concentration:

$$U(\tilde{c}_s) = -\frac{1}{e} \frac{dg}{d\tilde{c}_s} = V_0 - \frac{k_B T}{e} \ln \frac{\tilde{c}_s}{1 - \tilde{c}_s} - \frac{\Omega}{e} (1 - 2\tilde{c}_s)$$

where the standard potential  $V_0$  (V) derives from the energy difference between fully lithiated and delithiated state and  $\Omega$  (eV), the regular solution parameter, expresses the ion-vacancy interaction energy. The model (i.e., the regular solution model) has been coupled with wetting energy and mechanical energy factors to give rise to the phase-field models for active battery materials<sup>34</sup>. This method was highly successful when applied to LFP particles<sup>13,26,46</sup>. Its predictions allow us to reduce the complex chemo-mechanical features of the LFP particles in a reduced order approach, where a size-dependent  $\Omega$  can include the reduced energy barrier observed in nanosized LFP particles<sup>37,38,45</sup>. The resulting non-monotonic OCP reproduces flat voltage plateaus and thermodynamic hysteresis<sup>24,31,36,42,45</sup>, and naturally gives rise to inter-particle phase separation and its transport consequences.

The two particle formulations (1D-SPHM and 3D-SPHM) differ mainly in how electronic contact with the CBD is represented. In both cases, the outer surface is fully wetted by electrolyte. In the 3D-SPHM, for computational efficiency, the electrolyte concentration is assumed to be spatially uniform inside the particle. This assumption is justified because electrolyte diffusion occurs significantly faster than electrochemical reactions, as demonstrated in the following sections.

The 3D-SPHM model (Fig. 8.1a) is subjected to partial electric contact with the CBD; i.e. electric current can only enter the particle through discrete surface regions that are in contact with the CBD. These regions are modeled as circular caps located on the spherical surface of the particle, as depicted in Fig. 8.1a, with all the caps assumed to have the same electric potential. The total area of these caps is constrained to occupy a prescribed contact fraction  $f_c$  of the particle surface. To represent the morphology of the carbon distribution, the caps are randomly placed on the particle surface using a Monte Carlo algorithm governed by a morphology parameter  $m \in [0,1]$ . When  $m = 0$ , the patches are uniformly dispersed; when  $m = 1$ , they are clustered into a single region<sup>47</sup>. Intermediate values interpolate between these limits, with  $m = 0.5$  coinciding with random placement. This parameter effectively captures the influence of slurry formulation, mixing protocol, and carbon additive properties on the heterogeneity of CBD-particle contact. By enabling direct control over both extent and uniformity of electronic contact, we can investigate overpotential distributions, local reaction rates, and capacity utilization of the

secondary LFP particle. Details on the algorithm implemented to model the CBD-particle contacts can be found in the Supplementary Information.

In the 1D-SPHM, the effect of partial CBD contact is captured through a lumped constriction resistance  $R_c$  applied at the particle boundary (Fig. 1c). Electrolyte potential  $\phi_e$  and concentration  $c_e$  are assumed continuous with the electrode-scale values at the particle surface, while symmetry conditions are enforced at the center. As a result, single-particle simulations assume uniform external conditions, whereas in the DFN framework,  $\phi_e$  and  $c_e$  vary with position along the electrode. A size-dependent effective conductivity  $\sigma_{eff}(R_p)$  is also introduced to account for internal electronic transport limitations. Together  $R_c$  and  $\sigma_{eff}$  enable the 1D-SPHM to replicate the electrochemical behavior observed in the 3D-SPHM.

By embedding this reduced-order model within a DFN framework, we retain key features of the three-dimensional behavior while gaining the computational efficiency required for full-electrode simulations (Fig. 8.1d). Within each electrode volume, a population of hierarchical particles is represented, each governed by the one-dimensional formulation and weighted according to its frequency in the experimentally measured size distribution. This strategy captures the influence of particle size heterogeneity without the need to simulate each particle individually. The separator, modeled as ion-conducting only, imposes the current-driven flux boundary.

To bridge the particle and electrode scale, we generated a realistic microstructure using the measured particle size distribution and the volume fractions of active material and CBD (Fig. 8.1b)<sup>48</sup>. The tortuosities extracted from this structure<sup>49</sup> are used to model macroscopic transport in the DFN, while the contact fractions inform the fitting of  $\sigma_{eff}(R_p)$  based on the three-dimensional simulation data.

The resulting framework incorporates the latest insights into LFP dynamics and hierarchical structuring. It successfully captures the essential physics of the 3D-SPHM while enabling efficient simulation of entire electrodes, making it a practical tool for electrode-scale optimization at a fraction of the computational cost.

### 8.3 THE EFFECT OF CBD DISTRIBUTION ON THE SINGLE PARTICLE DYNAMICS

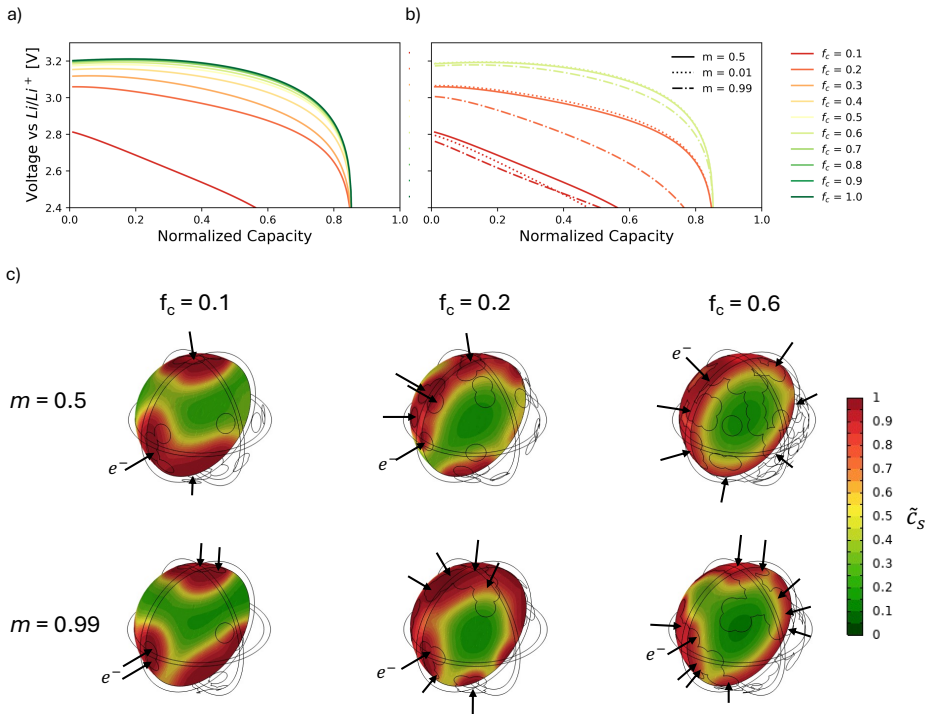


**Figure 8.2.** The effect of contact with the CBD. a) Effect of fraction of contact ( $f_c$ ) on the voltage profile of a single nanoporous LFP particle ( $m = 0.5$ ). b) Effect of the morphology parameter ( $m$ ) on the voltage profile of a single nanoporous LFP particle ( $f_c = 0.1, 0.2, 0.6$ ). c) Distribution of the normalized solid concentration ( $\tilde{c}_s$ ) within simulated LFP particle during lithiation at 50% depth of discharge (DOD) for the cases of  $f_c = 0.1, 0.2, 0.6$  and  $m = 0.5, 0.99$ .

Three-dimensional simulations of a  $5\text{-}\mu\text{m}$  nanoporous LFP particle were conducted to investigate how the contact fraction with the CBD ( $f_c$ ), varying from 10% to 90%, and its spatial distribution affect particle-level electrochemical performance.

In the reference case, where the entire surface is in contact with the CBD ( $f_c = 1$ ), the particle achieves  $\sim 85\%$  of its theoretical capacity at 20C. It displays a flat voltage plateau characteristic of phase-separating materials, followed by a sharp drop once the reaction kinetics becomes limiting.

For randomly distributed CBD patches ( $m = 0.5$ ), a contact fraction of  $f_c \geq 0.5$  is sufficient for full capacity utilization (Fig. 8.2a). The voltage profile closely matches the full-contact case, and the concentration field evolves symmetrically, with a lithiation front propagating inward. In this regime, contact resistance is negligible, and the particle behavior is nearly ideal. As the contact fraction decreases to  $0.3 < f_c < 0.5$ , a noticeable increase in overpotential is observed along the voltage plateau. This is attributed to *constriction resistance*: the reduced CBD coverage restricts the available electron transport pathways, inducing localized electric fields and increasing the effective resistance between the CBD and the LFP surface. Nonetheless, the system still maintains full capacity utilization. The lithiation pattern retains a symmetric “shrinking core” structure, although localized reaction zones emerge near the CBD caps (Fig. 8.2c).

In the low-contact regime ( $f_c < 0.3$ ), kinetic limitations become severe. The voltage profile departs from the flat plateau and shows early polarization. The concentration field becomes highly asymmetric, with lithiation occurring predominantly near the CBD contact zones (Fig. 8.2c). As local regions become fully lithiated, the reaction front is forced to propagate away from the CBD, increasing the effective path length for electron conduction and reducing overall kinetics. At  $f_c = 0.1$ , the particle cannot reach full capacity: only regions in close proximity to the CBD remain reactive, leading to significant underutilization.

The effect of CBD morphology is further explored by varying the morphology parameter  $m$ . As expected, more uniform distributions (lower  $m$ ) yield better performance at fixed contact fraction (Fig. 8.2b). Random distribution ( $m = 0.5$ ) or increased dispersion ( $m = 0.01$ ) lead to similar results across varying  $f_c$ . Once a radially symmetric concentration profile is established, the lithiation proceeds similarly, leading to almost overlapping voltage profiles. For the case of limited contact ( $f_c = 0.1$ ), the morphology plays a minor role and the particle’s behavior does not differ with varying  $m$ . At an intermediate  $f_c = 0.2$ , the morphological effects become more relevant, leading to a capacity loss and increased overpotentials for the case of  $m = 0.99$ . Thus, not only the quantity but also the spatial distribution of CBD plays a critical role in enabling efficient particle utilization.

These results underscore the importance of CBD engineering in LFP electrode design. To fully harness the electrochemical potential of hierarchical secondary particles, both an adequate contact fraction (above  $\sim 30\%$ ) and a uniform distribution of CBD contact points are necessary. This requires careful control over the CBD volume fraction and its dispersion during electrode fabrication. Moreover, CBD must form a percolating electronic network throughout the electrode to compensate for the intrinsically low electronic conductivity of LFP. The interplay between these factors highlights the complexity of optimizing LFP electrodes. For instance, improvements of the carbon coating of the primary particles might increase the kinetics

capabilities of the agglomerates, however, poor CBD optimization might hinder these effect on the electrode scale.

## 8.4 REDUCE ORDER MODELING OF THE EFFECT OF CBD DISTRIBUTION

The voltage profiles obtained from the three-dimensional simulations serve as a benchmark to calibrate the 1D-SPHM. While the former simulations require approximately 30 minutes of computation time per case, the efficient 1D-SPHM solves in tens of milliseconds, enabling its integration within a DFN framework for full electrode modeling.

The reduced model was constructed to preserve the essential properties of the three-dimensional system by matching the particle radius, solid and electrolyte volume fractions, diffusivities, and material parameters. The influence of incomplete CBD coverage and its spatial heterogeneity was captured through two effective quantities: a constriction resistance  $R_c$  and an effective solid-phase conductivity  $\sigma_{eff}$ .

These parameters were treated as free variables and optimized to reproduce the voltage profiles of the 3D-SPHM under identical current conditions. Fitting was performed for particles of radius 2–7  $\mu m$  and contact fractions  $f_c = 0.3$ –0.6, assuming a random CBD distribution ( $m=0.5$ ). Although real electrodes may contain particles with different degrees of contact uniformity, these conditions are consistent with realistic manufacturing scenarios<sup>23,47,50,51</sup>. This procedure yielded a consistent set of size- and contact-dependent effective parameters that form the basis for the subsequent analysis. The resulting fits allow us to directly compare the simplified 1D-SPHM with the full three-dimensional simulations, revealing how particle size and contact fraction influence the effective parameters and overall electrochemical response.

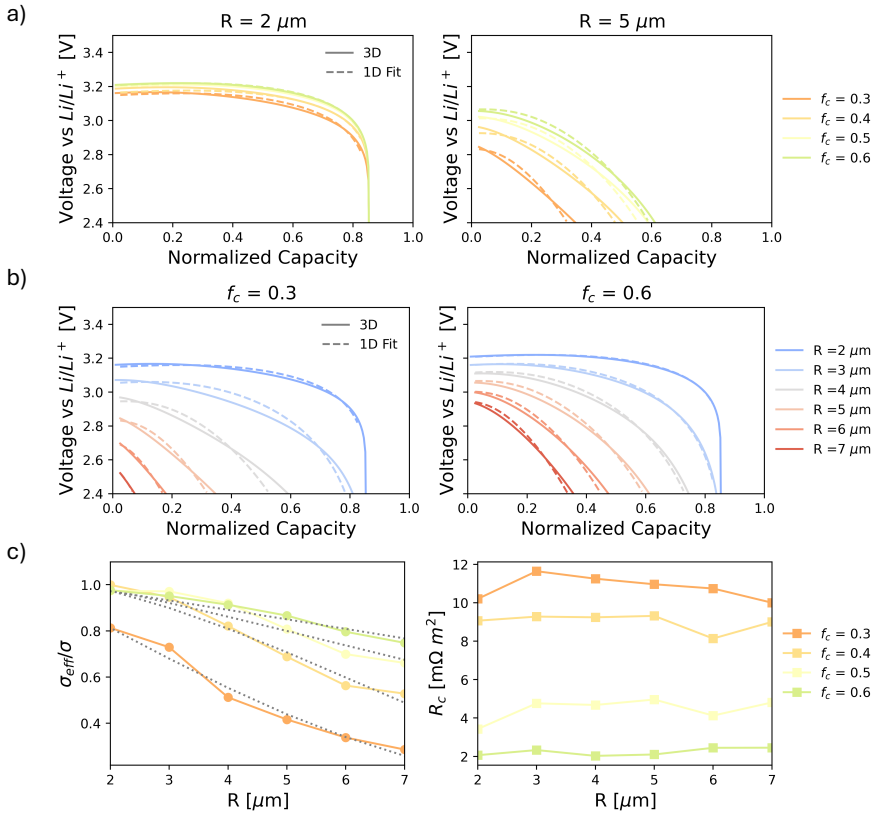


**Figure 8.3. One-dimensional approximation of the three-dimensional model.** a) Comparison between the simulated voltage profile from the 3D-SPHM and the result of the fitted 1D-SPHM for the cases of 2 and 5  $\mu\text{m}$  of radius at varying  $f_c$ . b) Comparison between the simulated voltage profile from the 3D-SPHM and the result of the fitted 1D-SPHM for the cases of  $f_c = 0.3$  and  $f_c = 0.6$  at varying particle radius. c) Evolution of the effective conductivity and the constriction resistance at varying  $f_c$  and particle sizes and relative fit (dotted line).

Comparisons between the 3D-SPHM and the 1D-SPHM are shown in Fig. 8.3a–b. The reduced model reproduces the voltage profiles across a wide range of  $f_c$  and particle sizes, capturing the increase in polarization and resistance through only two parameters: the constriction resistance  $R_c$  and the effective conductivity  $\sigma_{eff}$ . This demonstrates that a minimal parametrization can successfully condense the complexity of the full three-dimensional description.

As expected, larger particles exhibit reduced rate capability, but the decline is steeper than simple geometric scaling would suggest. The key factor is the relation between the reaction-front size

and the particle radius: the front is set by conductivity and interfacial kinetics, not by geometry. In larger particles, these fronts are separated by greater distances due to the wider spacing between CBD contact caps, forcing electrons to follow longer lateral paths. This effect is particularly severe at low  $f_c$ , where fewer entry points further extend the internal path length. To reproduce this behavior using the 1D-SPHM, the effective conductivity  $\sigma_{eff}$  must decrease with increasing particle radius (Fig. 8.3c). In contrast, the fitted constriction resistance  $R_c$  remains nearly constant, showing that the dominant size-dependent resistance arises from internal transport rather than interfacial contact. These results emphasize the need to account for heterogeneous electron pathways in larger particles and suggest that improving contact uniformity and connectivity becomes increasingly critical as particle size grows.

The calibrated 1D-SPHM captures the essential electrochemical response of LFP particles across particle sizes and CBD morphologies. To embed these results into the multi-particle DFN framework, the fitted  $\sigma_{eff}(R_p)$  values were interpolated with a sigmoid relation (dotted lines in Fig. 8.3c). For the representative case  $f_c \approx 0.3$ , consistent with the microstructural analysis (Fig. S1), the fitted function is reported in the Supplementary Information. The constriction resistance, independent of radius in these fits, is retained as an adjustable DFN parameter, since it reflects the uniformity and size of CBD contacts; quantities that are not directly measurable and remain sensitive to electrode formulation.

This methodology constitutes a data-driven model reduction. While alternatives such as Universal Differential Equations or other physics-informed machine learning strategies could enhance predictive accuracy<sup>52,53</sup>, their interpretability and transferability are limited. In contrast, the present approach preserves a direct connection to the underlying physics while enabling efficient multi-particle modeling.

## 8.5 PREDICTING THE VOLTAGE PROFILE WITH THE MULTI-PARTICLE DFN MODEL

Combining the obtained 1D-SPHM within a multi-particle DFN framework we can successfully fit the rate capability experiments for both thin ( $1 \text{ mAh cm}^{-2}$ ) and thick ( $4.6 \text{ mAh cm}^{-2}$ ) electrodes, as shown in Fig. 8.4. The samples show significant differences in electrochemical performance, clearly reflected in the voltage profiles: for the thin sample, the voltage remains flat for most of the capacity and only begins to drop when polarization introduces excess overpotentials, indicating particle-level limitations. In contrast, the thick sample shows a sloping

voltage profile across all tested rates, which is consistent with transport limitations at the electrode scale.

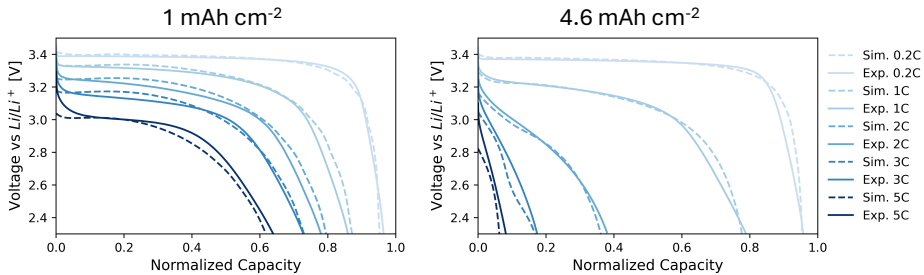


**Figure 8.4.** Comparison between the simulated and experimental discharge voltage profiles of the 1 mAh cm<sup>-2</sup> and 4.6 mAh cm<sup>-2</sup> samples at various C-rates.

To efficiently estimate the unknown model parameters, we first identified the dominant limiting mechanisms in each case, and then selected the appropriate dataset for parameter fitting. The 4.6 mAh cm<sup>-2</sup> sample has a thickness of 164 μm. Considering its electrolyte diffusivity  $D_e$ , porosity  $\epsilon_e$ , and tortuosity  $\tau_e$ , we can estimate the diffusion timescale:  $(L_p^2 \tau_e)/(\epsilon_e D_e) \sim 40$  minutes. This suggests that electrode-scale transport limitations become significant above 2C. On the other hand, the 1 mAh cm<sup>-2</sup> electrode, with a thickness of 35 μm, has a much shorter diffusion timescale of  $\sim 2$  minutes. Within the tested C-rates, this implies that its performance is primarily limited by particle-level phenomena, rather than electrode-scale transport.

8

Based on this analysis, we used the 1 mAh cm<sup>-2</sup> sample to calibrate particle-level parameters: specifically, the contact resistance  $R_c$ , and prefactor of the effective electrical conductivity  $\sigma$ . Among these,  $\sigma$  strongly influences the accessible capacity and can therefore be precisely determined by fitting the capacity–rate relationship, while  $R_c$  affects the initial overpotential. The analysis of parameter sensitivities and their effects is provided in Fig S5.

Since both electrodes were cast from the same slurry, once the particle-level parameters are established, they can be used as a baseline to fit the long-range transport properties. With the electrode porosity and tortuosity known, and assuming carbon black percolation ensures sufficient electronic conductivity, the electrolyte conductivity can be tuned by matching the experimentally observed capacity utilization.

## 8.6 ELECTRODE DYNAMICS

The validated model, capable of accurately reproducing the performance of both electrodes with a single parameter set, can now be used to investigate and explain the limiting factors governing the behavior of the electrodes.

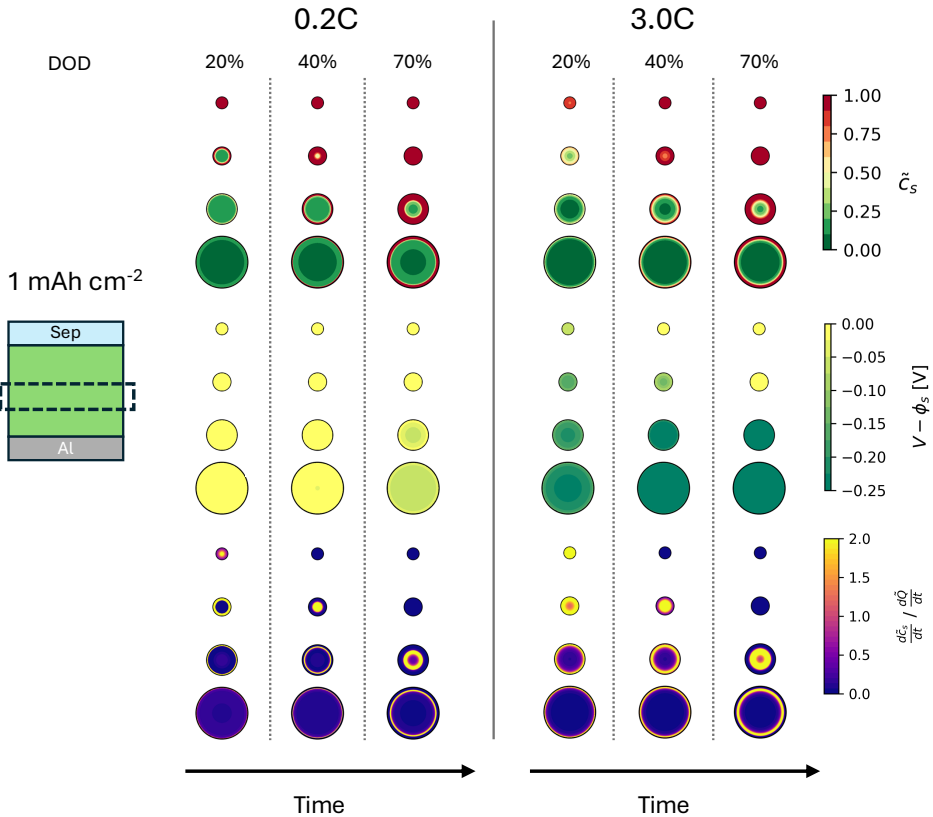


**Figure 8.5. Internal dynamics of the  $1 \text{ mAh cm}^{-2}$  electrode.** Particle-resolved profiles of solid concentration ( $\tilde{c}_s$ ), electric potential difference ( $V - \phi_s$ ) and normalized reaction rate ( $\frac{d\tilde{c}_s}{dt} / \frac{d\tilde{Q}}{dt}$ ), during  $0.2\text{C}$  and  $3\text{C}$  lithiations at various depths of discharge (DOD), where  $d\tilde{Q}/dt$  is the electrode Crate and  $d\tilde{c}/dt$  is the single local primary particle Crate. The represented particles are a subset of the simulated particles extracted from the mid-electrode position.

In Fig. 8.5 are shown the relevant particle's variables at various depths of discharge (DOD). We observe a strong gradient within the particles and between the various particle sizes. Smaller particles present higher degrees of lithiation at the same DOD, due to their shorter electron

pathways, leading to a more uniform reaction across the secondary particle volume. This is reflected in the lower potential drops within the smaller secondary particles, in which  $\phi_s$  aligns more closely with  $V$ . On the contrary, in larger particles, the reaction front moves from the external boundary towards the center in a relatively narrower front. As shown in Fig. S3, the depth-wise heterogeneities are instead limited due to the thin nature of this sample.

Notably, unlike a phase-field modeling approach, in this model each primary particle is assumed to lithiate uniformly. The secondary particle thus contains independent primary particles that only react based on the local electrochemical potential. Despite the observed steep concentration gradients, which might suggest a Cahn-Hilliard-type dynamics, this is only occurring due to a combination of electric potential losses and localized reaction dynamics, driven by the non-monotonic open circuit potential. Therefore, the observed phase separation occurring within the secondary particle is effectively an inter-primary particle phase separation. This difference changes the multi-particle dynamics. While remaining true that higher currents increase the number of active primary particles, in this hierarchical system, all the secondary particles participate in the reaction. The increased rates are instead changing the active volume fraction, corresponding to an increased number of active primary particles. This is visible in the wider reaction fronts of the 3C scenario compared to the 0.2C scenario, and in the monotonic increase of active volume fraction shown in Fig. S4.

Moreover, it is worth analyzing the relation between electric and ionic pathways since the particle-level limitations can originate from both electrical and ionic potentials as well as concentration gradient along the secondary particles' radii. While the electrolyte concentration presents minimal changes during lithiation (Fig. S3), the solid potential drops substantially within the particles as well as in between the particles due to both contact resistance and internal potential drops.

This can be clarified by analyzing the conductivities and the diffusion times with the secondary particles. Despite high tortuosities and low porosities within the nanoporous secondary particles ( $\epsilon_p = 0.15, \tau_p = 2.8$ ) the electrolyte diffusion timescale for a particle with a radius of  $10 \mu\text{m}$  results to be  $\sim 5$  minutes, suggesting that sensible electrolyte concentration gradients in the particles can be only observed at extreme rates. However, at these rates cut-off voltage is reached before the electrolyte polarization is completed. Similarly, the effective ionic conductivity in such a system ( $\sim 3 \cdot 10^{-3} \text{ S/m}$ ) is orders of magnitude greater than the electronic conductivity ( $\sim 10^{-5} \text{ S/m}$ ). Consequently, the particle-scale limiting factor coincides with the electronic conductivity  $\sigma$ , suggesting this as the most important parameter to improve for the next-generation of high-power electrodes composed of secondary particles.

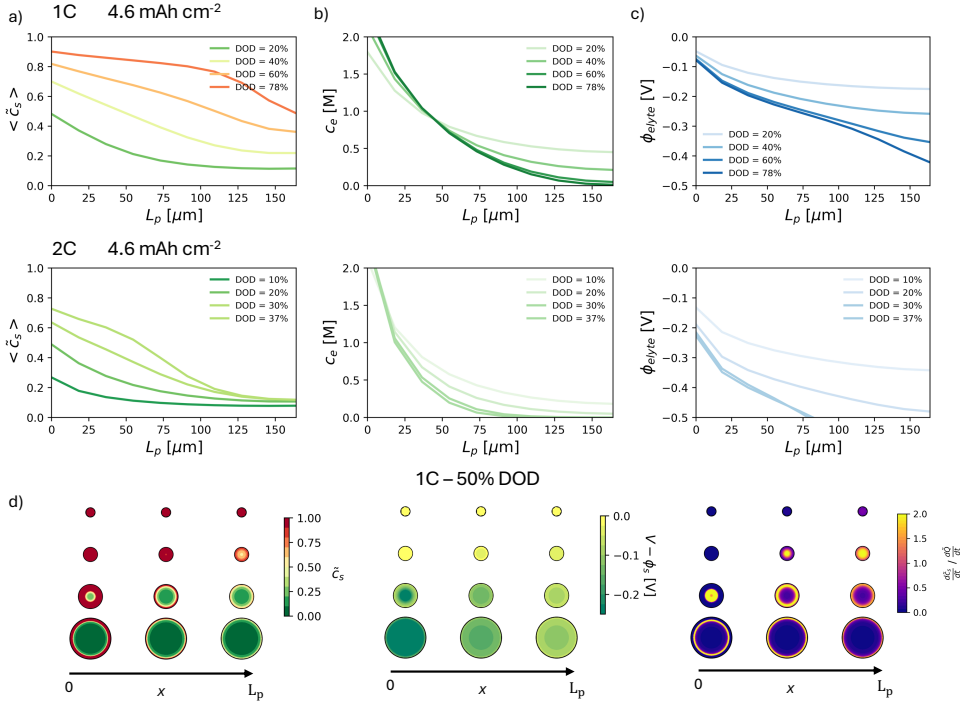


**Figure 8.6. Internal dynamics of the 4.6 mAh cm<sup>-2</sup> electrode.** Evolution of the averaged solid concentration (a), electrolyte potential (b), and electrolyte concentration (c) along the electrode thickness at various depths of discharge (DOD) for the 1C and 2C discharge protocols. The average solid concentration is a weighted average of the particle size distribution. d) Particle-resolved profile of solid concentration, electric potential difference, and normalized reaction rate, during a 1C lithiation at 50% DOD. The represented particles are a subset of the simulated particles extracted from the positions  $x = 0$  (separator side),  $x = L_p/2$  and  $x = L_p$  (current collector side).

In Fig. 8.6 are shown the results of the simulations of the 4.6 mAh cm<sup>-2</sup> sample, presenting a significantly different dynamics with respect to the 1 mAh cm<sup>-2</sup> scenario. The internal variables have a strong position dependency. The lithiation initiates from the separator side and proceeds with a wide reaction front towards the current collector (Fig. 8.6a). This is due to the strong electrolyte concentration and potential gradients generated along the thick electrode (Figs. 8.6c-d). When the rate is increased from 1C to 2C, the electrolyte polarization becomes severe already at low DODs, with the electrolyte concentration quickly reaching values close to zero and therefore stopping the electrochemical reaction.

Despite strong electrode-scale limitations, the various secondary particles also present great heterogeneity, with smaller particles able to fully lithiate across the electrode, while larger particles only react in the proximity of the separator.

### 8.7 OPTIMIZING ELECTRODE LOADING

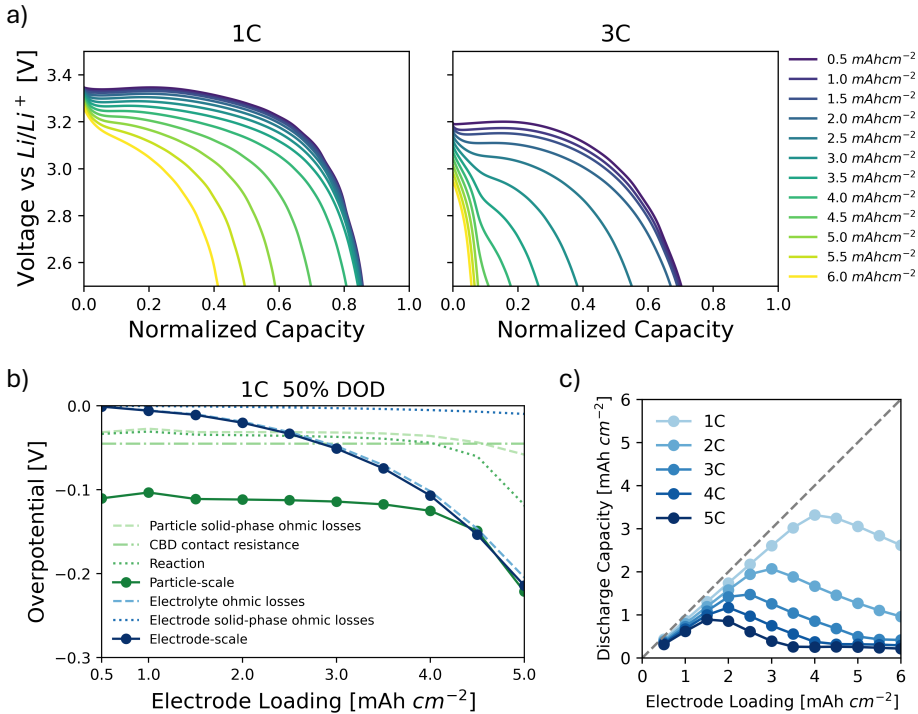


**Figure 8.7. Limiting factors and electrode optimization.** a) Comparison between the 1C and 3C discharge voltage profiles at various electrode loadings. b) Overpotential contributions at various electrode loadings for a discharge rate of 1C at 50% depth of discharge (DOD). c) Achieved discharge capacity vs electrode loading at various discharge rates.

Having obtained and validated our physics-based model against the electrochemical responses of two electrodes with extreme thicknesses, we can use it for rapid screening of electrode loading as a design variable. If, in fact, increasing loading raises areal energy density, it also amplifies transport limitations that restrict capacity utilization at higher rates. Therefore, a careful balance of these factors must be considered to obtain the best performance for the desired current output.

To exemplify the process, we present in Fig. 8.7a the simulated discharge voltage curves at 1C and 3C for loadings between 0.5 and 6 mA h cm<sup>-2</sup>. At 1C, most loadings deliver nearly the same capacity, with the principal change being a downward shift of the voltage plateau, signaling

greater internal resistance, while visible electrode-scale limitations only appear above  $4 \text{ mAh cm}^{-2}$ . At this rate the delivered capacity is mostly limited by particle-level transport limitations, and, therefore, even at extremely limited loadings, the electrode cannot deliver its full capacity. On the contrary, at 3C, the plateau shortens dramatically with loading above  $3 \text{ mAh cm}^{-2}$ , reaching the cut-off voltage before 50 % of their theoretical capacity is accessed.

To separate particle-level and electrode-level losses, we decompose the overpotentials of a 1C discharge at 50% depth of discharge and observe their changes with electrode loading (Fig. 8.7b). Particle-scale terms (solid-phase ohmic losses, CBD contact resistance, and reaction overpotential) remain nearly constant up to  $4 \text{ mAh cm}^{-2}$  and increase only when severe electrolyte polarization forces higher reaction overpotentials. Electrode-scale terms are instead negligible below  $1 \text{ mAh cm}^{-2}$  but grow monotonically thereafter, becoming the main source of overpotential at  $\sim 5 \text{ mAh cm}^{-2}$ .

Finally, these trends and simulations were used to obtain a current-dependent optimal loading (Fig. 8.7c). Low C-rates ( $\sim 1\text{C}$ ) continue to benefit from higher loadings until transport limits are reached, suggesting the use of loadings of  $\sim 4 \text{ mAh cm}^{-2}$  if these currents are expected. At faster rates, the optimum shifts to thinner electrodes, with the optimal loading for a 3C case being  $\sim 2.5 \text{ mAh cm}^{-2}$  and suggesting instead a loading of  $\sim 2 \text{ mAh cm}^{-2}$  in case higher rates are needed.

These observations lead to insightful design guidelines. Up to  $\sim 35\%$  of the capacity lost at high rates (e.g., 3C) originates from intra-particle limitations; mitigating this would then require smaller secondary particles or an increase in CBD content and its dispersion. Above  $\sim 2 \text{ mAh cm}^{-2}$ , ionic transport through the electrolyte becomes the main bottleneck, so further increases in loading must be paired with enhanced electrolyte conductivity or advanced electrode architectures, aimed at mitigating tortuosity and ensuring percolation.

## 8.8 CONCLUSIONS

In this work, we demonstrate how integrating physically consistent models in a multi scale framework enables accurate simulation of LFP electrodes composed of nanoporous secondary particles. These models build on years of experimental and theoretical validation. Long-range transport behavior is captured using porous electrode theory<sup>28,42</sup>, while thermodynamically derived chemical potentials provide a robust description of the open-circuit voltage, accounting for the phase-separating nature of LFP<sup>24</sup>. Moreover, the electron-coupled ion transfer (ECIT) kinetics incorporated here are supported by both theoretical and experimental studies<sup>39,54</sup>, offering a quantum-mechanically grounded understanding of interfacial electrochemical reactions.

By characterizing the effects of CBD contact fraction and morphology through three-dimensional simulations, we identified key transport limitations and extracted an accurate one-dimensional approximation. This reduced-order model introduces a constriction resistance and an effective electronic conductivity to account for the spatially inhomogeneous contact with the CBD. When embedded into a conventional porous electrode framework, the model successfully captures the electrochemical behavior of LFP electrodes across different thicknesses and operational regimes, with minimal additional computational cost. We further used the model to gain insight into internal particle dynamics and to identify the dominant limiting mechanisms under various design scenarios. Through electrode-scale simulations, we demonstrated its utility in guiding design choices such as optimal electrode thickness for targeted power or energy requirements.

Importantly, this modeling framework is not limited to LFP. Recent studies have shown that diffusion in secondary NMC particles is largely independent of particle size and instead governed by ionic transport along internal cracks<sup>15,16</sup>. Similarly, materials such as  $\text{LiMn}_x\text{Fe}_{1-x}\text{PO}_4$  and  $\text{Na}_3\text{V}_2(\text{PO}_4)_3$  exhibit improved performance when structured as nanoporous agglomerates of nanoscale crystals<sup>55</sup>. These findings suggest a shared transport-limited regime in hierarchical materials, which is well captured by the methodology developed in this study. Because the model explicitly resolves only electrolyte and electronic conduction (neglecting intra-primary-particle diffusion), it retains the same dimensionality and computational efficiency as conventional DFN models. This makes it readily compatible with existing simulation workflows and well-suited for future model-based optimization of next-generation battery chemistries as they mature toward commercial deployment.

## METHODS

The three-dimensional model was implemented with a finite element approach using COMSOL Multiphysics® using the porous electrode module and defining custom materials.

The DFN model was implemented in the open-source software PyBaMM<sup>56</sup> by creating a new class that extend the BaseModel class. To save computational resources, the discretization of the various particles sizes was done using a consistent mesh step size instead of the same number of mesh points.

The electrolyte used was EC:EMC 1:1 containing 1 M LiPF<sub>6</sub>. The electrolyte properties (diffusivity, conductivity, thermodynamic factor and transference number) were adjusted from the properties of Ref. <sup>57</sup> in order to match the experimental results of the 4.6 mAh cm<sup>-2</sup> sample.

The specific surface area of the secondary particles ( $a$ ) was calculated assuming primary particles of radius 50 nm that expose 30% of their surface area due to tight packing. While the particle size distribution was obtained by the supplier.

## REFERENCES

1. IEA. Global EV Outlook 2025. (2025).
2. Biro, D. F. Batteries and Secure Energy Transitions. *IEA* (2024).
3. Rozier, P. & Tarascon, J. M. Review—Li-Rich Layered Oxide Cathodes for Next-Generation Li-Ion Batteries: Chances and Challenges. *J. Electrochem. Soc.* **162**, A2490–A2499 (2015).
4. Malik, R., Abdellahi, A. & Ceder, G. A Critical Review of the Li Insertion Mechanisms in LiFePO<sub>4</sub> Electrodes. *J. Electrochem. Soc.* **160**, A3179–A3197 (2013).
5. Ahsan, Z. *et al.* Recent Progress in Capacity Enhancement of LiFePO<sub>4</sub> Cathode for Li-Ion Batteries. *J. Electrochem. Energy Convers. Storage* **18**, 010801 (2021).
6. Xiaoying, G., Yuanyuan, B., Wei, L., Siqin, Z. & Chao, H. Current research status on the structural properties and modification of LiFePO<sub>4</sub> cathode materials. *React. Chem. Eng.* **9**, 2830–2845 (2024).
7. Yan, G. & others. Identifying critical features of iron phosphate particle for lithium preference. *Nat. Commun.* **15**, 4859 (2024).
8. Wilcox, J. D., Doeff, M. M., Marcinek, M. & Kostecki, R. Factors Influencing the Quality of Carbon Coatings on LiFePO<sub>4</sub>. *J. Electrochem. Soc.*
9. Li, Y. *et al.* Effects of Particle Size, Electronic Connectivity, and Incoherent Nanoscale Domains on the Sequence of Lithiation in LiFePO<sub>4</sub> Porous Electrodes. *Adv. Mater.* **27**, 6591–6597 (2015).
10. Chueh, W. C. *et al.* Intercalation Pathway in Many-Particle LiFePO<sub>4</sub> Electrode Revealed by Nanoscale State-of-Charge Mapping. *Nano Lett.* **13**, 866–872 (2013).
11. Ye, N., Yan, T., Jiang, Z., Wu, W. & Fang, T. A review: Conventional and supercritical hydro/solvothermal synthesis of ultrafine particles as cathode in lithium battery. *Ceram. Int.* **44**, 4521–4537 (2018).
12. Li, Z. *et al.* Controlled Hydrothermal/Solvothermal Synthesis of High-Performance LiFePO<sub>4</sub> for Li-Ion Batteries. *Small Methods* **5**, 2100193 (2021).
13. Li, Y. *et al.* Current-induced transition from particle-by-particle to concurrent intercalation in phase-separating battery electrodes. *Nat. Mater.* **13**, 1149–1156 (2014).
14. Trevisanello, E., Ruess, R., Conforto, G., Richter, F. H. & Janek, J. Polycrystalline and Single Crystalline NCM Cathode Materials—Quantifying Particle Cracking, Active Surface Area, and Lithium Diffusion. *Adv. Energy Mater.* **11**, 2003400 (2021).
15. Min, J., Suk, W., Wong, S. C. Y. & Li, Y. Single-Particle Electrochemical Cycling Single-Crystal and Polycrystalline NMC Particles. *Adv. Funct. Mater.* **34**, 2410241 (2024).
16. Min, J., Gubow, L. M., Hargrave, R. J., Siegel, J. B. & Li, Y. Direct measurements of size-independent lithium diffusion and reaction times in individual polycrystalline battery particles. *Energy Environ. Sci.* **16**, 3847–3859 (2023).
17. Ni, L. *et al.* Fabrication and characteristics of spherical hierarchical LiFePO<sub>4</sub>/C cathode material by a facile method. *Electrochimica Acta* **147**, 330–336 (2014).
18. Wang, Q. *et al.* Hydrothermal synthesis of hierarchical LiFePO<sub>4</sub> microspheres for lithium ion battery. *J. Alloys Compd.* **553**, 69–74 (2013).
19. Daubner, S. *et al.* Simulation of intercalation and phase transitions in nano-porous, polycrystalline agglomerates. *Npj Comput. Mater.* **11**, 211 (2025).
20. Birkholz, O. & Kamlah, M. Electrochemical Modeling of Hierarchically Structured Lithium-Ion Battery Electrodes. *Energy Technol.* **9**, 2000910 (2021).

21. Lian, H. & Bazant, M. Z. Modeling Lithium Plating Onset on Porous Graphite Electrodes Under Fast Charging with Hierarchical Multiphase Porous Electrode Theory. *J. Electrochem. Soc.* **171**, 010526 (2024).
22. Dargaville, S. & Farrell, T. W. Predicting Active Material Utilization in LiFePO<sub>4</sub> Electrodes Using a Multiscale Mathematical Model. *J. Electrochem. Soc.*
23. Kench, S. *et al.* Li-ion battery design through microstructural optimization using generative AI. *Matter* S2590238524004466 (2024) doi:10.1016/j.matt.2024.08.014.
24. Ombrini, P., Bazant, M. Z., Wagemaker, M. & Vasileiadis, A. Thermodynamics of multi-sublattice battery active materials: from an extended regular solution theory to a phase-field model of LiMnyFe<sub>1-y</sub>PO<sub>4</sub>. *Npj Comput. Mater.* **9**, 148 (2023).
25. Park, J. *et al.* Fictitious phase separation in Li layered oxides driven by electro-autocatalysis. *Nat. Mater.* **20**, 991–999 (2021).
26. Ombrini, P. *et al.* Kinetically induced memory effect in Li-ion batteries. *EES Batter.* 10.1039/D5EB00014A (2025) doi:10.1039/D5EB00014A.
27. Schwietert, T. K. *et al.* Phase-Field Computational Framework for Addressing Challenges in Solid-State Batteries. *PRX Energy* **2**, 033014 (2023).
28. Doyle, M., Fuller, T. F. & Newman, J. Modeling of Galvanostatic Charge and Discharge of the Lithium/Polymer/Insertion Cell. *J. Electrochem. Soc.* **140**, 1526–1533 (1993).
29. Fuller, T. F., Doyle, M. & Newman, J. Simulation and Optimization of the Dual Lithium Ion Insertion Cell. *J. Electrochem. Soc.* **141**, 1–10 (1994).
30. Brosa Planella, F. *et al.* A continuum of physics-based lithium-ion battery models reviewed. *Prog. Energy* **4**, 042003 (2022).
31. Ombrini, P. *et al.* Modeling Single-Crystal Electrodes as a Network of Primary Particles.
32. Safari, M. & Delacourt, C. Mathematical Modeling of Lithium Iron Phosphate Electrode: Galvanostatic Charge/Discharge and Path Dependence. *J. Electrochem. Soc.* **158**, A63 (2011).
33. Thomas-Alyea, K. E. Modeling Resistive-Reactant and Phase-Change Materials in Battery Electrodes. *ECS Trans.* **16**, 155–165 (2008).
34. Bai, P., Cogswell, D. A. & Bazant, M. Z. Suppression of Phase Separation in LiFePO<sub>4</sub> Nanoparticles During Battery Discharge. *Nano Lett.* **11**, 4890–4896 (2011).
35. Zeng, Y. & Bazant, M. Z. Phase Separation Dynamics in Isotropic Ion-Intercalation Particles. *SIAM J. Appl. Math.* **74**, 980–1004 (2014).
36. Vasileiadis, A. *et al.* Toward Optimal Performance and In-Depth Understanding of Spinel Li<sub>4</sub>Ti<sub>5</sub>O<sub>12</sub> Electrodes through Phase Field Modeling. *Adv. Funct. Mater.* **28**, 1705992 (2018).
37. Cogswell, D. A. & Bazant, M. Z. Theory of Coherent Nucleation in Phase-Separating Nanoparticles. *Nano Lett.* **13**, 3036–3041 (2013).
38. Cogswell, D. A. & Bazant, M. Z. Size-dependent phase morphologies in LiFePO<sub>4</sub> battery particles. *Electrochem. Commun.* **95**, 33–37 (2018).
39. Bazant, M. Z. Unified quantum theory of electrochemical kinetics by coupled ion-electron transfer. *Faraday Discuss.* 10.1039/D3FD00108C (2023) doi:10.1039/D3FD00108C.
40. Fraggedakis, D. *et al.* Theory of coupled ion-electron transfer kinetics. *Electrochimica Acta* **367**, 137432 (2021).
41. Bai, P. & Bazant, M. Z. Charge transfer kinetics at the solid–solid interface in porous electrodes. *Nat. Commun.* **5**, 3585 (2014).
42. Ferguson, T. R. & Bazant, M. Z. Nonequilibrium Thermodynamics of Porous Electrodes. *J. Electrochem. Soc.* **159**, A1967–A1985 (2012).
43. Malik, R., Burch, D., Bazant, M. & Ceder, G. Particle Size Dependence of the Ionic Diffusivity. *Nano Lett.* **10**, 4123–4127 (2010).

44. Nadkarni, N. *et al.* Interplay of phase boundary anisotropy and electro-auto-catalytic surface reactions on the lithium intercalation dynamics in Li X FePO<sub>4</sub> plateletlike nanoparticles. *Phys. Rev. Mater.* **2**, 085406 (2018).
45. Ferguson, T. R. & Bazant, M. Z. Phase Transformation Dynamics in Porous Battery Electrodes. *Electrochimica Acta* **146**, 89–97 (2014).
46. Deng, H. D. *et al.* Beyond Constant Current: Origin of Pulse-Induced Activation in Phase-Transforming Battery Electrodes. *ACS Nano* **18**, 2210–2218 (2024).
47. Mistry, A. N., Smith, K. & Mukherjee, P. P. Secondary-Phase Stochastics in Lithium-Ion Battery Electrodes. *ACS Appl. Mater. Interfaces* **10**, 6317–6326 (2018).
48. Usseglio-Viretta, F. L. E. *et al.* MATBOX: An Open-source Microstructure Analysis Toolbox for microstructure generation, segmentation, characterization, visualization, correlation, and meshing. *SoftwareX* **17**, 100915 (2022).
49. Cooper, S. J., Bertei, A., Shearing, P. R., Kilner, J. A. & Brandon, N. P. TauFactor: An open-source application for calculating tortuosity factors from tomographic data. *SoftwareX* **5**, 203–210 (2016).
50. Kench, S. & Cooper, S. J. Generating three-dimensional structures from a two-dimensional slice with generative adversarial network-based dimensionality expansion. *Nat. Mach. Intell.* **3**, 299–305 (2021).
51. Gayon-Lombardo, A., Mosser, L., Brandon, N. P. & Cooper, S. J. Pores for thought: generative adversarial networks for stochastic reconstruction of 3D multi-phase electrode microstructures with periodic boundaries. *Npj Comput. Mater.* **6**, 82 (2020).
52. Kuzhiyil, J. A., Damoulas, T., Planella, F. B. & Widanage, W. D. Lithium-ion battery degradation modelling using universal differential equations: Development of a cost-effective parameterisation methodology. *Appl. Energy* **382**, 125221 (2025).
53. Panahi, A. A. *et al.* Fast and Generalizable parameter-embedded Neural Operators for Lithium-Ion Battery Simulation. Preprint at <https://doi.org/10.48550/arXiv.2508.08087> (2025).
54. Zhao, H. *et al.* Learning heterogeneous reaction kinetics from X-ray videos pixel by pixel. *Nature* **621**, 289–294 (2023).
55. Chen, H., Xu, S., Zhou, M., Zhang, X. & Zhou, H. Hierarchical porous Na<sub>3</sub>V<sub>2</sub>(PO<sub>4</sub>)<sub>3</sub>/graphene microspheres with enhanced sodium-ion storage properties. *J. Mater. Sci. Mater. Electron.* **34**, 2196 (2023).
56. Sulzer, V., Marquis, S. G., Timms, R., Robinson, M. & Chapman, S. J. Python Battery Mathematical Modelling (PyBaMM). *J. Open Res. Softw.* **9**, 14 (2021).
57. Valøen, L. O. & Reimers, J. N. Transport Properties of LiPF<sub>6</sub>-Based Li-Ion Battery Electrolytes. *J. Electrochem. Soc.*
58. Zhang, Y. *et al.* Lithium-ion intercalation by coupled ion-electron transfer. Preprint at <https://doi.org/10.26434/chemrxiv-2024-d00cp-v2> (2024).
59. Greenwood, J. A. Constriction resistance and the real area of contact. *Br. J. Appl. Phys.* **17**, 1621–1632 (1966).
60. Boyer, L. Contact resistance calculations: generalizations of Greenwood’s formula including interface films. *IEEE Trans. Compon. Packag. Technol.* **24**, 50–58 (2001).

## SUPPLEMENTARY INFORMATION

<b><i>Particle parameters</i></b>		
Ion-vacancy interaction energy ( $\Omega$ )	89 meV	Ref <sup>37</sup>
Maximum Li concentration ( $c_{max}$ )	22261 mol m <sup>-3</sup>	Ref <sup>24</sup>
Initial Li concentration ( $c_{init}$ )	556 mol m <sup>-3</sup>	Measured
Exchange current density ( $k_0$ )	15 A m <sup>-2</sup>	Ref <sup>41</sup>
Reorganization Energy ( $\lambda$ )	212 meV	Ref <sup>41</sup>
Mean particle size	1.3 $\mu$ m	Measured
Standard deviation of particle size	1.7 $\mu$ m	Measured
Particle porosity ( $\epsilon_p$ )	0.15	Estimated
Particle active material volume fraction ( $\epsilon_s$ )	0.85	Estimated
Particle solid phase tortuosity ( $\tau_s$ )	1.1	Estimated
Particle electrolyte tortuosity ( $\tau_p$ )	2.8	Estimated
Particle active volumetric surface area ( $a$ )	1.6 10 <sup>7</sup> m <sup>2</sup> m <sup>-3</sup>	Estimated
Contact resistance ( $R_c$ )	9.2 10 <sup>-2</sup> $\Omega$ m <sup>2</sup>	Fitted
Particle electrical conductivity prefactor ( $\sigma$ )	1.72 10 <sup>-5</sup> S m <sup>-1</sup>	Fitted
<b><i>Electrode parameters</i></b>		
Electrode thickness (1 mAh cm <sup>-2</sup> )	35 $\mu$ m	Measured
Electrode thickness (4.6 mAh cm <sup>-2</sup> )	164 $\mu$ m	Measured
Electrode porosity (1 mAh cm <sup>-2</sup> )	0.25	Measured
Electrode porosity (4.6 mAh cm <sup>-2</sup> )	0.29	Measured
Active material volume fraction (1 mAh cm <sup>-2</sup> )	0.61	Measured
Active material volume fraction (4.6 mAh cm <sup>-2</sup> )	0.56	Measured
CBD volume fraction	0.15	Measured
Electrode tortuosity	3.95	Calculated <sup>49</sup>
Bulk electrical conductivity ( $\sigma_{bulk}$ )	1 S m <sup>-1</sup>	Estimated
Initial electrolyte concentration	1 M	Measured
Adsorption coefficient ( $f_{ads}$ )	0.3	Ref <sup>58</sup>
Separator thickness	15 $\mu$ m	Measured
Separator porosity	0.6	Measured

Table S1. Simulation Parameters.

## Model's equations

Within the secondary particles, charge conservation requires the current in the electrolyte  $i_e$  and solid phase  $i_s$  ( $A/m^2$ ) of the particle to be coupled with the local reaction rate

$$\nabla \cdot i_e = a j \quad (\text{E1})$$

$$\nabla \cdot i_s = -a j \quad (\text{E2})$$

where  $a$  ( $m^2/m^3$ ) is the active specific surface area of the nanoporous particle and  $j$  ( $A/m^2$ ) is the current originating from the electrochemical reaction. The solid phase current ( $i_s$ ) is regulated by Ohm's law

$$i_s = -\frac{\varepsilon_s}{\tau_s} \sigma \nabla \phi_s \quad (\text{E3})$$

where the intrinsic electronic conductivity  $\sigma$  ( $S/m$ ) is multiplied by the solid material volume fraction inside the secondary particle  $\varepsilon_s$ , and divided by the tortuosity  $\tau_s$  of the solid conduction pathways. This equation regulates the solid phase electrical potential drop  $\phi_s$  ( $V$ ) within the particle. Similarly, the electrolyte current depends on the electrolyte conductivity  $\kappa$  ( $S/m$ ), the volume fraction occupied by the porosity  $\varepsilon_p$  and the relative tortuosity  $\tau_p$ , following this relation:

$$i_e = -\frac{\varepsilon_p}{\tau_p} \kappa \left[ \nabla \phi_e - \frac{k_B T}{e} 2(1-t^+) \left( 1 + \frac{\partial \ln f}{\partial \ln c_e} \right) \frac{\nabla c_e}{c_e} \right] \quad (\text{E4})$$

The electrolyte current is affected by both the electrolyte potential  $\phi_e$  and the electrolyte concentration distribution  $c_e$  ( $mol/m^3$ ) which comprehend the thermodynamic factor  $\left( 1 + \frac{\partial \ln f}{\partial \ln c_e} \right)$  and the transference number  $t^+$ . The electrolyte concentration is then evolving according to

$$\varepsilon_p \frac{dc_e}{dt} = \nabla \cdot \left( \frac{\varepsilon_p}{\tau_p} D_e \nabla c_e \right) + (1-t^+) \frac{a j}{F} \quad (\text{E5})$$

The specific current density  $j$  is regulated by the behavior of the primary particles and their surface reaction kinetics.

The particle's mass conservation is coupled with the local reaction rate, so that, defining the normalized solid concentration as  $\tilde{c}_s = c_s/c_{max}$ , we get

$$\varepsilon_s \frac{d\tilde{c}_s}{dt} = \frac{a j}{F c_{max}} \quad (\text{E6})$$

The current density  $j$  within the particle domain is then regulated by the reaction overpotential  $\eta$ , defined as  $\eta = \phi_s - \phi_e - U(\tilde{c}_s)$  (V), via electron-coupled ion transfer (ECIT) formalism<sup>39</sup>

$$j = k_0 \left( \frac{1 - \tilde{c}_s}{2} \right) \left( \frac{\tilde{c}_s}{1 + e^{-\tilde{\eta}_f}} - \frac{\tilde{c}_+}{1 + e^{\tilde{\eta}_f}} \right) \operatorname{erfc} \left( \frac{\tilde{\lambda} - \sqrt{\tilde{\eta}_f^2 + 1 + \sqrt{\tilde{\lambda}}}}{2\sqrt{\tilde{\lambda}}} \right) \quad (\text{E7})$$

where the formal overpotential  $\tilde{\eta}_f = \frac{e\eta}{k_B T} + \ln \left( \frac{\tilde{c}_+}{\tilde{c}_s} \right)$  is introduced and depends on the normalized electrolyte surface concentration  $\tilde{c}_+ = f_{ads} c_e / c_{ref}$ . This quantity reflects the ion adsorption on the particle's surface via an adsorption factor  $f_{ads}$  and the normalized the electrolyte concentration to the reference concentration  $c_{ref}$ , fixed at one molar. This formalism originates from CIET, that consider both ion and electron transition states and includes in a rate prefactor  $k_0$  ( $A/m^2$ ) and the electron reorganization energy  $\lambda$  (eV), here shown in its normalized form  $\tilde{\lambda} = \lambda/k_B T$ .

## Boundary conditions

In 3D-SPHM the electrolyte potential  $\phi_e$  and salt concentration  $c_e$  are fixed at the particle–electrolyte interface  $S_p$ :

$$\phi_e|_{S_p} = \phi_{elyte} \quad (\text{E8})$$

$$c_e|_{S_p} = c_{elyte} \quad (\text{E9})$$

Each cap is assumed to be at the same external potential  $V(t)$ , and an algebraic constraint is applied to the total current entering through the CBD contact area:

$$\int_{S_{CBD}} \mathbf{n} \cdot \mathbf{i}_s dS = I_{app}(t) \quad (\text{E10})$$

where  $i_s$  is the solid-phase current density, and  $S_{CBD}$  corresponds to the surface contact between the particle and the CBD caps.

In the 1D-SPHM, we consider an electrode of thickness  $L_p$  with spatial coordinate  $x \in [0, L_p]$ . At the particle–electrolyte interface ( $r = R_p$ ), the boundary conditions for the electrolyte potential  $\phi_e(r)$  and concentration  $c_e(r)$  are defined by continuity with the electrode-scale electrolyte variables:

$$\phi_e(R_p)|_x = \phi_{elyte}(x), \quad (E11)$$

$$c_e(R_p)|_x = c_{elyte}(x) \quad (E12)$$

where  $\phi_{elyte}(x)$  and  $c_{elyte}(x)$  represent the local electrolyte potential and concentration at position  $x$  along the electrode.

For the solid-phase potential  $\phi_s(r)$ , the boundary conditions are modified with respect to the three-dimensional case. Introducing a constriction resistance  $R_c$  between each secondary particle and the surrounding CBD<sup>59,60</sup>, gives

$$\phi_s(R_p)|_x = \phi_{bulk}(x) - R_c i_s(R_p) \quad (E13)$$

where  $\phi_{bulk}(x)$  is the macroscopic solid-phase potential, and  $i_s(R_p)$  is the solid-phase current density at the particle boundary.

Finally, at the particle center ( $r = 0$ ), radial symmetry enforces Neumann boundary conditions for all relevant fields:

$$\frac{d\phi_s}{dr}|_{r=0} = 0, \quad \frac{d\phi_e}{dr}|_{r=0} = 0, \quad \frac{dc_e}{dr}|_{r=0} = 0. \quad (E14,15,16)$$

In the DFN model, the local volumetric reaction rate  $RR(x)$  is expressed as a weighted sum of the interfacial currents from each particle size:

$$RR(x) = \frac{\varepsilon_{s,macro}}{e} \frac{\sum_i f_i S_i i_{e,i}(R_{p,i})}{\sum_i f_i V_i} \quad (E17)$$

Where  $S_i$ ,  $V_i$ , and  $R_{p,i}$  denote surface area, volume, and radius of the  $i$ -th particle type, respectively. The term  $i_{e,i}(R_{p,i})$  is the interfacial electrolyte current density for the particle evaluated at its surface ( $r = R_{p,i}$ ), and  $f_i(R_{p,i})$  is the frequency-based particle size distribution obtained from experimental data.

## Generation and implementation of CBD contact patches

To construct the solid-phase boundary conditions in the 3D-SPHM, the CBD contact area is defined as a set of spherical caps placed on the surface of a sphere of radius  $R_p$ . Each cap has geodesic radius  $r_c \ll R_p$ , and the total cap area corresponds to a target surface coverage fraction  $f_c$ . Cap centers are located on a discrete  $(\theta, \psi)$  grid that ensures uniform solid angle resolution across the sphere.

Following a similar methodology to Ref. 47: caps are added iteratively using a stochastic algorithm governed by a morphology parameter  $m$ . For each unoccupied grid cell in the  $(\theta, \psi)$  domain, the local “energy”  $E$  is computed based on the number of neighboring active-material cells  $n_s$  and existing CBD cells  $n_{CBD}$ :

$$E = (1 - m) \frac{n_s}{4} + m \frac{n_{CBD}}{4} \quad (\text{E18})$$

New caps are deposited with probability proportional to  $E$ , encouraging dispersion (low  $m$ ) or clustering (high  $m$ ). After each batch of depositions, the effective covered fraction is estimated using a Monte Carlo sampling method on the sphere. The process continues until the estimated coverage fraction converges to the target  $f_c$  within a tolerance of  $10^{-3}$ . The resulting cap centers and radius are exported to COMSOL® via MATLAB® APIs, where Boolean operations define the CBD region  $S_{CBD}$ .

### Fitted relation for effective conductivity

The effective conductivity values extracted from the 3D-SPHM were interpolated using a sigmoidal function of the particle radius  $R_p$ :

$$\sigma_{eff}(R_p) = \sigma \frac{\alpha}{1 + e^{-\beta(R_p - \gamma)}} \quad (E19)$$

Where  $\sigma$  is the bulk conductivity of the material, treated as an adjustable parameter in the DFN model, and  $\alpha, \beta$  and  $\gamma$  are fitted parameters. For the representative contact fraction  $f_c \approx 0.3$ , obtained from the generated microstructure (Fig. S1), the best-fit values were:  $\alpha = 1.74, \beta = -0.31, \gamma = 1.48 \mu m$ . The corresponding fitted values of the constriction resistance  $R_c$  showed no systematic dependence on particle size and were therefore treated as radius-independent. In the DFN framework,  $R_c$  is left as an adjustable parameter to account for electrode-to-electrode variability in CBD uniformity and contact size.

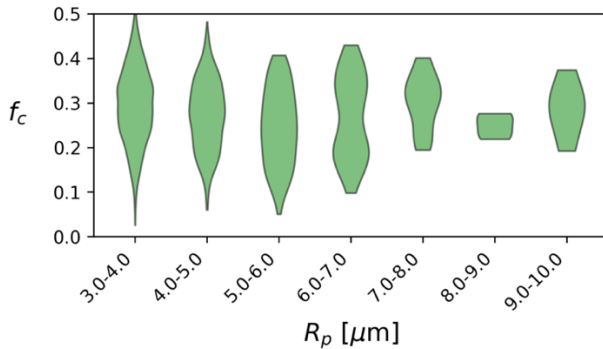


Figure S1. Relation between the particle radius and the contact fraction ( $f_c$ ) obtained from the generated microstructure.

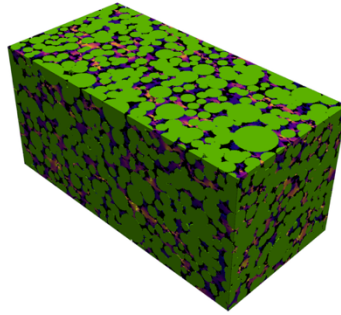


Figure S2. Computation of the tortuosity factor  $\tau$  of the generated microstructure. The green and black phases are the particle and the CBD, respectively. The purple-yellow colors represent the relative intensity of the ionic flux during the computation of the tortuosity.

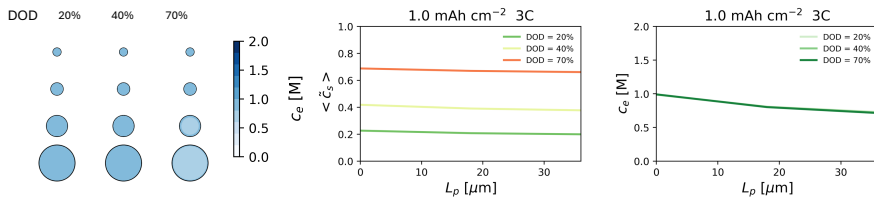


Figure S3. Depth-wise evolution of the internal variables during the 3C discharge on the 1 mAh cm<sup>-2</sup> sample.

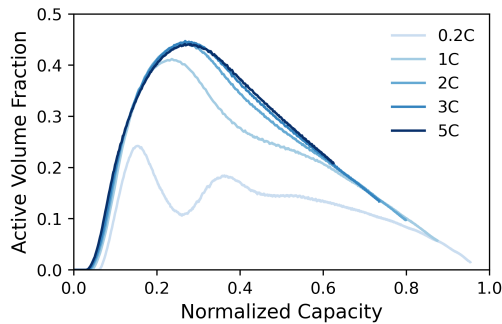


Figure S4. Evolution of the active volume fraction of the 1 mAh cm<sup>-2</sup> sample during discharging at various rates. The active volume is defined as having  $\tilde{c}_s$  within the miscibility gap ( $\tilde{c}_s \in [0.2, 0.8]$ ). It was calculated by volume-weighted averaging of the concentration variable within the particle size distribution.

# 8 | MULTISCALE MODELING OF LITHIUM IRON PHOSPHATE ELECTRODES COMPOSED BY NANOPOROUS SECONDARY PARTICLES

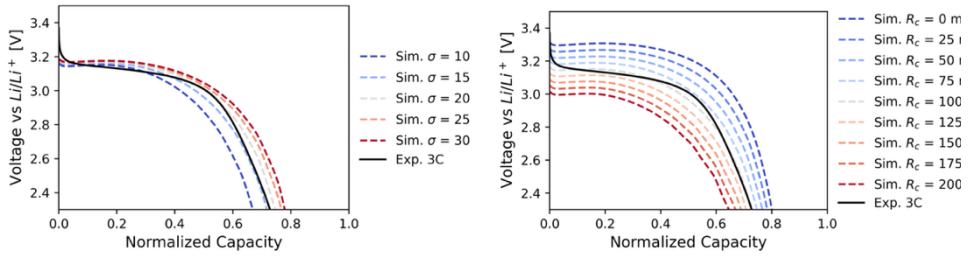


Figure S5. Effect of the electrical conductivity  $\sigma$  and constriction resistance  $R_c$  on the voltage response of the 3.0C discharge on the 1 mAh cm<sup>-2</sup> sample.





# 9 NON-FICKIAN IONIC DIFFUSION IN LITHIUM IRON PHOSPHATE

This chapter is part of a manuscript under review as: Yan G†, Ombrini Pt, Tang Z, Pathak P, Wang M, Lavina B, Vasileiadis A, Choi S, Wang M, Ying D, Li Q, Alp EE, Zhou H, Bazant MZ, Chen Q, Wagemaker M and Liu C. Crossover Dynamics of Non-Fickian Ionic Diffusion in Solids.

## ABSTRACT

Ionic diffusion in solids is crucial for energy storage, energy conversion, electronics, and catalysis, and thus vital for renewable energy solutions. Conventional diffusion models struggle with complexities introduced by confinements, crystallographic disorder, lattice distortions, and coupled transport involving phonons, electrons, or holes. Here, using one-dimensional (1D) olivine  $\text{LiFePO}_4$  (LFP) as a model system, we revisit ion transport and uncover crossover dynamics between distinct diffusion regimes through tracer exchange measurements. Single-file diffusion (SFD), diffusion through the narrow 1D channels where ions are unable to pass each other, emerges during  $^6\text{Li}$ - $^7\text{Li}$  exchange due to 1D  $\text{Li}^+$  propagation, followed by a transition to ordinary diffusion enabled by occasional  $\text{Li}^+$  passage events. Furthermore, Kinetic Monte Carlo (KMC) simulations, alongside chronoamperometry experiments, quantify both Faradaic and non-Faradaic surface exchange rates in nanoplatelet LFP w/wo carbon-coating, providing direct evidence that electron-transport is the rate-limiting step during reaction. Our findings uncover the complexity solid-state ionic diffusion dynamics, effectively uncovered through ICP-MS tracer exchange experiments, prompting a reevaluation of ion diffusion mechanisms in confined systems.

## 9.1 INTRODUCTION

Ionic diffusion in solids stands as a cornerstone across scientific domains, with pivotal roles extending from solid-state electrolytes<sup>1</sup> to mixed ionic-electronic conductors<sup>2</sup>, all critical for next-generation energy systems. Our current understanding of how ions move through crystalline lattices remains largely governed by classical diffusion laws. However, in many solids, ion transport is hindered or redirected by confinement<sup>3</sup>, polyanions rotational motion<sup>4</sup>, or coupling to electronic processes<sup>5,6</sup>, conditions under which conventional Fickian models break down<sup>7</sup>. For example, multi-ion concerted migration can be induced by excess  $\text{Li}^+$ , enhancing  $\text{Li}^+$ - $\text{Li}^+$  interactions and leading to superionic conductivity<sup>8</sup>.

Anomalous diffusion, where the ensemble-averaged mean-square displacement (eMSD) scales non-linearly with time ( $\text{eMSD} \propto t^\alpha$ ; Fig. 9.1a), is well documented in soft matter and biological systems<sup>9</sup>, but remains underexplored in crystalline solids. Continuum models of diffusion in solid-state systems typically assume that tracer diffusivity scales with the vacancy fraction, while still preserving an  $\text{eMSD} \propto t$  relation<sup>10</sup>. Distinct diffusion regimes can be revealed through scaling analysis: superdiffusion ( $\alpha > 1$ ) can emerge from occasional long-range displacements, as exemplified by Loopy Lévy flights in active swimmer systems like colloids and bacteria<sup>9</sup>, while subdiffusion ( $\alpha < 1$ ) can result from trapping mechanisms or strong spatial confinement, as in SFD dynamics<sup>11–13</sup>, where particles are constrained from bypassing each other in narrow channels. Despite its theoretical importance, anomalous diffusion in solids has received limited attention due to the lack of suitable approaches.

Here, we investigate the diffusion dynamics in olivine  $\text{LiFePO}_4$  (LFP), a model system that favors anisotropic 1D diffusion along [010], where diffusion along [100] and [001] is significantly less probable<sup>14–16</sup>. At short exchange times, we observe characteristic SFD behavior during  $^6\text{Li}$ - $^7\text{Li}$  exchange measured by ICP-MS over time, a universal crossover to normal diffusion emerges, driven by occasional  $\text{Li}^+$  passage events through surface or crystal imperfections such as Li-Fe anti-site defects. We finally employ Kinetic Monte Carlo (KMC) simulations to quantify the phenomena happening in the crystal, and we combine the findings with chronoamperometry to provide direct evidence for coupled ion-electron transfer (CIET) as the mechanism for  $\text{Li}^+$  intercalation in  $\text{LiFePO}_4$  solids<sup>17</sup>.

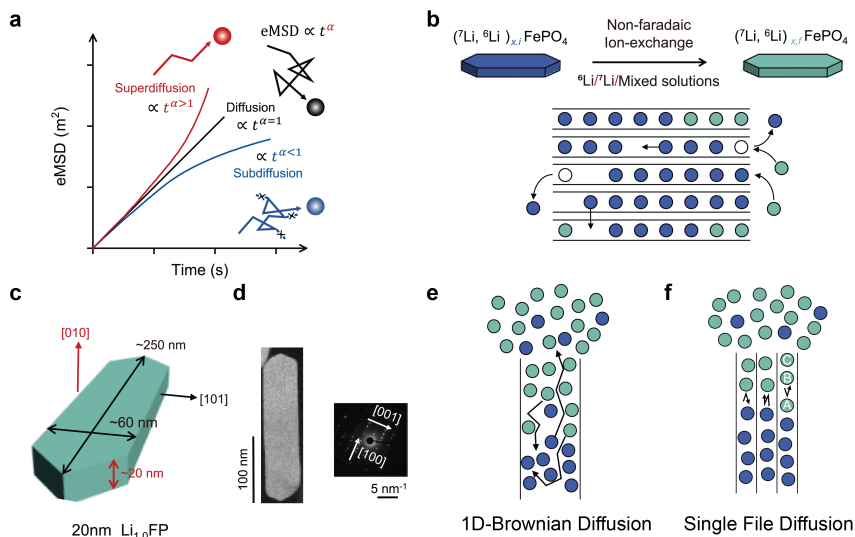


**Figure 1. Solid-state ionic diffusion and  ${}^6\text{Li}$ - ${}^7\text{Li}$  non-faradaic exchange.** a) Schematic illustration depicting the eMSD of particle ensembles over time. For ordinary Fickian diffusion (black), a linear time-dependence ( $\alpha = 1$ ) is expected. Superdiffusive motion (red) shows a super-linear time-dependence ( $\alpha > 1$ ). Subdiffusion (blue) indicates slow-than-normal diffusion rates ( $\alpha < 1$ ) due to constrained motions. b) Schematic illustration of the experimental design, with potential exchange pathways between host ions (blue) and solution ions (green) depicted below. c) Schematic of a representative nanoplatelet LFP particle (20nm), featuring the predominant (010) facet and  $\sim 20$  nm [010] diffusion channels highlighted in red. d) Scanning transmission electron micrograph (STEM) and selected area electron diffraction (SAED) pattern of one 20nm LFP nanoplatelet particle, with white arrows denoting the specific orientations. e) Schematic illustration showing 1D Brownian Diffusion (1D-BD) dynamics during ion exchange between  ${}^7\text{Li}$  ions (dark blue) and  ${}^6\text{Li}$  ions (light green). The hypothetical channel is larger than the lithium ions. Although macroscopic diffusion is unidirectional, the particles can bypass each other, leading to ordinary diffusion behavior. f) Schematic illustration showing SFD dynamics during ion exchange. The diffusion channel is only slightly larger than the lithium ions, constraining the ions from bypassing each other and leading to the preservation of initial order.

Direct tracking of the position of an ensemble of ions is experimentally challenging and requires advanced characterization techniques. While this has been obtained in the case of macroscopic particles<sup>13</sup>, the atomic resolution necessary to obtain the eMSD of  ${}^6\text{Li}$  in  $\text{FePO}_4$  crystal, prevents us from using the same techniques. Therefore, we opted for soaking various LFP particles (with naturally abundant  ${}^6\text{Li}$  and  ${}^7\text{Li}$ ) in a  ${}^6\text{Li}$ -enriched aqueous solution and tracked the time evolution of the fraction of  ${}^6\text{Li}$  exchanged from the solution<sup>46</sup> ( $\gamma - \gamma_0$ ). The use of this method is justified from the linear relation between the eMSD and the tracer exchange rate:

$$|\gamma(t) - \gamma_0| \sim \sqrt{\text{eMSD}(t)} \quad (9.1)$$

Therefore, by extracting the slope of  $\log(\gamma - \gamma_0)$  versus  $\log(t)$ , which is equal to  $\alpha/2$ , we can identify different diffusion mechanisms shown in Fig. 9.1a.

To prove Eq. 1, we consider a one-dimensional diffusion process occurring within a domain of length  $L$  that is in contact with a reservoir maintained at a constant tracer concentration ( $c_{\text{ext}} \neq c_0$ ), where  $c_0$  represents the initial tracer concentration within the domain. Over time, tracers ( $^6\text{Li}$  in our case) diffuse within the domain and exchange with the external reservoir, leading to a change in internal average concentration

$$\gamma(t) = \langle c(x, t) \rangle_x. \quad (9.2)$$

Here, eMSD is defined as:

$$\text{eMSD}(t) = \langle (x(t) - x_0)^2 \rangle \quad (9.3)$$

and  $x(t)$  is the position of an ion at time  $t$ ,  $x_0$  is its initial position, and the ensemble average  $\langle \cdot \rangle$  is taken over many independent realizations of the diffusion process. Notably, this ensemble-averaged quantity is distinct from the time-averaged mean-square displacement (tMSD) computed from a single particle's trajectory. Since our experimental approach monitors the compositional changes of the ensemble at a given time  $t$ , the eMSD is the pertinent descriptor for our system.

At time  $t = 0$ , the channel is uniformly filled with the tracer concentration  $c_0$ . To extend our analysis, we consider a generalized diffusion process along the spatial coordinate  $x$  that may exhibit either conventional Fickian behavior ( $\alpha = 1$ ) or subdiffusive dynamics ( $0 < \alpha < 1$ ). Consequently, the transport of a generic quantity  $\theta$  is governed by the fractional differential equation:

$$\frac{d^\alpha \theta}{dt^\alpha} = D_\alpha \frac{d^2 \theta}{dx^2} \quad (9.4)$$

Here,  $D_\alpha$  denotes the mobility factor with dimensions  $m^2 s^{-\alpha}$ . This fractional form arises naturally from a random walk model characterized by diverging waiting times while maintaining a constant jump length variance<sup>18</sup>. When the waiting-time probability density function exhibits a long tail, the ensemble-averaged mean-square displacement assumes the form<sup>19</sup>:

$$\text{eMSD}(t) = \frac{2D_\alpha}{\Gamma(1 + \alpha)} t^\alpha \quad (9.5)$$

$\Gamma(\cdot)$  represents the Gamma function. For the case of  $\alpha = 1$ , i.e. ordinary 1D Brownian Diffusion, this result reduces to the well-known Einstein equation,  $\text{eMSD}(t) = 2D_1t$ , where  $D$  is the self-diffusion constant ( $[D] = \text{m}^2\text{s}^{-1}$ ). This occurs because Brownian diffusion assumes that, while macroscopic displacement occurs only along the channel axis, the microscopic motions of particles remain 2D or 3D, allowing particle passages (Fig. 9.1e).

In contrast, in SFD, only single-file passage of Li ions is possible in the diffusion channel, preventing ion passage events and preserving the ion sequence (Fig. 9.1f). This significantly reduces the translational mobility of individual ions, resulting in a subdiffusive time dependence of the mean displacement changes to  $\text{eMSD}(t) = \frac{4}{\sqrt{\pi}}D_{1/2}t^{1/2}$ , where the mobility factor  $D_{1/2}$  ( $[D_{1/2}] = \text{m}^2\text{s}^{-1/2}$ ) is introduced<sup>11–13,20,21</sup>. This theoretical prediction has been experimentally validated through microrheology studies in zeolites<sup>12,22</sup>, confined colloidal systems<sup>13</sup>, and water uptake in carbon nanotubes<sup>23</sup>.

To derive a scaling relation between the eMSD and the exchange, we evaluate the evolution of the particle concentration. Assuming the interface instantaneously equilibration to  $c_{\text{ext}}$ , and that  $\lim_{x \rightarrow \infty} c(x, t) = c_0$ , the concentration profile along  $x$  is obtained by solving Eq. 9.4 with  $\theta(x, t) = \frac{c(x, t) - c_0}{c_{\text{ext}} - c_0}$ . As shown in the reference<sup>24</sup>, the solution is

$$\theta(x, t) = W_{-\frac{\alpha}{2}, 1} \left( \frac{-x}{\sqrt{Dt^\alpha}} \right) \quad (9.6)$$

where  $W$  is the Wright function

$$W_{\nu, \beta}(z) = \sum_{n=0}^{\infty} \frac{z^n}{n! \Gamma(\nu n + \beta)} \quad (9.7)$$

This solution results valid for short times, i.e. if  $L \gg \sqrt{Dt^\alpha}$ . Defining  $\theta(x, t) = \frac{c(x, t) - c_0}{c_{\text{ext}} - c_0}$  and assuming  $L \gg \sqrt{Dt^\alpha}$ , we obtain

$$c(x, t) = c_0 + (c_{\text{ext}} - c_0) W_{-\frac{\alpha}{2}, 1} \left( \frac{-x}{\sqrt{Dt^\alpha}} \right) \quad (9.8)$$

In the limiting case of  $\alpha = 1$  the established relation for a Fickian diffusion in a semi-infinite domain is recovered:

$$c(x, t) = c_0 + (c_{\text{ext}} - c_0) W_{-\frac{1}{2}, 1} \left( \frac{-x}{\sqrt{Dt}} \right) = c_0 + (c_{\text{ext}} - c_0) \operatorname{erfc} \left( \frac{-x}{\sqrt{4Dt}} \right) \quad (9.9)$$

Subsequently, the tracer exchange is quantified via

$$\gamma(t) = \gamma_0 + \frac{1}{L} \int_0^L c(x, t) dx \quad (9.10)$$

and, as shown by Metzler et al.<sup>20</sup>, this exchange scales according to

$$\gamma(t) - \gamma_0 \sim \frac{c_{\text{ext}} - c_0}{\Gamma \left( 1 + \frac{\alpha}{2} \right)} t^{\frac{\alpha}{2}} \quad (9.11)$$

proving Eq. 9.1 is universally valid for diffusive and subdiffusive systems. Consequently, the exchange rate can be effectively used as a proxy to monitor the ensemble-averaged mean-square displacement. This conclusion is robust even when exchange occurs simultaneously at both boundaries, provided that the two concentration fronts remain non-interacting. Moreover, it is necessary to state that the use of a generalized diffusivity to model a solid crystal is justified by the assumption of ideal solid solution, where only excluded volume effects are present in the lattice. In these cases, a constant chemical diffusivity can be assumed, and the tracer diffusivity scales with the vacancy concentration<sup>10</sup>. In case of a lower filling fraction of the lattice, ion-vacancy and ion-ion interactions might modify the diffusion kinetics, for example, leading to phase separation. For these cases, no analytical approximation can be derived.

## 9.2 SUBDIFFUSION IN ${}^6\text{Li}$ - ${}^7\text{Li}$ EXCHANGE

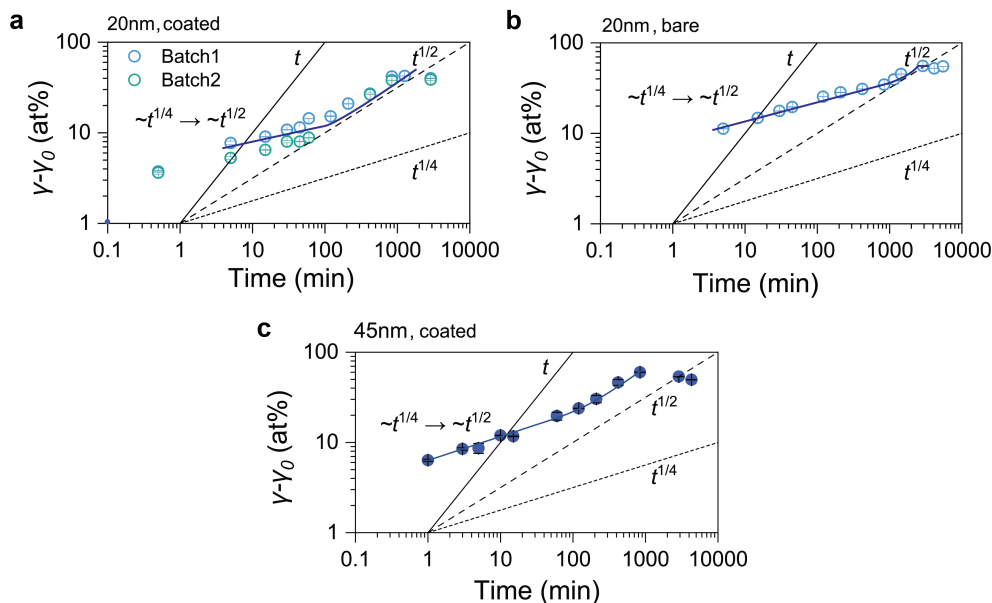


**Figure 9.2. Non-Faradaic  ${}^6\text{Li}$ - ${}^7\text{Li}$  exchange.** Logarithmic plot of  ${}^6\text{Li}$  tracer atomic ratio change ( $\gamma - \gamma_0$ ) over time during  ${}^6\text{Li}$ - ${}^7\text{Li}$  exchange in different batches of LFP particles: carbon-coated 20nm particles (blue open circles for Batch 1, green open circles for Batch 2) (a); bare 20nm particles without carbon coating (b); carbon-coated 45nm particles (c). The solid blue line is to guide the eye. Error bars in (a-c) represent the standard deviation of three replicate measurements.

9

For a tracer exchange measurement (Fig. 9.2), we used Inductively Coupled Plasma Mass Spectrometry (ICP-MS) to track the compositions ( ${}^6\text{Li}$ , and  ${}^7\text{Li}$  atomic ratios) of the particles over time after soaking them in 1M LiCl(aq), containing 94.8%  ${}^6\text{Li}$  and 5.2%  ${}^7\text{Li}$  (See Methods for preparation details). Since high-purity  ${}^7\text{LiOH}\cdot\text{H}_2\text{O}$  with 6.7%  ${}^6\text{Li}$  is used to synthesize all LFP particles;  ${}^6\text{Li}$  in the external reservoir serves as a tracer in our system (Table S1). The entire process is non-Faradaic, with no electron flow or applied potential. Two distinct particle batches with 20 nm, 45 nm, [010] diffusion channel lengths were synthesized using previous recipes<sup>45</sup> (Figs. 9.1d and Figs. S1-S2), followed by the surface carbon-coating treatment under calcination on a portion of the 20 nm batch (See Methods for more synthesis details). Rietveld refinement indicates low anti-site defect levels for all three particles (Fig. S3 and Table S3). We used two types of particles due to their distinct surface-to-volume ratios, affecting their reaction kinetics and subsequently ion exchange dynamics.

As shown in Fig. 9.2, subdiffusion behavior with a  $\sim t^{1/4}$ -time dependence is observed for all particle types investigated. The observed  $t^{1/4}$  time dependence is so confirming the presence of SFD dynamics in these olivine structures. Subsequently, the exchange exhibits a transition from  $t^{1/4}$  to  $t^{1/2}$  time dependence, ultimately recovering Fickian behavior in all the samples. The crossover between SFD and Fickian regime is expected in finite systems, where sustained anomalous diffusion is not possible<sup>25</sup>. In our case, the transition can arise from occasional particle-passing events, which disrupt particle ordering and break the single-file constraint<sup>37</sup>. As a result, dynamics shift from genuine SFD ( $t^{1/4}$  scaling) toward ordinary diffusion ( $t^{1/2}$  scaling). The sustained initial  $t^{1/4}$  slope in our data indicates a low passage rate, while at longer times, the collective motion of the isotopic ensemble dominates the exchange and follows an ordinary diffusion behavior, as predicted by theoretical results<sup>26</sup>.

### 9.3 KINETIC MONTE CARLO SIMULATIONS

To quantitatively and microscopically understand the observed  ${}^6\text{Li}$ - ${}^7\text{Li}$  subdiffusion behavior, we used KMC simulations with realistic constraints to explore the effects of various processes involved. The KMC methodology is based on defining a set of possible events and relative frequencies. Using a random number generator, an event is selected, with a probability proportional to its frequency. Updating the state of the system based on the selected event and the simulation time, depending on the total weighted frequency, the algorithm can predict the kinetics of the described physical system.

The `kmcoss` software<sup>27</sup> was used to implement the system based on the following steps (Fig. 9.3a):

- *Lattice setup.* A two-dimensional square lattice of  $66 \times 20$  positions is created to reproduce a section of a 20 nm thick particle. A fraction of lattice positions is filled in a set of random locations. The defect concentration was estimated from the delivered capacity and [010] diffusion channel length<sup>55</sup>, yielding a defect concentration of  $\sim 3\%$ . The remaining part of the lattice is filled with vacancies (0.1 %),  ${}^6\text{Li}$  and  ${}^7\text{Li}$  according to the experimental initial ratio.
- *Electrolyte reservoir.* An electrolyte reservoir is defined by placing two additional columns at the left and right boundaries. These columns are filled with the “electrolyte” specie. The electrolyte is composed of 94.8%  ${}^6\text{Li}$  and 5.2%  ${}^7\text{Li}$ , so that the probability of each species of being adsorbed during an adsorption event is equal to the electrolyte composition.

- *Surface exchange.* A surface exchange rate ( $\Gamma_S$ ) is defined at the right and left boundaries, dictating the surface exchange between the electrolyte and the atoms at the surface of the particle. To ensure mass conservation the probability of an ion being adsorbed on the surface must be equal to the probability of it being desorbed. To do so we define the adsorption probability of the species  $i$  as  $\Gamma_{ads,i} = p_i \Gamma_S (1 - d - v)$  and the desorption probability as  $\Gamma_{des} = \Gamma_S v$ ; where  $v$  is the vacancy concentration and  $d$  is the defect concentration.
- *Bulk diffusion.* A bulk diffusion rate ( $\Gamma_B$ ) is defined for the Li ions in the lattice. This rate assigns the hopping frequency of an ion between its position and a neighbor's empty position, along the [010] channel (horizontal direction). Ions can only jump into vacant sites. If a defect is present, the jump is prohibited.
- *Cross-channel defect-assisted hopping.* A cross-channel defect-assisted jump frequency ( $\Gamma_C$ ) is defined as the frequency of an ion jumping along the [001] direction (vertical direction in our lattice) when a defect is present. This is done since it has been shown that the presence of defects, while blocking the [010] diffusion, allows for a cross-channel<sup>16,28</sup>. Given an ion, if a defect is present on its right or left, and if the position below or above the defect is a vacancy, the ion can jump in that direction.

Having defined the model, we proceed with the estimation of the unknown parameters. The bulk diffusivity of Li was assumed to be within reasonable values from the literature ( $\Gamma_B \sim 10^4 - 10^5 \text{ s}^{-1}$ ). The surface exchange of the bare LFP sample has the bulk exchange as upper bound. This allowed to reduce the parameter space and fit the experimental data by using  $\Gamma_B = 10^5 \text{ s}^{-1}$  and  $\Gamma_S = 10^3 \text{ s}^{-1}$  on the bare sample. The surface exchange was then reduced for the carbon-coated case, and it was found to be  $\Gamma_S = 10^2 \text{ s}^{-1}$ , by carefully fitting the early-times data ( $< 10$  minutes). The cross-channel defect-assisted diffusion  $\Gamma_C = 1 \text{ s}^{-1}$  was eventually fitted to fit the late-times data ( $> 100$  minutes), with higher or lower values showing different crossover times (Fig. S6). These values correspond to a cross-channel activation barrier of 0.71 eV (See Supplementary Information for calculation details), and align well with DFT-computed Li-vacancy self-diffusivity along [010] channels ( $10^{-11} \sim 10^{-10} \text{ cm}^2 \text{ s}^{-1}$ )<sup>16</sup> and a cross-channel vacancy diffusion activation barrier of 0.7 ~ 0.8 eV under a concerted Li ions diffusion manner<sup>28</sup>. Therefore, in this system, while Li-Fe anti-site defects impede  $\text{Li}^+$  hopping along the channel, they allow for cross-channel hopping by lowering the average cross-channel activation barrier<sup>16,28,29</sup>.

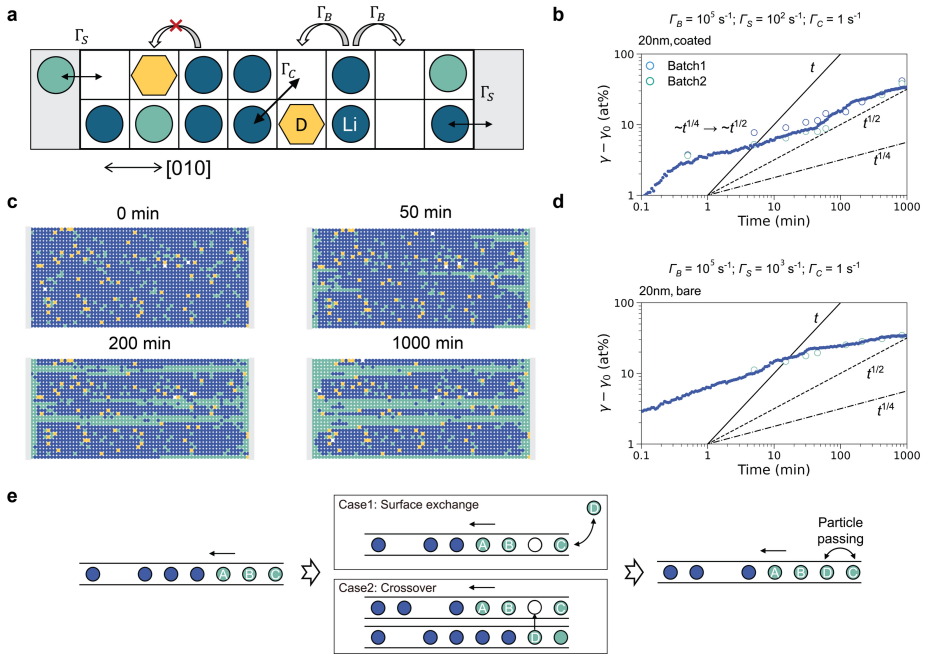


**Figure 9.3. KMC simulations results.** a) Illustration of events in the KMC simulation: Each square box represents a Li site in the channel, with  $^7\text{Li}$  ions shown as dark blue circles and  $^6\text{Li}$  ions as light green circles. The gray space outside the boxes represents the electrolyte. b) Logarithmic plot of  $^6\text{Li}$  tracer atomic ratio change ( $\gamma - \gamma_0$ ) over time during  $^6\text{Li}$ - $^7\text{Li}$  exchange in carbon-coated 20nm particles. The small solid blue dots represent  $^6\text{Li}$  tracer exchange obtained from KMC simulations. c) Snapshots of KMC simulations for carbon-coated 20nm particles during ion exchange at various times with  $^7\text{Li}$  ions (dark blue),  $^6\text{Li}$  ions (light green), and defects (yellow). d) Logarithmic plot of  $^6\text{Li}$  tracer atomic ratio change ( $\gamma - \gamma_0$ ) over time during  $^6\text{Li}$ - $^7\text{Li}$  exchange in bare 20nm particles. The small solid blue dots represent  $^6\text{Li}$  tracer exchange obtained from KMC simulations. e) Schematics showing atomistic origins of ion passage events due to surface exchange or cross-channel diffusion.

The KMC simulations were able to capture the SFD dynamics for 20nm particles with and without carbon coating, as shown in Fig. 9.3b-3d. The results of the KMC model can so provide insight into key features of the experimental results. Initially,  $^6\text{Li}$ - $^7\text{Li}$  exchange is dominated by surface interactions between the particle and the reservoir. After  $\sim 5$  mins, surface concentrations equilibrate with the reservoir, as also highlighted by the strong sensitivity of  $\Gamma_S$  in the early time regime (Fig. 9.4). The kinetics then enter an SFD regime, where defect-free channels exchange Li isotopes through double open boundaries. This one-dimensional, volume-excluded diffusion follows a characteristic  $1/4$  time dependence. Finally, once the defect-free channels are exchanged ( $\sim 200$  minutes; Fig. 9.3c), defect-assisted cross-channel diffusion ( $\Gamma_C$ ) becomes the main exchange driver, shifting the process toward 2D Fickian diffusion with a  $1/2$

time dependence. This shift is also evident from the influence of  $\Gamma_C$  on the  $1/4$  to  $1/2$  scaling transition (Fig. S6).

The KMC simulations clearly demonstrate that the transition from  $1/4$  to  $1/2$  arises from particle-passing events. Specifically, in our system, both surface exchange ( $\Gamma_S$ ) and cross-channel diffusion ( $\Gamma_C$ ) can enable such events (Fig. 9.3e), but our simulations indicate that defect-assisted cross-channel hopping is the primary factor (Fig. S6). As previously reported<sup>16,29</sup>, the anti-site defects reduce ion mobility along the channels while enhancing intra-channel diffusivity. We can now conclude that these defects not only alter the effective ionic diffusivity of the system, but also the diffusion dynamics itself. An increased defect concentration drives the system away from SFD towards Brownian motion.

## 9.4 THE ROLE OF CARBON COATING ON THE REACTION KINETICS

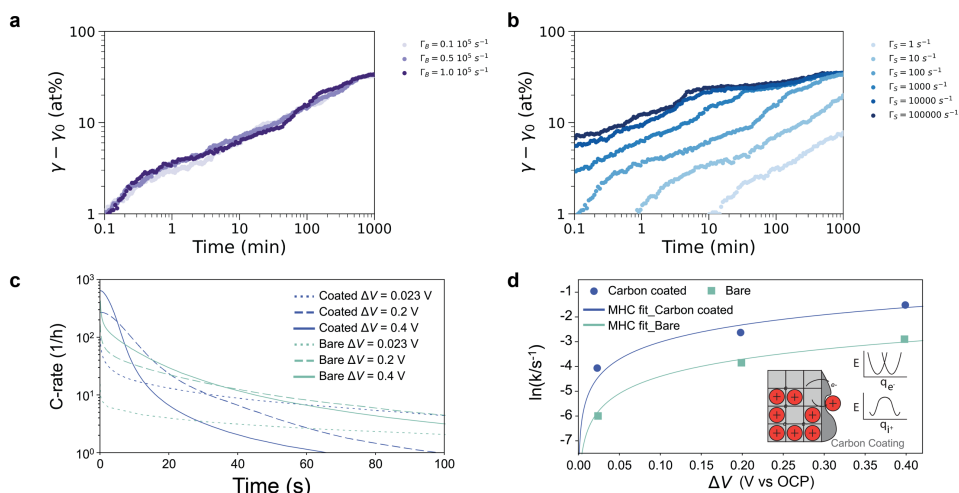


**Figure 9.4. Faradaic and non-Faradaic exchanges.** Effect of  $\Gamma_B$  (a) and  $\Gamma_S$  (b) on the KMC simulations of the  ${}^6\text{Li}$ - ${}^7\text{Li}$  exchange. The other parameters are kept the same as the ones described above for the carbon coated case:  $\Gamma_S = 10^2 \text{ s}^{-1}$ ,  $\Gamma_C = 1 \text{ s}^{-1}$ ;  $\Gamma_B = 10^5 \text{ s}^{-1}$ ,  $\Gamma_C = 1 \text{ s}^{-1}$ . c) Time evolution of the normalized current (C-rate) of bare and carbon-coated 20nm particles at various overpotentials. d) Tafel plot resulting from the chronoamperometry experiments and relative MHC fit. The schematic illustration shows the transition state energy landscape for electrons and ions.

Since the results of the KMC simulations are not particularly affected by the bulk exchange rate (Fig. 9.4a), while being strongly sensitive to the surface exchange frequency (Fig. 9.4b), we can use the obtained values to accurately quantify the non-Faradaic surface exchange rate  $\Gamma_S$  and decouple it from the Faradaic exchange rate, obtained with electrochemical experiments. Despite many studies show carbon-coated LFP having a higher exchange current densities ( $k_0$ ) under Faradaic conditions<sup>10,17,30</sup>, the bare particles exhibit faster isotopic exchange (higher  $\Gamma_S$ ) under non-Faradaic conditions. Specifically, we observe a two-order-of-magnitude higher  $\Gamma_S$  for bare particles, when compared to carbon-coated particles. This apparently inconsistent behavior can be explained if the electrochemical reaction kinetics is analyzed under the lens of coupled ion-electron transfer theory (CIET)<sup>17</sup>. This theory adds the electron transfer step to the common ionic-based transition state theory for electrochemical reactions (e.g. Butler-Volmer kinetics). Considering this theory, we can therefore assume that the observed limited electrochemical performances of the bare sample are attributed to the lack of electron transfer events at the particle's surface. In fact, the bare particles achieve only  $\sim 130$  mAh/g capacity during 17 mA/g cycling in 1M LiCl(aq) (Fig. S5; See Methods for more electrode preparation details).

To further investigate and quantify the difference between Faradaic and non-Faradaic phenomena (i.e., ion transfer and CIET) we performed chronoamperometry experiments on 20 nm particles w/wo carbon coating. Slurries composed of the 20 nm particles, carbon black, and polyvinylidene fluoride were drop-casted on a carbon paper current collector (See Methods). Constant voltage charging was applied at three different overpotentials ( $\Delta V = 0.023$  V, 0.2 V, 0.4 V) until a cutoff current of C/50 was reached. The obtained current evolution during time (Fig. 9.4c) allows for the quantification of the Faradaic exchange rate  $k(\Delta V)$ . The relation between the exchange rate and the overpotential was fitted by using Marcus-Hush-Chidsey (MHC) model<sup>31,32</sup>, yielding values of  $k_{0,bare} = 0.12 \text{ s}^{-1}$  and  $k_{0,coated} = 0.49 \text{ s}^{-1}$  for bare and carbon-coated particles, respectively (Fig. 9.4d; See Supplementary Information for calculations details). The fourfold higher rate observed for the carbon-coated particles suggests that bare particles only utilize a fraction of their reactive surface area. Specifically, since the MHC kinetic is still observed, we speculate they interact with the regions in direct contact with conductive carbon within the microstructure. On the contrary, if the bare LFP surface was the main driver of the reaction, a Marcus kinetics would manifest in the polarization<sup>33</sup>.

Additionally, the CIET theoretical framework allows us to assess the relative contributions of Faradaic and non-Faradaic mechanisms to the exchange frequency (see Supplementary Information). Based on the theory, we find the following relation:

$$k_0 = \frac{\Delta_e \Gamma_S}{h v_s} f(c, \lambda) \quad (9.12)$$

where  $\nu_s$  is the attempt frequency of the ions,  $\hbar$  is the Planck constant,  $\Delta_e/\hbar$  is relating to the quantum tunneling rate of electrons<sup>17</sup> and  $f(c, \lambda)$  is a function of the solid filling fraction  $c$  and reorganization energy  $\lambda$  in the Faradaic process. Inserting  $\Gamma_S = 10^2 \text{ s}^{-1}$  from the carbon-coated particles, we can reach  $k_0 \sim 0.48 \text{ s}^{-1}$ , by considering  $\Delta_e \sim 10^{-3} \text{ eV}$  for weakly adiabatic transition,  $\nu_s \sim 10^{12} \text{ s}^{-1}$  in the range of phonon frequency<sup>16</sup>,  $\lambda = 213 \text{ meV}$ <sup>31</sup>, and an average filling fraction of 0.5. The strong agreement between the predicted and the measured exchange frequency further validates the theoretical framework, also confirming how the reaction in the bare particles occurs predominantly at the carbon-coated interfaces or through the surface areas in direct contact with the carbon black.

## 9.5 CONCLUSIONS

Conventional electrochemical techniques such as cyclic voltammetry, galvanostatic or potentiostatic titration, and electrochemical impedance spectroscopy are fundamentally rooted in diffusion models derived from Fick's law. Recent advancements have extended these frameworks by incorporating thermodynamic refinements, including activity coefficients that vary with concentration profiles and account for excluded-site effects<sup>31,34</sup>. However, these models still fail to capture the distinct time evolution characteristic of SFD. The reason lies in the assumption of independent and overlapping particle motion, which has long dominated the interpretation of transport phenomena in electrochemical systems. However, this assumption breaks down in solid-state ionic conductors, where strong steric constraints prevent ion bypassing and give rise to complex, non-Fickian dynamics. Despite its relevance, this regime remains underexplored; even in well-studied materials like LFP.

Our study reveals pronounced non-Fickian ion diffusion of Li in FePO<sub>4</sub> hosts, where conventional Fickian models fail to capture the emergent behavior arising from confined, single-channel diffusion pathways. By employing a simple and reproducible technique, monitoring non-Faradaic ion exchange, we are able to probe the complex kinetics of the system, capturing the interplay between surface exchange, bulk, and diffusivities. Combined with KMC simulations, the analysis allows us to extract key material parameters, such as surface exchange rates and cross-channel hopping frequencies. Altogether, this methodology provides a powerful framework for understanding and controlling ionic diffusion in solids. Additionally, while carbon coating suppresses ionic surface exchange, it is essential for facilitating electron transfer across the interface, establishing interfacial electron transport as a critical rate-limiting factor in Faradaic processes.

More broadly, this study underscores the need to revisit diffusion frameworks in solid-state systems where confinement governs transport behavior. The methodological approach

presented here offers a foundation for dissecting ion transport in a wide range of solid-state systems, informing the development of next-generation technologies for energy storage, catalysis, and ion separation.

## MATERIALS AND METHODS

Preparation of 1 M  ${}^6\text{LiCl}(\text{aq})$  solution. The 150 ml of 2 M  ${}^6\text{LiOH}(\text{aq})$  was prepared as follows: 0.3 mol of  ${}^6\text{Li}$  metal (Cambridge Isotope Laboratories, 95 at%  ${}^6\text{Li}$ , 5 at%  ${}^7\text{Li}$ ) was brushed and weighed inside a glovebox to prevent oxidation. The  ${}^6\text{Li}$  metal was then quickly transferred into refrigerated deionized (DI) water (4°C) in an ice bath to generate  ${}^6\text{LiOH}(\text{aq})$ . The resulting solution was then transferred into a 150 ml volumetric flask, and the volume was adjusted with additional DI water. Concentrated  $\text{HCl}(\text{aq})$  (Sigma-Aldrich, 37 wt%  $\text{HCl}$ ) was then added dropwise to the prepared 2 M  $\text{LiOH}(\text{aq})$  in an ice bath until a neutral pH was reached. The final mixture was transferred to a 300 ml volumetric flask, and the volume was adjusted with additional DI water, yielding 1 M  ${}^6\text{LiCl}(\text{aq})$ . The composition was verified with ICP-MS (Supplementary Table 1), confirming a  ${}^6\text{Li}$  abundance of  $94.8 \pm 0.1$  at%, consistent with the provided purity.

Synthesis of 20nm/45nm- $\text{Li}_{1.0}\text{FP}$  particles. All three pristine  $\text{LiFePO}_4$  particles with different sizes were synthesized using a solvothermal method, following previously reported recipes<sup>35</sup>. After the solvothermal synthesis, all pristine  $\text{LiFePO}_4$  particles followed the same washing, carbon coating process described in the following. Specifically, the obtained  $\text{LiFePO}_4$  precipitates were centrifuged three times with deionized water and ethanol, followed by 60 °C drying overnight. To increase the electronic conductivity of the particles, surface carbon coating is utilized. The carbon coating procedure involved amalgamating pristine  $\text{LiFePO}_4$  with sucrose (as the carbon source) in a mass ratio of 5:1 ( $\text{LiFePO}_4$ : sucrose). The mixture was first calcinated in an Ar atmosphere at 200 °C for 0.5 h, followed by heating to 550 °C for 2.5 h. The heating rate was 3 °C  $\text{min}^{-1}$ . For the preparation of 20nm- $\text{Li}_{1.0}\text{FP}$  particles without carbon coating, the pristine 20nm- $\text{Li}_{1.0}\text{FP}$  particles were annealed under the same condition described above without mixing with sucrose.

Preparation of electrodes. All  $\text{LiFePO}_4$  electrodes were prepared by casting a slurry of  $\text{LiFePO}_4$ , Super P carbon black (MTI Corporation; Item Number: Lib-SP; average particle size ~40 nm; purity  $\geq 99.5\%$ ), and polyvinylidene fluoride (MTI Corporation; Item Number: Lib-PVDF; purity  $\geq 99.5\%$ ) with a mass ratio of 80:10:10, in N-methyl-2-pyrrolidone. The working electrodes (~2.5  $\text{mg}/\text{cm}^2$ ) were prepared by drop casting the slurry on a  $0.5 \times 0.5 \text{ cm}^2$  geometrical surface of a carbon paper (TGP-H-060, Fuel Cell Earth, 190  $\mu\text{m}$  in thickness, 78% porosity) current collector of  $2.5 \times 0.5 \text{ cm}^2$ . The  $0.5 \times 0.5 \text{ cm}^2$  drop-casting area was cleaned with argon plasma at 100 watts for 1 minute before the drop-casting of the slurry. 30 wt% active material (annealed bare 20nm- $\text{Li}_{1.0}\text{FP}$ ), 65% wt% carbon black and 5 wt% binder are used to prepare slurry, with an average mass loading of ~200  $\mu\text{g}$ .  $\text{FePO}_4$  counter electrodes were made with the slurry using the same mass ratios depositing on carbon felt (Alfa Aesar) disks (0.9525

cm diameter  $\times$  3.18 mm thickness, around 240 g/m<sup>2</sup> in areal weight). The active material mass loading on the counter electrodes ranged between 60 and 70 mg cm<sup>-2</sup>. Li<sub>x</sub>FePO<sub>4</sub> counter electrodes were prepared electrochemically. Specifically, FePO<sub>4</sub> counter electrodes were galvanostatic lithiation in 1M LiCl(aq) at a C/20 (8.5 mA/g) rate until reaching a -0.6 V versus Ag/AgCl voltage cutoff. The larger mass loading of the counter electrode ensures we have enough ion stock in the counter electrode to avoid side reactions from water splitting or pH fluctuations. C/N describes the current to (de)intercalate the electrode in Nh.

Electrochemical methods. All electrochemical operations were performed on a Bio-Logic VMP3 workstation using a three-neck round-bottomed flask at room temperature (20 ~ 25 °C). N<sub>2</sub> (purity > 99.998%) was continuously bubbled into the solution to avoid side reactions caused by dissolved O<sub>2</sub>. To verify the quality and measure the accessible capacity of fabricated working electrodes, the working electrodes were cycled in 60 mL 1 M LiCl aqueous solutions (17 mA/g; paired with Li<sub>x</sub>FePO<sub>4</sub> counter electrodes) between -0.6 V and 0.6 V (vs. Ag/AgCl (sat. KCl)) at room temperature (20 ~ 25 °C) (Supplementary Fig. 9.5).

Chronoamperometry experiments. Before each voltage step, the working electrodes were discharged at C/10 to -0.6V (vs. Ag/AgCl (sat. KCl)) and allowed to relax for 4 hours to reach equilibrium. The reference voltage was determined by averaging the voltage plateaus of charge and discharge during the 17 mA/g cycle of both the coated and uncoated samples. A cutoff current of C/50 was applied for each step.

Inductively coupled plasma-mass spectrometry (ICP-MS) characterization. 3% HNO<sub>3</sub>(aq) was used as the diluting matrix for all the Li recovery solutions. The non-Faradaic ion exchanged particles were first washed 3-5 times with 60 ml fresh distilled water and then digested with an aqua regia solution for three days to ensure complete dissolution. The resulting supernatant was diluted with 3% HNO<sub>3</sub> for later ICP-MS measurement. All the measurements used either Thermo iCAP Q ICP-MS or Thermo iCAP RQ ICP-MS.

Scanning electron microscopy (SEM) characterization. Scanning electron microscopy (SEM, Zeiss Merlin) was performed at the accelerating voltage of 10 kV.

## REFERENCES

1. Famprikis, T., Canepa, P., Dawson, J. A., Islam, M. S. & Masquelier, C. Fundamentals of inorganic solid-state electrolytes for batteries. *Nat. Mater.* 18, 1278–1291 (2019).
2. Maier, J. Nanoionics: ion transport and electrochemical storage in confined systems. *Nat. Mater.* 4, 805–815 (2005).
3. Lavrinenko, A. K. *et al.* Optimizing ionic transport in argyrodites: a unified view on the role of sulfur/halide distribution and local environments. *J. Mater. Chem. A* 12, 26596–26611 (2024).
4. Famprikis, T. *et al.* A New Superionic Plastic Polymorph of the Na<sup>+</sup> Conductor Na<sub>3</sub>PS<sub>4</sub>. *ACS Mater. Lett.* 1, 641–646 (2019).
5. Sood, A. & others. Electrochemical ion insertion from the atomic to the device scale. *Nat. Rev. Mater.* (2021) doi:10.1038/s41578-021-00314-y.
6. Bui, K. M., Dinh, V. A. & Ohno, T. Diffusion Mechanism of Polaron–Li Vacancy Complex in Cathode Material Li<sub>2</sub>FeSiO<sub>4</sub>. *Appl. Phys. Express* 5, 125802 (2012).
7. Poletayev, A. D., Dawson, J. A., Islam, M. S. & Lindenberg, A. M. Defect-driven anomalous transport in fast-ion conducting solid electrolytes. *Nat. Mater.* 21, 1066–1073 (2022).
8. Jun, K., Chen, Y., Wei, G., Yang, X. & Ceder, G. Diffusion mechanisms of fast lithium-ion conductors. *Nat. Rev. Mater.* 9, 887–905 (2024).
9. Kanazawa, K., Sano, T. G., Cairoli, A. & Baule, A. Loopy Lévy flights enhance tracer diffusion in active suspensions. *Nature* 579, 364–367 (2020).
10. Bazant, M. Z. Theory of Chemical Kinetics and Charge Transfer based on Nonequilibrium Thermodynamics. *Acc. Chem. Res.* 46, 1144–1160 (2013).
11. Levitt, D. G. Dynamics of a Single-File Pore: Non-Fickian Behavior. *Phys. Rev. A* 8, 3050–3054 (1973).
12. Kärger, J., Petzold, M., Pfeifer, H., Ernst, S. & Weitkamp, J. Single-file diffusion and reaction in zeolites. *J. Catal.* 136, 283–299 (1992).
13. Lutz, C., Kollmann, M. & Bechinger, C. Single-File Diffusion of Colloids in One-Dimensional Channels. *Phys. Rev. Lett.* 93, 026001 (2004).
14. Li, Y. & others. Fluid-enhanced surface diffusion controls intraparticle phase transformations. *Nat. Mater.* 17, 915–922 (2018).
15. Cogswell, D. A. & Bazant, M. Z. Coherency Strain and the Kinetics of Phase Separation in LiFePO<sub>4</sub> Nanoparticles. *ACS Nano* 6, 2215–2225 (2012).
16. Malik, R., Burch, D., Bazant, M. & Ceder, G. Particle Size Dependence of the Ionic Diffusivity. *Nano Lett.* 10, 4123–4127 (2010).
17. Bazant, M. Z. Unified quantum theory of electrochemical kinetics by coupled ion-electron transfer. *Faraday Discuss.* 10.1039/D3FD00108C (2023) doi:10.1039/D3FD00108C.
18. Metzler, R., Klafter, J. & Sokolov, I. M. Anomalous transport in external fields: Continuous time random walks and fractional diffusion equations extended. *Phys. Rev. E* 58, 1621–1633 (1998).
19. Metzler, R. & Klafter, J. The random walk’s guide to anomalous diffusion: a fractional dynamics approach. *Phys. Rep.* 339, 1–77 (2000).
20. Metzler, R., Rajyaguru, A. & Berkowitz, B. Modelling anomalous diffusion in semi-infinite disordered systems and porous media. *New J. Phys.* 24, 123004 (2022).
21. Harris, T. E. Diffusion with “collisions” between particles. *J. Appl. Probab.* 2, 323–338 (1965).
22. Kukla, V. & others. NMR Studies of Single-File Diffusion in Unidimensional Channel Zeolites. *Science* 272, 702–704 (1996).
23. Berezhkovskii, A. & Hummer, G. Single-File Transport of Water Molecules through a Carbon Nanotube. *Phys. Rev. Lett.* 89, 064503 (2002).

24. Choudhary, A., Kumar, D. & Singh, J. Numerical simulation of a fractional model of temperature distribution and heat flux in the semi infinite solid. *Alex. Eng. J.* 55, 87–91 (2016).
25. Hartich, D. & Godec, A. Thermodynamic Uncertainty Relation Bounds the Extent of Anomalous Diffusion. *Phys. Rev. Lett.* 127, 080601 (2021).
26. Hahn, K. & Kärger, J. Deviations from the Normal Time Regime of Single-File Diffusion. *J. Phys. Chem. B* 102, 5766–5771 (1998).
27. Hoffmann, M. J., Matera, S. & Reuter, K. kmos: A lattice kinetic Monte Carlo framework. *Comput. Phys. Commun.* 185, 2138–2150 (2014).
28. Dathar, G. K. P., Sheppard, D., Stevenson, K. J. & Henkelman, G. Calculations of Li-Ion Diffusion in Olivine Phosphates. *Chem. Mater.* 23, 4032–4037 (2011).
29. Liu, H. & others. Effects of Antisite Defects on Li Diffusion in LiFePO<sub>4</sub> Revealed by Li Isotope Exchange. *J. Phys. Chem. C* 121, 12025–12036 (2017).
30. Zhao, H. *et al.* Learning heterogeneous reaction kinetics from X-ray videos pixel by pixel. *Nature* 621, 289–294 (2023).
31. Bai, P. & Bazant, M. Z. Charge transfer kinetics at the solid–solid interface in porous electrodes. *Nat. Commun.* 5, 3585 (2014).
32. Zeng, Y., Smith, R. B., Bai, P. & Bazant, M. Z. Simple formula for Marcus–Hush–Chidsey kinetics. *J. Electroanal. Chem.* 735, 77–83 (2014).
33. Fraggadakis, D. *et al.* Theory of coupled ion-electron transfer kinetics. *Electrochimica Acta* 367, 137432 (2021).
34. Ferguson, T. R. & Bazant, M. Z. Nonequilibrium Thermodynamics of Porous Electrodes. *J. Electrochem. Soc.* 159, A1967–A1985 (2012).
35. Yan, G. & others. Identifying critical features of iron phosphate particle for lithium preference. *Nat. Commun.* 15, 4859 (2024).

## SUPPLEMENTARY INFORMATION

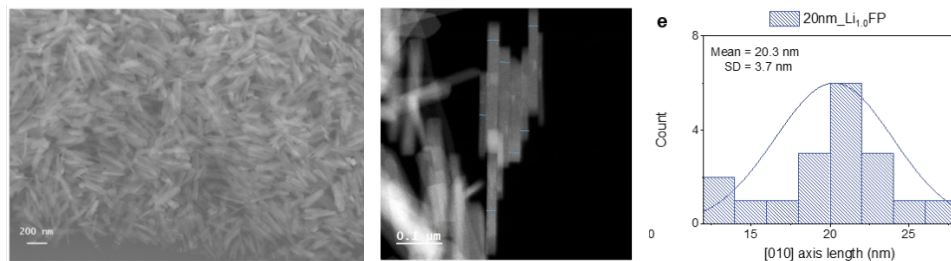


Figure S1. (a) SEM and (b) STEM images of the synthesized 20nm particles with corresponding particle dimension distribution along the (c) [101] axis, (d) [-101] axis, and (e) [010] axis. Only the isolated and fully exposed particles were counted; the thin lines in the SEM/STEM images denoted the measured length.

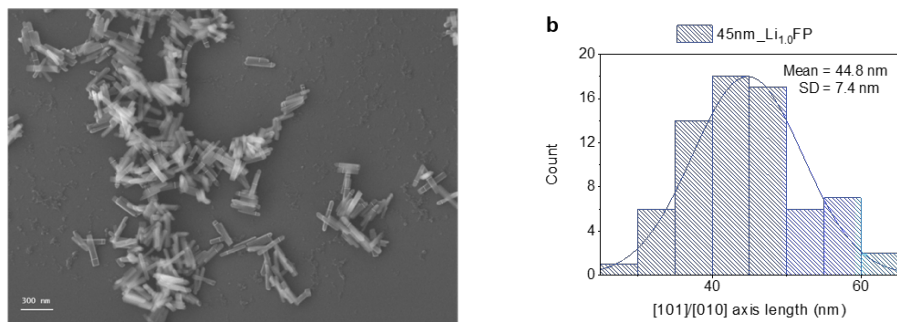


Figure S2. (a) SEM images of the synthesized 45nm particles with the corresponding particle dimension distribution along the (b) [101]/[010] axis, and (c) [-101] axis. Only the isolated and fully exposed particles were counted; the thin white lines in the SEM images denoted the measured length.

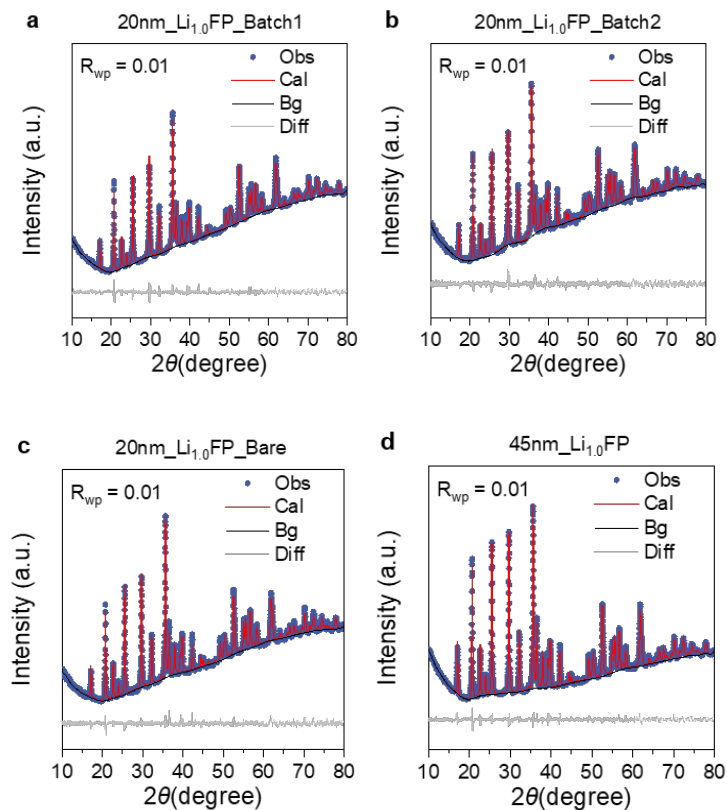


Figure S3. Rietveld refinement of (a) Carbon-coated 20 nm\_Batch1, (b) Carbon-coated 20nm\_Batch2, (c) 20nm\_Bare, (d) Carbon-coated 45nm.

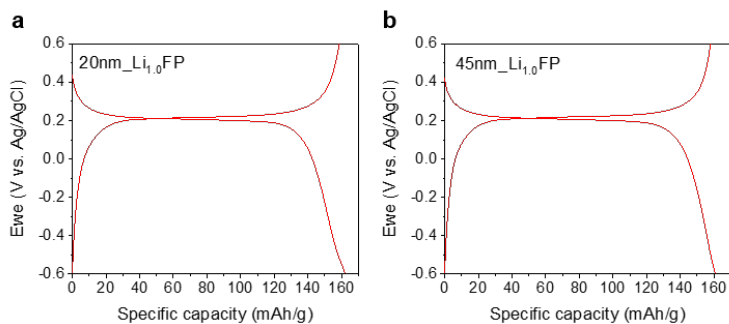


Figure S4. Electrochemical cycling of the carbon-coated particles in 60 mL 1 M LiCl aqueous solutions (17 mA/g; paired with  $\text{Li}_x\text{FePO}_4$  counter electrodes) between -0.6 V and 0.6 V (vs. Ag/AgCl (sat. KCl)) at room temperature. (a) 20nm\_Batch1, (b) 45nm.

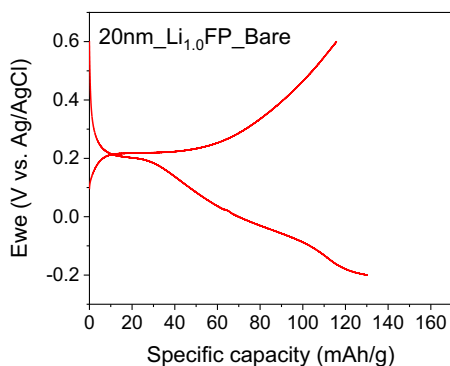


Figure S5. Electrochemical cycling of the bare 20nm\_Li<sub>1.0</sub>FP particles in 60 mL 1 M LiCl aqueous solutions (17 mA/g; paired with Li<sub>x</sub>FePO<sub>4</sub> counter electrodes) between -0.2 V and 0.6 V (vs. Ag/AgCl (sat. KCl)) at room temperature (20 ~ 25 °C).

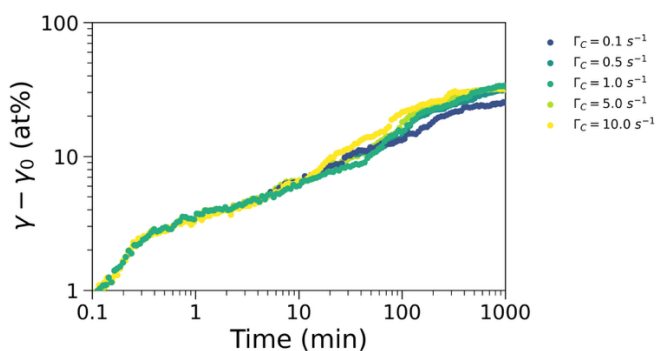


Figure S6. Effect of cross-channel exchange rate ( $\Gamma_C$ ) on the KMC simulations of the <sup>6</sup>Li-<sup>7</sup>Li exchange for the carbon-coated case.  $\Gamma_C$  influence the presence and timing of the transition to ordinary diffusion with  $\Gamma_C = 10 \text{ s}^{-1}$  showing the transition as  $\sim 10$  minutes, while  $\Gamma_C = 0.1 \text{ s}^{-1}$  saturating before reaching the transition time. The other parameters are kept the same as the ones described in the main text. Left:  $\Gamma_B = 10^5 \text{ s}^{-1}$ ,  $\Gamma_S = 10^2 \text{ s}^{-1}$ .

	${}^6\text{Li}$ abundance (at%)	${}^7\text{Li}$ abundance (at%)
1M ${}^6\text{LiCl(aq)}$	94.8 ± 0.1	5.2 ± 0.1

Table S1.  ${}^6\text{Li}$  and  ${}^7\text{Li}$  abundances of the prepared 1M  ${}^6\text{LiCl(aq)}$  and 1M  ${}^7\text{LiCl(aq)}$  solutions measured with ICP-MS. Error bars here represent the standard deviation of ICP-MS measurement.

	${}^6\text{Li}/({}^6\text{Li}+{}^7\text{Li})$ (at%)	${}^7\text{Li}/({}^6\text{Li}+{}^7\text{Li})$ (at%)
20nm_Batch1	6.7 ± 0.02	92.7 ± 0.04
20nm_Batch2	6.8 ± 0.07	92.5 ± 0.04
20nm_Bare	6.9 ± 0.06	92.7 ± 0.02

Table S2. Initial compositions of the investigated particles measured with ICP-MS. Error bars represent the standard deviation of three different electrodes in the same batch.

	20nm_Batch1	20nm_Batch2	20nm_Bare	45nm
a (Å)	10.302252	10.310223	10.307020	10.305038
b (Å)	5.998117	6.004354	5.999311	5.995944
c (Å)	4.693041	4.696314	4.689444	4.694987

$\alpha$	90
$\beta$	
$\gamma$	

Table S3 Fitted parameters from diffraction patterns in Supplementary Figure S3.

## Relationship between Li hopping rate, activation energy barrier, and Li diffusivity.

The Li hopping rate constant  $\Gamma$ , is related to Li free diffusion coefficient  $D$  via:

$$D = \frac{1}{2} \Gamma d^2 \quad (\text{E1})$$

where  $d$  is the distance between two hopping sites. For anti-site diffusion,  $d = 5.7 \text{ \AA}$ ; for diffusion in the same channel,  $d = 3.07 \text{ \AA}$ . The hopping rate constant is related to the activation energy barrier,  $E_a$ , according to transition state theory<sup>10,34</sup>:

$$\Gamma = \nu \exp\left(-\frac{E_a}{k_B T}\right) \quad (\text{E2})$$

where  $\nu$  is the attempt frequency, which is in the range of phonon frequencies  $10^{12} \text{ Hz}$ ,  $k_B$  is the Boltzmann constant and  $T$  is temperature.

## Parametrization of exchange current density based on chronoamperometry and Marcus–Hush–Chidsey model.

To obtain the reaction rate, we considered the current following an exponential decay:

$$I = I_0 e^{-k t} \quad (\text{E3})$$

where  $I_0$  is the initial current at  $t = 0$ ,  $k$  is the reaction rate, and  $t$  is the measured time. The rate constant can be found by considering the time requires by the system to reach  $I^*$ , that was set to 1% of  $I_0$ :

$$k = -\frac{\ln\left(\frac{I^*}{I_0}\right)}{t^*} \quad (\text{E4})$$

We proceeded in acquiring the reaction rate for both coated and bare particles, at three different overpotentials ( $\eta$ ): 0.025 V, 0.2 V, and 0.4 V. The reference voltage was the one obtained by considering the average between the voltage plateaus of charge and discharge of the 17 mA/g cycle of the coated sample. The obtained data were then fitted by the use of the Marcus–Hush–

Chidsey model as described by the work of Bai and Bazant<sup>31</sup>. The reaction rate can so be calculated as:

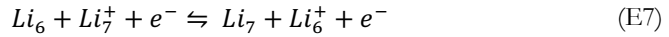
$$k = A \sqrt{\pi \lambda} \left( \frac{1}{1 + e^\eta} - \frac{1}{1 + e^{-\eta}} \right) \operatorname{erfc} \left( \frac{\lambda - \sqrt{1 + \sqrt{\lambda} + \eta^2}}{2\sqrt{\lambda}} \right) \quad (\text{E5})$$

where the reorganization energy  $\lambda$  is 213 meV<sup>31</sup> and  $A$  is the fitting parameter. Once  $A$  is fitted, the exchange current density can be taken as the limit for no overpotential:

$$k_0 = A \frac{\sqrt{\pi \lambda}}{2} \operatorname{erfc} \left( \frac{\lambda - \sqrt{1 + \sqrt{\lambda}}}{2\sqrt{\lambda}} \right) \quad (\text{E6})$$

### CIET framework for the estimation of the relation between the Faradaic and Non-Faradaic exchange.

The reaction for the Non-Faradaic case can be defined as



Let  $A$  denote  $Li_6$  and  $B$  denote  $Li_7$  then the driving for the reaction is given by,

$$\Delta G^{ex} = \mu_{A^+}^{ex} + \mu_B^{ex} - \mu_A^{ex} - \mu_{B^+}^{ex} = \mu_2^{ex} - \mu_1^{ex} = \eta_f \quad (\text{E8})$$

$$\Delta G_f^\ddagger = \mu^\ddagger - \mu_A^{ex} - \mu_{B^+}^{ex} \quad (\text{E9})$$

$$\Delta G_r^\ddagger = \mu^\ddagger - \mu_{A^+}^{ex} - \mu_B^{ex} \quad (\text{E10})$$

In the electrolyte phase, the chemical potentials are given by,

$$\mu_{i^+} = \mu_{i^+}^{ref} + \log(a_+) \quad (\text{E11})$$

Let  $\mu_1^{ex} = \mu_A^{ex} + \mu_{B+}^{ex}$  and  $\mu_2^{ex} = \mu_{A+}^{ex} + \mu_B^{ex}$ . The transition state excess chemical potential can be found by solving the intersection of  $\mu_1^{ex} = \mu_1^{ex}(\xi_1) + \beta(\xi - \xi_1)$  and  $\mu_2^{ex} = \mu_2^{ex}(\xi_2) + \beta(\xi_2 - \xi)$ . For  $\alpha = 0.5$ , the transition state (TS) would be half-way and  $\mu^\ddagger = \frac{\mu_1^{ex} + \mu_2^{ex}}{2} + \frac{\beta}{2}$ . The TS barriers for forward and reverse reactions become,

$$\Delta G_f^\ddagger = \frac{1}{2}(\Delta G^{ex} + \beta) \quad (E12)$$

$$\Delta G_r^\ddagger = \frac{1}{2}(-\Delta G^{ex} + \beta) \quad (E13)$$

For an attempt frequency of  $\nu_s$ , rate expression would be given by,

$$I = e\nu_s(\tilde{k}_f c_A c_{B+} - \tilde{k}_r c_{A+} c_B) \quad (E14)$$

Where the forward and backward rates are given by,

$$\tilde{k}_f = \frac{e^{-\Delta G_f^\ddagger}}{\gamma^\ddagger} \quad (E15)$$

$$\tilde{k}_r = \frac{e^{-\Delta G_r^\ddagger}}{\gamma^\ddagger} \quad (E16)$$

The transition state may be assumed to occupy  $n$  sites for which the  $\gamma^\ddagger = \frac{1}{\nu^n}$ , where  $\nu = 1 - c_A - c_B$  is the vacancy transition. Accordingly, the final rate expression becomes,

$$I = e\nu_s \nu^n (e^{-\Delta G_f^\ddagger} c_{B+} c_A - e^{-\Delta G_r^\ddagger} c_{A+} c_B) \quad (E17)$$

$$I = e\nu_s \nu^n e^{-\beta/2} (e^{-\eta_f/2} c_{B+} c_A - e^{\eta_f/2} c_{A+} c_B) \quad (E18)$$

Using  $\eta_f = \eta - \log\left(\frac{c_{A+} c_B}{c_B c_{A+}}\right)$ , we have,

$$I = e\nu_s \nu^n e^{-\beta/2} \sqrt{c_A c_B c_{A+} c_{B+}} (e^{-\eta/2} - e^{\eta/2}) \quad (E19)$$

$$R_{exch} = \frac{I}{e} = \nu_s e^{-\beta/2k_B T} (1 - c_A - c_B)^n \sqrt{c_A c_B c_{A+} c_{B+}} \quad (E20)$$

In KMC we converge the activation energy and the attempt frequency in one term so that,

$$R_{exch} = \Gamma_s (1 - c_A - c_B)^n \sqrt{c_A c_B c_{A+} c_{B+}} \quad (E21)$$

Resulting in

$$e^{-\beta/2k_B T} = \Gamma_s / v_s \quad (E22)$$

In contrast to this, the Faradaic case of CIET of (de)intercalation at LFP is,

$$R_{CIET} = \frac{\Delta_e}{h} e^{-\frac{\beta}{2k_B T}} (1 - c) \frac{c c_+}{c + c_+} \operatorname{erfc} \left( \frac{\lambda - \sqrt{1 + \sqrt{\lambda} + \ln^2 \left( \frac{c_+}{c} \right)}}{2\sqrt{\lambda}} \right) \quad (E23)$$

So that

$$R_{CIET} = \frac{\Delta_e \Gamma_s}{h v_s} (1 - c) \frac{c c_+}{c + c_+} \operatorname{erfc} \left( \frac{\lambda - \sqrt{1 + \sqrt{\lambda} + \ln^2 \left( \frac{c_+}{c} \right)}}{2\sqrt{\lambda}} \right) \quad (E24)$$

The CIET reaction rate is in general concentration dependent, but the PITT results, being an analytical approximation neglect this factor. The obtain  $k_0$  is so considered to be the one occurring at  $c = 0.5$ . Neglecting also the deviation of the electrolyte concentration ( $c_+ = 1$ ), we obtain

$$k_0 = \frac{\Delta_e \Gamma_s}{h v_s} 0.16 \operatorname{erfc} \left( \frac{\lambda - \sqrt{1 + \sqrt{\lambda} + \ln^2(0.5)}}{2\sqrt{\lambda}} \right) \quad (E25)$$

$$k_0 = \frac{\Delta_e \Gamma_s}{h v_s} 0.16 * 0.12 \quad (E26)$$

If  $\Delta_e = 1 \text{ meV}$  and  $v_s = 10^{12} \text{ s}^{-1}$

$$k_0 = \frac{10^{-3}}{4} \frac{10^2}{10^{-15}} \frac{10^2}{10^{12}} 0.16 * 0.12 = 0.48 \text{ s}^{-1} \quad (E27)$$



# LIST OF PUBLICATIONS

1. Ombrini P, Bazant MZ, Wagemaker M, Vasileiadis A. Thermodynamics of multi-sublattice battery active materials: from an extended regular solution theory to a phase-field model of  $\text{LiMnyFe1-yPO}_4$ . *npj Comput Mater*. 2023 Aug 21;9(1):148.
2. Schwietert TK, Ombrini P, Ootes LS, Oostrum L, Azizi V, Cogswell D, et al. Phase-Field Computational Framework for Addressing Challenges in Solid-State Batteries. *PRX Energy*. 2023 Sep 12.
3. Li Y, Vasileiadis A, Zhou Q, Lu Y, Meng Q, Li Y, Ombrini P, Zhao J, Chen Z, Niu Y, Qi X. Origin of fast charging in hard carbon anodes. *Nature Energy*. 2024 Feb;9(2):134-42.
4. Karanth P, Weijers M, Ombrini P, Ripepi D, Ooms F, Mulder FM. A phase inversion strategy for low-tortuosity and ultrahigh-mass-loading nickel-rich layered oxide electrodes. *Cell Reports Physical Science*. 2024 May;101972.
5. Wang Q, Zhao C, Wang S, Wang J, Wu F, Ombrini P, et al. Interphase Design for Lithium-Metal Anodes. *J Am Chem Soc*. 2025 Mar 19;147(11):9365–77.
6. Ombrini P, Wang Q, Vasileiadis A, Wu F, Gao Z, Hu X, van Hulzen M, Li B, Zhao C, Wagemaker M. Kinetically induced memory effect in Li-ion batteries. *EES Batteries*. 2025.
7. Karanth P, Prins JH, Gautam A, Cheng Z, Canals-Riclot J, Ganapathy S, et al. Multifunctional ion-conductive polymer coatings for high-performance sulfide solid-state batteries with Ni-rich cathodes. *J Mater Chem A*. 2025.
8. Ombrini P, Vasileiadis A, Wagemaker M. The Influence of Open Circuit Potential on Electrode Dynamics. *Journal of The Electrochemical Society*. 2025.

9. Ombrini P, Pathak S, Ntagkras D, Pal SK, Karanth P, Mulder FM, Wagemaker M, Bazant MZ, Vasileiadis A. Modeling Single-Crystal Electrodes as a Network of Primary Particles. *Energy and Environmental Science*. 2025.
10. Coppola R, Touloujian H, Ombrini P, Mazo J M. Reinforcement Learning for Robust Ageing-Aware Control of Li-ion Battery Systems with Data-Driven Formal Verification. *Under review*.
11. Yan G<sup>†</sup>, Ombrini P<sup>†</sup>, Tang Z, Pathak P, Wang M, Lavina B, Vasileiadis A, Choi S, Wang M, Ying D, Li Q, Alp EE, Zhou H, Bazant MZ, Chen Q, Wagemaker M and Liu C. Crossover Dynamics of Non-Fickian Ionic Diffusion in Solids. *Under Review*.

# CURRICULUM VITAE

Pierfrancesco Ombrini was born in Correggio, Italy, on December 8, 1996. He began his studies in 2015 with a bachelor's degree in Materials and Nanotechnology Engineering at Politecnico di Milano. He graduated in 2018 with a grade of 109/110, completing a thesis titled "Production and Characterization of Nanostructured Substrates for SERS Applications." During this work, he discovered a stronger interest in theoretical rather than experimental topics.

Motivated by his passion for physics, he pursued a master's degree in Nuclear Engineering at Politecnico di Milano, which he completed, this time, with 110/110 cum laude in April 2021. During the program, he joined the student council, contributing to student engagement and the improvement of course quality. He also took part in public outreach activities to explain the principles of nuclear engineering and the basics of energy systems, which gave him a broader perspective on the challenges of the energy transition. At the same time, he developed a strong interest in statistical mechanics, appreciating its ability to describe diverse and complex phenomena within a unified framework. To connect this interest with his goal of contributing to the energy transition, he focused his master's thesis on renewable energy conversion, titled "Thermally Rechargeable Supercapacitors: Modeling and Simulation of the Seebeck Effect in Electrolytes." This research was conducted under the supervision of Prof. Roberto Piazza (Politecnico di Milano) and Prof. René van Roij (Utrecht University). The project further confirmed his enthusiasm for theory, modeling, and scientific research.

In September 2021, he began a PhD at TU Delft in the Storage of Electrochemical Energy (SEE) group, supervised by Prof. Marnix Wagemaker and Dr. Alexandros Vasileiadis. His research focuses on the development of mesoscale models for simulating battery electrodes based on lithium iron phosphate. To expand his knowledge, he spent four months (October 2023–January 2024) visiting the Bazant group at MIT. Alongside his modeling work, he contributed to experiments and data analysis using Neutron Depth Profiling and broadened his computational expertise to include Kinetic Monte Carlo modeling. Consistent with his earlier experiences, he joined the PhD council, helping to improve doctoral programs by facilitating communication between candidates and the Graduate School.

# ACKNOWLEDGEMENTS

At the start of my PhD journey, I had barely explored the world of electrochemistry. In my Master's thesis I had only worked on supercapacitors, scared of investigating what goes beyond a potential threshold: the electrochemical reaction. That is why I want to begin by thanking my supervisors, Marnix and Alex, for believing in me despite my unusual background in nuclear engineering. Ever since the first days, they guided me, suggesting impactful research directions, while also allowing my independent exploration of interesting topics. A special thanks to Alex, for listening to all my random ideas, popping out almost on a weekly basis. With their guidance I learned to distinguish between what *can* be done and what is *important* to do: lots of projects can be defined and executed, but only few are worth it. I also want to thank Nicola, the company supervisor of my project, whose external and practical perspective helped me understand what really matters in today's battery world. And I'm grateful to Lars and Michel, for giving me confidence in first uncertain days of neutron experiments.

Deep gratitude also goes towards my colleagues; Victor, Mark, Swapna, Xuchang, Erik, Zhu, Lucas, Meera, Mark, Shengnan, Peter, Biffo, Tian, Rijk, Martijn, Remco, Alber, Xavier, Anastasiia, Luca, Meng-Fu and Wenxuan. Although my topic was different from theirs, I learned so much through our conversations: from the magical world of synthesis to the multiple little details necessary to make a real battery work. Beyond the science, I thank them for creating an atmosphere that was collaborative, fun, and supportive; I could not have hoped for a more collaborative and enjoyable environment in such a prestigious group. A special mention goes to Hanan, Tim, Jan and Alberto for making my first months in a new country memorable and fun. To my office mates, Chaofan, Hao, Pranav and Ajay, thank you for always being there for any advice, and for scientific and personal discussions. A big thanks to Pranav, always being ready to lend a hand in the lab and for involving me in projects that taught me so much. I am also thankful to former members of the group, Eveline, Tammo, Theo, Pedro, and Jeff, whose experience and critical thinking opened new perspectives and reminded me that there are many paths to becoming a successful scientist. To the lab technicians, Nirmal, Dan, Katarina, Frans, being aware of my little lab experience, you always helped me, even with the simplest tasks and questions. And to Martine and Ilse, thank you for your help with paperwork and the cheerful conversations around the coffee machine.

A profound thank you also goes to the students whose master's end project I supervised, Myrthe, Dimitrios, Floor and Arun. Thanks to you I could discover the pleasure of teaching and working

with brilliant students. I hope the projects we did together help both of us grow, I surely would not have learned so many things if it wasn't for you.

An awesome part of my PhD journey was the time I spent at MIT in the group of Professor Bazant. Precious months for both my scientific and personal development. I so want to thank Professor Bazant for the opportunity, and all the group members, Cristina, Debbie, Young, Suzy, Chan, Daniel, Arjun, Yash, Michael, Xiaochen, and Alex, for welcoming me as if I had always been part of the group. A special thanks to Sam and Shakul, who introduced me to the art of scientific programming and gave me new perspective about modeling, but most importantly, showed me how to have fun in Boston.

I am also very grateful to my flatmates Gabriele, Urbo, and Rudi. You made our home welcoming during those first years, and I am glad our friendship has continue since then; with a special thanks to Rudi who, aside from being a great friend, also became a great collaborator, expanding my scientific horizon, and making me appreciate the importance of the alternative version of reality we call simulations. To my friends spread around the world, both near or far, thank you for staying close and making these years richer in so many ways. A deep thank you to my partner, Ezgi, the best discovery I ever made. Always understanding when I could not sleep until I had tested an idea, always making me feel sure of the light at the end of the project, always happily listening to my presentations. Her advice made my papers and my presentations clearer, her presence made me feel relaxed even in the most difficult days.

Finally, I want to thank my family. They have always supported me with love. Without any pressure for success, they simply allowed my passions for science to grow, leading all the way to this PhD journey, where I could finally achieve my dream of becoming a scientist.

*Grazie*

